Unveiling the Physics of Broad Line Regions in AGNs with GRAVITY

Daryl Joe D. Santos

München 2025

Unveiling the Physics of Broad Line Regions in AGNs with GRAVITY

Daryl Joe D. Santos

Dissertation
der Fakultät für Physik
der Ludwig-Maximilians-Universität
München

vorgelegt von
Daryl Joe D. Santos
aus den Philippinen

München, den 05.06.2025

Erstgutachter: Prof. Dr. Reinhard Genzel
Zweitgutachter: PD Dr. Roberto Saglia
Tag der mündlichen Prüfung: 17.07.2025

Contents

List of Figures

List of Tables

Zusammenfassung

Man geht heute davon aus, dass sich im Zentrum der meisten Galaxien extrem massereiche schwarze Löcher (*supermassive black holes* oder SMBHs) befinden. Enge Korrelationen zwischen ihrer Masse und vielen Eigenschaften ihrer Wirtsgalaxie lassen auf eine wichtige Rolle die SMBHs bei der Entstehung und Entwicklung von Galaxien schließen. Daher ist es von entscheidender Bedeutung, die Massen der SMBHs genau zu messen. Dazu muss jedoch die Region, die vom Gravitationspotenzial der SMBHs dominiert wird, räumlich aufgelöst werden. Innerhalb dieser Region befindet sich die sogenannte *broad-line region* (oder BLR), die für die breiten Emissionslinien in den Spektren aktiver Galaxien verantwortlich ist. Für die genaue Messung der SMBH-Massen ist es daher wichtig, die Physik der BLR zu verstehen. GRAVITY, ein Instrument der zweiten Generation am Very Large Telescope Interferometer (VLTI), bietet eine noch nie dagewesene Präzision, die es ermöglicht, die BLR räumlich aufzulösen und die Masse der SMBHs durch dynamische Modellierung des differentiellen Phasensignals aus interferometrischen Beobachtungen zu messen. Die vorliegende Arbeit studiert anhand von GRAVITY-Daten die Physik der BLR und die Erkenntnisse, die sich daraus ergeben, für das Szenario der Koevolution von SMBHs und ihren Galaxien.

Diese Dissertation ist in drei Teile gegliedert, die auf drei Arbeiten zum Hauptthema des Verständnisses der BLR-Physik mit GRAVITY-Beobachtungen beruhen. Der erste Teil (GRAVITY Collaboration et al. 2024, A&A, 684, A167) zeigt neue Analysen von vier lokalen Galaxien mit aktiven galaktischen Kernen (*active galactic nuclei* oder AGNs), die mit GRAVITY beobachtet wurden. Ihre BLRs wurden räumlich aufgelöst, was genaue Messungen ihrer zentralen BH-Massen ermöglicht. Bei der Verwendung aller sieben mit GRAVITY beobachteten lokalen AGNs finden wir eine flachere Steigung in der Radius-Leuchtkraft (R-L)-Relation im Vergleich zur kanonischen R-L-Relation, die auf Messungen mit der Methode des *Reverberation Mappings* oder RM basiert. Für eine solche flachere Steigung spielt entweder die Akkretionsrate eine Rolle (durch Erzeugung kleinerer BLR-Größen bei gegebener Leuchtkraft), oder die Annahme, dass alle AGNs die gleichen Ionisationsspektren haben, ist falsch.

Der zweite Teil dieser Dissertation (Santos et al. 2025a, A&A, 696, A30) stellt eine spektroskopische Durchmusterung von 29 $z \sim 2$ AGNs vor, die mit NTT/SOFI für in Vorbereitung auf GRAVITY+ beobachtet wurden. GRAVITY+ enthält eine Serie von Verbesserungen gegenüber GRAVITY, die den Weg für die Beobachtung von schwächeren AGNs bei höheren Rotverschiebungen ebnen werden. Das Ziel der Durchmusterung ist es, die Quasar-Natur dieser Quellen zu bestätigen und ihre erwarteten interferometrischen

Signale für Beobachtungen mit GRAVITY+ zu bestimmen. Wir konnten jedoch auch interessante Rückschlüsse auf die Emissionslinien- und BLR-Eigenschaften unserer Ziele ziehen. Auf der Grundlage ihrer SOFI-Spektren stellen wir fest, dass die meisten ihrer Hα-Emissionslinien Linienformen (FWHM/σ) aufweisen, die unter dem Gaußschen Grenzwert von 2,35 liegen, was unserer Meinung nach dazu führt, dass die gemessenen Virialfaktoren dieser Quellen niedriger sind als unter der Annahme von Gaußschen Linienformen erwartet. Solche schmäleren Linienformen könnten entweder auf das Vorhandensein sowohl turbulenter als auch rotierender Komponenten in der BLR zurückzuführen sein, oder auf ein Zweikomponenten-BLR-Modell, bestehend aus einem inneren und einem äußeren Teil. Die Quellen weisen geringe Eddington-Verhältnisse auf ($\lambda_{Edd} \sim 0{,}1$), und die meisten von ihnen passen zum BLR-Modell, das von Keplerbewegungen dominiert wird. Zwei Quellen zeigen asymmetrische Hα-Emissionslinien, die nur mit einem BLR-Modell mit radialen Bewegungen rekonstruiert werden können. Schließlich geben die erwarteten differentiellen Phasensignale Aufschluss über die Beobachtbarkeit der Objekte unter Berücksichtigung ihrer (RM-basierten) BH-Massenschätzung und ihrer Abhängigkeit von der gewählten Art der Linienbreitenmessung.

Der dritte und letzte Abschnitt dieser Dissertation (Santos et al. 2025b, bei A&A einzureichen) untersucht das erwartete differentielle Phasensignal und dessen Rekonstruktion mittels eines dynamischen Modells einer strahlungsgetriebenen Fontäne (RDF), das weithin verwendet wird, um die Entstehung und die Physik der BLR durch Systeme mit strahlungsdruckgetriebenen vertikalen Ein- und Ausströmen zu erklären. Wir simulieren eine GRAVITY-Beobachtungskampagne eines aus der RDF-Simulation erzeugten BLR mit der gleichen BH-Masse und AGN-Leuchtkraft wie NGC 3783, einem der mit GRAVITY beobachteten AGNs mit niedriger Rotverschiebung, dessen BLR räumlich aufgelöst wurde. Mit Hilfe des Spektralsynthese-Codes CLOUDY wird das Brγ-Linienprofil des Modells erzeugt, während die differentielle Phase aus den Photozentren der Zellen in der Simulation berechnet wird. Die differentiellen Phasen- und Flussspektren der RDF-Simulation werden mit dem phänomenologischen Pancoast-Modell der BLR modelliert, das in GRAVITY- und RM-Arbeiten häufig verwendet wird. Unsere Ergebnisse zeigen, wie schwierig es für das Pancoast-Modell ist, die geometrischen und kinematischen Eigenschaften der Simulation wiederherzustellen, insbesondere die ausströmende Natur, obwohl die BH-Masse und die BLR-Größe konsistent mit unseren aus der Simulation abgeleiteten Werten übereinstimmen. Das Pancoast-Modell ist auch in der Lage, das durchschnittliche Bild der Simulation wiederherzustellen, nämlich das einer dünnen BLR-Scheibe, die von der Keplerschen Bewegung dominiert wird. Wir beobachten, dass die berechnete differentielle Phase der Simulation asymmetrisch ist, was wir auf die Asymmetrie der LoS-Geschwindigkeitsverteilung zurückführen. Wir betonen die Wichtigkeit zukünftiger Arbeiten zur Verbesserung unserer aktuellen Arbeit, wie z. B. das Hinzufügen von Streuphysik, um eine gleichmäßigere simulierte Brγ-Emissionslinie mit nur einer Spitze zu erzeugen, das Untersuchen weiterer Schnappschüsse der Simulation, das Untersuchen des Super-Eddington-Falls der Simulation, das Untersuchen anderer möglicher radialen und winkelmäßigen Verteilungen und die Untersuchung der Durchführbarkeit anderer Scheibenwindsimulationen anstelle der RDF-Simulation.

Summary

Supermassive black holes (SMBHs) are believed to reside in the centre of most galaxies and have a vital role in galaxy formation and evolution, as indicated by the tight correlation between their masses and their host galaxy properties. It is, therefore, crucial to accurately measure SMBH masses. However, doing so requires spatially resolving the sphere of influence where the gravitational potential of the SMBH dominates. Within this region is the broad line region (BLR), which is responsible for the broad emission lines detected in the spectra of active galaxies. This emphasises the importance of studying the physics of the BLR in accurately measuring SMBH masses. GRAVITY, the second-generation instrument at the Very Large Telescope Interferometer (VLTI), provides unprecedented precision, allowing one to spatially resolve the BLR and measure the SMBH mass through dynamical modelling of the differential phase signal taken from interferometric observations. This work exploits the capability of GRAVITY to unveil the physics of BLR for the grand purpose of better understanding the SMBH-galaxy coevolution scenario.

This dissertation is divided into three parts that all focus on understanding BLR physics with GRAVITY observations. The first one (GRAVITY Collaboration et al. 2024, A&A, 684, A167) shows the analyses of four new low-redshift active galactic nuclei (AGNs) observed with GRAVITY. Their BLRs have been spatially resolved, allowing accurate measurements of their central BH masses. Upon utilising all seven low-redshift GRAVITY-observed AGNs, we find a shallower slope in the radius-luminosity (R-L) relation compared to the canonical R-L relation based on reverberation mapping (RM) measurements. Several reasons for such a shallower slope include either the apparent role of accretion rate in producing smaller BLR sizes at higher luminosity, or the assumption that all AGNs have the identical ionising spectra is wrong.

The second part of this dissertation (Santos et al. 2025a, A&A, 696, A30) presents a preparatory spectroscopic survey of 29 $z \sim 2$ AGNs observed with NTT/SOFI for the advent of GRAVITY+, the series of improvements in GRAVITY which will pave the way for observations of fainter and high-redshift AGNs. The survey aims to confirm their quasar nature and determine their expected interferometric signals for GRAVITY+ observations. However, we were also able to draw interesting conclusions about the emission line and BLR properties of our targets. Based on their SOFI spectra, we find that most of their Hα emission lines have line shapes (full-width-half-maximum to dispersion ratio or FWHM/σ) less than the Gaussian value of 2.35, which we purport to cause the measured virial factors of these targets to be lower than expected assuming Gaussian line shapes. Such smaller

line shapes could be attributed to either the presence of both turbulent and rotational components in the BLR, or a two-component BLR model composed of an inner and outer part. The targets show moderate Eddington ratios ($\lambda_{\rm Edd} \sim 0.1$), and most are fitted with the BLR model dominated by Keplerian motion. Two targets show asymmetric Hα emission lines, which can only be fitted with a BLR model dominated by radial motions. Lastly, their expected differential phase signals provide insights into the observability of the targets while considering their single-epoch BH mass estimates and their dependence on the chosen line width measurement.

The third and last section of this dissertation (Santos et al. 2025b, to be submitted to A&A) studies the differential phase signal and reconstruction via dynamical modelling of the radiation-driven fountain (RDF) simulation that is widely used to explain the formation and physics of the BLR through vertical inflow-outflow systems due to radiative pressure. We simulate a GRAVITY observational campaign of a BLR generated from the RDF simulation with the same BH mass and AGN luminosity as NGC 3783, one of the low-redshift AGNs observed with GRAVITY, whose BLR has been spatially resolved. Using the spectral synthesis code, `CLOUDY`, the Brγ line profile of the model is generated, while the differential phase of the simulation is calculated from the photocentres of the cells in the simulation.The differential phase and flux spectra of the RDF simulation are fitted with the Pancoast model, a phenomenological model of the BLR that is widely used in GRAVITY and RM works. Our findings highlight the difficulty of the Pancoast model in recovering the geometric, angular, and kinematic properties of the simulation, especially its outflowing nature, despite successfully yielding consistent BH mass and BLR size with our ground truth values derived from the simulation. The Pancoast model is also able to recover the average picture of the simulation, which is a thin disc BLR dominated by Keplerian motion. We observe that the calculated differential phase of the simulation is asymmetric, which we purport is due to the asymmetry of its LoS velocity distribution. We emphasise the importance of future works in improving our current work, such as adding scattering physics to produce a smoother and single-peaked simulated Brγ emission line, investigating more snapshots of the simulation, looking into the super-Eddington case of the simulation, studying other possible prescriptions of the radial and angular distribution of the Pancoast model, and understanding the feasibility of studying other disc-wind simulations instead of the RDF simulation.

Chapter 1

Introduction

When French astronomer Charles Messier first discovered some "fuzzy" objects in the sky, he was worried that other comet hunters like himself might be confused spotting them. He therefore created a list of such objects called the Messier list, with the objects labelled as "M" for "Messier" followed by a number. An argument over whether these objects were "island universes" or nebula within our own Milky Way soon became prominent (Messier, 1781). It was not until the 1920s when Edwin Hubble measured the distance of one of the Messier objects (Hubble, 1922), proving the existence of galaxies outside the Milky Way. A century later, scientists' understanding of galaxies has improved; from their first formation to their evolution, current appearances, diverse morphologies, properties and underlying correlations, effects on their immediate environment and large-scale regions, and many others. However, there are still mysteries surrounding galaxy formation and evolution. One of the important ingredients in solving these is the understanding of the supermassive black hole (SMBH), which is believed to reside in the centre of most large galaxies (Kormendy and Ho, 2013). A black hole (BH) is a compact and massive astronomical object which has a very strong gravity that causes anything, even light, to be pulled towards it. BHs were not in the spotlight of galaxy formation and evolution until Schmidt (1963) discovered the high redshift of the radio source 3C 273, $z = 0.158$. Its very bright luminosity and variability first introduced the accretion of a central BH as its primary source of luminosity, and so decades of hard work related to the idea soon followed (e.g. Hoyle et al., 1964; Salpeter, 1964; Lynden-Bell and Rees, 1971).

Over the years, a new branch of astrophysics has been dedicated to studying BHs. However, since BHs cannot be directly observed, we turn to observing their indirect signatures, which we can recover from various observations (i.e. photometry, spectrometry, interferometry, gravitational lensing, etc.). By studying indirect signatures of SMBHs for decades, we have already come to the conclusion that the growth of the central SMBH and its host galaxy are interconnected via complex processes (Kormendy and Ho, 2013; Heckman and Best, 2014; Capelo et al., 2024; Harrison and Ramos Almeida, 2024). Most SMBH studies rely on detecting the electromagnetic radiation produced by their accretion of materials surrounding them. Such galaxies with actively accreting SMBHs are called active galaxies, and the core region of such a galaxy is called an active galactic nucleus (AGN) (Peter-

son, 1997; Krolik, 1999). The resulting electromagnetic radiation is of non-stellar origin and encompasses the infrared (IR), radio, ultraviolet (UV), and X-ray (Jones et al., 2015; Schneider, 2015). By studying AGNs, we can get a better picture of the interconnection between the central BH and host galaxy growth and how galaxies form and evolve across cosmic time.

1.1 Active Galactic Nucleus (AGN)

This section provides a brief definition of AGN and a brief history of studies focusing on AGN activity. Different kinds of AGNs and the unified model that tries to explain the existence of such classifications are also discussed in this section. Lastly, a discussion about the broad line region (BLR), which is the main focus of this thesis, is presented.

1.1.1 Definition and Brief History

An AGN is broadly defined as the manifestation of energetic phenomenon in the central region, or nucleus, of galaxies which cannot be directly connected with stellar processes (Peterson, 1997). An *active* galaxy is defined as a galaxy that hosts an AGN. The history of AGN studies began with the first optical spectrum of an active galaxy from the object NGC 1068, which was taken and presented by Fath (1909) at the Lick Observatory (a more detailed discussion of the history of AGN studies is presented in Shields 1999). About 8 years later, Slipher (1917) published a higher quality and resolution spectrum of NGC 1068 taken at the Lowell Observatory. An important point from the work of Slipher (1917) is that the emission lines observed from NGC 1068 are resolved, are similar to those of planetary nebulae, and have widths of hundreds of kilometres per second. It was Carl Seyfert who first realized that other galaxies possess similar properties as NGC 1068 (Seyfert, 1943). In his work, he discovered that the spectrograms of six galaxies he observed showed very broad lines, with widths of about 3000 - 8000 km s^{-1}. However, these Seyfert galaxies did not gain traction until radio astronomy flourished in the next decades, which started with the detection of radio waves from the central region of the Milky Way, which is called Sagittarius A by Karl Jansky (Jansky, 1932). Several works have continued in Jansky's work, which included mapping the sky and observing distinct sources other than the Sun in radio wavelengths (e.g. Reber, 1944; Hey et al., 1946; Bolton and Stanley, 1948; Bolton et al., 1979)

The biggest milestone of such radio astronomy studies was when Maarten Schmidt obtained the spectra of 3C 273, which allowed him to infer through the observed wavelengths of the Balmer series that the redshift of 3C 273 is $z = 0.158$ (Schmidt, 1963). Greenstein and Schmidt (1964) proposed a model to explain such phenomenon observed in 3C 273 and 3C 48 which also showed similar properties as the former: a central source with a mass of order 10^9 $M_\odot$ emitting optical continuum is surrounded by an emission-line region and a much larger radio-emitting region, and the resulting bright glare from such a bright source obscures the host galaxy. This became the foundation of our current un-

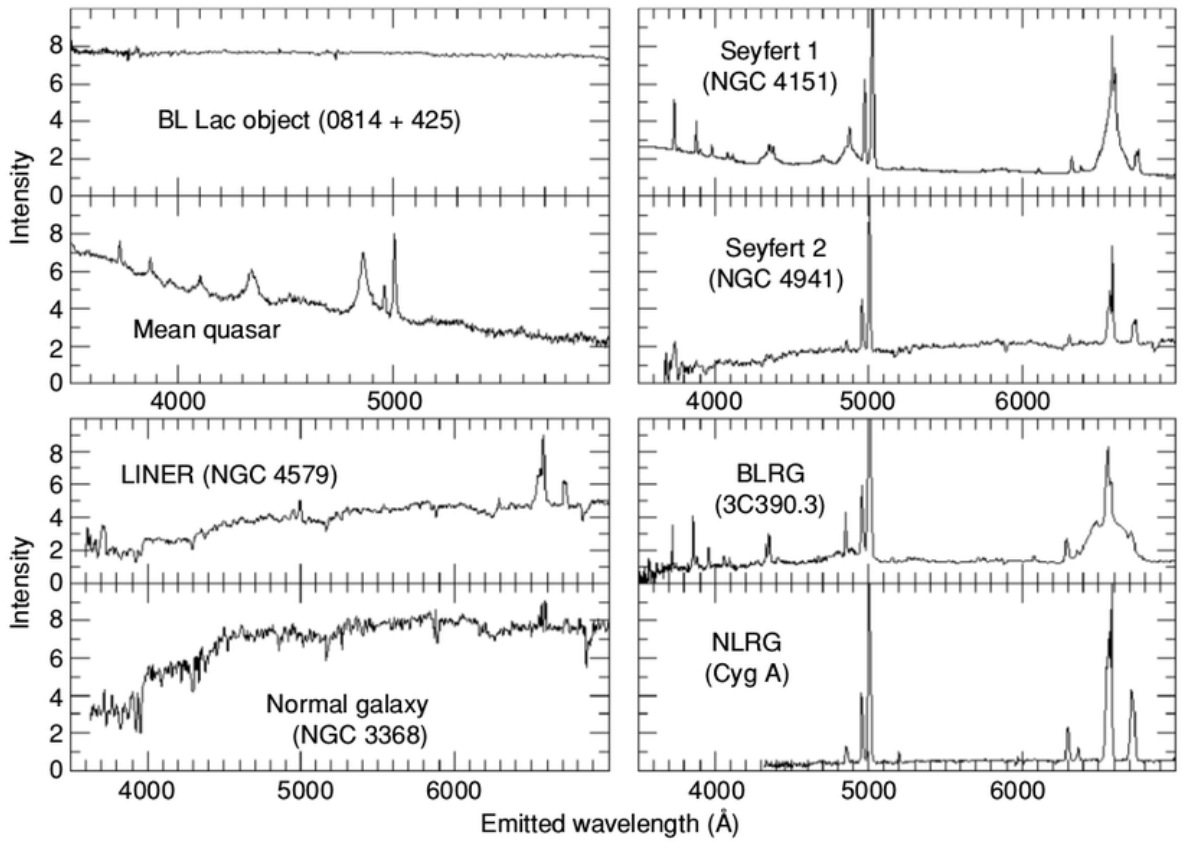

Figure 1.1: Typical optical spectra of different types of AGNs. Taken from W. Keel (priv. comm.)

derstanding of AGNs. Eventually, more and more radio sources with starlike images and broad emission lines are discovered. They were named *quasi-stellar radio sources (QSRS), quasi-stellar sources (QSS), quasi-stellar objects (QSO), or quasars*. Their large redshifts proved quasars to be potential tools to study cosmology (e.g. Terrell, 1964; Arp, 1966; Gunn, 1971), making studies of quasars much more enticing to the astronomy community.

1.1.2 AGN Classifications

AGN terminologies are usually perplexing and may require looking into their historical context before fully understanding them. In this section, we attempt to summarise the major classifications of active galaxies. AGN classifications normally depend on the observed properties of the AGN in a certain waveband. For instance, due to the roots of AGN studies from radio astronomy, AGNs are usually classified as radio-quiet and radio-loud AGNs, with the former producing energetically insignificant ejections from the central region and the latter exhibiting large-scale radio jets and lobes. Radio-quiet AGN host galaxies are usually spiral galaxies, while radio-loud AGN host galaxies are usually elliptical galaxies that have undergone recent mergers (Wilson and Colbert, 1994). Radio-quiet AGNs are comprised of Seyfert galaxies, radio-quiet quasars, and low-ionisation nuclear emission-line

regions (LINERs). In contrast, radio-loud AGNs are composed of radio galaxies, radio-loud quasars, and blazars. Fig. 1.1 shows a sample spectrum for each type.

Seyferts

Seyferts or Seyfert galaxies consist of AGNs of lower luminosity, which allow detection of their host galaxies. Their AGNs have a comparable luminosity to their host galaxies, i.e. $\sim 10^{11}$ $L_\odot$. Most of these host galaxies have spiral morphologies. Spectroscopically speaking, their AGNs produce strong, high-ionisation emission lines. The width of their emission lines (usually the Balmer series) dictates two subclasses of Seyfert galaxies: Type 1 and Type 2. Type 1 Seyferts produce lines which are a superposition of a "narrow component" with several hundreds of kilometers per second of line width and originates from a low-density ($n_e \approx 10^3$-10^6 cm^{-3}) region of ionized gas, and a "broad component" usually present in the permitted lines only and with widths ranging from 10^3-10^4 km s^{-1} and originates from a ionised gas region of much higher density ($n_e \gtrapprox 10^9$ cm^{-3}). On the other hand, Type 2 Seyferts do not show broad components in their permitted lines, thus presenting only the narrow lines (Dibai, 1971; Peterson, 1997; Curran, 2000). This dichotomy is due to the potential obscuration of the broad line-emitting region due to a dusty structure (to be discussed in The AGN Unified Model subsection).

More recent works have introduced newer notations of Seyfert subclassifications based on optical spectrum properties and are considered subclasses between Type 1 and Type 2 Seyferts (Osterbrock, 1978). However, caution is needed in using these other subclasses as the broad component of Seyferts are known to exhibit variability with timescales ranging from days to years (Peterson, 1997; Leighly, 1999; Rosenblatt et al., 1999; Markowitz et al., 2003; Klimek et al., 2004; Hernández-García et al., 2015). On the other hand, Type 1 Seyferts are further classified as narrow-line Seyfert 1 (NLSy1) and broad-line Seyfert 1 (BLSy1), with the latter understood as the more common definition of Type 1 Seyferts. NLSy1s comprise a more distinct class of Type 1 Seyferts as they have relatively narrower Balmer lines (only slightly broader than the widths of their forbidden lines, $\lesssim 2000$ km s^{-1}), [OIII]λ5007/Hβ intensity ratio smaller than 3, strong Fe II emission lines, and steeper soft and hard X-ray spectra (Osterbrock and Pogge, 1985; Boller et al., 1996; Nagao et al., 2001; Véron-Cetty et al., 2001). Their extreme properties are believed to be caused by their relatively lower BH masses and higher Eddington rates than most Type 1 Seyferts (e.g. Boroson, 2002).

Quasars

Quasars are star-like in appearance due to their very high luminosities and compact sizes. They comprise the most luminous AGNs in the Universe, and they are so bright that there are dedicated studies in separating the host galaxy light from the AGN for these objects (e.g. Laor, 1998; Percival et al., 2001; Ding et al., 2023). They can be observed at a large cosmological distance due to their brightness, making them good laboratories for studying cosmology and probing galaxy evolution (e.g. Falomo et al., 2004; Peng et al.,

2006; Mortlock, 2016). In fact, quasars have been detected from $z \sim 0.3$ (Russell et al., 2024) up to $z \sim 11$ (Maiolino et al., 2024). Quasars have spectra similar to those of Seyferts, except they have weaker (or almost non-existent) stellar absorption features due to the AGN overpowering the host galaxy, and weaker narrow lines relative to their broad lines compared with Seyferts (Peterson, 1997). Quasars can be further classified as radio-loud and radio-quiet depending on their radio power (Goldschmidt et al., 1999).

Radio galaxies

Radio galaxies are sources with substantial nuclear and extended radio emissions found in the optical wavelengths (Matthews et al., 1964). This radio emission is due to synchrotron radiation, radiation emitted by highly relativistic electrons and/or positrons in the presence of magnetic fields (Hardcastle and Croston, 2020). Radio galaxies usually appear more often as elliptical galaxies than spirals (Peterson, 1997) and are usually characterised by the existence of jets where material from the central region of the galaxy is expelled at relativistic speeds (e.g. Saikia, 2022). Similar to Type 1 Seyferts, they are also subclassified into broad-line radio galaxies (BLRGs) and narrow-line radio galaxies (NLRGs), and so these subclassifications can be considered as the radio counterparts of Type 1 Seyferts (Peterson, 1997).

LINERs

LINERs, or low-ionisation nuclear emission-line region galaxies, comprise the low nuclear-luminosity AGNs and were first identified by Heckman (1980). Compared with other types of AGNs, LINERs are more common in the Universe and are believed to be detectable for almost half of all spiral galaxies (Ho et al., 1994; Peterson, 1997). Compared with higher luminosity AGNs like Seyferts and quasars that have high-ionisation emission lines, the spectra of LINERs are more dominated by low-ionisation lines (Hermosa-Muñoz et al., 2020). LINERs are usually identified via spectral diagnostic diagrams (i.e. Baldwin-Phillips-Terlevich or BPT diagrams; Baldwin et al. 1981) using optical (Veilleux and Osterbrock, 1987; Kewley et al., 2006) or mid-infrared (Sturm et al., 2005, 2006; Herpich et al., 2016) emission line ratios. However, there are also a few numbers of LINERS that are explained by shock ionisation models (Franceschini et al., 2005), photoionisation due to post-asymptotic giant branch (AGB) stars (Binette et al., 1994), and merger activities in ultraluminous infrared galaxies (Monreal-Ibero et al., 2006).

Blazars

Blazars are AGNs whose relativistic jets are directed almost towards the observer, causing them to appear much brighter than they would be if their jets are pointed away from the Earth due to relativistic amplification (Blandford and McKee, 1982a). They are classified further as either flat-spectrum radio quasars (FSRQs) or BL Lac objects, which are named after the prototype BL Lacertae, which was the first of its kind. The two subclasses are defined based on their rest-frame equivalent width (EW) of their optical emission lines

(Stickel et al., 1991), with FSRQs showing broad emission lines with EW $>$ 5 Å while BL Lacs show weak or almost no emission (and absorption) lines in their optical spectra. The first BL Lac object, BL Lacertae, was initially classified as a variable star (Hoffmeister, 1929), but its radio counterpart was found almost 40 years after (MacLeod and Andrew, 1968). Now, blazars, including BL Lacs, are believed to exhibit rapid variability at almost all wavelengths from radio to gamma rays (Urry, 1996). Another subclass of blazars called optically violently variable (OVV) quasars are radio-loud galaxies similar in observed properties to that of BL Lacs; the only difference is that OVV quasars show high polarisation (much higher than the usual $\sim$1% for most AGNs) which also varies in both magnitude and position angle (Peterson, 1997; Wright et al., 1998).

X-ray AGNs

Aside from AGN classifications via radio observations and optical spectra, AGNs can also be identified via X-ray observations. For instance, the Fe (iron) Kα line at 6.4 keV is a characteristic emission line of AGNs detected in most X-ray spectra of AGNs. This emission line is produced when an X-ray photon interacts with an Fe atom, causing its K-shell electron to be knocked out, and a higher energy (L-shell) electron drops down to fill the vacancy (Eze, 2004). By studying the variability, velocity shift, and other properties of the Fe Kα line and even the FeII emission lines in the UV/optical wavelengths, one could gain insights about the geometry of the accretion disc, the mass and spin of the SMBH, and the location of the line-emitting region (Yu and Lu, 2001; Baldwin et al., 2004; Jovanović, 2012; Kinch et al., 2016). The X-ray flux of an object could also serve as smoking gun evidence of the presence of an AGN. Most point-like (physical sizes smaller than 2 kpc) sources in X-ray surveys with integrated (soft) X-ray luminosities $\geq 10^{42}$ erg s^{-1} are normally identified as AGNs (Mushotzky, 2004; Hickox and Alexander, 2018).

One could identify dust-obscured X-ray AGNs by measuring the hardness ratio of their X-ray spectra, which is defined as the ratio of the hard ($\sim$ 5-10 keV) X-ray photons (H) and soft ($\lesssim$ 5 keV) X-ray photons (S): $HR = (H - S)/(H + S)$ (e.g., Wang et al., 2004; Stern et al., 2012). Hardness ratios are used to estimate column densities (e.g., Tajer et al., 2006); a high hardness ratio indicates a significant amount of X-ray absorption, which is normally caused by high column densities ($N_H \geq 10^{22}$ cm^{-2} Tozzi et al. 2006). Some obscured X-ray AGNs have so much dust with column densities as high as $N_H \sim 10^{24}$ cm^{-2}. Such heavily obscured AGNs cause X-ray photons from the accretion disc to be attenuated via Compton scattering, which yields an X-ray spectrum dominated by reflected emission (the so-called Compton hump which peaks between 20-30 keV). These heavily obscured AGNs are called Compton-thick AGNs (e.g., Comastri, 2004; Hickox and Alexander, 2018), and these are challenging to observe with X-ray wavelengths, making multiwavelength observations crucial for detecting them (e.g., Daddi et al., 2007; Severgnini et al., 2012; Guo et al., 2021).

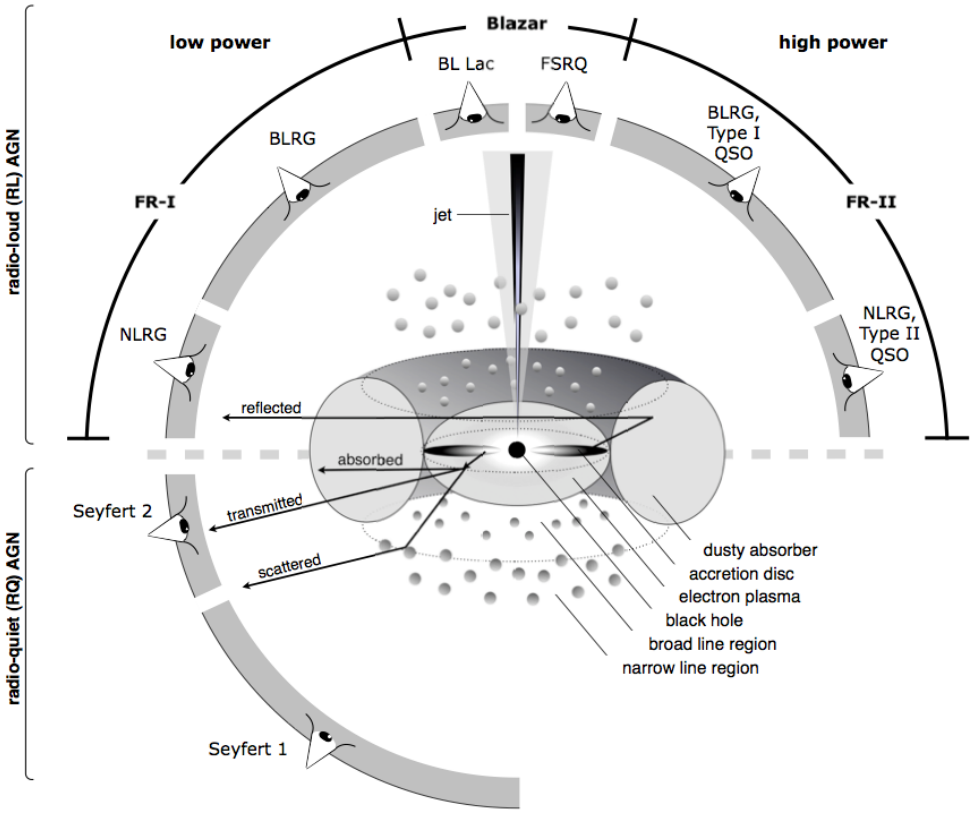

Figure 1.2: The AGN unified model. Taken from Beckmann and Shrader (2012)

The AGN Unified Model

Why are there so many types of AGNs? The unified model of AGN tries to explain this by correlating the variety of AGNs with the viewing angle of the observer with respect to the AGN and not due to any intrinsic differences among AGN types (Antonucci, 1993; Urry and Padovani, 1995; Netzer, 2015). Fig. 1.2 shows the schematic diagram of the AGN unified model from Beckmann and Shrader (2012). According to this model, the AGN is composed of the BH at the center, the accretion disc which is created from the angular momentum of the infalling material and is responsible for the extreme ultraviolet radiation (EUV) emission of the system (e.g. Ross et al., 1992), the corona or electron plasma which is a hot cloud of electrons that produces that hard X-ray power-law continuum (e.g. Fabian et al., 2017), the broad line region (BLR) which is responsible for the broad emission lines seen in the optical and UV spectra of AGNs (e.g. Shapovalova et al., 2009), the narrow line region (NLR) which is less compact and larger in size compared to the BLR and is responsible for the narrow emission lines in the AGN spectra (e.g. Netzer and Laor, 1993), and the dusty absorber (which is also called the dusty torus in other literature) which is believed to contain very optically-thick dusty clouds (e.g. Krolik and Begelman, 1988) and whose obscuration is responsible for the observed variety of AGNs (e.g. Nenkova et al., 2008). The dusty torus covers the central engine of the AGN, and is responsible for the dichotomy between narrow- and broad-line AGNs: when the line of sight is almost perpendicular to the axis of the torus (i.e. face-on geometry), the BLR can be observed, causing broad lines to appear in the AGN spectrum. Otherwise, when the line of sight is parallel to the axis of the torus (i.e. edge-on geometry), the torus hides the BLR, and only the narrow lines are present in the AGN spectrum. The existence of a dusty structure obscuring the central region was also motivated by findings of previous works wherein some Type 2 objects exhibit polarised broad emission lines, which suggests that these broad emission lines were scattered into our line of sight (Moran et al., 2000; Nagao et al., 2006). The presence of a jet in the AGN and its relative position with respect to the observer's line of sight also gives rise to the different types of radio-loud AGNs as shown in Fig. 1.2.

1.1.3 The SMBH mass and the Broad Line Region (BLR)

Eddington accretion

What could be the typical mass of a SMBH in the centre of a galaxy? This can be estimated by assuming a simple model where the system is virialised (i.e. stable under the sole influence of gravity), no anisotropy is present in the emission of the system and only completely ionised hydrogen gas is present (Peterson, 1997). For accretion to proceed, the inward gravitational force must be greater than or equal to the radiation pressure exerted by the photons on the electrons:

$$\begin{aligned} F_{\text{grav}} &\geq F_{\text{rad}} \\ \frac{GMm_p}{r^2} &\geq \frac{\sigma_e L}{4\pi c r^2} \end{aligned} \tag{1.1}$$

where G is the gravitational constant, M is the SMBH mass, m_p is the mass of the proton, r is the radius of the SMBH, σ_e is the Thomson cross-section of the electron, L is the luminosity of the system, and c is the speed of light. Rearranging this equation to calculate L gives us:

$$L \leq \frac{4\pi GMcm_p}{\sigma_e} \tag{1.2}$$

This is the Eddington limit: any source that illuminates beyond the luminosity will have the radiation pressure overpower the inward gravitational force, causing gas to be blown away. A source accreting within this limit is said to undergo the Eddington accretion-limited scenario. Beyond this limit, the source is said to have a very high mass accretion rate, causing its luminosity to increase such that the inflowing/accreting material starts to be blown away due to increased radiation pressure (Eddington, 1926). Such a process is called super-Eddington accretion.

By using the values of the known constants, this equation can be further simplified in units of BH mass:

$$L_{\text{edd}} \approx 1.26 \times 10^{38}\ (M/M_\odot)\ \text{ergs s}^{-1} \tag{1.3}$$

The Eddington ratio is defined as the ratio between the (bolometric) luminosity of the source and the Eddington luminosity. The Eddington accretion rate, on the other hand, is the mass accretion rate at which the source can reach L_{edd}. This is defined as:

$$\dot{\text{M}}_{\text{Edd}} = \frac{L_{\text{Edd}}}{\eta c^2} \tag{1.4}$$

where η is the accretion efficiency constant, which defines the efficiency of the object in converting the accreted material into radiation. This constant has varying definitions across literature as it is also a function of the accretion rate (Marziani et al., 2024).

For a Seyfert AGN luminosity of 10^{44} erg s^{-1} assuming the AGN is radiating at approximately the Eddington (accretion) rate (which is usually defined as $\dot{\text{M}}$ and has units of $M_\odot$ yr^{-1}), the resulting SMBH mass is about 10^6 $M_\odot$. On the other hand, a quasar luminosity of 10^{46} erg s^{-1} will yield a SMBH mass of about 10^8 $M_\odot$.

Sphere of Influence

To measure the BH mass, one needs to probe the sphere of influence of the BH where its gravitational potential dominates. This is well-defined with the following equation:

$$\text{r}_{\text{BH}} = \frac{GM_{\text{BH}}}{\sigma_*^2} \tag{1.5}$$

where σ_* is the (bulge) stellar velocity dispersion. Assuming a typical BH mass of 10^8 $M_\odot$ and a typical stellar velocity dispersion of 200 km s^{-1}, the radius of the BH's sphere of influence is $r_{BH} \sim 10$ pc. Since the BLR has a scale of about 10^{-2} to 1 pc (e.g. Netzer, 1990; Bentz et al., 2013), the BLR gas is well within this region (Denney et al., 2009), which makes the BLR play an important role in BH mass measurements: resolving the BLR which occurs inside the sphere of influence will lead to an accurate BH mass measurement.

Properties of the BLR

Earlier studies of the broad lines in the AGN spectra have allowed us to infer the properties of the BLR. First, the broad lines are all from permitted line transitions (e.g. hydrogen Lyman and Balmer series, Mg II, CI IV, etc.), which means that the clouds which emit such broad lines are of high density, causing all forbidden lines to be collisionally suppressed. Indeed, hydrogen densities within the BLR are at least 10^8 cm^{-3} and go as high as 10^{13} cm^{-3} (Netzer, 1990; Ilić et al., 2009; Müller and Romero, 2020). In addition, the widths of these broad lines reach up from thousands to tens of thousands of km s^{-1} (Müller and Romero, 2020). The BLR temperatures have been found to be high as well, ranging from about 5000 K to $\sim 10^4$ K (Ilić et al., 2009; Peterson, 1997). This corresponds to thermal line widths/velocity dispersions of the order of tens of km s^{-1} by using the following formula:

$$v \approx \frac{k_B T}{m_p} \tag{1.6}$$

where k_B is the Boltzmann constant and m_p is the mass of the proton. Since the observed line widths in the broad lines of AGN spectra are in the order of thousands of km s^{-1}, this would mean that there is another process aside from thermal broadening that causes such large line widths. In this case, the answer is Doppler broadening: different velocities of BLR clouds produce a cumulative broadening of the line. This implies that the BLR is located in a deep gravitational potential and is therefore close to the central BH (Peterson, 1997).

BLR Models

One of the essential questions about the BLR is what it looks like. Most works have suggested that the BLR possesses a thin disk-like geometry that is gravitationally dominated by the central BH and may possess winds as well (e.g., Wills and Browne, 1986; Murray and Chiang, 1997; Popović et al., 2004). In line with this, several arguments were put forward to describe the BLR either as a system composed of discrete clouds or a smooth, continuous medium. Earlier pictures of the BLR were based on previous observations of Galactic nebulae by astronomers who previously worked on nebular physics. This caused them to consider the cloud model of BLR; that is, the BLR is comprised of a large number of identical line-emitting clouds with a certain radius (Peterson, 1997). A typical number of clouds ranges from 10^7 to 10^8 (Peterson, 1997; Arav et al., 1997, 1998). Several models have been put forward to explain the origin of such discrete clouds: bloated supergiant

stars due to their ionising radiation field, gas streams generated by tidally disrupted stars or by star-disk collisions, gravitationally unstable outer disk, or density enhancements due to accretion shocks (see Laor et al. 2006a and references therein). However, such a discrete model of the BLR is challenged by the observed smoothness of broad line profiles taken at high spectral resolution, which should not be viable if the line-emitting region is composed of discrete units (unless the BLR has an almost infinite number of discrete clouds; Arav et al. 1997, 1998). An alternative description of the BLR, which is a continuous hydrodynamical flow of material, has also been put forward. The continuous flow model is preferred over the discrete cloud model due to the observed lack of microstructures in the line profiles, which are expected if the BLR emission is a result of contributions from individual emitting clouds (Dietrich et al., 1999; Arav et al., 1997, 1998).

Although many works have shown that the dominant motion in the BLR is Keplerian or circular (e.g. Gaskell, 2000; Denney et al., 2009; Bentz et al., 2010; Williams et al., 2018; Bentz et al., 2021b; Villafaña et al., 2023), there have also been works that show evidence of considerable turbulence in the direction perpendicular to the BLR midplane, with significant inflow and outflow velocity components (Osterbrock, 1978; Ulrich and Horne, 1996; Grier et al., 2017b). Several pieces of evidence of possible inflow and outflow signatures for some BLRs have also been found (e.g., Kollatschny and Dietrich, 1997; Denney et al., 2009; Bentz et al., 2009, 2010; Du et al., 2016b). This has led previous works to hypothesize the BLR to be composed of radially-moving (inflowing/outflowing) clouds, as seen by earlier and recent observational works (e.g. Done and Krolik, 1996; Ferland et al., 2009; Gaskell, 2010). Hence, outflowing models of BLR have been proposed to explain such phenomena. Most of these models consider the torus or the accretion disk as the source of such outflows. For instance, the outflow model by Elvis (2000) suggests that the instabilities in the accretion disk produce vertical winds that flow in the shape of a funnel. The observed line strength and width depend on the orientation of the observer with respect to the plane of the BLR. These dusty winds are believed to be launched from parsec scales and reach up to subparsec environments (Hönig, 2019). Similar models could explain the existence of double-peaked broad emission lines, variabilities in line profile asymmetries, and peak shifts in low-ionisation lines such as Hα, Hβ, and Mg II (Murray et al., 1995; Chiang and Murray, 1996; Czerny and Hryniewicz, 2011; Waters et al., 2016; Naddaf, 2024). Another slightly similar explanation is the failed radiatively accelerated dusty outflow (FRADO) model, wherein the winds from the accretion disk cause material to infall after rising enough for the radiation support to dissipate (Czerny and Hryniewicz, 2011; Czerny et al., 2015, 2017). An alternative explanation is that the BLR connects the outer edge of the accretion disk to the inner edge of the hot dust structure (dusty torus), which lies above the bowl-shaped torus. Such BLR model could explain the reverberation data of several AGNs (e.g., Kawaguchi and Mori, 2010, 2011; Goad et al., 2012; Ramolla et al., 2018). The dusty torus has also been suggested to be created similarly to how the BLR was formed. With the "radiation-driven fountain" model of the dusty torus, the changing-look phenomenon (i.e. an AGN changes from type 1 to type 2 and vice versa) and obscuration of AGNs can be well-explained (Wada, 2011, 2015; Wada et al., 2023). Baskin and Laor (2018) also purported that such winds would also lead to the creation

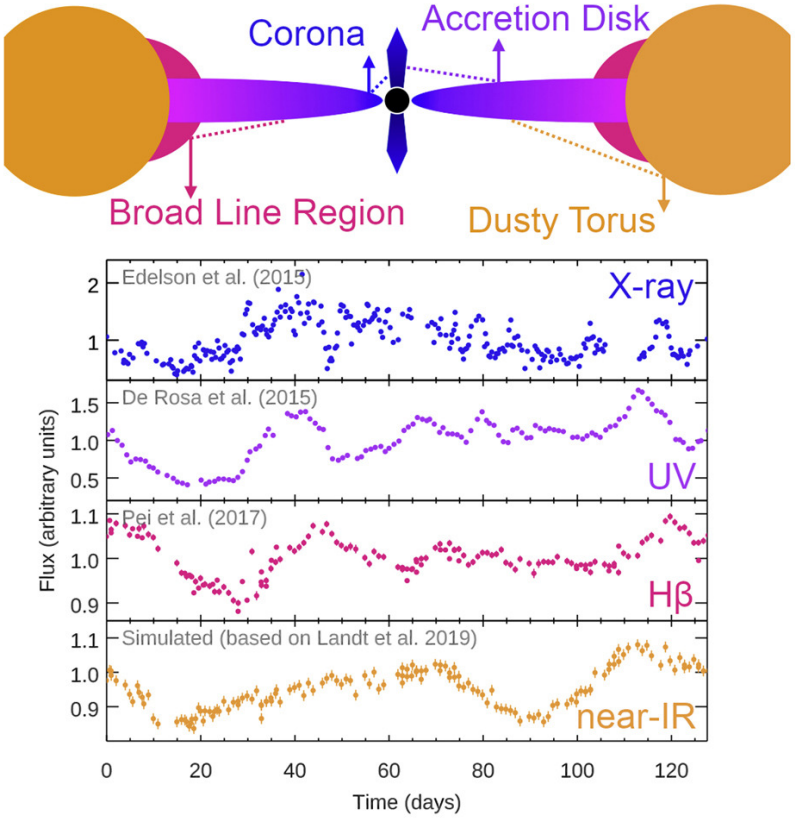

Figure 1.3: Schematic diagram showing how RM works. The corona and accretion disk emit the presented X-ray and UV continuum (as a function of time), respectively, and these continua reach the BLR before being reemitted, yielding the observed Hβ spectrum whose peaks are shifted by a few days with respect to the peaks in the X-ray and UV continuum. The simulated near-infrared (NIR) continuum, which is expected from the dusty torus after reprocessing the light from the corona and accretion disk, is also shown. Figure taken from Cackett et al. (2021).

of a BLR with an inflated torus-like shape. To summarise, the connection between the accretion disk, the BLR, and the dusty torus remains a mystery, and dusty wind models serve as the leading answer to such a dilemma.

Reverberation Mapping (RM) and Dynamical Modelling

How can one resolve the BLR to estimate the BH mass? Many earlier works have noted the observed flux variability in the AGN spectra, which has a time scale of days to weeks (e.g. Bahcall et al., 1972; Blandford and McKee, 1982a; Peterson, 1998). Such variabilities can be utilised to probe the geometry and dynamics of the BLR through a method called reverberation mapping (RM), wherein one could measure the time lag between the flux variations in the ultraviolet (UV)/optical continuum and the broad emission line fluxes. This is because the UV/optical continuum comes directly from the central ionising region,

the accretion disk. Some of this light goes through the BLR and gets reprocessed and emitted as the observed broad emission line fluxes. Fig. 1.3 shows a schematic diagram of how RM works.

The time it takes for the UV/optical light to reach the BLR is the observed time lag and should correspond to the size of the BLR, considering the speed of light:

$$R_{\rm BLR} \sim c \times \tau_{\rm lag} \tag{1.7}$$

Observations show that higher ionised lines yield shorter time lags, suggesting a stratified ionisation structure for the BLR, and broader line widths, suggesting a virial relationship between the time lag and line width: $\tau_{\rm lag} \propto 1/\Delta v^2$. The resulting $R_{\rm BLR}$ can then be plugged into the virial equation to calculate the central BH mass:

$$M_{\rm BH} = f\frac{R_{\rm BLR}\Delta v^2}{G} \tag{1.8}$$

where G is the gravitational constant, Δv^2 is the line width of the observed broad emission line (either the full-width at half maximum/FWHM or the second moment of the line/$\sigma_{\rm line}$; Dalla Bontá et al. 2020), and f is the so-called "virial factor". Eqn. 1.8 assumes that the BLR is mostly influenced by gravity, exhibiting gravitationally dominated kinematics (Peterson and Wandel, 1999; Peterson et al., 2004).

The virial factor encapsulates the kinematics and geometry of the BLR, making it an uncertain factor as these properties are still unclear, making f the main source of uncertainty in the resulting BH mass (Peterson et al., 2004; Woo et al., 2015; Liu et al., 2024). The resulting $M_{\rm BH}$ uncertainty from reverberation-based masses goes by a factor of ~ 3 (Onken et al., 2004), and the uncertainty goes higher to a factor of ~ 4 when $M_{\rm BH}$ estimated from scaling relations (i.e. $M_{\rm BH}$ vs. the 5100 Å luminosity or L_{5100}; Kaspi et al. 2000; Bentz et al. 2013; Du and Wang 2019; Yu et al. 2020) are considered (Vestergaard and Peterson, 2006a). The chosen line width also plays a role in the uncertainty of $M_{\rm BH}$: the Balmer lines Hα and Hβ have been shown to have consistent line widths and are well-studied in RM and size/radius-luminosity (R-L) relation works (Kaspi et al., 2000; Bentz et al., 2006), while MgII has shown promise as a substitute to the aforementioned Balmer lines due to its line width correlating with that of Hβ despite fewer works of studying MgII time lags (Metzroth et al., 2006; Yu et al., 2021; Wang et al., 2019). However, the C IV line, which is the only viable option for $z \gtrsim 2$ quasars observed with ground-based instruments (Vestergaard, 2002), has been suggested to be a less reliable estimator of BH mass due to its highly blueshifted and asymmetric profile, indicative of possible presence of outflowing gas (Gaskell, 1982; Tytler and Fan, 1992; Marziani et al., 2017).

The earliest RM works have led to the conclusion that the BLR has small scales that are within the sphere of influence of the central BH (Bentz et al., 2013). Most RM projects extend their work from measuring BH masses via time lags to estimating the geometry and kinematics of the BLR. Others extend their work by utilising dynamical modelling of higher-quality data sets with clearly observed velocity-resolved lag structures across the emission line profile of AGNs to obtain BH masses (e.g., Grier et al., 2013a; Du et al., 2018a;

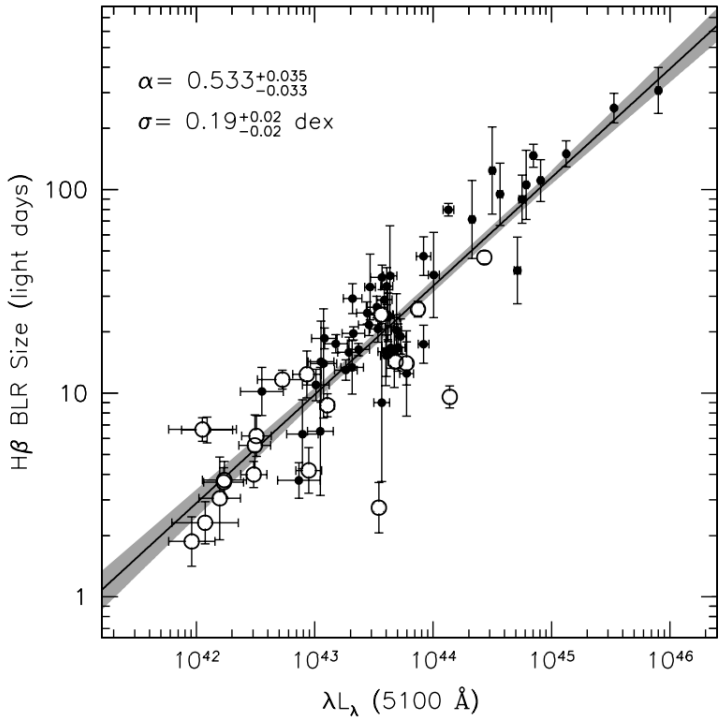

Figure 1.4: The canonical R-L relation based on RM results of low-luminosity AGNs showing the Hβ BLR radius versus the 5100 Å AGN luminosity (Bentz et al., 2013). The figure shows all 71 data points, including the new measurements from Bentz et al. (2013) as open circles. The error bars pertain to 1σ uncertainties, while the black solid line and the grey shaded region are for the best-fit relation and its 1σ uncertainty.

U et al., 2022). Dynamical modelling of the RM data does not rely on the assumption of the virial factor, where most of the uncertainty in the BH mass estimate comes in (Pancoast et al., 2011). One of the widely used dynamical models of the BLR is the one introduced by Pancoast et al. (2014a) and Pancoast et al. (2014b). In their model, the BLR is described as a collection of non-interacting "clouds" that encircle the central BH due to its gravitational potential. The usage of "clouds" in its terminology does not necessarily mean that it follows the discrete cloud model of the BLR. Instead, they should be treated as "line emitting entities" as line emission distribution is the one being modelled and not the physical clouds that comprise the BLR (Kuhn et al., 2024).

The size/radius-luminosity (R-L) relation of AGNs

A critical result of RM studies is confirming the R-L relation in AGNs, which shows that the BLR size increases with increasing AGN luminosity, i.e. $R \propto L^{0.5}$. The relation can be revealed from a simple photoionisation-related derivation (Netzer, 1990; O'Brien et al., 1995; Bentz et al., 2013) starting with the *ionisation parameter*, the ratio of the ionising

photon flux to the gas density, which is given by:

$$U(R) = \frac{Q}{4\pi R^2 N c} \tag{1.9}$$

where $U(R)$ is the ionisation parameter as a function of the distance from the central source, R, N is the cloud density, c is the speed of light, and

$$Q = \int_{\nu_1}^{\infty} \frac{L_\nu}{h\nu} d\nu \tag{1.10}$$

is the flux of ionising photons emitted by the central source. In most cases, $Q(H)$ is calculated, which refers to the photon flux that is ionising the hydrogen atoms. Assuming that U, Q, and N (that is, on average, the ionisation parameters, cloud densities, and ionising spectral energy distribution (SEDs) of AGNs are the same throughout), it can be easily inferred that $R \propto U^{1/2}$. If the above assumptions hold, it implies that the radius at which a specific emission line is most likely produced simply depends on the intensity of the ionising flux. Assuming that the ionising continuum shape does not depend on luminosity, i.e. $L \propto Q$, one could also imply that $R \propto L^{1/2}$.

We note that the result above can apply to any emitting system. The validity of this result is actively sought by works that focus on the NLR (e.g., Dempsey and Zakamska, 2018) and the dusty torus (e.g., Tristram and Schartmann, 2011; Koshida et al., 2014; Mandal et al., 2024). In this work, we will focus on the R-L relation of BLRs (henceforth referred to as just the "R-L relation"). Confirming such a relation for the BLRs of AGNs has become the goal of most RM works (e.g., Kaspi et al., 2000, 2005; Bentz et al., 2006, 2009). The R-L relation is essential in understanding galaxy formation and evolution as it provides an easy way of estimating the BLR size across cosmic time by just acquiring a single-epoch spectrum of a target to acquire its AGN luminosity and the velocity dispersion of an emission line, which in turn can be used to estimate the central BH mass following the virial equation (Eqn. 1.8). However, the validity of the R-L relation in different redshifts and the formulation of an R-L relation using other emission lines is an active topic of research, Initial works have used the Hβ line observed in the optical wavelengths in deriving the BLR R-L relation at z $\lesssim$ 0.8–0.9, but at higher redshifts, calibration of UV/NIR emission lines and continuum luminosities serve as an alternative (e.g., McLure and Dunlop, 2002; Landt et al., 2011).

The canonical R-L relation ($R \propto L^{1/2}$; Fig. 1.4) is a result expected from several assumptions that imply that AGNs are *the same* regardless of their properties. However, an increasing number of works suggest otherwise, showing that the slope of the R-L relation is shallower than 0.5 (Du et al., 2018b; Du and Wang, 2019). There are many possible reasons for such a shallow slope. For instance, McLure and Dunlop (2002) suggests that the 3000 Å (UV) luminosity yields a slope of 0.5 with the BLR radius instead of the 5100 Å (optical) luminosity, which is much more commonly used in fitting the R-L relation. This suggests that choosing the right luminosity to describe the ionising luminosity in the R-L relation is important to formulate the relation correctly. This also implies a nonlinear relationship among different luminosities (Netzer, 2019). On the other hand, the offset

of BLR sizes from the canonical R-L relation has been found to correlate strongly with the Eddington ratio (Du et al., 2015, 2018b; Du and Wang, 2019). This suggests that the accretion rate may play a role in shortening time lags from RM measurements and, therefore, inferred BLR sizes. A particular phenomenon that could lead to such speculation is the increased self-shielding of the accretion disk due to increased accretion rate, which causes the inner part of the disk to become geometrically thick and suppress the amount of ionising photons that reach the BLR (Wang et al., 2014; Du et al., 2018b). There is also a lack of studies that focus on the redshift evolution of the R-L relation. The presence of a redshift evolution in the R-L relation would mean biased BH mass estimates at higher redshift. Nevertheless, the R-L relation of AGNs remains essential in providing a new perspective on galaxy formation and evolution, thus highlighting the need to investigate it.

The $M_{\rm BH}$-σ_* Relation and SMBH-galaxy coevolution

By studying the correlation of the SMBH mass with other galaxy properties, we are able to shed light on the SMBH-galaxy coevolution scenario. Many works have shown that the SMBH mass is correlated with the stellar velocity dispersion of the host galaxy, which is usually measured at the bulge of the host galaxy where most of the stars reside (at least for bulge-dominated galaxies). This relation is called the $M_{\rm BH}$-σ_* relation and is one of the strong evidence for SMBH-host galaxy coevolution (e.g. Magorrian et al., 1998; Gebhardt et al., 2000; Treu et al., 2004; Kormendy and Ho, 2013; Caglar et al., 2020). Other works have also shown possible evidence that the central BH mass is also correlated with the host galaxy's stellar mass (e.g. Lamastra et al., 2010; Reines and Volonteri, 2015; Delvecchio et al., 2019), stellar bulge mass (e.g. McLure and Dunlop, 2002; Häring and Rix, 2004), and dark matter halo mass (e.g. Booth and Schaye, 2010; Somerville et al., 2018).

Many works have studied the exact mechanisms that regulate SMBH and host galaxy growth, which possibly lead to the relations described above. For instance, kinetic feedback mechanisms (AGN-driven winds), which originate from nuclear, sub-pc scales, could go all the way out to galactic and circumgalactic medium scales. These winds have been shown to either suppress SF activities of their host galaxies due to stripping the galaxies of their fuel or enhance SF activities of their host galaxies due to their pressure-triggering of the collapse of dense clouds (Silk, 2005; Page et al., 2012; Silk, 2013; Zubovas and Bourne, 2017; Almeida et al., 2023). Other modes of AGN feedback, such as radiative feedback (due to radiation pressure and photoionisation) and accretion-induced feedback, could also produce similar effects (Wagner et al., 2016; Morganti, 2017; Capelo et al., 2024). Determining the dominant role of AGN feedback mechanisms on the SF activities of the host galaxy is believed to be dependent on various factors, such as galaxy mass (Stemo et al., 2020), AGN luminosity (Bollati et al., 2024), the amount of cold gas in the system (Shangguan et al., 2020), and even the column depth and spatial distribution of the clouds in the galaxy (Wagner et al., 2016). While these works focus on how SMBH processes affect the growth of their host galaxies, there are also works that focus on how the host galaxies affect the growth of their SMBHs. One possible mechanism is through galaxy mergers, although its

efficiency in promoting SMBH growth is still under scrutiny (Yang et al., 2017; McAlpine et al., 2020; Prieto et al., 2021; Lin et al., 2023). Star formation within compact regions of the host galaxy could also serve as a pathway for SMBH growth (Diamond-Stanic and Rieke, 2012). Secular processes, processes that happen over very long timescales and are related to the evolution of the galaxy as it rearranges its energy and mass over time, have also been suggested to influence SMBH growth (Kormendy and Kennicutt Jr, 2004). Some examples of these galactic secular processes that influence SMBH growth/suppression are inflows in galactic bars (Smethurst et al., 2019) and the presence of pseudo-bulges, which are created through the secular evolution of the host galaxy's disk (Orban De Xivry et al., 2011; Cisternas et al., 2011). Similar to SMBH-related processes, the dominant role of these host galaxy mechanisms in SMBH growth is also dependent on several factors, such as the mass ratio (Capelo et al., 2015) and galaxy types (Johansson et al., 2008) of merging galaxies, and stellar mass and stellar surface density for secular processes (Yang et al., 2017; Byrne et al., 2023). These findings highlight the complexity of the SMBH-galaxy coevolution scenario, and this thesis seeks to help reduce some of the uncertainties within that framework by providing more accurate SMBH mass measurements.

1.2 Optical Interferometry

This work utilises a new and independent method of resolving the BLR of AGNs, which is the very long-baseline interferometry with the VLTI/GRAVITY instrument. This section will focus on laying the foundations of interferometry and its ability to resolve small scales such as the BLR.

1.2.1 High-Angular Resolution Astrophysics

It has been known for a long time that larger optical systems can resolve smaller objects. The *Rayleigh criterion of resolution* dictates the angular resolution of an optical system with a diameter D and operating at a wavelength λ:

$$\theta = 1.22\frac{\lambda}{D} \tag{1.11}$$

The equation above assumes diffraction via circular aperture, which results in an Airy disc pattern, while diffraction via a single slit follows the same equation but without the 1.22 factor.

The angular resolution dictates the smallest size it can resolve clearly. For instance, if two stars are separated by a distance smaller than the angular resolution of a telescope, the telescope will not be able to resolve the two stars and will, therefore, see just a single blob of light. However, the Rayleigh criterion is just one example of a two-point resolution criterion to determine whether two overlapping Airy disks can be distinguished or not.

Seeing and Adaptive Optics (AO)

The atmosphere degrades the image quality detected by the telescope due to its volatile nature. This phenomenon is called *seeing*. Many telescopes nowadays implement ways to mitigate the diminishing effect of the atmosphere, and one important example is through adaptive optics (AO).

To start our discussion with seeing, we start with Kolmogorov's theory of turbulence, which states that the large-scale eddies from the turbulent flow of incompressible fluids (e.g. atmosphere) break down into smaller-scale eddies (Roddier, 1989). During this breakdown process, the energy of the large-scale eddies gets passed down to their smaller counterparts. Such small-scale energies are then dissipated by viscosity as heat. This will result in random fluctuations in temperature and pressure, which lead to refractive index variations in the air. When light from outside the Earth enters our atmosphere, different parts of its wavefront are delayed or advanced, causing distortion to the observed wavefront by the telescope. These distortions could cause blurriness or twinkling of the images.

A measure of the atmosphere's turbulence is Fried's parameter r_0. This describes the size of the region over which air-induced distortions have minimal effect on the quality of an optical wavefront (Fried, 1994). The Fried's parameter is expressed as:

$$r_0 = \left[0.423k^2 \int_0^\infty C_n^2(z)dz\right]^{-3/5} \tag{1.12}$$

where k is the wavenumber ($k = 2\pi/\lambda$) and C_n^2 is the refractive index structure constant, which quantifies the turbulence strength and is a function of the altitude z. The integral $\int_0^\infty C_n^2(z)dz$ represents the total effect of turbulence along the optical path through the atmosphere. Eqn. 1.12 briefly tells us that Fried's parameter is a function of wavelength λ and altitude z. In particular, $r_0 \propto \lambda^{6/5}$. The larger the value of r_0, the less phase distortion is present over larger spatial regions of the wavefront.

The Fried's parameter is an important measurement because in seeing-limited conditions, when the atmosphere has a considerable effect, the angular resolution of a telescope is not limited anymore to its aperture, but to r_0 such that:

$$\theta \sim \frac{\lambda}{r_0} \tag{1.13}$$

A typical value of r_0 at 500 nm is about 10 cm (e.g. Irbah et al., 2016), but r_0 changes strongly from time to time.

Adaptive optics, or AO, compensates for the wavefront distortions caused by atmospheric turbulence. First, a wavefront sensor detects these distortions, which are then sent to a deformable mirror that has many small actuators that can bend many regions of the mirror surface. This mirror adjusts in real time, changing shape from hundreds to thousands of times per second, as the distortions also happen in real time. As the distorted wavefront passes through the deformable mirror, the resulting wavefront becomes relatively flat again, allowing one to approach the diffraction limit of the telescope without being limited by seeing (Roddier, 1999; Davies and Kasper, 2012). AO technology has been used

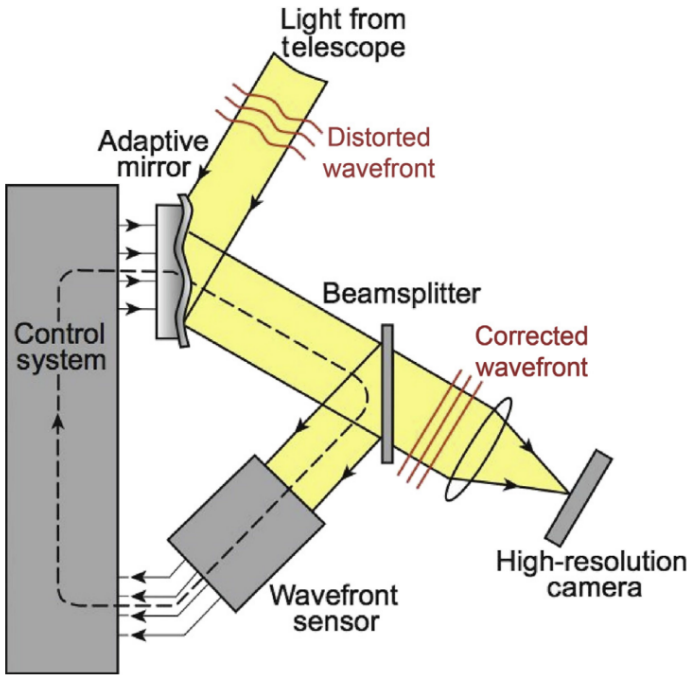

Figure 1.5: A simple schematic diagram presenting how AO works. The wavefront sensor picks up the distortion from the incoming wavefront, which then transmits to the adaptive mirror to change shape in real time and correct the wavefront before it gets detected by the high-resolution camera. Figure taken from Tokunaga (2014).

by many telescopes, such as the Very Large Telescope (VLT) (Rousset et al., 1998, 2000), Keck Observatory (Wizinowich et al., 2006), the Gemini Observatory (Blain et al., 2024), and the Subaru Telescope (Minowa et al., 2010), to name a few.

Setting the stage of interferometry

Despite the introduction of AO to alleviate seeing conditions and bring back observations to being diffraction-limited, we are still limited by the aperture size of our telescope. So, how do we achieve better angular resolution? Instead of building larger telescopes, another possibility is to coherently combine the light from several individual telescopes. This is called "long-baseline interferometry", and the resulting angular resolution from combining the light from two telescopes is now affected by the distance between the two telescopes, which is defined as the "baseline" (B), instead of the diameter of one telescope. To calculate the angular resolution of an interferometer formed by two telescopes separated by a baseline B, we use the following approximation:

$$\theta \approx \frac{\lambda}{B} \tag{1.14}$$

The bulk of the following sections will cover topics taken from several textbooks, such as Hariharan (2010) and Lawson (2000).

1.2.2 Optics and Interference

We begin our discussion with the concept of interference, which is a phenomenon that arises when two electric (light) fields are superimposed. The resulting field depends on whether the two light fields reinforce (constructive interference) or cancel (destructive interference) each other. Fig. 1.6 shows a schematic diagram of an idealised interferometer, which consists of a pair of telescopes observing the same target. We first start with the simple case: observing a monochromatic (emitting in one wavelength or frequency only) object. The baseline $\vec{B}$ = $\vec{x_2}$ - $\vec{x_1}$, where $\vec{x_j} = x_j\ \hat{a}$ where j = 1,2 and $\hat{a}$ is normal vector of the wavefronts emitted by the source and is defined as the direction from the source to the telescopes, i.e. $\hat{a} \equiv \vec{A}/A$. Let $\vec{A_j}$ be the field that the jth telescope receives. This can be written as $A_j = a_j e^{i\vec{k}\cdot\vec{x_j}} e^{-i\omega t}$ where a_j is the amplitude of the wave. We can therefore define the received wavefronts of the two telescopes as:

$$\begin{aligned}
\vec{A_1} &= a_1 e^{i\vec{k}\cdot\vec{x_1}} e^{-i\omega t} \\
&= a_1 e^{-ik\hat{a}\cdot\vec{x_1}} e^{-i\omega t} \\
\vec{A_2} &= a_2 e^{i\vec{k}\cdot\vec{x_2}} e^{-i\omega t} \\
&= a_2 e^{i\vec{k}\cdot(\vec{B}+\vec{x_1})} e^{-i\omega t} \\
&= a_2 e^{-ik\hat{a}\cdot\vec{B}} e^{-ik\hat{a}\cdot\vec{x_1}} e^{-i\omega t}
\end{aligned} \tag{1.15}$$

Where $\vec{k}\cdot\vec{x_j} = -k\hat{a}\cdot\vec{x_j}$. Both $\vec{A_1}$ and $\vec{A_2}$ have a common factor $e^{-ik\hat{a}\cdot\vec{x_1}}$ and we can redefine the amplitudes a_1 and a_2 so that this factor is absorbed into them as part of the normalization process. This gives us:

$$\begin{aligned}
\vec{A_1} &= a_1 e^{-i\omega t} \\
\vec{A_2} &= a_2 e^{-ik\hat{a}\cdot\vec{B}} e^{-i\omega t}
\end{aligned} \tag{1.16}$$

The field $\vec{A_2}$ travels farther to the second telescope than the other field $\vec{A_1}$. This difference in their travelled distances due to the separation of the two telescopes is encapsulated by the term $\hat{a}\cdot\vec{B}$ and is called the *geometric delay*. Once the telescopes receive the fields, they are propagated to the power-linear detector where they are combined to form fringes, an alternating signal due to the interference of the fields. During this stage, the fields separately travel over distinct distances d_1 and d_2. To explicitly compensate for these distances, adjustable *delay lines* are introduced. Adding delay lines also introduces corresponding phase shifts in the received wavefronts:

$$\begin{aligned}
\vec{A_1} &= a_1 e^{ikd_1} e^{-i\omega t} \\
\vec{A_2} &= a_2 e^{ikd_2} e^{-ik\hat{s}\cdot\vec{B}} e^{-i\omega t}
\end{aligned} \tag{1.17}$$

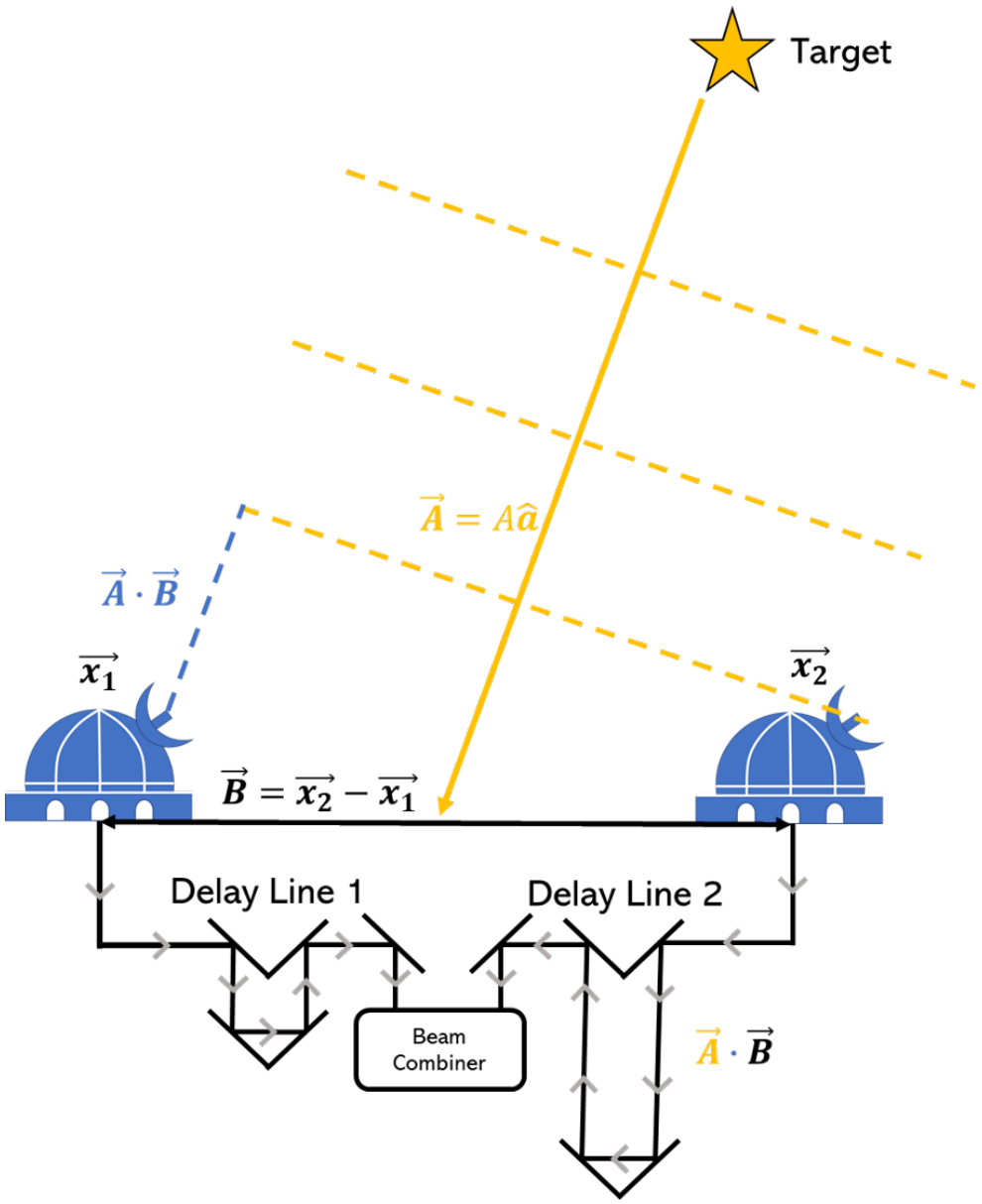

Figure 1.6: Schematic diagram showing how an idealised interferometer works. The observed target emits a light wave $\vec{A} = A\hat{a}$ where $\hat{a}$ is defined as the direction going to the telescope. Since two telescopes are observing the target simultaneously, with a baseline separation of $\vec{B} = \vec{x_2} - \vec{x_1}$, the light wave will travel a longer distance to one of the telescopes. This further distance is geometric delay defined as $\vec{A} \cdot \vec{B}$. After the telescopes receive the light waves, they travel further to the delay lines 1 and 2, which provide additional phase shift to compensate for the geometric delay before they are combined in the beam combiner to create fringe patterns. The grey arrows show the direction of the light traveling through the system.

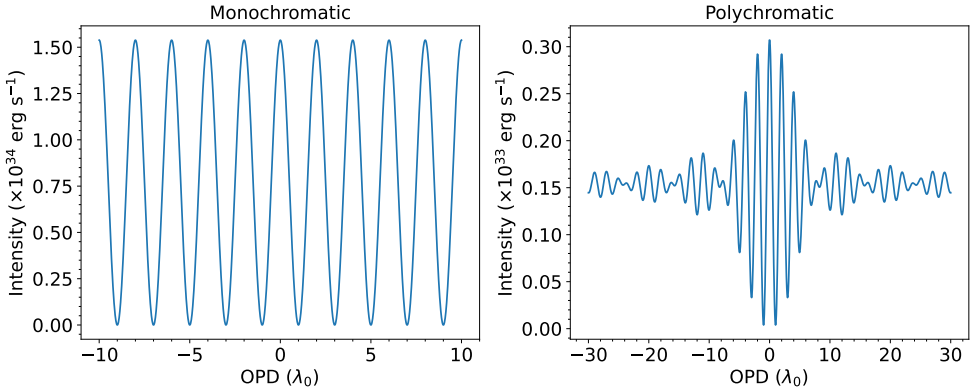

Figure 1.7: Sample fringes (intensity in units of erg s^{-1} vs. OPD in units of central wavelength λ_0) created by a monochromatic object observed with an infinite filter bandpass (left panel) and polychromatic object observed with a top-hat filter bandpass (right panel). For both cases, we assume that the target has a constant flux equal to the solar luminosity and the filter is centred at $\lambda_0 = 2$ μm. For the polychromatic case, we assume the top-hat filter to have a bandwidth of $\Delta\lambda = 0.5$ μm and a constant throughput of $\eta_0 = 0.04$.

Assuming that the telescopes have similar sensitivity ($a_1 = a_2$) and letting $\mathrm{D} = d_1 - d_2 + \hat{s} \cdot \vec{B}$, the total intensity of the two fields after interference is therefore calculated as:

$$\begin{aligned} I_{\mathrm{mono}} &= |A_1 + A_2|^2 \qquad (1.18) \\ &= |A_1|^2 + |A_2|^2 + 2\Re(A_1 A_2^*) \\ &= a_1^2 + a_2^2 + 2a_1 a_2 \cos k\mathrm{D} \\ &= 2I_0(1 + \cos k\mathrm{D}) \qquad (1.19) \end{aligned}$$

where $I_0 = a_1^2 = a_2^2 = a_1 a_2$ and is the incident flux from the source in unit energy per time and per area (intensity), and D is called the relative delay or optical path difference (OPD; Lawson 2000). This result shows us that combining the beams received by two different telescopes produces a sinusoidal pattern which is a function of OPD, as shown in the left panel of Fig. 1.7.

However, most astronomical objects are polychromatic (emitting in many wavelengths or frequencies), and we usually observe them with filters of defined bandpasses. This should result in a finite series of fringes as opposed to the monochromatic case. To start with the polychromatic case, we assume that the the target has a spectral intensity of $I_{\nu,0}$ which is independent of frequency, and we are observing with a top-hat filter bandpass with a width of $\Delta\nu$ centered at a central frequency ν_0 and has a constant throughput of η_0. The total intensity observed from the target should be the sum of the detected intensity at each frequency, which therefore calls for a summation:

$$
\begin{aligned}
I_{\text{poly}} &= \int d\nu [2F_{\nu,0}(1+\cos kD)][\eta(\nu)] && (1.20)\\
&= 2I_{\nu,0}\eta_0 \int_{\nu_0-\frac{\Delta\nu}{2}}^{\nu_0+\frac{\Delta\nu}{2}} 1+\cos\left(\frac{2\pi\nu}{c}D\right) d\nu && k = 2\pi\nu/D\\
&= 2I_{\nu,0}\eta_0 \left[\nu + \frac{\sin(2\pi\nu\tau)}{2\pi\nu\tau}\right]_{\nu_0-\frac{\Delta\nu}{2}}^{\nu_0+\frac{\Delta\nu}{2}} && \tau = D/c\\
&= 2I_{\nu,0}\eta_0\Delta\nu\left[1+\frac{\sin(\pi\tau\Delta\nu)}{\pi\tau\Delta\nu}\cos(2\pi\tau\nu_0)\right]\\
&= 2I_{\lambda,0}\eta_0\Delta\lambda\left[1+\underbrace{\frac{\sin(\frac{\pi D}{\Lambda_{coh}})}{(\frac{\pi D}{\Lambda_{coh}})}}_{M(\Lambda_{coh},D)}\cos(k_0 D)\right] && \text{Converting from } \nu \text{ to } \lambda \quad (1.21)
\end{aligned}
$$

The result at Eqn. 1.21 is reminiscent of the sinc function. This means that instead of seeing fringes at all values of D in the monochromatic case, we see fringes modulated by a sinc function symmetrically centred at $D = 0$ and whose width is set by the coherence length Λ_{coh}. The term Λ_{coh} serves as a measure of coherence length, and in this case, Λ_{coh} defines the typical width of the OPD at which fringes are present (Lawson, 2000). By adjusting the delay lines so that $D << \Lambda_{coh}$ is always achieved, we are able to make sure that fringes are generated. The term $M(\Lambda_{coh}, D)$ is also defined as the fringe envelope function, while the cosine term, specifically $k_0 D$, defines the position of the fringe envelope. We want this to be as close to zero as possible to achieve maximum intensity at all wavelength channels. Hence, it is convenient to define the geometric delay $d_2 - d_1$ to be equal or similar in order with $\hat{s} \cdot \vec{B}$. Hence, D could be simply represented as $\hat{s} \cdot \vec{B}$.

Furthermore, not all objects are point sources. When observing extended sources, the assumption is that they can be represented as collections of point sources with varying values of $\hat{s}$ with respect to the reference vector $\hat{s_0}$ such that $\hat{s} = \hat{s_0} + \Delta s$. If we assume the maximum intensity to be at $\hat{s_0}$, $\hat{s_0}$ is called the *phase reference*, and the resulting intensity at $\hat{s}$ is therefore:

$$I = 2I_{\lambda,0}\eta_0\Delta\lambda[1 + M(\Lambda_{coh}, \Delta D)\cos(k_0\Delta D)] \quad (1.22)$$

where $\Delta D = \Delta s \cdot \vec{B}$. We now focus on deriving the detected *power* of the optical system, which is intensity times the cross-sectional area of the detector, to understand what the observables are in interferometry. Assuming that the source intensity and cross sectional area are functions of $\hat{s}$ and $\hat{s_0}$, i.e. $I_0 = I(\hat{s}, \hat{s_0})$ and $A = A(\hat{s}, \hat{s_0})$, the resulting power should be the integral of Eqn. 1.22 with the addition of A and the removal of the fringe envelope function for notational convenience:

$$P = \int d\Omega A(\Delta s) I(\Delta s)[1 + cos(k(\Delta s \cdot \vec{B}))] \qquad \Omega = \text{any angular coordinates} \quad (1.23)$$

When a small delay offset δ is added by one of the delay lines, the power equation becomes:

$$P(\hat{s_0}, \vec{B}, \delta) = \int d\Omega A(\Delta s) I(\Delta s)[1 + cos(k(\Delta s \cdot \vec{B} + \delta))] \tag{1.24}$$

$$= \underbrace{\int d\Omega A(\Delta s) I(\Delta s)}_{P_0} + \cos(k\delta) \int d\Omega A(\Delta s) I(\Delta s) \cos k(\Delta s \cdot \vec{B}) - \sin(k\delta) \int d\Omega A(\Delta s) I(\Delta s) \sin k(\Delta s \cdot \vec{B}) \tag{1.25}$$

Let us define the *complex visibility* $V(k, \vec{B}) = \int d\Omega A(\Delta s) I(\Delta s) e^{ik\Delta s \cdot \vec{B}}$. The result at 1.25 becomes:

$$\begin{aligned} P(\hat{s_0}, \vec{B}, \delta) &= P_0 + \Re(V) \cos k\delta - \Im(V) \sin k\delta \\ &= P_0 + \Re(V e^{-ik\delta}) \end{aligned} \tag{1.26}$$

Eqn. 1.26 is an important result because this allows the connection between the observable $P(\hat{s_0}, \vec{B}, \delta)$ to be converted into the complex visibility $V(k, \vec{B})$ which contains information about the observed target. To understand this, we look at at $V(k, \vec{B})$ where Δs is defined as $\vec{x} = (\alpha, \beta, 0)$ where α and β are angular coordinates and $\vec{x}$ is perpendicular to $\hat{s_0}$.. We can transform $V(k, \vec{B})$ in units of α and β such that:

$$V = \int d\alpha \; d\beta \; A(\alpha, \beta) I(\alpha, \beta) e^{-ik(\alpha B_x + \beta B_y)} \tag{1.27}$$

We define spatial frequencies u and v, which represent the projection of the baselines on the sky. They are defined as:

$$u = \frac{B_x}{\lambda} = \frac{kB_x}{2\pi}; \; v = \frac{B_y}{\lambda} = \frac{kB_y}{2\pi} \tag{1.28}$$

Transforming $A(\Delta s) I(\Delta s) d\Delta s$ to $P(\vec{x}) = A(\vec{x}) I(\vec{x}) d\vec{x}$, Eqn. 1.27 therefore becomes:

$$V(u, v) = \int P(\vec{x}) \; d\vec{x} \; e^{-2\pi i(\vec{u} \cdot \vec{x})} \tag{1.29}$$

Finally, the brightness distribution of $I(\vec{x}) = P(\vec{x})/A(\vec{x})$ can be recovered from the inverse Fourier transform of Eqn 1.29:

$$I(\vec{x}) = \frac{1}{2\pi A(\vec{x})} \int V(u, v) \; d\vec{x} \; e^{-2\pi i(\vec{u} \cdot \vec{x})} \tag{1.30}$$

Eqn. 1.30 is better known as the *van Cittert-Zernike Theorem*, which states that *"the complex visibility is the Fourier transform of the angular intensity distribution of the source"* (van Cittert, 1934; Zernicke, 1938).

1.2.3 Complex Visibility and Visibility Modelling

The complex visibility is the main observable of interferometric observations and is measured through the contrast of the fringes. To start our discussion, Michelson (1920) defined the so-called "Michelson visibility" as:

$$V_M = \frac{I_{\max} - I_{\min}}{I_{\max} + I_{\min}} \tag{1.31}$$

The quantity V_M has a value between 0 and 1, and is also defined as the modulus of the complex visibility, i.e. $V_M = |V(u,v)|$. The normalised visibility ($\mathcal{V}$), on the other hand, is the complex visibility normalised to the intensity distribution:

$$\mathcal{V} = \frac{\int P(\vec{x}) d\vec{x}\ e^{-2\pi i(\vec{u}\cdot\vec{x})}}{\int P(\vec{x}) d\vec{x}} = \frac{V(u,v)}{P_0} \tag{1.32}$$

This subsection briefly discusses the three typical cases of observed targets and their expected visibilities.

Unresolved (Point) source

Assuming a point source at $\vec{x_0} = (\alpha_0, \beta_0)$, its brightness distribution can be represented with Dirac delta functions, i.e. $I(\alpha,\beta) = I_0\delta(\alpha-\alpha_0)\delta(\beta-\beta_0)$. Plugging in this expression in Eqn. 1.27 gives us:

$$V(u,v) = P_0 e^{-2\pi i(\vec{u}\cdot\vec{x_0})} \tag{1.33}$$

and the resulting normalised complex visibility $\mathcal{V}$ is just the result above but dividing out P_0. Due to noise, most optical interferometers measure the square of the modulus of the normalised complex visibility, which is also called the *visibility squared*, and it is symbolised as $|\mathcal{V}|^2$. It is easy to find out, therefore, that for an unresolved (point) source, $|\mathcal{V}|^2 = 1$. This result is a typical characteristic of an unresolved source: when the visibility amplitude is 1, the observed target is unresolved.

Resolved point source binary of equal brightness

Suppose we are observing two point sources, one at $\vec{x_0} = (\alpha_0, \beta_0)$ and another at $\vec{x_1} = (\alpha_1, \beta_1)$. Due to the linearity of Fourier transforms, the resulting complex visibility of a system of multiple objects is just the sum of the individual objects' complex visibilities. If the brightness distribution of a binary system can be represented with Dirac delta functions, i.e. $I(\vec{x_0}, \vec{x_1}) = I_0\delta(\vec{x}-\vec{x_0}) + I_1\delta(\vec{x}-\vec{x_1})$, with the two point sources separated by a distance

$\Delta x = \vec{x_1} - \vec{x_0}$, the resulting complex visibility and normalised complex visibility will be:

$$V(u,v) = \underbrace{A(\vec{x_0})I_0}_{P_0} e^{-2\pi i(\vec{u}\cdot\vec{x_0})} + \underbrace{A(\vec{x_1})F_1}_{P_1} e^{-2\pi i(\vec{u}\cdot\vec{x_1})} \tag{1.34}$$

$$\begin{aligned}\mathcal{V} &= \frac{P_0 e^{-2\pi i(\vec{u}\cdot\vec{x_0})} + P_1 e^{-2\pi i(\vec{u}\cdot\vec{x_1})}}{P_0 + P_1} \\ &= \frac{e^{-2\pi i(\vec{u}\cdot\vec{x_0})}[1 + re^{-2\pi i(\vec{u}\cdot\vec{\Delta x})}]}{1+r}\end{aligned} \tag{1.35}$$

where $r = \frac{I_1}{I_0}$ is the intensity ratio of the two point sources. If we assume these sources to be of equal brightness ($r = 1$) and $\vec{x_0}$ to be at the origin so that $\vec{x_0}$ is the reference, the resulting normalised complex visibility will be $\mathcal{V} = \frac{1}{2}[1 + e^{-2\pi i(\vec{u}\cdot\vec{\Delta x})}]$ and therefore, the visibility amplitude will be $|V|^2 = \frac{1+\cos[2\pi(\vec{u}\cdot\vec{x})]}{2}$. When such a binary system is observed by an optical interferometer, the visibility amplitude will be a cosine function that alternates between 0 and 1.

Uniform disk

A more realistic model we should look into as we observe the BLR of AGNs is the case of a uniform disk. If the disk centred at $\vec{x_0} = (\alpha_0, \beta_0)$ has an angular diameter of θ, its brightness distribution can be written in terms of polar coordinates:

$$I(\rho) = \begin{cases} \frac{4}{\pi\theta^2} \text{ if } \quad \rho \leq \theta/2 \\ \\ 0 \text{ if } \quad \rho > \theta/2 \end{cases} \tag{1.36}$$

where ρ is the radial distance of an arbitrary point measured from the central point. The total power is therefore $P_0 = A_0 I_0 \pi\theta^2/4$ where A_0 is the total cross-sectional area of the detector and I_0 is the total intensity of the source. Transforming Eqn. 1.27 from Cartesian coordinates (α, β) into polar coordinates gives us $\alpha = \rho\cos\theta$ and $\beta = \rho\sin\theta$. We also have to transform the spatial frequencies into their angular counterparts, such that $u = v_r\cos\phi$ and $v = v_r\sin\phi$ where v_r and ϕ are the radial spatial frequency and axial angle, respectively. Eqn. 1.27 therefore becomes (Berger and Segransan, 2007):

$$V(u,v) = e^{-2\pi i(\vec{u}\cdot\vec{x_0})} \int d\alpha d\beta A(\alpha,\beta) I(\alpha,\beta) e^{-2\pi i(\vec{u}\cdot\vec{x})} \tag{1.37}$$

$$\begin{aligned} &= A_0 e^{-2\pi i(\vec{u}\cdot\vec{x_0})} \int d\rho d\theta \rho I(\rho) e^{-2\pi i\rho(u\cos\theta + v\sin\theta)} \\ &= A_0 e^{-2\pi i(\vec{u}\cdot\vec{x_0})} \int d\rho d\theta \rho I(\rho) e^{-2\pi i\rho v_r(\cos\theta\cos\phi + \sin\theta\sin\phi)} \\ &= A_0 e^{-2\pi i(\vec{u}\cdot\vec{x_0})} \int d\rho d\theta \\ &= A_0 e^{-2\pi i(\vec{u}\cdot\vec{x_0})} \int d\rho d\theta \rho I(\rho) e^{-2\pi i\rho v_r\cos(\theta-\phi)} \end{aligned} \tag{1.38}$$

We can disregard ϕ in the integral as $I(\phi)$ is constructed axially symmetric. The integral with θ, on the other hand, is reminiscent of the zeroth-order Bessel function of the first kind:

$$\int_0^{2\pi} e^{ix\cos\theta} d\theta = 2\pi J_0(x) \tag{1.39}$$

We can therefore calculate the complex visibility further as:

$$2\pi A_0 e^{-2\pi i(\vec{u}\cdot\vec{x_0})} \int_0^{\infty} d\rho\rho I(\rho) J_0(2\pi\rho v_r) \tag{1.40}$$

where we apply the fact that even-ordered Bessel functions are even functions. Applying the definition of $I(\rho)$ and P_0 gives us the final expression for the complex visibility, normalised complex visibility, and visibility squared of a uniform disk:

$$\begin{aligned}
V(v_r) &= 2\pi A_0 e^{-2\pi i(\vec{u}\cdot\vec{x_0})} \left(\frac{4P_0}{\pi A_0 \theta^2}\right) \int_0^{\frac{\pi}{2}} d\rho\rho J_0(2\pi\rho v_r) \\
&= \frac{8P_0}{\theta^2} e^{-2\pi i(\vec{u}\cdot\vec{x_0})} \int_0^{\frac{\theta}{2}} d\rho\rho J_0(2\pi\rho v_r) \\
&= \frac{8P_0}{\theta^2} e^{-2\pi i(\vec{u}\cdot\vec{x_0})} \int_0^{x=2\pi(\theta/2)v_r} \left(\frac{dx}{2\pi v_r}\right)\left(\frac{x}{2\pi v_r}\right) J_0(x) && \text{Let } x = 2\pi\rho v_r \\
&= \frac{8P_0}{\theta^2} e^{-2\pi i(\vec{u}\cdot\vec{x_0})} \int_0^{x=\pi\theta v_r} \frac{x dx}{(2\pi v_r)^2} J_0(x) \\
&= \frac{8P_0}{\theta^2} e^{-2\pi i(\vec{u}\cdot\vec{x_0})} \frac{1}{(2\pi v_r)^2} x J_1(x) && \int_0^x x dx J_0(x) = x J_1(x) \\
&= e^{-2\pi i(\vec{u}\cdot\vec{x_0})} 2P_0 \frac{J_1(\pi\theta v_r)}{\pi\theta v_r} \\
&= e^{-2\pi i(\vec{u}\cdot\vec{x_0})} 2P_0 \frac{J_1(\pi\theta B_\perp/\lambda)}{\pi\theta B_\perp/\lambda} && v_r^2 = u^2 + v^2 = B_\perp^2/\lambda^2 \quad (1.41) \\
\mathcal{V} &= e^{-2\pi i(\vec{u}\cdot\vec{x_0})} \frac{2J_1(\pi\theta B_\perp/\lambda)}{\pi\theta B_\perp/\lambda} && (1.42) \\
|\mathcal{V}|^2 &= \left[\frac{2J_1(\pi\theta B_\perp/\lambda)}{\pi\theta B_\perp/\lambda}\right]^2 && (1.43)
\end{aligned}$$

Eqn. 1.43 shows the disk is getting resolved (getting to $|\mathcal{V}|^2$ smaller than 1) as the angular diameter θ of the disk increases. At $\theta \approx 1.22\ \lambda/B_\perp$, $|\mathcal{V}|^2$ reaches zero (fringes disappear), and eventually increases afterwards, albeit at a much lower amplitude (weaker fringe reappear).

Fig. 1.8 shows the $|\mathcal{V}|^2$ vs. baseline length for the three cases discussed in this subsection. This figure tells us two things: (1) the visibility amplitude provides information about the shape and size (or intensity distribution via the van Cittert-Zernike Theorem) of the target, and (2) stronger constraints about the shape or intensity distribution of the target

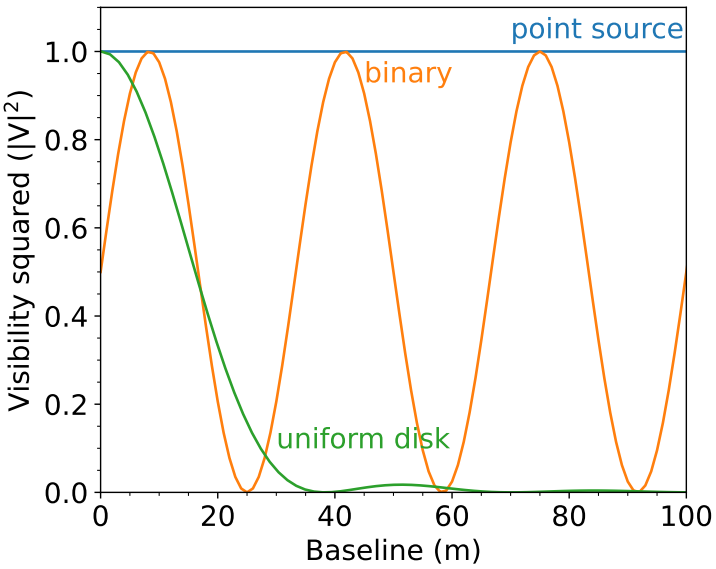

Figure 1.8: Plots of visibility amplitude $|\mathcal{V}|^2$ as a function of baseline length in meters for three different cases: (i) an unresolved point source in blue, (ii) a binary point source of equal brightness, and (iii) a uniform disk.

is achieved with longer baselines, as shorter baselines will find it difficult to distinguish certain cases, e.g. uniform disk and binary cases. However, beyond very long baselines, the visibility (squared) goes to zero; hence, baselines must match the scale of the observed object.

1.2.4 Differential interferometry and differential phase

We now focus our discussion on a specific interferometric technique called differential interferometry (D.I.) or spectro-interferometry/spectro-astrometry. By measuring interferometric phase at different wavelengths, D.I. can measure the position difference or *shift* of the fringes in two simultaneous images at different wavelengths. The resulting shift as a function of wavelength provides physical information about the target as it produces wavelength-dependent emission (Buscher and Longair, 2015; Petrov and Lagarde, 1992). We derive the formulation of this shift by calculating the sum of normalised visibilities of the continuum and the line-emitting region (i.e. the BLR). Following Eqn. 1.32, the normalised visibility of the line-emitting region can be written in the form

$$V = |V|e^{i\phi} = \frac{\int P(\vec{x})d\vec{x}\ e^{-2\pi i(\vec{u}\cdot\vec{x})}}{\int P(\vec{x})d\vec{x}} \tag{1.44}$$

where $|V|$ and ϕ are the amplitudes and phase of the visibility, respectively (note that we are doing the integral on the full sky, not on the target yet). Suppose the target is *marginally resolved*, i.e. between fully resolved and unresolved, which is usually the case

for most interferometric observations. The resulting visibility of such a marginally resolved target is close to 1, and therefore $\vec{u} \cdot \vec{x} \ll 1$, which leads us to the first-order expansion of the exponentials:

$$1 + i\phi \approx \frac{\int P(\vec{x})\ d\vec{x}[1 - 2\pi i(\vec{u} \cdot \vec{x})]}{\int P(\vec{x}) d\vec{x}}$$
$$i\phi_l \approx -2\pi i\vec{u} \cdot \frac{\int P(\vec{x})\ \vec{x}\ d\vec{x}}{\int P(\vec{x}) d\vec{x}} \tag{1.45}$$

The integral on the right is the first-order moment of $\vec{x}$, which refers to the intensity-weighted average position on the sky of the line-emitting region. This is defined as the photocentre $\vec{\epsilon}(\lambda)$, and therefore the final result becomes:

$$\phi = -2\pi\ [\vec{u} \cdot \vec{\epsilon}(\lambda)] \tag{1.46}$$

Since the observed (NIR) emission from the AGN is a combination of the flux from the BLR and the flux from the continuum, it is imperative to calculate the sum of their normalised visibilities. Adding normalised visibilities is flux weighted (recall the normalised complex visibility form of a point source binary in Eqn. 1.35), i.e.:

$$V = \frac{F_c V_c + F_l V_l}{F_c + F_l} \tag{1.47}$$

Assuming that the continuum flux F_c is set to be 1, and the line flux F_l is measured with respect to the continuum and is represented by f, the equation above turns into $V_{\rm tot} = \frac{V_c + fV_l}{1+f}$. Writing the complex equivalents of the visibilities, this translates into:

$$|V|e^{i\phi} = \frac{|V_c|e^{i\phi_c} + f|V_l|e^{i\phi_l}}{1+f} = \frac{V_c + fV_l}{1+f} \tag{1.48}$$

where we assume that the continuum flux F_c is set to 1 and the line flux f is measured with respect to the continuum. By writing the visibilities of the BLR and continuum to their exponential forms and applying their first-order expansions due to the marginally resolved case, the equation becomes:

$$|V|(1 + i\phi) = \frac{|V_c|(1 + i\phi_c) + f|V_l|(1 + \phi_l)}{1+f} \tag{1.49}$$

The real part of this visibility (visibility amplitude) can be written as:

$$|V| = \frac{|V_c| + f|V_l|}{(1+f)} \tag{1.50}$$

while the imaginary part can be written as:

$$\phi = \frac{|V_c|\phi_c + f|V_l|\phi_l}{|V|(1+f)} \tag{1.51}$$

We define the *differential phase* as the difference between the phase of the total visibility and the mean phase across the spectrum, which is usually the continuum phase. It is also the phase of the average cross-spectrum produced by the light measured from a reference wavelength channel and another wavelength channel (Petrov, 1989; Petrov and Lagarde, 1992; Domiciano de Souza et al., 2004). We then now calculate the differential phase $\Delta\phi = \phi - \phi_c$ by substituting Eqn. 1.50 to yield:

$$\begin{aligned}\Delta\phi &= \frac{|V_c|\phi_c + f|V_l|\phi_l - |V|\phi_c(1+f)}{|V|(1+f)} \\ &= \frac{|V_c|\phi_c + f|V_l|\phi_l - |V_c|\phi_c - f|V_l|\phi_c}{|V|(1+f)} \\ &= \frac{f|V_l|}{|V|(1+f)}(\phi_l - \phi_c) \end{aligned} \tag{1.52}$$

We assume the BLR is unresolved ($|V_l| = 1$) and the total visibility amplitude is $|V| = 1$. Using the definition of phase as given in Eqn. 1.46, the final equation for the differential phase becomes:

$$\Delta\phi = -2\pi\frac{f}{1+f}\vec{u}\cdot[\vec{\epsilon}(\lambda) - \vec{\epsilon}(\lambda_r)] \tag{1.53}$$

where $\vec{\epsilon}(\lambda)$ is the photocentre of the BLR, $\vec{\epsilon}(\lambda_r)$ is the photocentre of the continuum, and their difference is the photocentre displacement between one channel and another reference channel (Petrov, 1989; Domiciano de Souza et al., 2004). For simplicity, we can assume that $\vec{\epsilon}(\lambda_r) = 0$; that is, the continuum is positioned in the origin of the coordinate system. This would mean that the contribution of the continuum to the differential phase is zero (Petrov et al., 1996), and therefore $\Delta\phi = -2\pi\frac{f}{1+f}\vec{u}\cdot\vec{\epsilon}(\lambda)$. Since the BLR photocentre is wavelength-dependent, the resulting differential phase without the continuum phase is also wavelength-dependent. On the other hand, the continuum phase is expected to be wavelength-independent as the hot dust structure is not expected to change significantly over the relatively narrow wavelength range of a single emission line. In addition, the contribution of the continuum to the differential phase follows the shape of the emission line. This can be shown by setting $\phi_l = 0$ and calculating ϕ_c:

$$\Delta\phi = -\frac{f}{1+f}\phi_c \tag{1.54}$$

Generally, we get the normalised visibility amplitude $|V|$ and the differential phase $\Delta\phi$ during interferometric observations, and the line flux f can be determined from a simultaneous spectroscopic observation of the same target. One could rearrange Eqn.1.52 to produce an equation that relates all observables with the non-observable quantities:

$$-\frac{|V|(1+f)}{f}\Delta\phi = 2\pi\vec{u}\cdot\vec{\epsilon}(\lambda) + \phi_c \tag{1.55}$$

The equation above allows one to estimate $\vec{\epsilon}(\lambda)$ in each wavelength channel (wavelength-dependent) and ϕ_c in each baseline (wavelength-independent), given the spatial coordinates of the baselines $\vec{u}$. The differential phase allows us to measure the BLR size through the BLR photocentres. We expect the differential phase of a BLR to have a rise and dip similar to an S-shape, which reflects a velocity gradient due to the continuum variation of the redshifted and blueshifted sides of the BLR (Shen, 2012b). If the direction of a radio jet launched from the central BH is shown to be perpendicular to the velocity gradient of the BLR photocentres, the BLR can be ruled to undergo ordered rotation/Keplerian motion, and such BLRs show the S-shape differential phase (GRAVITY Collaboration et al., 2018, 2020b; Abuter et al., 2024). This is why an S-shape differential phase usually indicates that the observed system is rotating. The strength of differential interferometry can also be applied to marginally resolved sources like the BLR and even unresolved sources like stars. By measuring the differential phase, which is dependent only on the signal-to-noise ratio of the phase measurement and is not limited by the diffraction limit of the instrument (Petrov, 1989), the smallest displacements and therefore the size of the source can still be measured.

Table 1.1 summarises the differential interferometric observables discussed in this section and which properties they are correlated to.

1.2.5 GRAVITY and GRAVITY+ at the VLTI, and prospects for AGN studies

One of the few astronomical instruments that exploit high-angular interferometry is the GRAVITY instrument at the Very Large Telescope Interferometer (VLTI) on Cerro Paranal, Chile. GRAVITY is a beam combiner that coherently combines the light from the four unit telescopes (UTs) to create fringes which contain important information about the observed target (GRAVITY Collaboration et al., 2017). The maximum baseline of the UTs is $\sim$ 130 m, and GRAVITY operates in the near-infrared (NIR), specifically at the astronomical K-band (1.95 - 2.45 μm), which overall yields milliarcsecond angular resolution. It can operate in either low ($R \approx 22$), medium ($R \approx 500$), or high ($R \approx 4500$) resolution modes, and it also has an instrument called a *fringe tracker* which is used to simultaneously observe a reference target (i.e. a bright star offset from the target) together with the main target to correct the OPD for both the reference and main target.

One of the major science goals of GRAVITY is to shed light on the physics of small-scale structures in AGNs. Due to the unprecedented milliarcsecond angular resolution of GRAVITY, it can probe the BLR of bright AGNs at the local Universe and therefore lead to more precise central SMBH mass measurements. In addition, the resulting interferometric data from GRAVITY observations, such as the differential phase, in conjunction with the K_s-band spectra of the AGN, could provide kinematic and geometric information about the BLR and the surrounding dusty torus. For most local Seyferts ($z < 0.1$), the Brγ line (restframe wavelength $\sim$ 2.166 μm) is observable in the K_s band, while for local QSOs ($z < 0.2$), the Paα line (restframe wavelength $\sim$ 1.870 μm) is observable. Since the expected

Figure 1.9: A picture of VLTI with the GRAVITY instrument zoomed in. Image taken from the MPE website.

Interferometric Observable	Definition	Formula	Related quantity
Visibility amplitude	Measurement of the amplitude of the fringes	$\|V\| = \frac{\|V_c\|+f\|V_l\|}{(1+f)}$	Size and shape of object
Differential phase	Measurement of the position of the photocentre	$\Delta\phi = -2\pi\frac{f}{1+f}\vec{u}\cdot[\vec{\epsilon}(\lambda)-\vec{\epsilon}(\lambda_r)]$	Photocentre positions (astrometry)

Table 1.1: Interferometric observables and their definitions and related quantities.

strengths of Balmer lines such as Brγ and Paα lines with respect to the continuum are known, the expected differential phase of local Seyferts and QSOs can be determined by using the formula:

$$\phi_{\rm diff} = -2\pi \frac{f}{1+f} \vec{u} \cdot \vec{R}_{\rm BLR} \tag{1.56}$$

where the $\vec{R}_{\rm BLR}$ can be estimated from the AGN luminosity of the AGN and f is the line strength of the observed line relative to the continuum. Typical values of differential phase for Seyferts and AGNs range from 0.1° - 3° (assuming a typical order of $\vec{R_{\rm BLR}}$ to be 100 μas). GRAVITY can observe bright targets with $m_K \sim$ 8-10, and with fringe tracking, this is further pushed to fainter magnitudes of $m_K \sim 13$.

GRAVITY+, on the other hand, is a series of improvements in GRAVITY and VLTI. Implementing these will push the sensitivity of GRAVITY, allowing observations of even fainter and farther AGNs. Fig. 1.10 shows the summary of these improvements, which include upgrades on the AO and vibration control of each UT, addition of laser guide stars for all telescopes, grism upgrade, and providing wide-field off-axis fringe tracking (GRAVITY-Wide), which allows the fringe tracker star to be situated at a larger separation from the target object than the typical field-of-view (FoV) of VLTI which is $\sim 2''$ (GRAVITY+ Collaboration et al., 2022a,b). With the full implementation of GRAVITY+, we expect to increase significantly the possible number of AGNs to be observed from tens to hundreds, as the limiting K-band magnitude of GRAVITY+ is expected to reach as faint as $m_K \sim 19$ and therefore we are most likely to probe higher redshifts (Fig. 1.11a). Recently, Abuter et al. (2024) presented the first dynamical mass measurement of an SMBH located at $z \sim 2$ with GRAVITY-Wide. The target, abbreviated as SDSS 1615, has $m_K \sim 15$ and its fringe tracking star is $\sim$12.7$''$ away from the QSO. At $z \sim 2$, the Hα line is observable in the K_s band, and so with the Hα line, Abuter et al. (2024) were able to resolve the BLR of SDSS 1615, showing a strong S-shape differential phase signal with a peak of $\sim 2°$ (Fig. 1.11b and c).

1.3 Thesis outline

The main results of this work are based on several works that are published (GRAVITY Collaboration et al., 2024; Santos et al., 2025a) and to be submitted very soon (Santos et al., 2025b). Chapter 2 is based on GRAVITY Collaboration et al. (2024) and is aimed at highlighting the importance of accurately measuring BH masses for a better understanding of the SMBH-galaxy coevolution and a novel method in spatially resolving the BLR through interferometric observations with GRAVITY. We analysed the interferometric signals of four new low-redshift AGNs observed with GRAVITY and provided dynamical mass measurements for their central BHs and precise measurements of their BLR sizes. We calculated their BLR photocentres to gain insight into their BLR kinematics and compared their BLR sizes to the canonical R-L relation (Bentz et al., 2013). We also calculated their

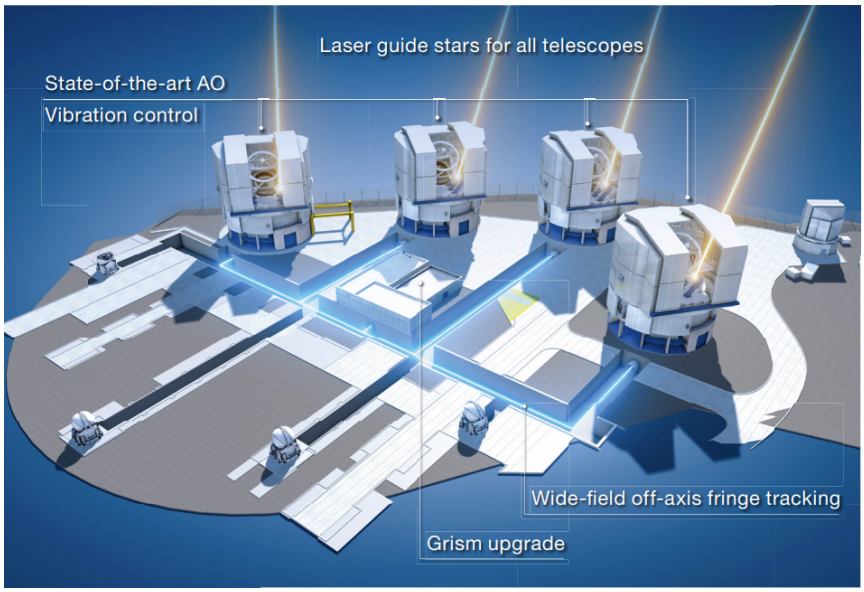

Figure 1.10: Schematic diagram showing the improvements to be implemented for GRAVITY+. Image taken from the ESO website.

virial factors and compared them to what previous works have used while assuming that AGNs have the same $M_{BH} - \sigma_*$ relation as those of quiescent galaxies (Onken et al., 2004; Woo et al., 2010; Park et al., 2012; Batiste et al., 2017).

To expand our work on SMBH mass measurements with GRAVITY, we look into two prospects: one is by extending our work to higher redshifts, and the other is by testing and improving our BLR model, which is based on Pancoast et al. (2014a). The premises of Chapters 3 and 4 are the former and latter, respectively. In Chapter 3, which is based on Santos et al. (2025a), we look into 29 quasar candidates that could be observed with GRAVITY+. These targets are situated at the cosmic noon at $z \sim 2$ when both the star formation (SF) and black hole accretion histories were at their peaks (Madau and Dickinson, 2014). We conducted a spectroscopic survey of these targets with the Son of ISAAC (SOFI) instrument located at the New Technology Telescope (NTT) in La Silla Observatory, Chile. Through this survey, we confirmed their quasar nature through their broad Balmer line profiles, estimated their bolometric luminosities and BH masses via the single-epoch BH mass estimate formula, and assessed their observability by estimating their expected interferometric signals to be detected by the longest baseline of VLTI.

Chapter 4, which is based on Santos et al. (2025b), focuses on determining the interferometric signal of the radiation-driven fountain simulation Wada (2011). This simulation assumes that the radiation pressure from the accretion disk drives dust and gas outflows, which eventually flow back in due to gravity, causing a circulation of materials that create the dusty torus and the BLR. The resulting interferometric signal of the model is then fitted with the Pancoast model of the BLR to test its performance and identify its areas for improvement.

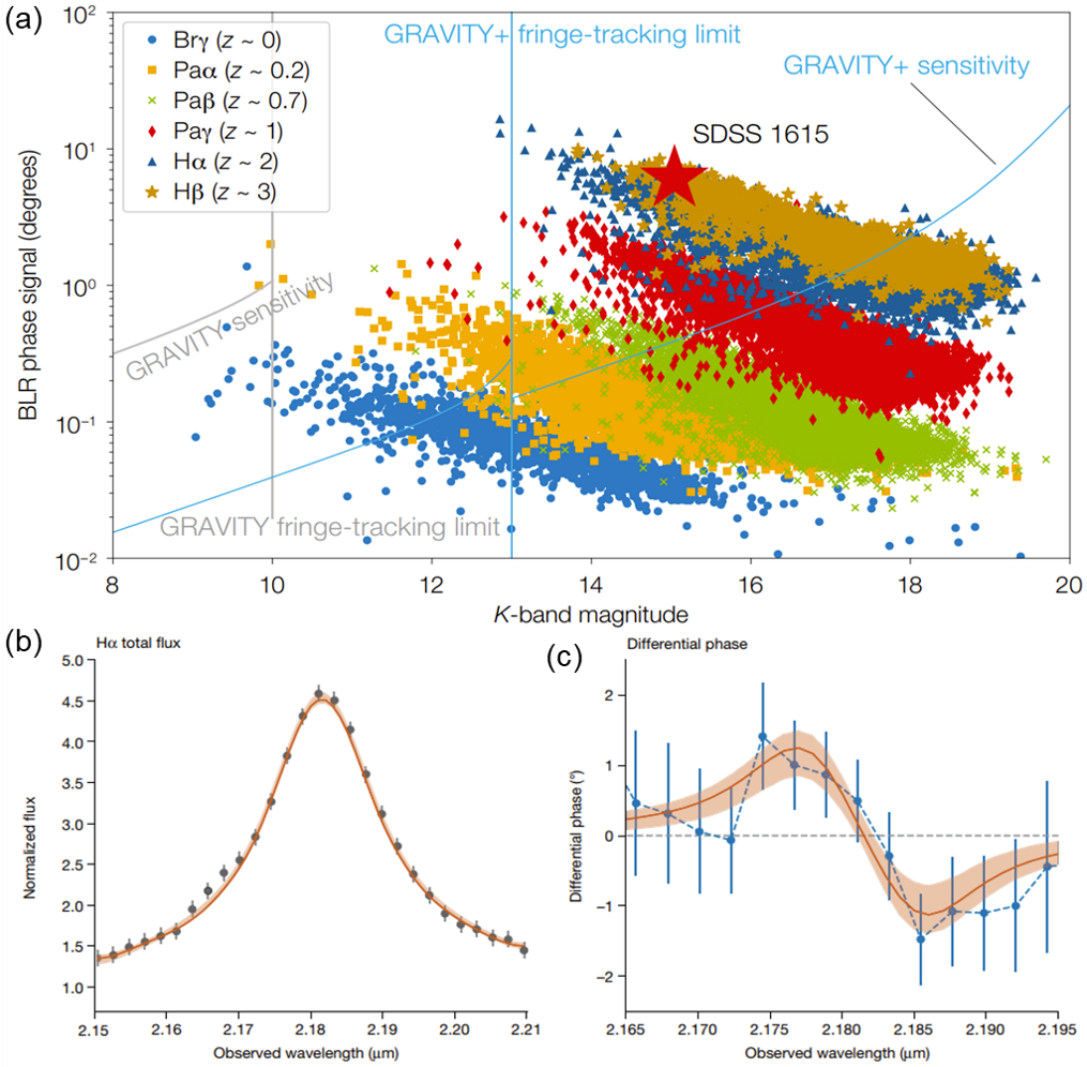

Figure 1.11: (a) Plot showing the expected BLR phase signal as a function of K-band magnitude. The grey lines pertain to GRAVITY, with the curve showing its sensitivity and the vertical line its fringe-tracking limit. The blue lines pertain to GRAVITY+, with the same legend as that of GRAVITY.

With GRAVITY+, we expect to observe fainter AGNs as the limiting magnitude is now pushed to fainter values. SDSS 1615, the first $z \sim 2$ AGN to have its SMBH mass dynamically measured with GRAVITY-Wide, is shown as a red star in the plot. Image taken from GRAVITY+ Collaboration et al. (2022b) (b) The Hα total flux of SDSS 1615 taken from Abuter et al. (2024). (c) The differential phase signal of SDSS 1615 also taken from Abuter et al. (2024).

Chapter 5 provides the overall summary and conclusions of this thesis, and potential outlooks for future work. Finally, the rest of the chapters show the appendices of this thesis.

Chapter 2

The size-luminosity relation of local active galactic nuclei from interferometric observations of the broad-line region

This chapter is published as a paper: GRAVITY Collaboration et al. (2024), A&A, 684, A167.

2.1 Introduction

Many earlier works have shown that SMBHs reside in the centre of most galaxies (e.g. Soltan, 1982; Rees, 1984; Ferrarese and Ford, 2005; Davis, 2014; Padovani et al., 2017). The $M_{\rm BH}$-σ_* relation provides strong evidence for SMBH-host galaxy coevolution (e.g. Magorrian et al., 1998; Gebhardt et al., 2000; Treu et al., 2004; Kormendy and Ho, 2013; Caglar et al., 2020). This requires robust measurements of BH masses. There are many ways of doing this, such as spatially resolving stellar kinematics (e.g. Gebhardt et al., 2000; Sharma et al., 2014), measuring the kinematics of (ionised) gas (e.g. Davies et al., 2004a,b; Hicks and Malkan, 2008; Davis et al., 2013), utilising megamaser kinematics with very long baseline interferometry (VLBI) (e.g. Kuo et al., 2020; Wagner, 2013; van den Bosch et al., 2016), and reverberation mapping (RM) (e.g. Peterson, 1993; Lira et al., 2018; Cackett et al., 2021). Other indirect methods involve scaling relations, relying on single-epoch optical/near-infrared (NIR) spectroscopy to observe several line estimators and to measure their fluxes and widths (e.g. Hα, Hβ, Mg II λ2798, and C IV λ1549) (e.g. Kaspi et al., 2000; Greene and Ho, 2005; Shen and Liu, 2012a) as well as coronal lines to estimate the accretion disc temperature (e.g. Prieto et al., 2022).

When the SMBH is "active", it accretes surrounding material and forms an accretion disc. The brightness of the resulting AGN dilutes the signal from the stars and gas surrounding it (in addition to the gas being subject to forces other than gravity, e.g. radiation

pressure, winds, etc.), hindering BH mass measurements via stellar and gas kinematics (Gebhardt et al., 2000). The intense radiation can trigger megamasers and thus allow for this SMBH mass measurement method, but the need for a nearly edge-on line of sight (LOS) allows for only type 2 AGNs (van den Bosch et al., 2016) to be observed.

RM campaigns utilise the fluctuations over time of the continuum flux originating from the accretion disc (Blandford and McKee, 1982a; Peterson, 1993; Peterson et al., 2004). These variations are then echoed or reverberated in the surrounding gas of the broad-line region (BLR). The time lag between the continuum and BLR variations can be measured from their light curves and utilised to estimate the radius of the BLR under the assumption that the measured time delay represents the light-crossing time between the accretion disc and BLR. The mass of the central BH is then calculated using the virial equation (Eqn. 1.8). As discussed earlier, the virial factor f accounts for the unknown geometry and structure of the BLR.

Previous works have revealed that local AGNs exhibit a relationship between the BLR radius measured from AGN emission lines (e.g. Hα and Hβ) and AGN continuum luminosity (usually at 5100 Å), the so-called R-L relation (Kaspi et al., 2000; Bentz et al., 2013). The R-L relation, combined with a measurement of the gas velocity (e.g. the FWHM of the broad emission lines), can then be used to estimate BH masses of distant AGNs using Eq. 1.8 (e.g. Laor, 1998; Vestergaard and Peterson, 2006a; Shen et al., 2023). However, BH mass estimations via single-epoch spectroscopy are only accurate if the R-L relation accurately represents the whole AGN population. Hence, confirming the relation with a more diverse and broad AGN sample is important. The accretion rate or $L/L_{\rm edd}$ has been suggested to serve as a 'third' parameter in the R-L relation, as highly accreting AGNs seem to have smaller BLR sizes than what is predicted by the canonical R-L relation (Du et al., 2014b, 2015, 2016a; Du and Wang, 2019). Most of these highly accreting sources are also highly luminous ($\log \lambda L_\lambda(5100\text{Å})/\text{erg s}^{-1} \gtrsim 44$; Du et al. 2018b), and hence the deviation from the canonical R-L relation is more prominent at higher luminosities. Du et al. (2018b) and Du and Wang (2019) show that using $\mathcal{R}$(Fe II) (the equivalent width ratio of Fe II and Hβ) as a proxy of accretion rate can reduce the scatter of the R-L relation. Not accounting for the accretion rate could then lead to BH mass estimations via single-epoch spectroscopy and the R-L relation to be overestimated by as much as ~ 0.3 dex (Alvarez et al., 2020; GRAVITY Collaboration et al., 2023).

RM measurements have concluded that the BLR gas is mostly dominated by Keplerian motion and is therefore orbiting around the central BH (e.g. Gaskell, 2000; Denney et al., 2009; Bentz et al., 2010; Du et al., 2016a; Grier et al., 2017a; Williams et al., 2018; Bentz et al., 2021b; Villafaña et al., 2023). The BLR could also have considerable turbulence in the direction perpendicular to the BLR mid-plane, with significant inflow and outflow velocity components (Osterbrock, 1978; Ulrich and Horne, 1996). Several pieces of evidence of possible inflow and outflow signatures for some BLRs have been found (e.g., Kollatschny and Dietrich, 1997; Denney et al., 2009; Bentz et al., 2009, 2010; Du et al., 2016a). On the other hand, three BLRs whose kinematics were resolved by GRAVITY were found to be rotation dominated (GRAVITY Collaboration et al., 2018, 2020a, 2021a). Hence, a single description of the BLR has not been established yet.

A crucial limitation of RM is the uncertain virial factor, f. Usually, f is calibrated assuming that AGNs follow a similar $M_{\rm BH}$-σ_* relation with those of quiescent galaxies. Although f is different for each AGN and cannot be determined without velocity-resolved RM data, the average f can be calculated for a sample of AGNs. The average virial factor, $\langle f \rangle$, serves as a scaling factor of RM-derived BH masses to match the said relation. Various works have different values of $\langle f \rangle$ (e.g. Onken et al., 2004; Woo et al., 2010; Graham et al., 2011; Park et al., 2012; Batiste et al., 2017). Source variability and line width uncertainties could also lead to uncertainties in the measured time lag (see Vestergaard et al. 2011 and references therein). RM campaigns are also usually limited by the luminosity of the AGNs they can target, as more luminous targets should require much longer RM campaigns to measure the expected time lags. Recent RM surveys though are working to expand the high luminosity range (e.g. Woo et al., 2023).

Spatially resolving the BLR was initially difficult to accomplish due to its very small angular size ($\lesssim 10^{-4}$ arcseconds; Blandford and McKee 1982a). However, thanks to GRAVITY, the second-generation NIR beam combiner in the Very Large Telescope Interferometer (VLTI), the sensitivity of NIR interferometry has been exceptionally improved, and the light received by all four 8m unit telescopes (UTs) has been combined to yield six simultaneous baselines (GRAVITY Collaboration et al., 2017). This has allowed us to not just spatially resolve the BLR, but also obtain measurements of the SMBH mass and investigate the BLR structure at a high-angular resolution. To this end, we carried out an ESO Large Programme to observe the brightest type 1 AGNs, which span four orders of magnitude in luminosity, to spatially resolve their BLR and measure their central BH masses. This programme also aims to further understand the BLR structure and its intricacies, such as inflow and outflow motions that may be present in some systems, and to investigate GRAVITY-derived BLR radius and BH mass measurements and how they compare with scaling relations of local AGNs, such as the R-L and $M_{\rm BH}$-σ_* relations. Three BLRs from this sample have already been spatially resolved by GRAVITY (GRAVITY Collaboration et al., 2018, 2020a, 2021a,b). In parallel, several works have focussed on resolving the dust sublimation region (GRAVITY Collaboration et al., 2020b, 2021a), and using the observed dust size to estimate BLR sizes (GRAVITY Collaboration et al., 2020c, 2023).

In this work, we present an analysis of four new GRAVITY observations of type 1 AGNs, namely Mrk 509, PDS 456, Mrk 1239, and IC 4329A, all in the local Universe ($z < 0.2$). For the entirety of our paper, we adopt a Lambda Cold Dark Matter (ΛCDM) cosmology with $\Omega_m = 0.308$, $\Omega_\Lambda = 0.692$, and $H_0 = 67.8$ km s^{-1} Mpc^{-1} (et al., 2016). We discuss the targets' properties in Sect. 2.2. We describe the observations, data reduction, and the resulting flux and differential phase spectra in Sect. 2.3. We report the model-independent photocentre positions of each target's BLR in Sect. 2.4. We describe our BLR model in Sect. 2.5, and discuss the importance of differential phase data in our BLR modelling in Sect. 2.6. We present the results of our BLR model fitting in Sect. 2.7, while we place the derived BLR sizes and BH masses of our targets in the context of the R-L and $M_{\rm BH}$-σ_* relations in Sects. 2.8 and 2.9, respectively. We also observed an offset between the BLR and continuum photocentres of our targets and discuss its possible origin in Sect. 2.10. We also explain how we calculated the virial factors of our targets in Sect. 2.11.

Finally, we present our conclusions and future prospects in Sect. 2.12.

2.2 Targets

All four targets were observed with GRAVITY as part of a large programme (and initial pilot projects) that aims to spatially resolve the BLR and measure BH masses for a sample of the brightest (nuclear luminosity of $K \lesssim 10$ mag and $V \lesssim 15$ mag) type 1 (Sy1 or QSOs with broad Paα or Brγ emission lines) AGNs in the local Universe[1]. Table 2.1 summarises the properties of our four targets and the three other targets that are already published.

2.2.1 Mrk 509

Mrk 509 is a type 1 Seyfert galaxy that shows significant outflow signatures in terms of mildly relativistic ($\sim$ 0.14-0.2c) FeXXVI Kα and Kβ absorption features (Cappi et al., 2009) detected in its X-ray spectra. These imply a possible varying structure and geometry (Cappi et al., 2009). RM campaigns have estimated the BLR size of Mrk 509 to be $R_{\rm BLR} \sim$ 80 ld (Carone et al., 1996; Peterson, 1998; Bentz et al., 2009; Shablovinskaya et al., 2023). Its central BH mass was also calculated to be $M_{\rm BH} = 10^{7.9} - 10^{8.3}\ M_\odot$ (Peterson, 1998; Peterson et al., 2004).

2.2.2 PDS 456

PDS 456 is known to be the most luminous radio-quiet AGN in the local Universe ($z \lesssim$ 0.3) (Torres et al., 1997; Simpson et al., 1999; Bischetti et al., 2019; Yun et al., 2004). Aside from its brightness and proximity, it has been extensively studied due to its ultra-fast outflows (UFOs) of highly ionised Fe (Reeves et al., 2003). These outflows possess high kinetic power ($\sim$20% of its bolometric luminosity; Luminari et al. 2018) and are also radiatively driven, which can be explained by the AGN's high Eddington ratio (Matzeu et al., 2017). Its BH mass, unfortunately, is not well-studied. No RM measurements are available for PDS 456 because such a luminous target should produce very long time lags ($\sim$ several years), requiring decade-long RM campaigns. Therefore, BH mass estimations based on empirical relations from RM are used (Reeves et al., 2009; Nardini et al., 2015). Its central BH mass is estimated to be $M_{\rm BH} \sim 10^9\ M_\odot$. Its BLR size is also implied to be large; GRAVITY Collaboration et al. (2020c) partially resolved the continuum hot dust emission region of PDS 456 and used the measured continuum size from the fringe tracker data and the differential visibility amplitude data from the science channel (SC) to indirectly infer its BLR size. However, their estimate is highly uncertain due to the weak correlation between the SC differential amplitude and the BLR size for very small angular sizes relative to the baseline resolution. GRAVITY Collaboration et al. (2023) estimated its BH mass and BLR radius to be $M_{\rm BH} \sim 10^{8.68}\ M_\odot$ and $R_{\rm BLR} \sim 150$ ld from

[1]All GRAVITY observations were made using the ESO Telescopes at La Silla Paranal Observatory with programme IDs 1104.C-0651(C), 1103.B-0626(B), 099.B-0606(A), and 0101.B-0255(B).

Table 2.1: Physical properties of our four new targets and the three targets that were already observed by GRAVITY.

Object	RA (J2000)	Dec (J2000)	z	log λL_λ (5100 Å) (erg s^{-1})	Ref.	σ_* (km s^{-1})	Ref.	D_A (Mpc)
(1)	(2)	(3)	(4)	(5)	(6)	(7)	(8)	(9)
Mrk 509	20:44:09.738	−10:43:24.54	0.0344	44.19	1	182	8	144
PDS 456	17:28:19.796	−14:15:55.87	0.185	46.30	2	182[1]	This work	657
Mrk 1239	09:52:19.102	−01:36:43.46	0.020	44.40[2]	3	∼250[3]	9	86
IC 4329A	13:49:19.266	−30:18:33.97	0.016	43.51	4	∼225	9	69
3C 273	12:29:06.700	+02:03:08.60	0.158	45.90	1	210	10	582
NGC 3783	11:39:01.762	−37:44:19.21	0.0097	43.02	6	95	11	42
IRAS 09149-6206	09:16:09.39	−62:19:29.90	0.0573	44.92d	5,7	250[4]	7	236

[1] The stellar velocity dispersion of PDS 456 is estimated in this work by using the measured dynamical mass of PDS 456 by Bischetti et al. (2019) and virial theorem.

[2] Although Pan et al. (2021) measures the extinction-corrected optical luminosity of Mrk 1239, caution is still needed as Mrk 1239 is widely known to show high polarisation and high extinction.

[3] The stellar velocity dispersion of Mrk 1239 is highly uncertain due to the shallowness of its stellar features (Onken et al., 2004)

[4] The dispersion of IRAS 09149-6206 is based on the [OIII] line and is very uncertain (GRAVITY Collaboration et al., 2020a).

Notes: Col. (1): Object name. Col. (2): Right ascension. Col. (3): Declination. Col. (4): Redshift from NASA/IPAC Extragalactic Database (NED). Col. (5): AGN optical luminosity at 5100 Å. Col. (6): References for λL_λ (5100 Å). Col. (7): Stellar velocity dispersion. Col. (8): References for σ_*. Col. (9): Angular diameter distance.

References: (1) Du and Wang (2019), (2) Nardini et al. (2015), (3) Pan et al. (2021), (4) Bentz et al. (2023) (5) Koss et al. (2017), (6) Bentz et al. (2021a), (7) GRAVITY Collaboration et al. (2020a), (8) Grier et al. (2013b), (9) Oliva et al. (1999), (10) Husemann et al. (2019), (11) Onken et al. (2004)

the relation between the BLR and dust continuum size. It is interesting to note that GRAVITY Collaboration et al. (2023) measured a smaller BH mass than previous works have estimated, and this deviation is suggested as a consequence of its high Eddington ratio (Du and Wang, 2019) that has been implied by its strong FeII features and lack of [OIII] emission lines (e.g., Simpson et al., 1999).

2.2.3 Mrk 1239

Mrk 1239 is an NLSy1 galaxy well known for its high polarisation (Goodrich, 1989; Smith et al., 2004), relatively redder optical-IR colour compared to other typical NLSy1s, and presence of a radio jet-like structure (Orienti and Prieto, 2010; Doi et al., 2015) oriented perpendicular to the polarisation angle. Mrk 1239 has not been a target for RM campaigns, but previous works have estimated its BH mass and BLR size via indirect estimates from various scaling relations. They all point to the same conclusion that Mrk 1239 has a small but uncertain BH mass, $M_{\rm BH} \sim 10^{5.7} - 10^{7.0}\ M_{\odot}$ (e.g. Kaspi et al., 2005; Greene and Ho, 2005; Ryan et al., 2007; Du et al., 2014a; Buhariwalla et al., 2020; Pan et al., 2021; GRAVITY Collaboration et al., 2023). Its BLR size is also estimated to be $R_{\rm BLR} \sim 10$ to 20 ld (e.g. Du et al., 2014a; GRAVITY Collaboration et al., 2023).

2.2.4 IC 4329A

IC 4329A is a type 1 Seyfert galaxy that is well-observed in X-ray (e.g., Madejski et al., 1995; Delvaille et al., 1978; Piro et al., 1990; Nandra and Pounds., 1994). Several RM campaigns were implemented to measure the BLR size and BH mass of IC 4329A. For instance, Winge et al. (1996) presented the first RM data for IC 4329A, which was reanalysed by Peterson et al. (2004). However, the poor quality of the light curves raised caution about their estimated BH masses and BLR sizes. Wandel et al. (1999) calculated a BLR size and BH mass of $R_{\rm BLR} = 1.4^{+3.4}_{-2.9}$ ld and $M_{\rm BH} \sim 10^{7.4}\ M_{\odot}$ after re-analysing the spectrum taken by Winge et al. (1996). Bentz et al. (2023) presented the latest RM campaign for IC 4329A, and together with BLR model fitting, they acquired a BLR size of $R_{\rm BLR} = 14.2^{+7.2}_{-3.7}$ ld and a BH mass of $M_{\rm BH} = 4^{+10}_{-2} \times 10^{7.0}\ M_{\odot}$. GRAVITY Collaboration et al. (2023) also estimated the BLR size of IC 4329A via dust size measurements, yielding $R_{\rm BLR} \sim 17.4$ ld.

2.3 Observations and data reduction

2.3.1 Observations

The GRAVITY observations were done over several nights between August 2017 and July 2021. We used the single-field on-axis mode with combined polarisation for all observations. Each observation sequence follows that described in GRAVITY Collaboration et al. (2020a). First, the telescopes pointed to the target and closed the adaptive optics (MACAO, Arsenault et al. 2003) loop. The light was then propagated to GRAVITY,

Table 2.2: Observation logs of our target AGNs observed with GRAVITY. The table shows the dates, total on-source time of all the data used in the analysis after rejection via our fringe tracking ratio criterion, weather conditions (average seeing in arcseconds and coherence time in ms), and astrometric accuracy at the line peak (estimated from the photocentre fitting results; discussed more thoroughly in Sect. 2.4) of our observations.

Object	Dates	Total on-source time (min.)	Ave. Seeing ($''$)	Ave. Coherence time (ms)	Astr. Accuracy μas
Mrk 509	25, 26 Jul. 2021	100	0.66	3.2	48.0
PDS 456	26, 27 Aug. 2018 14, 15, 16, 18 Jul. 2019 12, 16 Aug. 2019 27 Jul. 2021	295	0.66	4.8	12.8
Mrk 1239	7, 30 Jan. 2021 1 Feb. 2021 1, 2, 31 Mar. 2021	366	0.72	6.8	32.7
IC 4329A	1 Feb. 2021 1, 2, 31 Mar. 2021	210	0.76	5.2	47.4

where the fringe tracking (FT) and science channel (SC) fibres align on the target via internal beam tracking of GRAVITY. The exposures were acquired after the fringe tracker found the fringes and began tracking. The integration time for each exposure frame is DIT = 30 seconds, and the number of frames for each set of exposures is NDIT = 12. All observations were taken in MEDIUM resolution. The number of obtained exposures varied among objects. A calibrator star (usually an A- or B-type star) close to the target was also observed and used to calibrate the flux spectrum of the AGN. This ensures that atmospheric and vibrational effects, coherence loss, and birefringence are all accounted for. We adopted the same pipeline data reduction as GRAVITY Collaboration et al. (2020a) to calculate the complex visibilities from the raw data, enabling us to extract quantities correlated to the physical properties of our targets. Table 2.2 shows the date, exposure time and weather conditions (seeing and coherence time) during observations.

We use all available GRAVITY data for three of the four targets. However, we only use the observations of Mrk 509 from 2021. This is because earlier (2017 and 2018) observations of Mrk 509 show differential phase errors that are ∼50% larger than those from 2021, which benefit from the factor two better throughput of the science channel spectrometer after the grating upgrade at the end of 2019 (Yazici et al., 2021).

2.3.2 Differential phase spectra

To produce the differential phase curve on each baseline for all the targets, we first selected exposures with fringe tracking ratio (percentage of utilised time that fringe tracking was working) greater than or equal to 80%, removing 16, 17, 8, and 33 exposures for Mrk 509, PDS 456, Mrk 1239, and IC 4329A, respectively. We followed the method from GRAVITY Collaboration et al. (2020a) in removing instrumental features from the differential phase curves, estimating their uncertainties in each channel, and polynomial flattening. To check whether our uncertainties match the observed noise in the differential phase spectra and are a good representation of the actual dispersion of the differential phase spectra, we compare the average uncertainty in the whole spectra and the dispersion of the differential phase in regions beyond the wavelength range where the broad emission line is expected to be found. Our comparison suggests that only Mrk 1239 shows a significant discrepancy: the uncertainties in its differential phase spectra (which are ∼0.06-0.08° on average for all baselines) are lower compared to the dispersion of the differential phase values at around 2.18-2.20 μm and 2.22-2.24 μm (which are ∼0.08-0.14° on average). Hence, we adopted the dispersion of the differential phase values at these wavelength ranges as the representative uncertainty/error bar of all channels in each baseline. However, we emphasise that we also tried adopting the uncertainties in Mrk 1239's differential phase spectra as its representative uncertainty, and we conclude that this does not greatly affect our results.

The definition of differential phase in the partially resolved limit that is appropriate for our AGN observations (e.g. GRAVITY Collaboration et al., 2018, 2020a) is as follows:

$$\Delta\phi_\lambda = -2\pi \frac{f_\lambda}{1+f_\lambda} \vec{u} \cdot \vec{x}_{\mathrm{BLR},\lambda}, \tag{2.1}$$

The equation above is the same as Eqn. 1.53 with a simplified notation for the BLR photocentres, $\vec{x}_{\mathrm{BLR},\lambda}$. In Eqn. 2.1, $\Delta\phi_\lambda$ is the differential phase measured in a certain wavelength channel λ, f_λ is the normalised flux in that channel, $\vec{u}$ is the uv coordinate of the baseline, and $\vec{x}_{\mathrm{BLR},\lambda}$ denotes the BLR photocentres. The differential phases are referenced to the continuum photocentre, which is placed at the origin. If the centre of the BLR coincides with the continuum photocentre, the differential phase signal reflects the kinematics of the BLR. Meanwhile, if the BLR to continuum offset is much larger than the BLR size, the $\vec{x}_{\mathrm{BLR},\lambda}$ becomes a constant approximately over different channels. The differential phase signal will be proportional to $\frac{f_\lambda}{1+f_\lambda}$ and resemble the profile of the broad line (see more discussion in Section 2.10). Hereafter, we call the phase signal generated by the global offset between the BLR and the continuum emission the "continuum phase". Such a global offset is observed in IRAS 09149-6206 and NGC 3783 primarily due to the asymmetry of the hot dust emission (GRAVITY Collaboration et al., 2020a,b). More details about the derivation of Eqn. 2.1 are shown in Appendix B of GRAVITY Collaboration et al. (2020a).

Fig. 2.1 shows the differential phase spectra of our 4 targets averaged for each baseline. Most of the baselines of the targets show signals in their differential phase curve that are either negative (Mrk 509 and PDS 456) or positive (Mrk 1239 and IC 4329A) and mostly coincide with the peak of their line profiles. As for IRAS 09149-6206 (GRAVITY Collaboration et al., 2020a), this indicates that their differential phase spectra show signatures of a continuum phase. The signals are also relatively small with absolute values $\lesssim 0.6°$. We can, therefore, conclude that their BLRs are either intrinsically small or viewed at a very low inclination angle.

2.3.3 Normalised profiles of the broad Brγ and Paα emission lines

Modelling the dynamics and deriving the velocity gradient of a target's BLR requires a well-measured nuclear emission line profile (Brγ for Mrk 509, Mrk 1239, and IC 4329A, and Paα for PDS 456). In general, the stacking and calibration of the line profiles are as follows: after fitting for and removing the Brγ absorption line of the calibrator star, each spectrum was normalised by fitting a third-degree polynomial to the continuum before stacking. We then followed the method of extracting the final line profile from GRAVITY Collaboration et al. (2020a) wherein we considered the statistical uncertainty (i.e. the rms from each individual spectrum's uncertainties) and the systematic uncertainty (i.e. mainly caused by variations in the calibrator data and sky absorption) of the spectra in producing the final flux error of the spectra. Lastly, the narrow components of the emission lines were also accounted for and removed following previous work (GRAVITY Collaboration et al., 2020a). Removing the narrow components from the flux spectra of our targets is important because the flux spectra, together with the differential phase spectra, are fitted together with our BLR model (to be discussed in Sect. 2.5). Eqn. 2.1 assumes that all of the flux in the line profile is only partially resolved. Narrow line emission that enters the GRAVITY fibres occurs on large scales and is over-resolved and thus does not contribute to

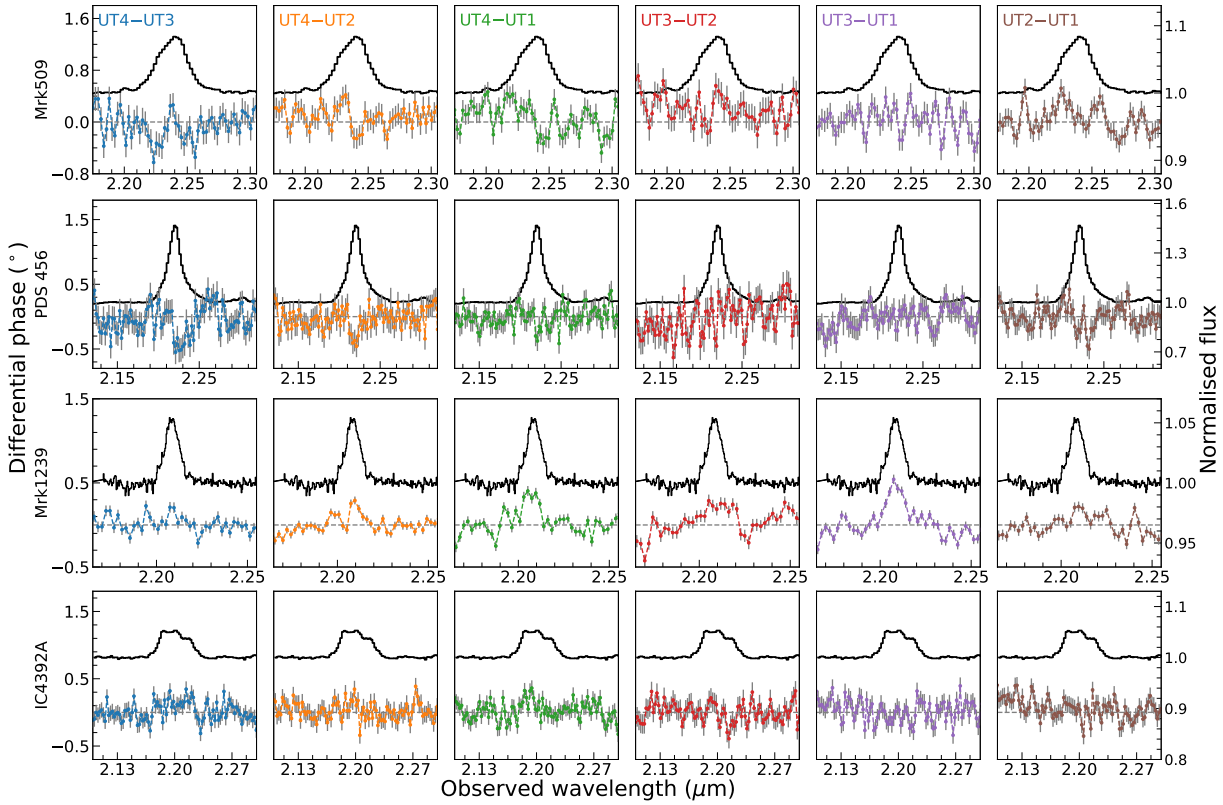

Figure 2.1: Averaged differential phase spectra (coloured, based on their respective baselines labelled in the top row) and the normalised Brγ (for Mrk 509, Mrk 1239, and IC 4329A) and Paα (for PDS 456) spectra (black histogram) of Mrk 509 (first row), PDS 456 (second row), Mrk 1239 (third row), and IC 4329A (fourth row). The curves show negative signals in Mrk 509 and PDS 456 with peaks ranging from $\sim$-0.4° to -0.5°, and positive signals in Mrk 1239 and IC 4329A with peaks ranging from $\sim$0.5°-0.6°.

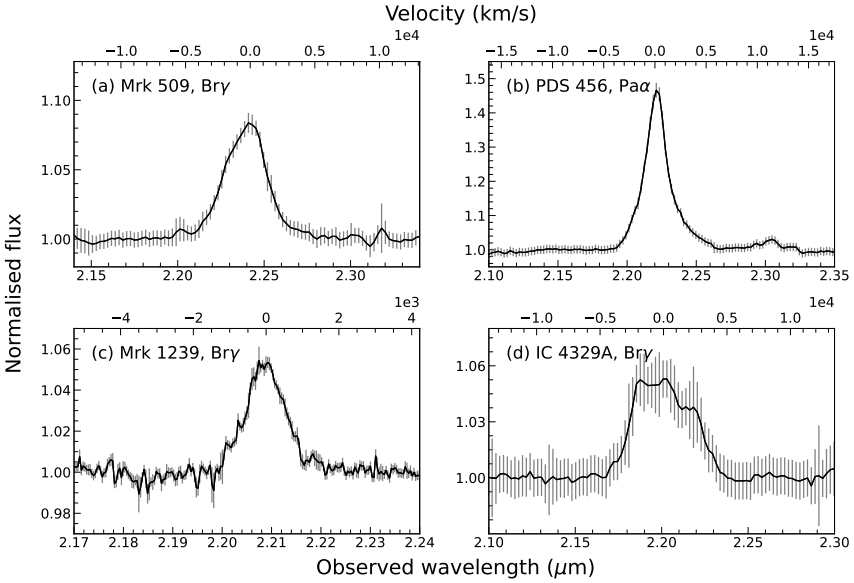

Figure 2.2: Average AGN flux spectra (black steps with grey error bars) of (a) Mrk 509 and (b) PDS 456 taken by GRAVITY, (c) Mrk 1239 taken by APO/TRIPLESPEC, and (d) IC 4329A taken by GRAVITY, all normalised to the continuum. The name of the emission lines for each target is shown in each panel.

the differential phase. We note that the narrow component removal is only applied to the flux spectra and does not affect the interferometric data. We use the GRAVITY spectra of Mrk 509, PDS 456, and IC 4329A, while we use the spectrum from the Apache Point Observatory's (APO) TRIPLESPEC instrument of Mrk 1239. The APO spectrum of Mrk 1239 has a higher spectral resolution than that of GRAVITY, and we decided to use it to better remove the narrow component and characterise the line profile. Our comparison between the two Mrk 1239 spectra confirms that they are both consistent in terms of line shape and flux levels.

GRAVITY spectra: Mrk 509, PDS 456, and IC 4329A

The flux spectra (1.95-2.45 μm) of Mrk 509, PDS 456, and IC 4329A were taken with GRAVITY in medium resolution mode ($R = \lambda/\Delta\lambda \approx 500$) with 90 independent spectral elements, which were extracted and resampled (and interpolated, if needed) into 210 channels. We extracted the final spectra of Mrk 509, PDS 456, and IC 4329A by weight-averaging 3, 10, and 3 GRAVITY spectra, respectively. Due to the low number of individual spectra to average for Mrk 509, we cannot simply estimate the flux errors in each channel based on multiple observations. Hence, we decided to multiply the flux errors by a factor of 3 to balance the weight of the flux spectrum and differential phase spectrum during BLR modelling. We also did the same for IC 4329A, but we decided to remove the factor of the flux error as it does not greatly affect the results of our analyses. To remove the Mrk 509's narrow Brγ emission component, we used the optical spectrum of

Mrk 509 taken by the Kitt Peak National Observatory (KPNO) 2.1m telescope (Shang et al., 2005). We utilised the optical blue spectrum (0.33-0.55 μm), adopting [O III]λ5008 Å as our narrow line template. For PDS 456, we assume all of its light originates from the BLR. Simpson et al. (1999) showed very little [O III] emission in PDS 456's optical spectrum, which strongly suggests negligible narrow emission in its broad Paα line. Hence, no narrow-line component removal was performed. For IC 4329A, no narrow line template was used to fit its narrow component. Although there is available VLT/SINFONI K-band (1.93 - 2.47 μm) spectrum for IC 4329A, it was taken last Jun. 2019, which is too distant in time for variability to be neglected. Therefore, we simply fit the Brγ line profile with 6 Gaussian components and subtracted the component describing the narrow component at the central wavelength of Brγ. We note that for the flux spectrum of IC 4329A, any number of Gaussian components below 6 is insufficient to provide a good fit, while above 6 does not provide a better fit.

APO and XSHOOTER spectra: Mrk 1239

We acquired 3 Mrk 1239 spectra (0.94-2.47 μm) with the TRIPLESPEC instrument at the Apache Point Observatory (APO) 3.5m telescope on two nights of 27th and 29th Dec., 2020. Since the GRAVITY interferometric observations were done ∼1-3 months after the APO spectroscopic observations, variability of spectral shape and intensity should be negligible as confirmed by Pan et al. (2021) after checking multi-epoch observations of Mrk 1239 in various wavelength ranges. The resolution of our Mrk 1239 flux spectrum is $R = 3181$, almost 6 times that of GRAVITY's, making it a better choice for our analysis. We used a 1.1" × 45" slit for our APO observations. The spectra were reduced using the modified version of the `Spextool` package (Cushing et al., 2004). An A0V star was also used for telluric correction and flux calibration (Vacca et al., 2003).

To get a narrow line template suitable for removing the narrow component of Mrk 1239's Brγ emission line, we observed Mrk 1239 with XSHOOTER in Dec. 2021 (PI: Shangguan, programme ID 108.23LY.001). The VIS (0.56-1.02 μm, $R = 18400$, using slit dimensions of $0.7'' \times 11''$) spectrum of Mrk 1239 was reduced using the XSHOOTER pipeline version 3.5.3 running under the EsoReflex environment version 2.11.5. From this spectrum, we utilise [S II]λ6716 Å as a template for the narrow component.

We implement two methods to study the BLR of our targets: photocentre measurements (a model-independent method that reveals the BLR's possible velocity gradient and offset with respect to the hot dust) and BLR modelling (reveals BLR properties and central BH mass). More details about each method are discussed in Sects. 2.4 and 2.5.

2.4 Measuring the BLR photocentres

We start our analysis of the BLR structure by measuring the photocentre positions of the line emission. This model-independent method provides a direct representation of the differential phases in the various baselines. By measuring the BLR photocentres, we can

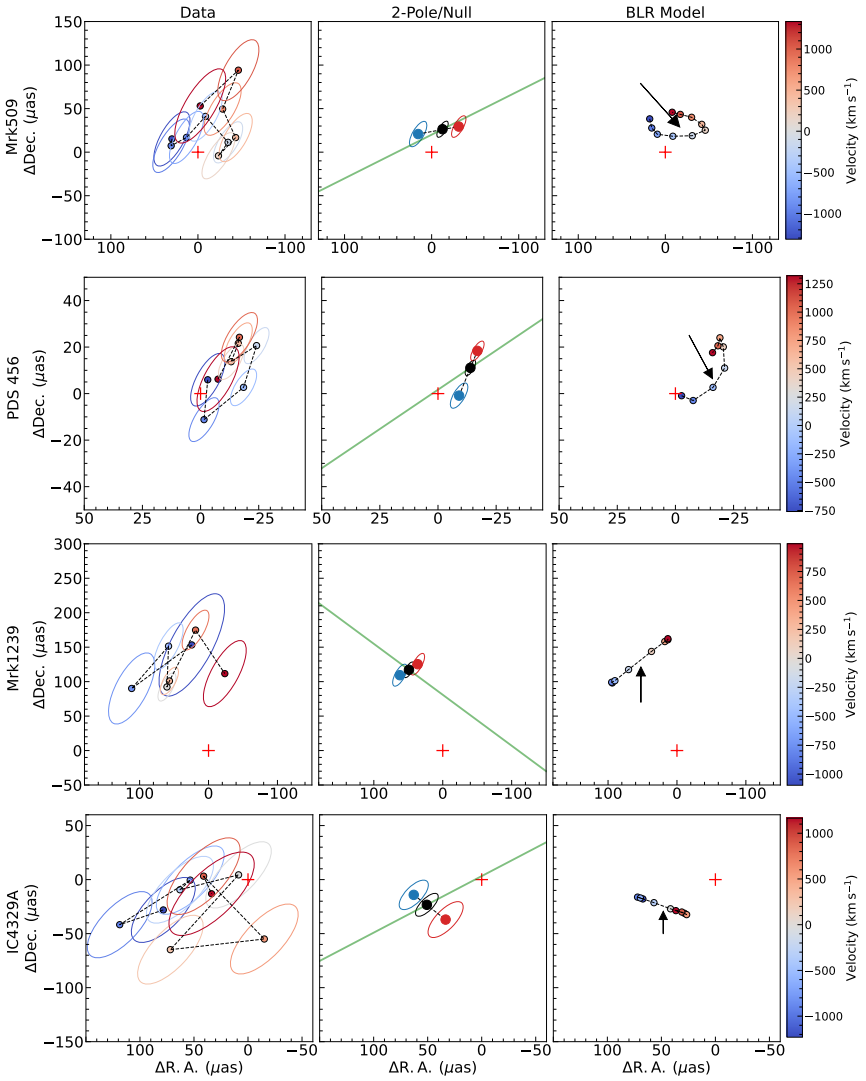

Figure 2.3: Best-fit BLR photocentres of our four targets. The columns from left to right show the photocentres from the data, the "2-pole" and "null" photocentre models (described in Sect. 2.4), and the photocentres from the best-fit BLR model of each target. The red cross refers to the continuum photocentre. The direction of the radio jet is shown as a green solid line. The black arrow shows the position of the best-fit "null" model fitted from the best-fit BLR model. The ellipses around each centroid refer to 68% (1σ) confidence intervals. The colours refer to the corresponding velocity of each spectral channel. The (significant) separation of the red- and blueshifted photocentres confirms that we have resolved the BLRs of our targets. For Mrk 1239 and IC 4329A, the perpendicular alignment between the radio jet and red-blue photo centres from the "2-pole" model fitting of the data and the straight alignments of their model photo centres indicate that their BLR is rotation-dominated. On the other hand, for Mrk 509 and PDS 456, the radio jet and red-blue photocentres are not closely perpendicular, and the model photocentres are curved, which suggests that their BLRs are radial motion-dominated.

confirm whether there is an overall velocity gradient in the BLR and investigate the offset between the BLR and hot dust photocentres, which previous works have also measured (GRAVITY Collaboration et al., 2020a, 2021a).

We first select the spectral channels where the Brγ/Paα emission dominates. This criterion gives us 9, 8, 7, and 9 spectral channels to fit for Mrk 509, PDS 456, Mrk 1239, and IC 4329A, respectively. The photocentre displacement for each channel can then be calculated using Eqn. 2.1. We also estimate the astrometric accuracy of each target (listed in Table 2.2) by averaging the errors of each photocentre position.

The left column of Fig. 2.3 shows the BLR photocentres of the 4 targets as a function of wavelength. The photocentres show a velocity gradient in the BLR, indicated by the separation between the blueshifted and redshifted channels. To investigate the significance of this gradient, we fit all blueshifted and redshifted channels, assuming a single photocentre for each side. We call this our "2-pole" model. We also fit *all* spectral channels into one photocentre, which we call our "null" model. The results of the 2-pole/null model fitting are shown in Fig. 2.3, middle column. The resulting 2-pole model fittings reveal the separation between the red and blue poles (velocity gradient) of Mrk 509, PDS 456, Mrk 1239, and IC 4329A to be 48, 20, 30, and 37 μas, respectively. These correspond to 0.034, 0.064, 0.013, and 0.012 pc, respectively. An F-test was utilised to confirm the significance of the velocity gradient, with the null model as the null hypothesis and the 2-pole model as the alternative hypothesis. Mrk 509, PDS 456, and IC 4329A reveal p-values that are $<<$ 0.05, indicating 6.7σ, 6.9σ, and 6.6σ significance, respectively. However, the red-blue photocentre offset of Mrk 1239 has a p-value of 0.88, meaning we cannot reject the null hypothesis of a single photocentre describing the BLR. In this case, the confidence in the offset between the red and blue photocentres and the resulting position angle begs a more detailed model fitting.

The BLR photocentres of our targets also reveal a systematic offset to the continuum photocentre (red cross in Fig. 2.3). This offset, which we call the "BLR offset", is measured as the distance between the continuum photocentre and the BLR null photocentre, and is about 28, 17, 137, and 34 μas (0.020, 0.054, 0.057, and 0.011 pc) for Mrk 509, PDS 456, Mrk 1239, and IC 4329A, respectively. The offsets are mostly close to perpendicular to the BLRs' velocity gradient, which is similar to what was observed with IRAS 09149-6206 (GRAVITY Collaboration et al., 2020a). To avoid the impact of possible data correlation between neighbouring channels during photocentre measurements, we re-binned the spectra by a factor of 2. The same method still yields a significance $>4.5\sigma$ (except Mrk 1239), regardless of the inclusion of the bluest/reddest channels that are furthest from the photocentres of the other channels.

On the right column of Fig. 2.3, we also show the model photocentres, which are produced from the mock differential phase and flux spectra of the best-fit BLR model (See Sect. 2.7). These model photocentres show the average photocentres of the BLR clouds of the best-fit BLR model in each wavelength channel and provide another way to see the cloud distribution, which can be linked to the differential phase data. These are discussed in more detail in Sect. 2.7, where they are used to explain the observed differential phases of our targets.

Since we were able to constrain the BLR velocity gradient of most of our targets, we can compare the alignment of the red and blue photocentres with the jet alignment, as revealed by radio observations. The orientation of the radio jet is shown as the green line in the middle 2-pole/null model fitting results. The radio jet orientations are taken from Ulvestad and Wilson (1984) for Mrk 509, Yang et al. (2021) for PDS 456, Doi et al. (2015) and Orienti and Prieto (2010) for Mrk 1239, and Colbert et al. (1996) for IC 4329A. It is clear that the red-blue photocentre orientations of Mrk 1239's and IC 4329A's BLRs are perpendicular to their radio jets, indicating that their BLRs are rotating, similar to what is found for 3C 273 (GRAVITY Collaboration et al., 2018). However, Mrk 509 and PDS 456 reveal that the red-blue photocentre orientations of their BLRs are closely aligned to their radio jets.

To conclude our photocentre fitting analysis, we find significant ($> 5\sigma$) velocity gradients between the blueshifted and redshifted channels of all our targets except Mrk 1239. These velocity gradients are perpendicular to the BLR offsets. Our comparison between the red and blue photocentres and the orientation of the radio jets shows that the BLRs of Mrk 1239 and IC 4329A are rotating. However, Mrk 509 and PDS 456 show otherwise. Photocentre fitting cannot explain this phenomenon, let alone fully constrain the physical BLR size, as the photocentre offsets average over the emission of the channel bandpass and will therefore underestimate the BLR size. Therefore, a flexible model fit to the full differential phase spectra must be utilised to investigate our targets' BLR structure and kinematics.

2.5 Description of the BLR model

We follow the BLR model described in Pancoast et al. (2014a) (henceforth called the *Pancoast model*). The Pancoast model is a phenomenological model that has been used in modelling light curves and RM measurements (e.g. Pancoast et al., 2014b; Mangham et al., 2019; Bentz et al., 2023) and even interferometry data in conjunction with flux spectra (Stock, 2018; GRAVITY Collaboration et al., 2018, 2021a, 2020a). In this section, we will present the important assumptions and definitions in the model, but for a more comprehensive discussion of the Pancoast model, we refer the readers to Pancoast et al. (2014a).

The Pancoast model defines the BLR as a collection of non-interacting clouds encircling the central SMBH. The resulting structure can be defined as a Monte Carlo approximation of the density field of emission. This is a convenient way to model the kinematics and structure of the BLR, but we do not mean to imply that the BLR specifically comprises discrete clouds. The physical structure of the BLR is described by several parameters that dictate the clouds' position and motion. Table 2 of GRAVITY Collaboration et al. (2020a) summarises the parameters included in the model and their possible ranges of values. We use the same priors as GRAVITY Collaboration et al. (2020a), with a few exceptions, which are discussed later. Hence, we refer the readers to GRAVITY Collaboration et al. (2020a) for the full list of parameters in the model.

The radial distribution of the point clouds is described by a shifted Gamma function:

$$p(x|\alpha,\theta,r_0) = \frac{(x-r_0)^{\alpha-1}e^{-\frac{(x-r_0)}{\theta}}}{\Gamma(\alpha)\theta^{\alpha}} \tag{2.2}$$

where α is the shape parameter (describes how peaked the distribution is), θ is the scale parameter (describes how wide the distribution is), r_0 is the location or shift parameter (determines where the distribution starts), and $\Gamma(\alpha)$ is the Gamma function. α and β are not straightforward quantities that can be interpreted physically, hence the Pancoast model uses a different parameterization in terms of three parameters:

$$\mu = r_0 + \alpha\theta \tag{2.3}$$

$$\beta = \frac{1}{\sqrt{\alpha}} \tag{2.4}$$

$$F = \frac{r_0}{r_0 + \alpha\theta} \tag{2.5}$$

where μ ($R_{\rm BLR}$) is the average (emissivity-weighted) BLR radius. In this parameterization, r_0 ($R_{\rm min}$) is now interpreted as the minimum BLR radius, F is the fractional inner radius defined as $R_{\rm min}/R_{\rm BLR}$, and β flexibly dictates qualitatively different radial distributions: Gaussian ($0 < \beta < 1$), exponential ($\beta = 1$), and heavy-tailed/steep ($1 < \beta < 2$) profiles. The distance of the clouds from the central BH is then represented by the following equation:

$$r = R_s + \mu F + \mu g(1-F)\beta^2 \tag{2.6}$$

where $R_s = 2GM_{\rm BH}/c^2$ is the Schwarzschild radius, and g is the random number taken from the shifted Gamma distribution shown in Eqn. 2.2.

The model also has an opening angle parameter θ_0, which describes the maximum angle the clouds can take with respect to the midplane. The angular distribution of the clouds is then expressed as:

$$\theta = \cos^{-1}(\cos\theta_0 + (1-\cos\theta_0) \times U^{\gamma}) \tag{2.7}$$

In the equation above, the half-opening angle of the disc, θ_0, describes the thickness of the BLR: $\theta_0 = 90^\circ$ produces a spherical BLR, while $\theta_0 = 0^\circ$ produces a thin disc. In addition, U is a random number between 0 and 1, and γ is a parameter between 1 and 5. The parameter γ controls the angular concentration of BLR clouds relative to θ_0. When set to 1, it pertains to the uniform case with the clouds equally distributed as a function of angular height. Increasing $\gamma > 1$ redistributes the BLR clouds more and more to the outer faces of the disc, with $\gamma = 5$ as the maximum possible value. In the Pancoast model that we are using, we are free to turn on or off this angular distribution irrespective of the presence of other parameters. In the case that it is turned off, γ is removed in Eqn. 2.7, creating a cloud distribution that is much thicker in the midplane than at the maximum angular height θ_0. On the other hand, if the angular distribution is turned on, γ is included

as a free parameter in the model, thus creating a cloud distribution that becomes more concentrated at θ_0.

Aside from θ_0, the model also has certain orientation parameters, such as the inclination angle i and position angle PA. The former is measured between a face-on BLR geometry and the line-of-sight (LoS) of the observer, with $i = 0°$ pertaining to a face-on view, and $i = 90°$ as an edge-on view. The latter is not included in the original conception of the model but is added to fit interferometric and flux spectra (Stock, 2018), and defines the model's amount of rotation within the sky plane.

The parameter γ, when fitted as a free parameter, produces asymmetric/anisotropy in the cloud distribution of the BLR model. Aside from γ, there are other ways to introduce anisotropy in the BLR model. For instance, we can introduce anisotropic emission from each individual BLR cloud via the parameter κ. We assign a weight "w" to each cloud that defines how much BLR emission is directed into the LOS:

$$w = 0.5 + \kappa \cos \phi \tag{2.8}$$

where κ ranges from -0.5 to +0.5. When $\kappa > 0$, it results in preferential emission from the BLR's near side (side closer to the observer), while $\kappa < 0$ results in preferential emission from the BLR's far side. The parameter ϕ describes the angle between the LOS of the observer and the LOS of the BLR cloud to the central ionising source. Anisotropic emission from the near side could be caused by BLR clouds situated closer to the observer obstructing the emission from the gas farther away. On the other hand, preferential emission from the far side of the BLR could be caused by self-shielding within individual BLR clouds, resulting in emission only at the back towards the central continuum source.

Finally, the transparency of the midplane can be modelled with the parameter ξ, which ranges from 0 to 1. When $\xi = 1$, the clouds are evenly distributed on both sides of the equatorial plane, while $\xi = 0$ means that the emission from the clouds behind the equatorial plane is obscured. The physical cause of possible BLR mid-plane opacity is not well-understood (GRAVITY Collaboration et al., 2020a), and it should be interpreted cautiously.

For the kinematics of the Pancoast model, each cloud is assigned a tangential velocity (v_ϕ) and a radial velocity (v_r) component. These components are randomly distributed around a point on an ellipse in the $v_r - v_\phi$ plane with a semi-major axis at (v_r=$\pm v_{\rm esc}$, v_ϕ=0) and a semi-minor axis at (v_r=0, $v_\phi = \pm v_{\rm circ}$). A parameter $f_{\rm ellip}$ controls the percentage of the clouds that are in circular or bound orbits. Those that are in circular orbits are located in the $v_r - v_\phi$ plane at (0, $\pm v_{\rm circ}$) where $v_{\rm circ} = \sqrt{GM_{\rm BH}/r}$. On the other hand, the rest of the clouds possess highly elongated orbits and are dominated by radial motion with a maximum radial velocity equal to the escape velocity $v_{\rm esc} = \sqrt{2} v_{\rm circ}$ and are located in the $v_r - v_\phi$ plane at ($\pm v_{\rm esc}$, 0). The direction of the radial motion is controlled by a binary parameter $f_{\rm flow}$, with $f_{\rm flow} < 0$ as inflow, and $f_{\rm flow} > 0$ as outflow. For clouds dominated by radial motion, an additional parameter $\theta_e = \tan^{-1}(|v_\phi / v_r|)$ allows such clouds to have radial velocities smaller than the escape velocity. It also describes the boundness of the radial-dominated clouds' orbits: as explained by Villafaña et al. (2023), when θ_e approaches

0°, the clouds are in nearly unbound orbits, but when θ_e approaches 90°, the clouds are in nearly circular and bound orbits. A value of $\theta_e = 45°$ means that the inflowing/outflowing clouds are in highly elliptical yet bound orbits. The circular bound clouds are distributed in the $v_r - v_\phi$ plane such that they follow a Gaussian distribution centred at (v_r=0, v_ϕ = $v_{\rm circ}$) and standard deviations defined on the v_r and v_ϕ direction, which are $\sigma_{\rho,\rm circ}$ and $\sigma_{\Theta,\rm circ}$, respectively. On the other hand, the inflowing/outflowing clouds are distributed in the $v_r - v_\phi$ plane such that they follow a Gaussian distribution centred at (v_r=$\pm v_{\rm esc}\cos\theta_e$, $v_\phi = v_{\rm circ}\sin\theta_e$) with the positive (negative) sign corresponding to outflowing (inflowing) radial motion, and standard deviations defined on the v_r and v_ϕ direction, which are $\sigma_{\rho,\rm radial}$ and $\sigma_{\Theta,\rm radial}$, respectively.

Aside from these parameters, the central wavelength λ_c, the peak flux with respect to the continuum ($f_{\rm peak}$), and the central offset of the BLR with respect to the origin (x_0, y_0) are included as nuisance parameters (i.e. do not contribute to the BLR geometry but are still considered as free parameters) in the model. In this work, we do not focus our discussion on these nuisance parameters and θ_e but instead on the best-fit kinematic parameters $f_{\rm ellip}$ and $f_{\rm flow}$ of each target.

We consider two variations of the Pancoast model in our work. One is termed the *circular* model. This model sets $\kappa = 0$ and $\xi = 1$ to ensure that all clouds emit isotropically and are uniformly distributed above and below the BLR mid-plane. No angular asymmetry is considered in this model; that is, $\gamma = 1$. All BLR clouds are then subject to circular Keplerian rotation (i.e., $f_{\rm ellip} = 1$). The second model is the *elliptical/radial* model. In this model, angular asymmetry (γ) and all parameters corresponding to the asymmetrical properties of the BLR (κ, ξ) are fitted. Inflowing/outflowing clouds ($f_{\rm ellip}$ and $f_{\rm flow}$) are fitted as well (together with the Keplerian clouds). We fit the circular and elliptical/radial models to our 4 targets, but we only show the best-fit results for each target. We discuss the reason for our choice of BLR model during the fitting of each target in Sect. 2.7.

For the exceptions compared to GRAVITY Collaboration et al. (2020a), we fix the angular and radial standard deviations of circular and radial orbit distributions and the standard deviation of turbulent velocities to zero because they do not affect the model fitting. We limit the parameter space of the inclination angle to be Uniform(cos i(0, π/4)). We tested the fitting for all targets with a much larger range, Uniform(cos i(0, π/2)), and found that all targets except Mrk 509 and IC 4329A prefer a smaller inclination. Hence, we decided to use Uniform(cos i(0, π/2)) for the parameter space of the inclination angle of Mrk 509 and IC 4329A, while we adopt the smaller parameter space, Uniform(cos i(0, π/4)), to the rest of the targets to avoid multiple peaks in the posterior distribution. More discussion about the inclination angle of Mrk 509 and IC 4329A is presented later (in Sect. 2.7.1 and 2.7.4, respectively).

We fit the models to the total flux line profile and differential phase curves from all baselines simultaneously. The chosen wavelength channels for fitting each target cover the wavelength range where Brγ/Paα emission flux is relevant. All models utilise 2×10^5 clouds, which are randomly given parameter values based on their model distributions.

The interferometric data and prior information about the source and model are used to infer the best-fit model parameters via Bayes' theorem. We use the Python package

`dynesty` (Speagle, 2020) to implement posterior distribution sampling (random walk) of 2000 live points for each BLR fitting. `dynesty` allows the nested sampling algorithm to be utilised, which is powerful in estimating Bayesian evidence and dealing with complex models with presumably multimodel posteriors. The Bayesian evidence or marginal likelihood, Z, measures how well the probability distributions are constrained. The larger the Z, the stronger the constraint to the probability distributions. The Bayes factor, or the ratio of the Bayesian evidences, is then calculated to identify which model is more apt to fit the data.

We prefer to fit two models (inflowing and outflowing elliptical/radial model) separately and compare their Bayes factor, or the ratio of the outflowing model evidence to the inflowing model evidence, due to the nature of $f_{\rm flow}$ parameter as a binary flag. We do this by fitting an elliptical/radial model with $f_{\rm flow}$ restricted to a value between 0-0.5 (for inflowing clouds, representing an inflow elliptical/radial model) or 0.5-1.0 (for outflowing clouds, representing an outflowing elliptical/radial model). If the Bayes factor > 1, the source prefers outflowing radial motions; otherwise, it prefers inflowing radial motions. For all of our fittings, we use the nesting sampling algorithm (`NestedSampler`) as the sampler and random walk (`rwalk`) as the sampling method.

In this work, we report the best-fit values and their 68% (1σ) credible intervals of each parameter. We also show the model-inferred photocentre fitting results in Fig. 2.3, right column, where we simulate the differential phase and flux spectra from the best-fit BLR models of our targets. We observe that our model-inferred photocentre fitting results are consistent with what we get from fitting the photocentre from our data.

A caveat using the Pancoast model is that this does not mean that the BLR, by definition, consists of physical gas clouds, nor does it prefer the cloud model over other models mentioned in Sect. 4.1 and instead treats the point-like clouds as line-emitting entities (Kuhn et al., 2024). Another assumption of this model is that no photoionisation physics is included in the model. The point particles' physical sizes are not considered in the model. Thus, the model cannot describe physical covering factors and local surface emissivities in the BLR, preventing it from determining whether there are enough ionising photons to ionise the BLR at a certain radius (Raimundo et al., 2020). This also means that the model does not consider the absolute flux scaling and instead focusses more on the BLR geometry and kinematics as it fits the data with the most probable line emission distribution (Santos et al., 2025a). Furthermore, the model assumes that the clouds are subjected only to the gravitational force of the central BH. Non-gravitational forces such as radiation pressure from the ionising source, and fluid viscosity and gravitational interactions between particles are neglected (Pancoast et al., 2014a).

2.6 Importance of differential phase data in BLR fitting

2.6.1 Resulting posterior distribution from BLR fitting with and without phase data

As discussed in the previous section, the differential phase and flux spectra are our key inputs for BLR fitting. The differential phase measures the broad emission line's photocentre shift at different wavelength channels with respect to the continuum, providing spatial information. On the other hand, the flux spectrum gives information on the distribution of gas velocities in the BLR (see Raimundo et al. 2019, Raimundo et al. 2020, and references therein), as well as the inclination angle of the BLR, which is degenerate with the observed BH mass (Rakshit et al., 2015; GRAVITY Collaboration et al., 2018). The work of Pancoast et al. (2014a), from which our model is derived, performed fitting of broad emission lines (usually Hβ). In this section, we investigate the importance of adding the differential phase spectrum in fitting the broad emission line with our BLR model.

First, we fit our four targets with and without their differential phase spectra, assuming the same priors as the fitting with the differential phase spectra, and then compare their posterior distributions. We focus on the posterior distributions of the BLR radius, log $R_{\rm BLR}$ [ld], and BH mass, log $M_{\rm BH}$ [$M_\odot$] since these are the parameters that cannot be constrained with only a line profile. Fig. 2.4 shows the comparison between the posterior distributions of our BLR fitting with (orange line) and without (blue line) differential phase spectra for our 4 targets. It is clear that without the phase data, our BLR fitting fails to constrain these parameters. Our simple comparison shows that the phase data is crucial for unveiling more accurate estimates of our targets' BLR size and BH mass and more precise pictures of their BLR geometry and kinematics. This still holds true even for cases when there is no differential phase signal detected.

2.6.2 Expected differential phase signals of Mrk 1239 and IC 4329A

In the previous subsection, we highlight the importance of differential phase data in our BLR model fitting even if there is no phase signal detected. We investigated further by estimating the expected phase signals for Mrk 1239 and IC 4329A if only their flux profile were available for fitting. We focus on these two objects because, among our 4 targets, they have very weak signals that are still below their noise level ($\sim$0.05° and $\sim$0.10° for Mrk 1239 and IC 4329A, respectively). To constrain the possible phase signals of Mrk 1239 and IC 4329A without the phase data, we ran our BLR fitting for these two objects without their differential phase spectra while fixing their BH masses into their possible maximum and minimum values from previous works. For Mrk 1239, the maximum BH mass is log $M_{\rm BH}$ [$M_\odot$] = 7 from Pan et al. (2021), while the minimum BH mass is log $M_{\rm BH}$ [$M_\odot$] = 5.9 from Kaspi et al. (2005) and Greene and Ho (2005). For IC 4329A, the maximum BH

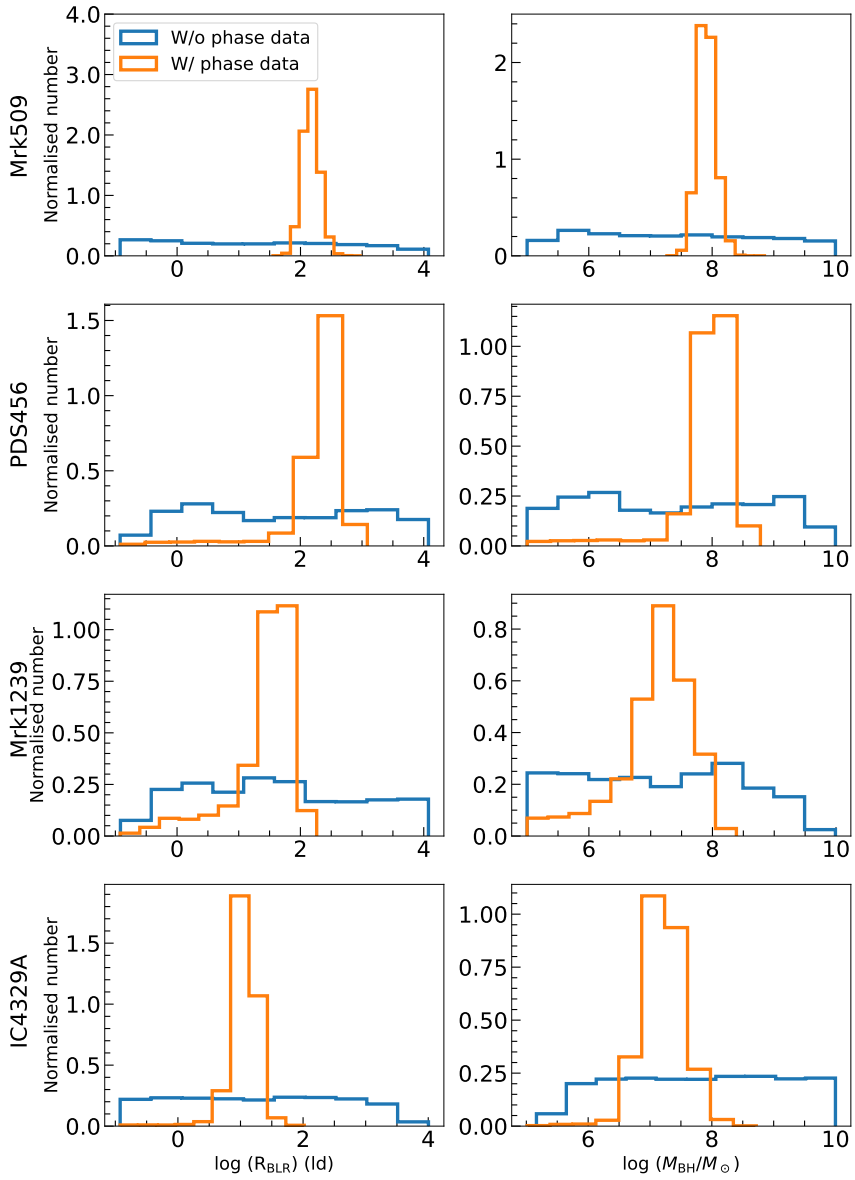

Figure 2.4: Posterior distributions of BLR radius (left column) and BH mass (right column) resulting from BLR fitting without differential phase data (blue histogram) and with differential phase data (orange histogram). Each row corresponds to each target; from top to bottom: Mrk 509, PDS 456, Mrk 1239, and IC 4329A. The histograms are normalised such that they integrate into 1. It is clear that the spatial information from the differential phase significantly constrains both the BLR radius and BH mass.

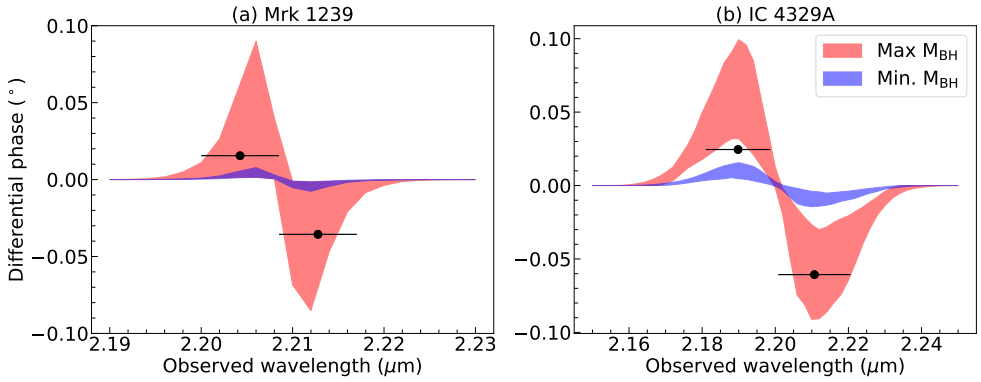

Figure 2.5: Expected differential phase signals for Mrk 1239 (left panel) and IC 4329A (right panel) when their line profiles were fitted with our circular model assuming their maximum (red shaded region) and minimum (blue shaded region) BH masses were fixed during fitting. The assumed BH masses for Mrk 1239 and IC 4329A are taken from previous literature as discussed in the text. The shaded regions refer to 1σ uncertainty. The chosen baselines to average are the same as the ones used to create Fig. 2.6: UT4-UT3, UT4-UT2, and UT4-UT1 for Mrk 1239; UT4-UT2, UT4-UT1, and UT3-UT2 for IC 4329A. The black points refer to the maximum and minimum observed phase signals at the line region of Mrk 1239 and IC 4329A after averaging the differential phase spectra from the same chosen baselines. The horizontal lines show the wavelength range of the maximum and minimum observed phase signals.

mass is log $M_{\rm BH}$ $[M_\odot]$ = 7.6 from Bentz et al. (2023), while the minimum BH mass is log $M_{\rm BH}$ $[M_\odot]$ = 6.8 from Kaspi et al. (2000). The expected averaged phase signals are shown in Fig. 2.5 as a 1σ shaded region. The chosen baselines to average are UT4-UT3, UT4-UT2, and UT4-UT1 for Mrk 1239, and UT4-UT2, UT4-UT1, and UT3-UT2 for IC 4329A. To create Fig. 2.5, the PA of each object were also fixed to their best-fit values (see best-fit results in Table 2.4). Since there is a degeneracy between the BH mass, BLR size, and inclination angle (Rakshit et al., 2015; GRAVITY Collaboration et al., 2018), the expected phase signal will then reflect the possible BLR sizes and inclination angles for these targets; that is, the larger the expected phase signal is, the bigger the inferred BLR size and inclination angle are.

Fig. 2.5 shows the range of differential phase signals that we are expecting based on what was previously known. The expected phase signals for the two objects span a large range when the maximum BH mass is assumed, indicating the wide range of possible BLR radius and inclination angles. The resulting absolute phase signal goes as high as ∼0.09° for Mrk 1239 and ∼0.10° for IC 4329A. The opposite is true when the minimum BH mass is assumed; the resulting absolute phase signals are very small (∼0.005° for Mrk 1239, and ∼0.02° for IC 4329A) and cover a very narrow area in the differential phase parameter space. The areas covering the expected phase signals for Mrk 1239 and IC 4329A when the maximum BH masses are assumed are much larger than the typical signals shown in the differential phase spectra of these objects (see Fig. 2.1). This emphasises the importance of phase data in our fitting; without the phase data, the constraining power of our fitting

is lessened, and the resulting posterior distributions of their BLR radius and inclination angle span a much wider range. The rather weak signals of Mrk 1239 and IC 4329A have a discriminating power, allowing us to limit the possible values of their BLR radii and inclination angles. Another way to look at this is that the small phase signals of Mrk 1239 and IC 4329A rule out higher values of inclination angle because these would lead to stronger phase signals.

The expected phase signals of Mrk 1239 and IC 4329A could also be used to infer the possible BH masses of these targets by comparing them with their observed phase signals. In Fig. 2.5, we plot the average differential phase on the line region channels located at the left and right of the line centre. These represent the average observed phase signals of Mrk 1239 and IC 4329A. For Mrk 1239, its average observed phase signal runs from -0.04° to +0.02°. Based on the expected phase signals in Fig. 2.5, this indicates that Mrk 1239 may not have as low of a BH mass as Kaspi et al. (2005) measured, and instead, it may have a large BH mass close to what Pan et al. (2021) measured. The average observed phase signal of IC 4329A (from -0.06° to +0.02°) also suggests that IC 4329A may not possess such a low BH mass similar to what Kaspi et al. (2000) measured. This indicates that IC 4329A may have a large BH mass similar to the value Bentz et al. (2023) measured. The BLR fitting results discussed next section will confirm if these points are true or not.

2.7 BLR modelling results

Fig. 2.6 summarises our BLR modelling results. We compare the differential phase spectra from our data with the ones predicted by the model, using the weighted average of the differential phase spectra from the longest baselines and/or the baselines that show the strongest or most prominent BLR phase signal after continuum phase removal (note that all the baselines were used for the actual BLR fitting; we only do this step for clearly visualising the averaged phase of each target). We show the 16-to-84 percentile range (1σ confidence interval) of the model phase and flux spectra as a red-shaded region by randomly sampling the posterior distribution of our fitting results 100 times.

The differential phase signal will vary over different baselines due to their different orientation with respect to the observed target. Therefore, for visualisation purposes, we have the freedom to choose which baselines we should average to compare the data and model fitting results. For Mrk 1239, the averaged differential phase spectrum is derived from averaging the differential phase spectra from three baselines: UT4-UT2, UT4-UT1, and UT4-UT3. For IC 4329A, the chosen baselines are similar to that of Mrk 1239, except that UT3-UT1 is chosen instead of UT4-UT3. For Mrk 509 and PDS 456, we averaged the spectra from all baselines. The observed differential phase includes both the continuum phase and the BLR differential phase. We are only interested in the latter. Hence, we subtract the former based on our model fitting. Mrk 509 and PDS 456 show a strong asymmetric signal in their averaged BLR differential phase. Mrk 509 also shows a slight asymmetry in its flux spectrum. On the other hand, Mrk 1239 and IC 4329A reveal weak BLR signals, which are below their respective noise. Considering this, we decided to fit

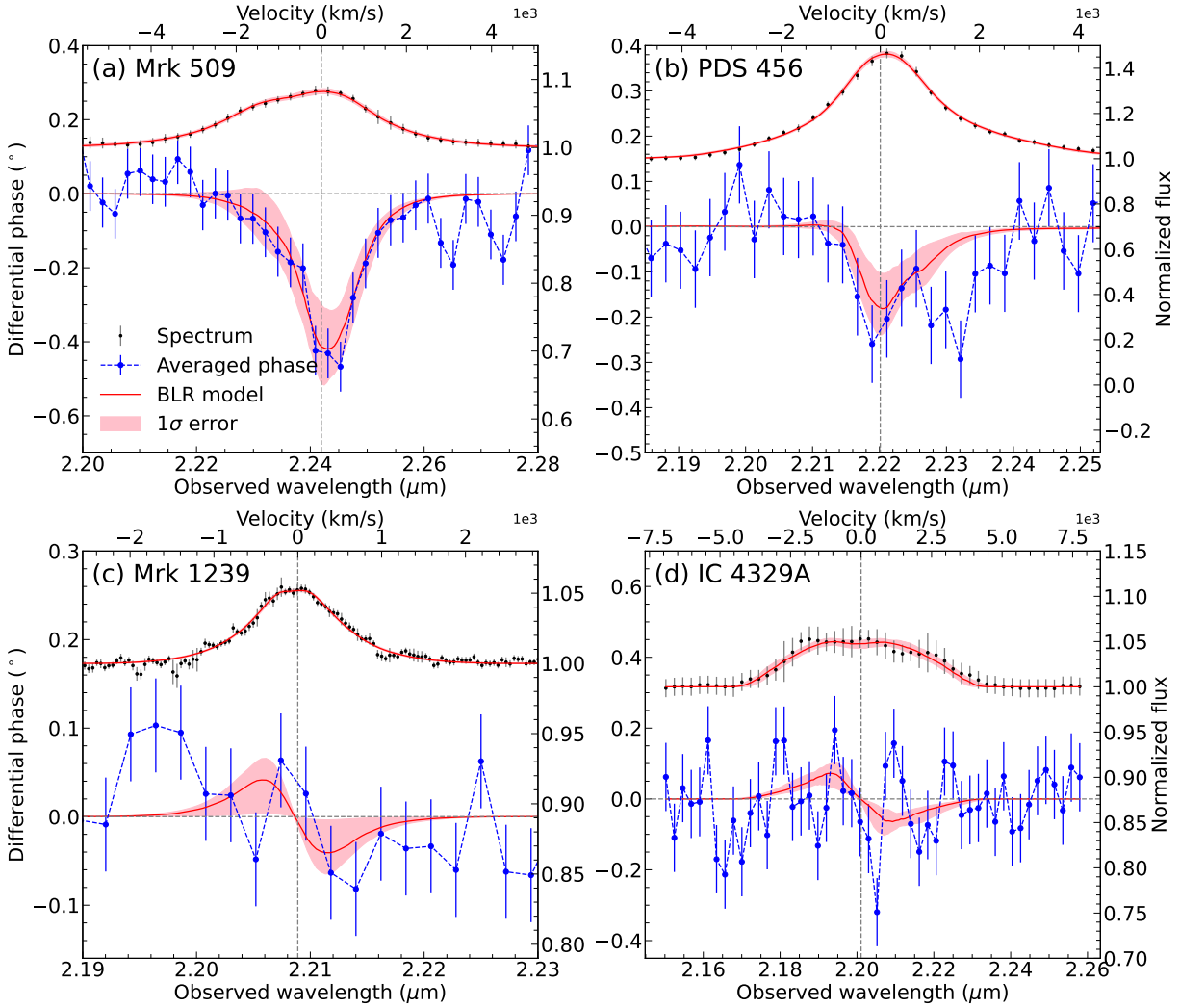

Figure 2.6: Summary of BLR fitting results for (a) Mrk 509, (b) PDS 456, (c) Mrk 1239, and (d) IC 4329A. The observed averaged differential phase spectra with the continuum phase signal removed are shown in blue, while the median differential phase spectra from the best-fit BLR model are shown in red (see text for the details of averaging the differential phase spectra for each target). Above each panel, the observed line profile (black) is shown together with the median best-fit model line profile (red). The central wavelengths of the line profiles are shown by the grey vertical dashed lines. The red-shaded region shows the 16-to-84 percentiles of the averaged differential phase spectra and flux spectra from the best-fit model, which was created by getting randomly selected samples of each parameter in 100 different instances and then recreating the averaged differential phase spectra. Mrk 509 and PDS 456 clearly show an asymmetrical signal typical for the Pancoast model, while Mrk 1239 and IC 4329A show the S-shape signal typical for the Keplerian model.

the elliptical/radial model for Mrk 509 and PDS 456 data, while we fit the circular model for Mrk 1239 and IC 4329A data. The low signal-to-noise ratio (S/N) data of Mrk 1239 and IC 4329A cannot be well-constrained by the elliptical/radial model, and even if we fit them with the elliptical/radial model, the resulting BH mass and BLR size are not much different given our uncertainties, similar to what is found for IRAS 09149-6206 in GRAVITY Collaboration et al. (2020a).

Tables 2.3 and 2.4 show the best-fitting parameters of the elliptical/radial and circular models for our 4 targets. We discuss each target's BLR modelling results (i.e., averaged differential phase spectra, best-fit parameter values, and their interpretation) in the following subsections.

2.7.1 Mrk 509

Mrk 509 is best fit with the elliptical/radial model, which better reproduces its asymmetric flux spectrum. The Bayesian evidence from the elliptical/radial Pancoast model, which is $\sim 100\times$ greater than that from the circular Pancoast model, strongly indicates the need for including both asymmetric emission and radial motion. Fig. A.1 in the Appendix shows the corner plot of the resulting posterior distributions of all fitted parameters. The inferred inclination angle is $\sim 69°$. Although it is quite high for a face-on target, we note that with the presence of radially moving clouds, the definition of the inclination angle is not as straightforward as that of a BLR possessing only rotation-dominated clouds.

The inferred BLR radius for Mrk 509 is $\log R_{\rm BLR}$ [ld] $= 2.29^{+0.01}_{-0.26}$. This is slightly larger than what is measured previously by other works (Peterson, 1998). However, the best-fit BH mass of Mrk 509 is $\log \mathrm{M_{BH}}$ $[M_\odot] = 8.00^{+0.06}_{-0.23}$, consistent with previous estimates (e.g., Peterson, 1998; Grier et al., 2013b). The inferred inner BLR radius is $\log R_{\rm BLR,min}$ [ld] $= 0.93^{+0.40}_{-0.39}$

Our BLR model for Mrk 509 prefers only ∼30% of the clouds to be in circular orbits, meaning the majority (∼70%) of the clouds have significant radial (highly elliptical) motion. The resulting Bayes factor after fitting an inflowing and outflow radial model is 12.55, indicating a strong preference for the outflow radial model over inflow. This supports the result that outflows dominate the BLR of Mrk 509.

Mrk 509 shows an asymmetric line profile with a blueshifted shoulder, and a negatively peaked differential phase signal shifted redwards of the Brγ central wavelength (see Fig. 2.6a). Such profiles can only be produced by a BLR possessing asymmetric properties. Our best fit angular distribution parameter is $\gamma \sim 4.1$, indicating that most of the BLR clouds are on the outer faces of the BLR disc, and fewer clouds are located in the midplane of the BLR. This is physically consistent with what one would expect for an outflowing BLR. Our best fit BLR model prefers a BLR with low mid-plane transparency ($\xi \sim 0.21$) and a moderate preference for the emission to originate from the far side of the clouds ($\kappa \sim$ -0.18). Fig. 2.7a shows the edge-on view of Mrk 509, emphasising the lack of clouds seen below the midplane. We note that this does not necessarily mean that there are actually fewer clouds below the midplane since we are only modelling the *observed* broad-line emission. The high inclination angle allows the observer to look directly into the edge of the disc, causing the

Table 2.3: Inferred maximum a posteriori value and central 68% credible interval for the modelling of the spectrum and differential phase of Mrk 509 and PDS 456 with the elliptical and radial model.

Parameter	Mrk 509	PDS 456
log $R_{\rm BLR}$ [ld]	$2.29^{+0.01}_{-0.26}$	$2.49^{+0.08}_{-0.38}$
log $\rm R_{BLR,\ min}$ [ld]	$0.93^{+0.40}_{-0.39}$	$1.16^{+0.42}_{-0.30}$
β	$1.07^{+0.15}_{-0.14}$	$1.83^{+0.06}_{-0.20}$
$i[^\circ]$	69^{+6}_{-12}	13^{+9}_{-2}
$PA[^\circ]$	185^{+25}_{-7}	265^{+2}_{-214}
$\theta_0[^\circ]$	64^{+11}_{-9}	42^{+14}_{-6}
log $M_{\rm BH}$ $[M_\odot]$	$8.00^{+0.06}_{-0.23}$	$8.23^{+0.01}_{-0.49}$
γ	$4.1^{+0.3}_{-2.4}$	$1.55^{+1.37}_{-0.18}$
κ	$-0.18^{+0.09}_{-0.11}$	$-0.44^{+0.07}_{-0.04}$
ξ	$0.21^{+0.10}_{-0.17}$	$0.75^{+0.11}_{-0.10}$
$f_{\rm ellip}$	$0.30^{+0.13}_{-0.10}$	$0.52^{+0.04}_{-0.25}$
x_0 [μas]	$-3.6^{+26.3}_{-13.4}$	$-7.3^{+3.4}_{-2.6}$
y_0 [μas]	$166.9^{+4.8}_{-65.7}$	$13.6^{+0.7}_{-5.8}$

Note: log $\rm R_{BLR,\ min}$ was calculated using the formula $F = R_{\rm BLR,\ min}/R_{\rm BLR}$, where both F and $R_{\rm BLR}$ are both fitted parameters.

Table 2.4: Similar to Table 2.3, but for Mrk 1239 and IC 4329A with the circular model.

Parameter	Mrk 1239	IC 4329A
log $R_{\rm BLR}$ [ld]	$1.77^{+0.03}_{-0.74}$	$1.13^{+0.10}_{-0.23}$
log $\rm R_{BLR,\ min}$ [ld]	$0.64^{+0.27}_{-0.28}$	$0.64^{+0.27}_{-0.28}$
β	$1.21^{+0.29}_{-0.31}$	$1.81^{+0.09}_{-0.92}$
$i[^\circ]$	11^{+6}_{-3}	54^{+22}_{-20}
$PA[^\circ]$	197^{+19}_{-49}	155^{+8}_{-53}
$\theta_0[^\circ]$	42^{+18}_{-15}	54^{+26}_{-29}
log $M_{\rm BH}$ $[M_\odot]$	$7.47^{+0.15}_{-0.92}$	$7.15^{+0.38}_{-0.26}$
x_0 [μas]	$55.1^{+4.2}_{-10.0}$	$47.0^{+10.7}_{-5.8}$
y_0 [μas]	$130.0^{+11.3}_{-11.6}$	$-25.9^{+6.0}_{-10.0}$

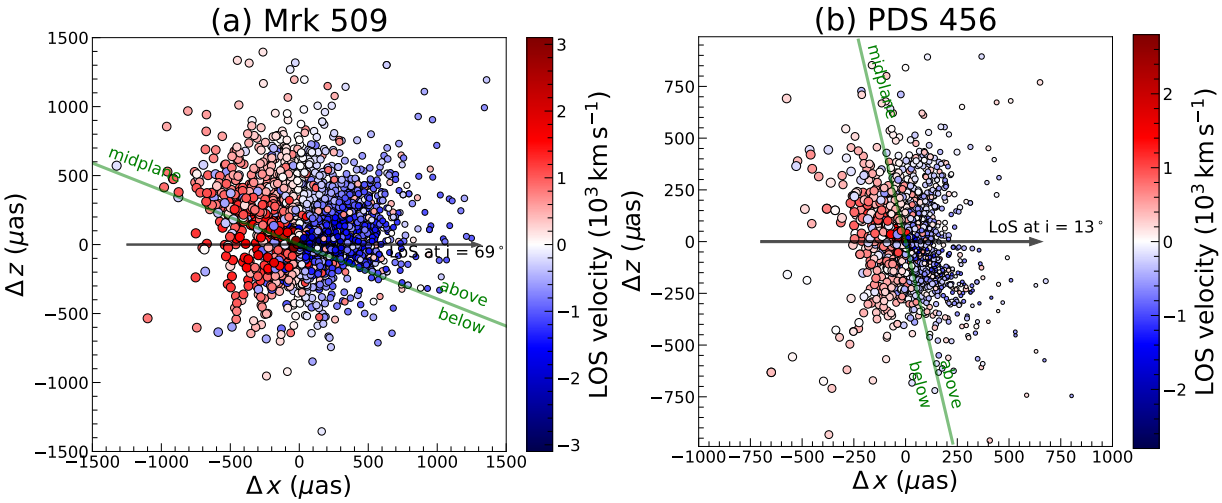

Figure 2.7: Edge-on views of the best-fit outflow model for (a) Mrk 509 and (b) PDS 456. For clarity, the PA for both configurations is adjusted to 180°, and the BLR centre is positioned to the origin. The LOS at the best-fit inclination angle is shown as a black arrow. The midplane, represented as a green line, is defined as the line passing through the origin and is perpendicular to the LOS at $i = 0°$. The regions above (closer to the observer) and below (farther to the observer) the midplane are also labelled. The colours of each cloud refer to their LOS velocity, while their sizes reflect the weight given to each cloud towards the total emission; the larger the size of the cloud, the more this cloud contributes to the broad-line emission. The edge-on view of the BLRs of Mrk 509 shows that its asymmetry is due to a highly obscuring midplane; for PDS 456, a preference for broad-line emission to come from the far side of the BLR.

observed differential phase on the blueshifted side to be small. On the other hand, the preferential emission on the far side (where the redshifted BLR clouds are mostly found, as shown in Fig. 2.7) creates a larger phase on the redshifted side of the line centre. In addition, the midplane obscuration affects more redshifted clouds than blueshifted clouds due to the inclination angle, and therefore produces an increase on the blue wing of the flux spectrum. Therefore, the best-fit BLR model of Mrk 509 (e.g., high inclination angle, large thickness, presence of BLR asymmetry) can recreate the asymmetric flux and differential phase spectra of Mrk 509. The combination of the effects of midplane obscuration and a significant fraction of outflowing BLR clouds causes the photocentres to be curved around the centre (right column, first row in Fig. 2.3), producing a strong dip in the averaged differential phase signal. This also explains why the red-blue photocentres of Mrk 509's BLR are not perpendicular to its radio jet, as the red-blue photocentres are dominated by the clouds dominated by radial motion and not by tangential/Keplerian motion.

2.7.2 PDS 456

Similar to Mrk 509, PDS 456 is best fit with the elliptical/radial model. This model better fits PDS 456's asymmetric differential phase spectrum, which is difficult to achieve with

the circular model. The Bayesian evidence for the elliptical/radial model is ∼14× greater than that from the circular Pancoast model fitting. Fig. A.2 shows the resulting corner plot of its BLR model fitting. It has a small inclination angle ($i \sim 13°$), and the opening angle ($\theta_0 \sim 42$) suggests that its BLR is moderately thick. This indicates that the system, despite the thickness, is unobscured. The BLR cloud distribution also has a steep profile ($\beta \sim 1.83$). Our BLR modelling with PDS 456 infers a BLR radius of log $R_{\rm BLR}$ [ld] = $2.49^{+0.08}_{-0.38}$; the largest among our sample. The best-fit BH mass of PDS 456 is log $M_{\rm BH}$ [$M_\odot$] = $8.23^{+0.01}_{-0.49}$. Our BH mass is a factor of 10 smaller than that measured by Reeves et al. (2009) and Nardini et al. (2015) via scaling relations. This is similar to what GRAVITY Collaboration et al. (2023) concluded via dust size measurements as they also measured a smaller BH mass than previous works, albeit 0.5 dex higher than our result. This also suggests that the discrepancy in the BH mass between our work and that estimated by GRAVITY Collaboration et al. (2023) is just due to the assumed virial factor to calculate the latter. The inferred BLR inner radius is log $R_{\rm BLR,min}$ [ld] $1.16^{+0.42}_{-0.38}$.

Our modelling results with PDS 456 emphasise that almost half of the BLR system is dominated by radial motions, as the best-fit value of $f_{\rm ellip} \sim 0.52$. Letting $f_{\rm flow}$ as a free parameter causes the BLR fitting results to slightly prefer inflowing radial motions ($f_{\rm flow} < 0.5$). However, the Bayes evidence of fitting with $f_{\rm flow}$ fixed to inflow and outflow is equal to 1.818, which means that PDS 456 does not show a preference between inflow and outflow radial motions. Therefore, we conclude that the data cannot distinguish between the inflow and outflow model, and we choose to fix $f_{\rm flow} > 0.5$ for PDS 456 as other observations reveal outflowing signatures at both smaller and larger scales than the BLR (Reeves et al., 2003; Luminari et al., 2018; Bischetti et al., 2019).

PDS 456 also exhibits a negative averaged differential phase spectrum almost centred at the Paα central wavelength, similar to Mrk 509. Its phase signal is more asymmetric compared to that of Mrk 509, as it shows a more extended redward tail. Again, we look at the best-fit asymmetry parameters and the model photocentres to explain this phase signal. The best-fit value of ξ is ~ 0.75, indicating that the midplane is mostly transparent. However, the best-fit value of κ is $\sim$ -0.44, suggesting that the BLR clouds emit preferentially from the far side. The effects of these parameters are evident in Fig. 2.7b, where the edge-on view of its BLR is shown. Here, the number of observable BLR clouds above and below the midplane are very similar, as expected for the best-fit ξ. However, the clouds below the midplane are displayed with larger sizes compared to those above the midplane, which reflects the best-fit κ. The preferential emission of the far side of the BLR, where the redshifted clouds reside, creates a larger phase on the redshifted side of the line centre. In addition, similar to Mrk 509, the combination of the effects of outflowing BLR clouds and their preferential emission cause the locus of model photocentres of PDS 456 to look curved (right column, second row, in Fig. 2.3). The null model BLR photocentre of PDS 456 is located above the BLR photocentres, which creates the negative differential phase signal. Similar to that of Mrk 509, the dominance of radial motion in the BLR clouds causes the red-blue photocentres to be shifted less perpendicular to its radio jet. In conclusion, the cause of the asymmetric signal in PDS 456's average differential phase spectrum is due to (1) the BLR clouds' outflowing radial motions and (2) the preference of the Paα emission

to originate from the far side of the BLR.

2.7.3 Mrk 1239

The red- and blueshifted photocentres of Mrk 1239 show an insignificant separation (see Fig. 2.3). The photocentre fitting results of Mrk 1239 suggest that the differential phase is dominated by the continuum phase, and the BLR differential phase is very moderate (low S/N). However, the perpendicular orientation of the BLR velocity gradient and continuum photocentre and the radio jet is consistent with the picture of a rotating BLR. Despite the relatively weak signal of Mrk 1239, we argue that this aids in adding further constraint to our BLR fitting compared to when we only fit its flux spectrum (as proven in Sect. 2.6). Given the low signal, we choose to fit the data with the simpler, circular model. The flux and differential phase spectra of Mrk 1239 are well-fit with the circular model as shown in Fig. 2.6c. While there is no clear differential phase signal for Mrk 1239, the combined fitting of the emission line profile and differential phase allows for meaningful constraints on the BLR size and SMBH mass as shown in the corner plot (see corner plot in Fig. A.3). While Fig. 2.6c does not show a clear differential phase signal, the very lack of a signal combined with the impressively low noise level still allows the model to converge and constrain the key BLR and SMBH properties of Mrk 1239.

The measured BLR PA of Mrk 1239 is $\sim 197°$, similar to what is measured for the red-blue photocentres of Mrk 1239, even if their separation is insignificant. The best-fitting parameters indicate that the data favours a face-on disc ($i \sim 11°$) with a thickness of $\theta_0 \sim 42°$. This geometry is consistent with the results of Pan et al. (2021), who suggest the observed broad emission of Mrk 1239 is actually reprocessed through scattering by polar dust. Effectively, we are observing from the LOS of the polar dust, which has a face-on viewing angle.

The cloud distribution follows an exponential profile ($\beta \sim 1.21$), while the mean radius is measured to be $\log R_{\rm BLR}$ [ld] $= 1.77^{+0.03}_{-0.74}$. The inferred BH mass is $\log M_{\rm BH}$ [$M_\odot$] $= 7.47^{+0.15}_{-0.92}$. Our inferred BLR radius is consistent within uncertainties with those published previously (Du et al., 2014a; GRAVITY Collaboration et al., 2023), and so is our BH mass (Kaspi et al., 2005; Du et al., 2014a; GRAVITY Collaboration et al., 2023). Lastly, the inferred BLR inner radius is $\log R_{\rm BLR,min}$ [ld] $= 0.64^{+0.27}_{-0.28}$. However, we caution that the BLR size of Mrk 1239 is marginally constrained, as its lower error is relatively larger than its upper error. This means that the BLR size and, therefore, the BH mass of Mrk 1239 has a higher chance of being lower than our reported best-fit values.

As discussed in Sect. 2.6.2, the average observed differential phase signal of Mrk 1239 suggests that its BH mass may be similar to the Pan et al. (2021) measurement. Indeed, from the modelling, the best-fit BH mass is $\log M_{\rm BH}$ [$M_\odot$] $= 7.47$, close to the $\log M_{\rm BH}$ [$M_\odot$] $= 7$ measurement of Pan et al. (2021).

2.7.4 IC 4329A

Even though the noise level of individual differential phase spectra in each baseline is $\sim 0.1°$, the S-shape signal is not as obvious as that of Mrk 1239 (after removing the continuum phase). Nevertheless, the radio jet of IC 4329A is shown to be perpendicular to the red-blue photocentre orientation of its BLR, indicating the rotation of its BLR and we therefore fit the data with the simpler circular model. As for Mrk 1239, the combination of the emission line profile and differential phase data strongly constrains the BLR structure and SMBH mass. Similar to Mrk 1239, IC 4329A does not show a clear phase signal (Fig. 2.6d). As discussed in Sect. 2.6, this lack of clear phase signal acts as a strong constraining factor in IC 4329A's BLR and SMBH properties. Without the differential phase spectrum, the BLR properties of IC 4329A will not be well constrained.

The cloud distribution of its BLR ($\beta \sim 1.81$) suggests it has a steep inner radial profile. The inclination angle is $i \approx 54°$; similar to Bentz et al. (2023), the high inclination angle of IC 4329A suggests that the AGN system and its host galaxy disc are misaligned significantly. The opening angle is $\theta_0 \approx 54°$, indicating that the BLR is thick. We resolved the BLR of IC 4329A, with a BLR radius of $\log R_{\rm BLR}$ [ld] $= 1.13^{+0.10}_{-0.23}$ and a BH mass of $\log M_{\rm BH}$ [$M_\odot$] $= 7.15^{+0.38}_{-0.26}$. The inferred BLR inner radius is $\log R_{\rm BLR,min}$ [ld] $= 0.64^{+0.27}_{-0.28}$.

Bentz et al. (2023) recently published results of a new RM campaign for IC 4329A which spanned about 5 months during 2022. They used `CARAMEL` (Bentz et al., 2021b, 2022) to fit their RM data with the BLR model from Pancoast et al. (2014a), which is similar to what we use. Our best-fit BLR size, BH mass, i, and θ_0 are all consistent with RM measurements from Bentz et al. (2023). Indeed, the average observed phase signal of IC 4329A spans the same range as the expected phase signal of IC 4329A with its BH mass fixed to what Bentz et al. (2023) measured.

2.8 The GRAVITY-AGN radius-luminosity relation

One of the main objectives of our GRAVITY-AGN large programme is to place AGN properties derived by GRAVITY in the context of AGN scaling relations previously derived by other methods, namely the R-L and $M_{\rm BH}$-σ_* relations. In this section, we show the first non-RM-derived R-L relation. To start, we have the BLR radius and BH mass measurements of our 4 targets, and adding the measurements of the 3 previously published targets (IRAS 09149-6206 from GRAVITY Collaboration et al. 2020a, 3C 273 from GRAVITY Collaboration et al. 2018, and NGC 3783 from GRAVITY Collaboration et al. 2021a), gives us 7 AGNs to plot in the R-L space, now spanning a wide range of luminosity ($\log \lambda L_\lambda(5100\text{Å}) \sim 43.0$ - 46.5). We fit these data points with a power-law relation similar to that of Bentz et al. (2013):

$$\log (R_{\rm BLR}/\text{ld}) = K + \alpha \log(\lambda L_\lambda / 10^{44} \text{ erg s}^{-1}). \tag{2.9}$$

We employed the `LINMIX` algorithm (Kelly, 2007), a package that utilises a hierarchical Bayesian approach to linear regression with measurement errors and a parameter, σ^2,

which encapsulates the intrinsic random scatter around the regression. We calculate the 16th, 50th, and 84th percentile of the resulting posterior distributions of each parameter to get their best-fit values and their 1σ uncertainties. We use the optical AGN luminosities of our targets listed in Table 2.1 and the best-fit BLR sizes of our targets to produce our GRAVITY-AGN R-L relation. However, we emphasise that Mrk 1239 is known to be a physically complicated object based on various observed properties (e.g., Balmer decrement, polarisation) leading to the high obscuration of its nucleus (Goodrich, 1989; Doi et al., 2015). Its observed broad lines and optical continuum are also suggested to originate from scattering by polar dust around the BLR (Pan et al., 2021). Therefore, we cannot directly use the observed $\lambda L_\lambda(5100\text{Å})$ of Mrk 1239. We opt to use the extinction-free $\lambda L_\lambda(5100\text{Å})$ of Mrk 1239 from Pan et al. (2021).

Fig. 2.8 shows the result of our R-L relation fit compared with that of Bentz et al. (2013). The best-fit values for our GRAVITY-observed AGNs are $K = 1.69^{+0.23}_{-0.23}$, $\alpha = 0.37^{+0.18}_{-0.17}$, and $\sigma^2 = 0.23^{+0.48}_{-0.13}$. The large uncertainties in our best-fit parameters are inevitable due to our small sample size. By observing more AGNs with GRAVITY, we can increase the sample size and, therefore, better constrain the R-L relation independent of RM (see Sect. 2.12 for more discussion of these prospects). We emphasise that our approach allows us to extend the R-L relation to much higher luminosities without needing decade-long time baselines to observe their expected year-long time lags. Our results suggest that the GRAVITY R-L relation has a flatter slope (~ 0.4) compared to that of the canonical R-L relation from Bentz et al. (2013), which has a slope of ~ 0.5. Woo et al. (2023) recently showed a similar conclusion as this work by focussing on reverberation mapping of high-luminosity AGNs (10^{44} $L_\odot < \lambda L_\lambda(5100\text{Å}) < 10^{45}$ $L_\odot$, with a few sources possessing $\lambda L_\lambda(5100\text{Å}) > 10^{45}$ $L_\odot$).

We also consider the relative time lags of the emission lines with respect to the Hβ time lag based on the predictions of photoionisation models. These models (e.g., Netzer, 2020; Korista and Goad, 2004) predict that the BLR size is dependent on certain parameters such as the optical depth of the observed emission line and the variability and the photoionisation flux of the central engine. Kuhn et al. (2024) recently confirmed the consistency of observed relative time lags of several emission lines (e.g., Hα, He I) with respect to Hβ time lag with what the radiation pressure confined (RPC) BLR model by Netzer (2020) described. According to this model, the time lags of Brγ and Paα are about 1.0-1.2 and 1.5-1.7 times larger than that of Hβ. It is clear, therefore, that BLR sizes derived from Paα are greatly affected, and thus, an adjustment must be taken into consideration. We show the adjusted BLR sizes of 3C 273 and PDS 456 (the objects with Paα line profiles) as open symbols in Fig. 2.8. If we consider these adjusted BLR sizes in our GRAVITY R-L relation fit, we get $K = 1.66^{+0.24}_{-0.24}$, $\alpha = 0.30^{+0.19}_{-0.19}$, and $\sigma^2 = 0.27^{+0.54}_{-0.16}$,. We, therefore, conclude that the resulting slope of the R-L relation will be shallower if we consider prescriptions from photoionisation models and adjust BLR sizes measured from Paα lines. As for the effect of this "BLR stratification" phenomenon on the rest of the BLR model parameters, future work (Kuhn et al., 2024) on NGC 3783 has shown that the geometry beyond the radial distribution of the line emission (e.g., inclination angle, opening angle, black hole mass) are consistent among the different emission lines (Hα, Hβ, Paα, Paβ, HeI).

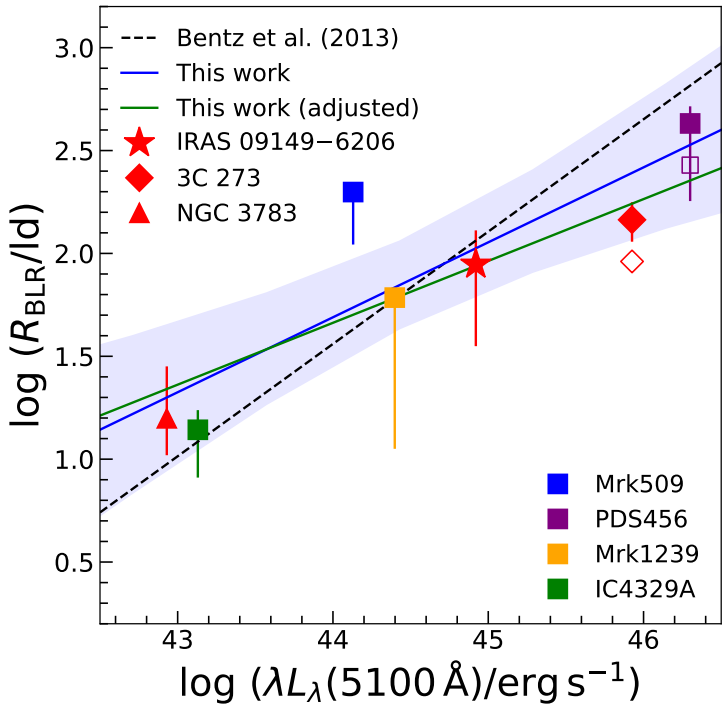

Figure 2.8: Logarithm of the BLR radius as a function of log λL_λ(5100Å) (R-L relation). The blue line shows the best-fit line derived from all 7 GRAVITY-observed AGNs, and the blue shaded region is its 1σ confidence interval. The AGN luminosity is taken from Table 2.1. The dashed line represents the best-fit radius luminosity relation from Bentz et al. (2013). The 3 published AGNs (IRAS 09149-6206 from GRAVITY Collaboration et al. 2020a, 3C 273 from GRAVITY Collaboration et al. 2018, and NGC 3783 from GRAVITY Collaboration et al. 2021a) are shown as a red star, red diamond, and red square, respectively. Our 4 targets are shown in differently coloured filled squares with 1σ errors. Our best-fit R-L (power-law) relation has a slope of $\alpha = 0.37^{+0.18}_{-0.17}$, which is lower but, given the current large uncertainty, still consistent within uncertainties with the slope of R-L relation fit from Bentz et al. (2013) ($\alpha = 0.533^{+0.035}_{-0.033}$). If we follow the prescription from photoionisation models, the BLR sizes of 3C 273 and PDS 456 will be adjusted (shown as open symbols), and the fitted GRAVITY R-L relation is shown as the green line.

2.8.1 Effect of Eddington ratio in our results

An important aspect to discuss with the GRAVITY R-L relation fit is the Eddington ratio of our targets since previous works have suggested that it is the "third" parameter in the R-L relation, and it can explain the smaller observed BLR sizes compared to what the canonical R-L relation expects (Du et al., 2018b; Du and Wang, 2019) especially for PDS 456 whose best-fit BH mass and BLR size are much smaller than previous estimates. In this work, we calculate the Eddington ratio as $\lambda_{\rm Edd} = L_{\rm bol}/L_{\rm Edd}$, where $L_{\rm Edd} = 1.3 \times 10^{38}$ $(M_{\rm BH}/M_{\odot})$ erg s^{-1}. We also calculate the dimensionless accretion rate, $\dot{\mathcal{M}}$, based on the standard disc model (Shakura and Sunyaev, 1973) shown in Eqn. 4 of Du et al. (2018b). We calculate the former to easily facilitate comparison with other literature, while we calculate the latter to compare with the super-Eddington accreting massive black hole (SEAMBH) sample of Du et al. (2018b). We use the best-fit inclination angle of each object to calculate $\dot{\mathcal{M}}$. However, due to the presence of outflowing radial motion in Mrk 509 and PDS 456, their best-fit inclination angles may not be easily as straightforward as the rest of the GRAVITY-observed AGNs, and therefore, the values of their $\dot{\mathcal{M}}$ should be taken with caution.

For Mrk 509, IC 4329A, NGC 3783, and IRAS 09149-6206, we use the 14-195 keV luminosity from the BAT AGN Spectroscopic Survey (Koss et al., 2017), which is directly taken from the 70-month Swift-BAT survey (Baumgartner et al., 2013), to calculate $L_{\rm bol}$ through the calibration in (Winter et al., 2012). For 3C 273 and PDS 456, we decided to use the bolometric luminosity calculated from the 5100 Å luminosity and the bolometric correction of Trakhtenbrot et al. (2017), which was also used by GRAVITY Collaboration et al. (2020c). This is because 3C 273 is most likely dominated by the jet in the X-ray regime (Dermer et al., 1997; Vasudevan and Fabian, 2007), and PDS 456 exhibits strong X-ray variability, causing the observed $L_{2-10\ \rm keV}$ to be 0.2% of its bolometric luminosity (Reeves et al., 2009). We also use the 5100 Å luminosity and bolometric correction of Trakhtenbrot et al. (2017) to get the bolometric luminosity of Mrk 1239 from the $L_{\lambda}(5100\text{Å})$ measurement of Pan et al. (2021). This bolometric luminosity is comparable to (only slightly larger than) the bolometric luminosity estimated from *WISE* W3 (12 μm). Both of these $L_{\rm bol}$ values are much larger than the bolometric luminosity estimated from the 2-10 keV X-ray luminosity (Jiang et al., 2021), which is likely because of the high obscuration that is not accounted for.

Table 2.5 lists the calculated $\lambda_{\rm Edd}$ and $\dot{\mathcal{M}}$ of our 7 targets based on GRAVITY-derived properties, together with the $L_{\rm bol}$ used to calculate $\lambda_{\rm Edd}$ in this work. The $\lambda_{\rm Edd}$ values calculated from GRAVITY-derived values are consistent with those taken from the literature, except PDS 456. As for $\dot{\mathcal{M}}$, we see that the range of the $\dot{\mathcal{M}}$ of our targets are similar to that of Du et al. (2018b) (about 10^{-3} to 10^{3}). PDS 456 shows a relatively large Eddington ratio compared to the previous estimate assuming a bolometric luminosity of $\sim 10^{47}$ erg s^{-1} (Reeves et al., 2000) and a BH mass of $\log M_{\rm BH}/M_{\odot} = 9.24$ (Nardini et al., 2015). However, Yang et al. (2021) also find evidence that the accretion rate of PDS 456 may exceed the Eddington rate based on the observed X-ray wind velocities on PDS 456.

Our Eddington ratio calculations suggest that the BLR sizes of our targets are consis-

Table 2.5: Eddington ratio ($\lambda_{\rm Edd} = L_{\rm bol}/L_{\rm Edd}$ and dimensionless accretion rate $\dot{\mathcal{M}}$ from Eqn. 4 of Du et al. 2018b) of all seven targets calculated from GRAVITY observations and by other literature. The $L_{\rm bol,use}$ for each target is also presented.

Object	log $L_{\rm bol}$ (erg s^{-1})	$\lambda_{\rm Edd}$ (GRAVITY)	$\lambda_{\rm Edd}$ (other works)	$\dot{\mathcal{M}}$ (GRAVITY)
Mrk 509	45.32[a]	0.16[1]	0.19[5]	1.9
PDS 456	47.01[b]	4.64[1]	0.44[6]	2.0 $\times 10^2$
Mrk 1239	45.36[c]	0.60[1]	0.10 - 2.8[7]	13
IC 4329A	45.12[a]	0.72[1]	0.13 - 0.46[8,9]	1.4
3C 273	46.64[b]	1[2]	0.6[10]	22
NGC 3783	44.52[a]	0.05[3]	0.06[11]	0.02
IRAS 09149-6206	45.29[a]	0.1[4]	0.4[12]	5

[a] log $L_{\rm bol,14-195keV}$ from Koss et al. (2017) and Baumgartner et al. (2013).

[b] Based on converting the log λL_λ(5100Å) to log $L_{\rm bol,5100Å}$ using the prescription from Trakhtenbrot et al. (2017).

[c] log $L_{\rm bol,5100Å}$ calculated from Pan et al. (2021).

References: (1) This work, (2) GRAVITY Collaboration et al. (2018), (3) GRAVITY Collaboration et al. (2021a), (4) GRAVITY Collaboration et al. (2020a), (5) Fischer et al. (2015), (6) Calculated using the BH mass from Nardini et al. (2015) and the bolometric luminosity from Reeves et al. (2000), (7) Jiang et al. (2021), (8) Ogawa et al. (2019), (9) de La Calle Pérez et al. (2010) (10) Husemann et al. (2013), (11) Brenneman et al. (2011), (12) Walton et al. (2020)

tent with the picture that the accretion rate plays a role in the observed deviation from the canonical R-L relation, as shown by Du et al. (2018b) and Du and Wang (2019). These previous works have shown that $\mathcal{R}$(Fe II), which is thought to be an indicator of accretion rate, is correlated with the deviation of AGNs from the canonical R-L relation. These works have suggested that self-shadowing effects, which are stronger at higher accretion rates, may also push the emissivity-weighted BLR radius to lower values. This phenomenon arises when the BLR "puffs up" due to increased accretion activity and becomes geometrically thick, especially in the inner regions, preventing the central radiation from reaching farther central distances. As a result, the regions farther out from the equatorial plane are under-illuminated, and the observed flux-weighted BLR size is smaller (Wang et al., 2014). However, recent results from Woo et al. (2023) find that after adding more luminous sub-Eddington AGNs, the correlation between Eddington ratio and deviation of the BLR radius from the canonical R-L relation is weaker. They argue that this is because there is a self-correlation between the Eddington ratio and AGN luminosity. Therefore, the relationship between the Eddington ratio and deviation of the BLR radius from the canonical R-L relation is likely to be a luminosity effect. Nevertheless, our sample size is limited, and therefore, more AGN observations with GRAVITY will help provide independent evidence to test this hypothesis further.

2.8.2 Effect of used luminosity in the R-L relation

We also investigate what happens to the R-L relation if we use a different indicator of AGN luminosity other than $\lambda L_\lambda(5100\text{Å})$, the standard luminosity for reporting the R-L relation. It is possible $\lambda L_\lambda(5100\text{Å})$ is not a good measure of a target's ionising luminosity at high luminosities if, for example, the SED shape changes significantly. In this case, the bolometric luminosity (measured from X-ray observations) might be considered. If we use the log $L_{\rm bol}$ listed in Table. 2.5 to plot the R-L relation, we get a best-fit slope of $\alpha = 0.49^{+0.30}_{-0.30}$ (in our discussion, we disregard the effect of relative time lags with respect to Hβ for simplicity). This suggests that a non-linear UV-to-optical relationship might instead cause the apparent decrease in the slope of the R-L relation. Similarly, Netzer (2019) presents a luminosity-dependent bolometric correction. Using this to convert our log $\lambda L_\lambda(5100\text{Å})$ values to $L_{\rm bol}$, we find the slope of the R-L_{AGN} relation to be $0.48^{+0.22}_{-0.21}$. Therefore, while we are limited to our small sample size, our large luminosity range has revealed that a changing SED shape could instead explain the apparent departure of the R-L relation from R $\sim L^{0.5}$. This will be further assessed with a much larger sample of GRAVITY-observed AGNs.

Woo et al. (2023) also recently investigated the possibility of log $\lambda L_\lambda(5100\text{Å})$ not being a good representative of the AGN luminosity of their targets. Their tests show the systematic change of the SED slope between the UV and optical wavelengths may be partly responsible for the deviation from the 0.5 slope of the R-L relation, similar to what our test above suggests.

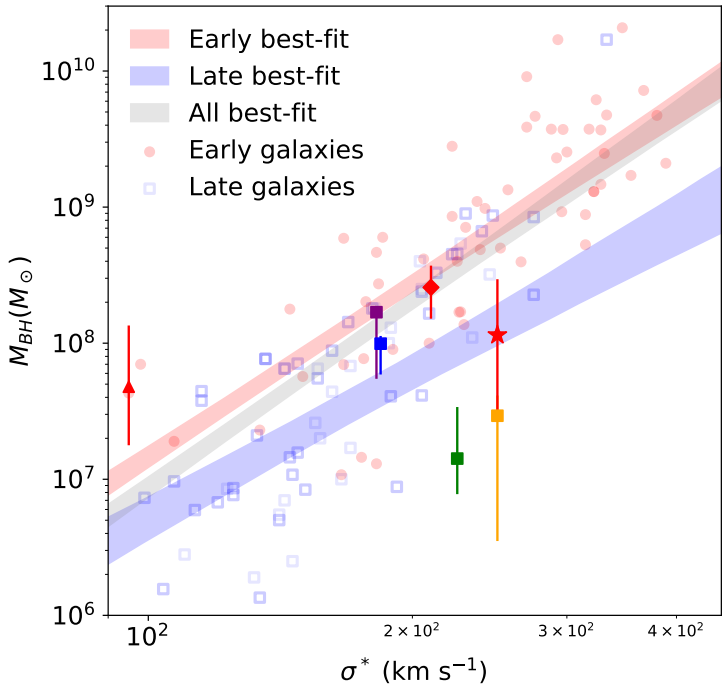

Figure 2.9: Plot showing BH mass vs. stellar velocity dispersion ($M_{\rm BH}$-σ_* relation). The symbols of our 7 AGNs are similar to that of Fig. 2.8. The figure is redrawn from Fig. 3 of Greene et al. (2020), but with the addition of the 4 targets introduced in this work. Early- and late-type galaxies are shown as red circles and blue hollow squares, respectively, while BH mass upper limits of some low-mass late-type galaxies are shown as inverted blue triangles. All these galaxies' measurements are taken from Greene et al. (2020) and referenced therein. The best-fit $M_{\rm BH}$-σ_* relation for early- and late-type galaxies are shown as red and blue-shaded regions, while the best-fit relation for all galaxies is shown as a grey-shaded region. The best-fit lines are surrounded with their 1σ confidence interval, and all best-fit values are also taken from Greene et al. (2020).

2.9 The black hole mass - stellar velocity dispersion relation

Since one of the ultimate goals of our work is to acquire precise BH masses, we are also interested in where our targets lie in the $M_{\rm BH}$-σ_* relation. Fig. 2.9 compares our data points with $M_{\rm BH}$-σ_* relations from other studies. We focus our comparison with Greene et al. (2020), wherein they fit the $M_{\rm BH}$-σ_* relations for early- and late-type galaxies. This sample comprises various subsamples of galaxies from different works (e.g., Kormendy and Ho, 2013; Greene et al., 2016; Saglia et al., 2016; Krajnović et al., 2018; Thater et al., 2019; den Brok et al., 2015; Nguyen et al., 2018, 2019). Upper limits of galaxies with smaller stellar velocity dispersions were estimated via stellar dynamics (see Table 4 of Greene et al. 2020 and references therein). The stellar velocity dispersions of our targets are drawn from the literature. For Mrk 509, Mrk 1239, and IC 4329A, we adopt the measurements from

Oliva et al. (1999) derived from Si 1.59 μm, CO (6,3) 1.62 μm, and CO(2,0) 2.29 μm. We use the average σ_* if there are two or more available measurements for each object, and the typical errors of their measured σ_* are about $\pm$20 km/s. For PDS 456, we use the calculated dynamical mass from Bischetti et al. (2019) to derive its tentative stellar velocity dispersion. They acquired CO(3-2) emission maps of PDS 456, from which they measured the dynamical mass of PDS 456 within 1.3 kpc. The inferred dynamical mass is 1.0 $\times$ 10^{10} $M_{\odot}$. We can estimate the stellar velocity dispersion via virial theorem: σ_* = $\sqrt{\frac{GM}{R}}$, where G is the gravitational constant, M is the dynamical mass measured at R = 1.3 kpc. With this method, we estimate σ_* $\sim$ 182 km/s for PDS 456. However, we caution readers that this estimate is uncertain, as an unknown geometric correction factor C is usually added (especially if the object is not a disc) (Binney and Tremaine, 2008). In a variety of galactic mass distributions, C = 6.7 could be an appropriate value to assume (e.g., Förster-Schreiber et al., 2009). In addition, the most accurate way of measuring the stellar velocity dispersion of a target is through measuring equivalent widths of stellar absorption lines (e.g., Oliva et al., 1999). However, this is yet to be done for PDS 456. We also caution that the σ_* of IRAS 09149-6206 used in this work is based on the [OIII] line and therefore is very uncertain (GRAVITY Collaboration et al., 2020a).

All of our objects lie close to the standard relation, showing similar scatter to other samples. However, Mrk 1239 and IC 4329A are shown to be below the local $M_{\rm BH}$-σ_* relation. As shown in Table 2.5, these two objects also have relatively high Eddington ratios. These results are consistent with previous works showing highly accreting BHs to be below the local BH-galaxy scaling relations (Ding et al., 2022; Zhuang and Ho, 2023). However, we find 3C 273 and PDS 456, the sources with the highest Eddington ratios from our sample, to be placed consistently with the $M_{\rm BH}$-σ_* relation of early-type galaxies and above the $M_{\rm BH}$-σ_* relation of late-type galaxies. We note that the σ_* of PDS 456 is very uncertain, but it is not the case for 3C 273. Nevertheless, the two sources are the most luminous AGNs at low redshift, which by selection requires a high BH mass and high accretion rate.

2.10 Possible origin of the spatial BLR offset and its relation with AGN luminosity

Previously in Sect. 2.4, we find a spatial offset between the BLR and the continuum photocentre for all of our targets. We call this the "BLR offset", and it ranges from $\sim$30-140 μas for our four targets. Upon investigation, we find a strong positive (Pearson correlation coefficient = 0.81) correlation (p = 0.026) between the BLR offsets (henceforth called $R_{\rm off}$) and optical AGN luminosity of all GRAVITY-observed AGNs. We show this in Fig. 2.10a, where we also compare the data with R-L relation taken from Bentz et al. (2013), the fitted R-L relation in this work, and the dust continuum R-L relation derived from our GRAVITY data (GRAVITY Collaboration et al., 2023). Our comparison with these relations suggests two things about the BLR offsets: (1) that they are all within the

dust sublimation radius and (2) that they are of the same scale as BLR sizes. Due to the latter, we can rule out the BLR structure as a possible origin of the observed BLR offsets.

We include the BLR offsets of the 3 previously published GRAVITY AGNs in Fig. 2.10a. The photocentre of IRAS 09149-6206 is reported in GRAVITY Collaboration et al. (2020a). We newly measured the photocentre offsets of 3C 273 and NGC 3783. For 3C 273, the reduction method in GRAVITY Collaboration et al. (2018) removed the continuum phase signal, so we reduce the data again with our new method based on that of GRAVITY Collaboration et al. (2020a). For NGC 3783, we already reduce the data with our new method, so we simply perform photocentre and BLR fitting again[2]. We measure a new BLR offset of 22.8 ± 2.1 μas and 71.6 ± 6.2 μas for 3C 273 and NGC 3783, respectively. This does not affect the derived BLR differential phase of the two targets.

Given the luminosity dependence of the offsets, we propose that the offset between the BLR and continuum photocentres results from asymmetric K-band emission from the hot dust. This asymmetry can then be simply modelled as the hot dust having a side with a brighter flux and a side with a fainter flux. Fig. 2.11 shows the schematic diagram for an easy visualisation of the model. This asymmetry can be produced by several factors, for example, the presence of a parcel of dusty cloud/s with significant flux located within the hot dust (similar to that of GRAVITY Collaboration et al. 2021a) or the dusty clouds are optically thick at ∼2 μm, so one preferentially sees the side illuminated by the AGN. Some of the emitting hot dust structures of AGNs could also have irregularities or clumpy regions, or the edge of a foreground dust lane could coincide with the LOS to the nucleus (GRAVITY Collaboration et al., 2020a). If the asymmetric K-band emission from the hot dust is caused by the coincidence of the LOS to a BLR irregularity, a connection between the BLR offsets and inclination angles might be implied. However, the Pearson correlation coefficient and p-value of the log $R_{\rm BLR,off}$ [pc] and i [°] are -0.42 and 0.35, respectively, indicating the absence of a significant correlation between the two. Even if we exclude Mrk 509 and PDS 456, the targets whose best-fit inclination angles may not represent their "true" inclination angle due to the presence of outflowing radial motion in their BLRs, the resulting Pearson correlation coefficient and p-value are -0.39 and 0.51, respectively. Therefore, the asymmetric K-band emission from the hot dust could not be due to the coincidence of the LOS to any BLR irregularities.

The next objective is to determine how bright (in terms of flux) the brighter side of the hot dust is relative to the fainter side. Following our model, we investigate this by deriving a formula based on the concept of the centre of mass that will give us the flux ratio between the two sides. We arrive at the following relation (see Appendix B for more discussion):

$$\frac{W_r}{W_l} = \frac{2 + \pi R_{\rm ratio}}{2 - \pi R_{\rm ratio}} \tag{2.10}$$

where $R_{\rm ratio} = \frac{R_{\rm off}}{R_{\rm dust}}$, $R_{\rm dust}$ is the dust sublimation radius derived from the dust radius -

[2]The BLR offset reported in Table 2 of GRAVITY Collaboration et al. (2021a) has the "secondary" component in its differential phase removed. This component is due to an offset hot dust ∼0.6 pc away from the main central hot dust component. Our new photocentre fitting does not remove this component.

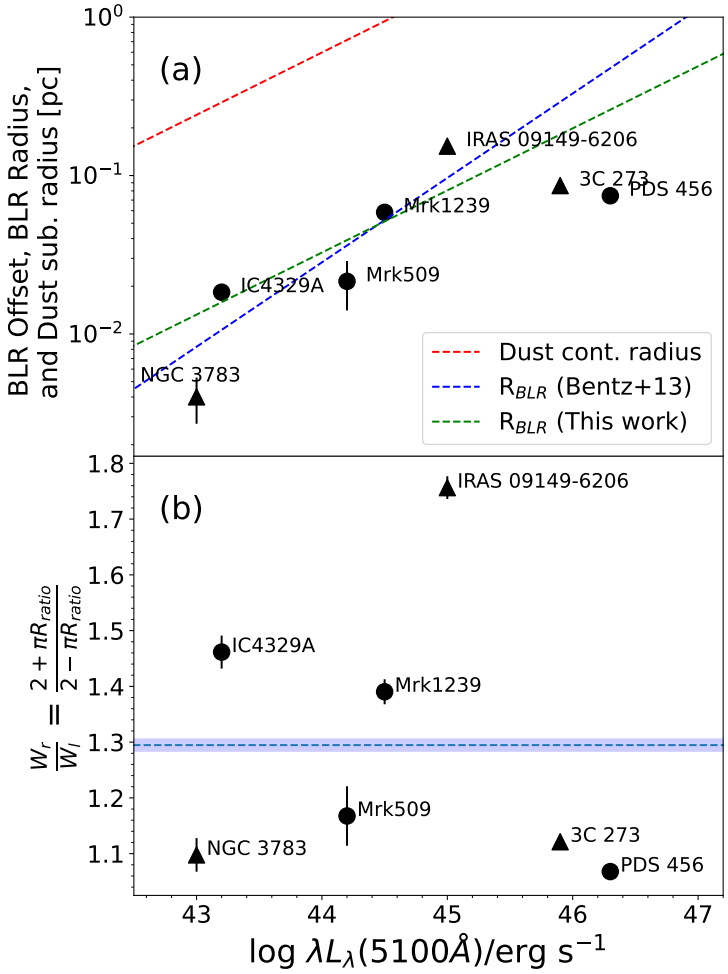

Figure 2.10: Plots showing the spatial offset between the BLR and continuum photocentres and its possible physical representation and their connection with optical AGN luminosity. (a) The BLR offset and (b) the flux ratio of two sides of the hot dust ($W_\mathrm{r}/W_\mathrm{l}$) as a function of optical AGN luminosity, assuming that the hot dust emits asymmetrically as explained in Sect. 2.10. The 4 targets introduced in this work are shown in circles, while the previously published AGNs (3C 273, IRAS 09149-6206, and NGC 3783) are shown in triangles. The error bars are 1σ errors calculated through the propagation of uncertainties from the centroid position of the null photocentre fitting. For comparison, the relation between hot dust size and AGN luminosity (GRAVITY Collaboration et al., 2023) is shown by the red dashed line, while the relation between the BLR radius and AGN luminosity (the so-called R-L relation) based on Bentz et al. (2013) is shown by the blue dashed line. We also show the fitted R-L relation in this work depicted by the green dashed line. The Pearson correlation coefficients and p-values for the left and right plots are 0.81 and 0.026, and -0.15 and 0.73, respectively.

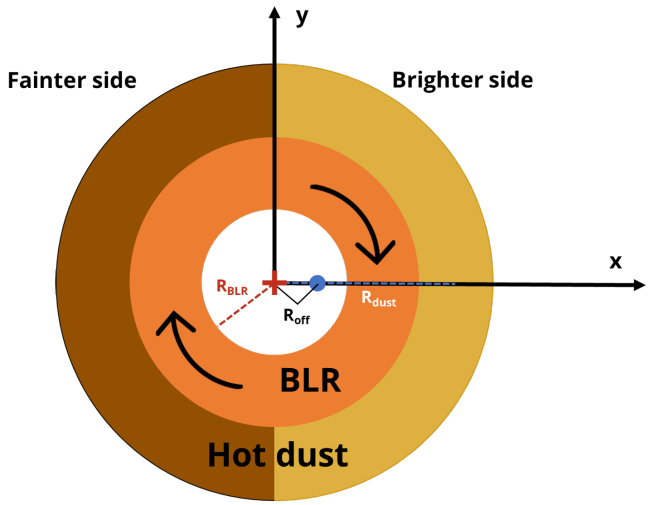

Figure 2.11: 2D schematic diagram showing our explanation for the observed offset between the BLR and hot dust. The BLR (orange disc) is rotating, has a size of $R_{\rm BLR}$, and its photocentre is marked as a red cross and is assumed to be the same as the position of the central BH. For simplicity, the hot dust (with a radius of $\rm R_{dust}$) is assumed to have two sides: the left side being the fainter one and the right side being the brighter one. This causes the continuum photocentre (blue dot) to shift to the brighter side of the hot dust. The observed offset between the BLR and hot dust photocentres is labelled $\rm R_{off}$.

luminosity relation from GRAVITY Collaboration et al. (2023), W is the flux, and the subscripts l and r refer to the left and right sides of the hot dust, respectively.

We show $W_{\rm r}/W_{\rm l}$ as a function of optical AGN luminosity in Fig. 2.10b. The average value of $W_{\rm r}/W_{\rm l}$ is 1.29 $\pm$ 0.01, meaning that the brighter side of the hot dust has a $\sim$ 30% higher flux than its fainter side. The Pearson correlation p-value of $W_{\rm r}/W_{\rm l}$ vs. log $\lambda L_{\lambda}(5100\text{Å})$ is $\sim$ 0.73, suggesting insignificant correlation between the two quantities.

The absence of a significant relationship between the BLR offsets and inclination angle also purports that the "tilted torus" model (Lawrence and Elvis, 2010) could not explain the presence of BLR offsets. Other possible reasons include variable obscuration on the BLR and smaller scales. Dehghanian et al. (2019) proposed that a "holiday" period (a period when the covering factor of the LOS obscurer varies) can explain the decorrelation of the emission lines and continuum variations observed on NGC 5548. However, it would be too much of a coincidence to conclude that *all* the targets were observed during their "holiday" periods so that their BLR photocentres are offset with respect to their continuum photocentres.

2.11 Virial factors

Finally, we calculate the virial factors of our 4 targets. Dalla Bontá et al. (2020) argued that the dispersion or σ (i.e., square root of the second moment of the line profile) is better

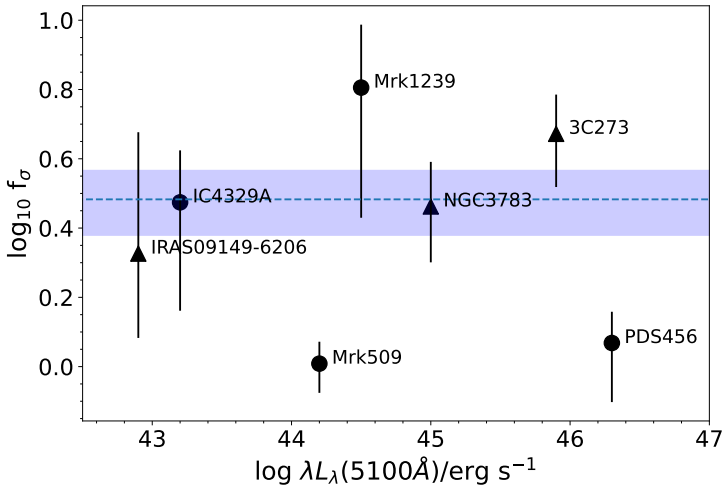

Figure 2.12: Virial factor (f_σ) as a function of optical AGN luminosity. The legends are similar to that of Fig. 2.10. The Pearson correlation p-value is $\sim$ 1.0, indicating an insignificant correlation between the two quantities.

than the FWHM in calculating the virial factor due to the latter introducing a bias in the BH mass scale. Yu et al. (2019) and Wang et al. (2019) also purported a similar conclusion as they found the σ is insensitive to the inclination angle, and hence, the BLR geometry doesn't affect the resulting BH mass. Hence, we follow this prescription and measure the σ of the model line profile. Afterwards, the values of the relevant model parameters are drawn randomly from the sampled posterior parameter space created during BLR model fitting. We use the formula $f_\sigma = GM_{\rm BH}/(R_{\rm BLR}v_\sigma^2)$ to calculate the virial factor.

Fig. 2.12 shows the virial factors of our sources as a function of optical AGN luminosity. The virial factors of Mrk 509, PDS 456, Mrk 1239, and IC 4329A are $1.10^{+0.16}_{-0.18}$, $1.17^{+0.27}_{-0.38}$, $6.39^{+3.32}_{-3.37}$, and $2.98^{+1.23}_{-1.53}$, respectively. The virial factor of 3C 273 was taken from GRAVITY Collaboration et al. (2018), while the virial factors of NGC 3783 and IRAS 09149-6206 are calculated from the posterior distributions of their parameters. The average virial factor of all 7 AGNs is $\langle f_\sigma \rangle = 3.04 \pm 0.64$. This is lower than that calculated by previous works that assumed their AGN sample follows the same $M_{\rm BH}$-σ_* as those of quiescent galaxies (Onken et al., 2004; Woo et al., 2010; Park et al., 2012; Batiste et al., 2017), which is $\langle f_\sigma \rangle$ $\sim$ 5. It is not clear whether we should expect a match here, since the host galaxy type plays a role in the determination of the $M_{\rm BH}$-σ_* relation. And, our average virial factor is consistent with that of Grier et al. (2017a) and Williams et al. (2018), who also calculated the individual virial factors of their AGN sample and got $\langle f_\sigma \rangle \sim 3$. We also note that we find lower f_σ values for Mrk 509 and PDS 456, which intriguingly are the two targets with significant radial motion in their BLR.

The resulting Pearson correlation coefficient between log f$_\sigma$ and log λL_λ(5100Å) is $\sim$ -0.02, and the p-value is $\sim$ 0.96, indicating insignificant correlation. Previous works (Villafaña et al., 2023; Williams et al., 2018) reported an positive correlation, although non-significant (p-values >> 0.05), between the two quantities. They also reported a

possible positive correlation between log f_σ and log $M_{\rm BH}/M_\odot$. However, calculating the Pearson correlation coefficient and p-value of these two quantities in our work suggests otherwise (-0.27 and 0.56, respectively). Hence, we conclude that there is no correlation between the virial factor and optical luminosity or BH mass for our targets. However, the uncertainties are large, and bigger samples will be needed to confirm this result.

2.12 Conclusions and future prospects

We investigate the broad Brγ line-emitting regions of Mrk 509, Mrk 1239, and IC 4329A, and the broad Paα line-emitting region of PDS 456. To study the kinematics and properties of their BLRs, we performed photocentre and BLR model fitting. Our results support many of the assumptions and scaling relations used and derived by RM, and they provide an independent method that can be extended to high-z and large BH mass:

1. Most of the AGNs observed by GRAVITY can be well described by a thick, rotating disc of clouds, consistent with RM assumptions. However, two of our targets (Mrk 509 and PDS 456) show evidence of outflowing BLR clouds, while the other two targets (Mrk 1239 and IC 4329A) have relatively weaker differential phase signals that limit the constraints of their BLR sizes and BH masses. Nevertheless, we prove from our analyses that the differential phase is crucial in providing stronger constraints on the BLR kinematics.

2. By adding the other three AGNs that were previously observed with GRAVITY (3C 273, IRAS 09149-6206, and NGC 3783), we derived a new R-L relation based on GRAVITY-derived BLR sizes only. We derived a slope and intercept of $\alpha = 0.37^{+0.18}_{-0.17}$ and $K = 1.69^{+0.23}_{-0.23}$, respectively. Our results are consistent with works showing shallower R-L relation slopes, although the effect of the Eddington ratio in this relation cannot be fully realised with our relatively small sample.

3. Most of the GRAVITY AGNs are consistent within the scatter of the standard $M_{\rm BH}$-σ_* relation. Mrk 1239 and IC 4329A, two of our targets with relatively high Eddington ratios, are placed below the $M_{\rm BH}$-σ_* relation consistent with previous works, while 3C 273 and PDS 456, the targets possessing the highest Eddington ratios among our sources, are still consistent within the $M_{\rm BH}$-σ_* relation, suggesting that their high luminosity may play a role in their difference compared to other high Eddington-ratio sources such as Mrk 1239 and IC 4329A.

4. We find a significant correlation between the offset between the BLR and continuum photocentre and optical AGN luminosity, and the offsets of all GRAVITY AGNs are found to be of a similar scale as their BLR sizes. This correlation is surmised to be due to asymmetric K-band emission of the hot dust, and a simple model was created to estimate that this emission is $\sim$30% brighter on one side than the other for our sample.

5. Lastly, we calculated the virial factors of our four targets and found an average virial factor (based on the dispersion of the model line profiles) of $\langle f_\sigma \rangle = 3.04 \pm 0.64$ for all GRAVITY-observed AGNs. This is consistent with previous works that calculated the individual virial factors of their targets.

There are two possible pathways for expanding this work: one is by probing higher redshifts with GRAVITY+, and another is by improving the Pancoast model. With the advent of GRAVITY+, the limits of GRAVITY will be pushed even further, providing wide-field off-axis fringe-tracking, newer adaptive optics systems on all the UTs, and laser guide stars, allowing observations of hundreds of AGNs and even those at high redshift will be achievable (GRAVITY+ Collaboration et al., 2022b). An example of this feat is the first dynamical mass measurement of a $z \sim 2$ quasar with GRAVITY-Wide (Abuter et al., 2024). The third chapter of this thesis focuses on this premise: by conducting a preparatory spectroscopic study of high-redshift AGNs that could be observed with GRAVITY+, we are able to assess the expected parameter space and BLR properties that GRAVITY+ will uncover in the near future. On the other hand, we are also interested in improving the dynamics of the Pancoast model to have a more physically motivated prescription of inflow/outflow motions in the BLR. One consequence of the current prescription of the Pancoast model regarding radial motion is that inflowing/outflowing clouds are only contained within the BLR plane (i.e. moving radially towards or away from the BH). Physically motivated models of the BLR have shown various prescriptions of such ejections, which are believed to originate from the accretion disc and are ejected in (offset angles with respect to the) polar direction (e.g., Czerny and Hryniewicz, 2011; Wada, 2011; Matthews et al., 2016). This is the main topic of the fourth chapter, wherein we investigate how well the Pancoast model can recover the BLR properties of a physically motivated BLR model, which will eventually point out areas of improvement in our current BLR model. These efforts will be crucial to provide a more physically motivated understanding of inflows/outflows in the BLRs of Mrk 509, PDS 456, and higher-redshift AGNs with the potential to possess inflow/outflow-dominated BLRs and a more accurate picture of the R-L relation which will be a key in achieving more accurate BH mass measurements at higher redshifts.

Chapter 3

Spectroscopic active galactic nucleus survey at $z \sim 2$ with NTT/SOFI for GRAVITY+ observations

This chapter is published as a paper: Santos et al. (2025), A&A, 696, A30.

3.1 Introduction

In this chapter, we highlight the importance of studying the physics of BLRs and accurately measuring BH masses at *higher redshifts*. As discussed in the previous chapter, the coevolution scenario between the SMBH and its host galaxy is still shrouded with mysteries, which include how scaling relations between the properties of the two objects evolve with redshift (Dalla Bontá et al., 2020; Shen and Liu, 2012; Prieto et al., 2022). This is particularly important in early cosmic times when direct SMBH measurements are scarce. Observations of high-redshift quasars have become a much more active topic of research with the launch of the James Webb Space Telescope (JWST). Recent studies with JWST have revealed that some high-redshift SMBHs grew early and fast, leading to extremely high M_{BH}/M_* ratios (e.g. Maiolino et al., 2024; Adamo et al., 2024). However, these results are based on local scaling relations, highlighting the need for more robust scaling relations at higher redshifts. Most methods for measuring SMBH mass, which include spatially resolved stellar (Saglia et al., 2016) or gas kinematics (Boizelle et al., 2019; Osorno et al., 2023), megamaser kinematics (Greene et al., 2010; Kuo et al., 2020), and reverberation mapping (RM) (Peterson, 1993; Peterson et al., 2004; Li et al., 2023), are all limited at *low redshifts*. Notably, performing RM at high redshifts requires long (multi-year) campaigns due to the cosmological time dilation and also because the targeted quasars (QSOs) tend to be luminous and thus have large broad line regions (BLRs) and, therefore, high SMBH masses (a recent summary of such efforts is given by Kaspi et al. 2021). Although several observational studies have already investigated the coevolution scenario at higher redshifts (Lapi et al., 2014; Carraro et al., 2020), these works used SMBH masses derived from

scaling relations and so are based on the assumption that those relations, derived at a low redshift, are also applicable at a high redshift. As such, there is a need to measure SMBH masses at a high redshift independently via direct dynamical methods.

With the unprecedented precision and resolution of GRAVITY (GRAVITY Collaboration et al., 2017), the beam combiner at the Very Large Telescope Interferometer (VLTI), spatially resolving the BLR kinematics to measure SMBH masses has become possible in the local Universe (GRAVITY Collaboration et al., 2018, 2020a, 2021a, 2024) with very long baseline interferometry (Eisenhauer et al., 2023). Extending this endeavour to higher redshifts was one of the imperatives for upgrading GRAVITY. The GRAVITY+ project aims to add wide-field off-axis fringe tracking (called GRAVITY-Wide) and new adaptive optics systems with laser guide stars (LGSs) on all the unit telescopes (UTs). This will enable observations of both fainter and high-redshift quasars (GRAVITY+ Collaboration et al., 2022b). A key epoch to focus on is the cosmic noon in the redshift range $1 < z < 3$, corresponding to about 8-12 billion years ago when star formation and BH growth both peaked (Madau and Dickinson, 2014; Tacconi et al., 2020). Abuter et al. (2024) recently performed the first dynamical mass measurement of a $z \sim$2 QSO with GRAVITY-Wide. With the other improvements from GRAVITY+, a vastly wider sky coverage will open up the possibility of selecting larger samples of active galactic nuclei (AGNs) and measuring their SMBH masses.

To prepare for this, we undertook a preparatory near-infrared (NIR) spectroscopic survey of promising AGN candidates for GRAVITY+. This program aims to confirm suitable targets as QSOs based on their K band Hα line profiles and fluxes. We identified the best targets for high-priority follow-up observations with GRAVITY+ by fitting their line profiles with a BLR model and estimating their expected interferometric signals. This also yields information about their BLR geometries, giving us a first glimpse of what we can learn from their BLR structure. We present 29 high-redshift targets ($z \sim 2$) observed in this initial survey. For our analyses, we adopted a Lambda cold dark matter (ΛCDM) cosmology with $\Omega_m = 0.308$, $\Omega_\Lambda = 0.692$, and $H_0 = 67.8$ km s^{-1} Mpc^{-1} (et al., 2016). We describe our sample selection and observations in Sect. 3.2. We discuss our data reduction methods in Sect. 3.3. We summarise the emission line properties of our targets in Sect. 3.4. We discuss the BLR model used for this study, our fitting methodology and results in Sect. 3.5. We present the estimated differential phase signals of our targets based on our BLR model fitting in Sect. 3.6. Finally, we present our conclusions in Sect. 3.7.

3.2 Targets and observations

The targets were selected from the Million Quasar (Milliquas) catalogue (Flesch, 2021) version 7.5 (updated last 30th Apr. 2022), which provides a catalogue of type 1 QSOs and AGNs complete from literature, as well as from the Quaia spectroscopic catalogue (Storey-Fisher et al., 2024) that is based on Gaia candidates with unWISE (reprocessing of data from Wide-field Infrared Survey Explorer or WISE) infrared data. Our selections of type 1 QSOs required (i) $2.1 \lesssim z \lesssim 2.6$ so that Hα is redshifted into the K band, (ii) enabling

GRAVITY+ observations either on-axis (i.e., $K < 13$) or off-axis (i.e., $K < 16$ as well as with a $K < 13$ star within $20''$), and (iii) an initial prediction of the differential phase signal $> 0.3°$ to ensure that the integration times with GRAVITY+ would be reasonable. The differential phase is an interferometric observable that measures the centroid position as a function of wavelength (see Sect. 3.6 and GRAVITY Collaboration et al. 2020a for more details). The expected differential phase signal was estimated by assuming all targets lie on the Bentz et al. (2013) R–L relation. The 5100Å luminosity was estimated by scaling the mid-IR luminosity (Krawczyk et al., 2013) SED to the observed *Gaia* $G_{\rm RP}$ magnitude. The phase signal was then calculated using $\Delta\phi = [f/(f+1)]RB$ where f is the typical line-to-continuum ratio of 3 for Hα, R is the BLR radius (in radians), and B is the projected baseline length of 100m for the VLTI divided by the wavelength. To make an initial assessment of the properties of the selected quasars, we also looked into the archival data, particularly within the Sloan Digital Sky Survey (SDSS) Data Release 16 Quasar Catalogue (DR16Q; Lyke et al. 2020) and the UV Bright Quasar Survey Catalogue (UVQS; Monroe et al. 2016) for their optical and ultraviolet (UV) spectra, respectively, to confirm AGN features such as the blue continuum and broad CIV, MgII, or Lyα lines.

After the sample selection, 72 observable unique targets were selected. Observations were performed between April 2022 and February 2023 with the infrared spectrograph Son of ISAAC (SOFI) at the 3.6-m New Technology Telescope (NTT), which is operated by the European Southern Observatory (ESO). Due to weather conditions, we were able to observe 49 targets with NTT/SOFI. Since our goal is to pick objects that are suitable for GRAVITY+ observations, we only analysed those with sufficiently strong Hα lines (i.e. integrated flux $\gtrsim 5 \times 10^{-16}$ erg s^{-1} cm^{-2}). We then narrowed our sample to 29 targets. Some of the faint targets have signal-to-noise ratio (S/N) values between 4 and 10, while the brightest targets have S/N as high as 40-55. Table C.1 lists the 29 targets with good spectra, which are analysed for this study, together with a summary of their observations, which include the date of observation, exposure time, airmass, seeing, and S/N.

The initial two runs were performed using medium resolution spectroscopy with the K_s filter (2.00-2.30 μm, grism no. 3 with R$\sim$2200, with a dispersion of 4.62 Å pixel^{-1}) and a $1''$ slit. For the remainder of the runs, we switched to the low-resolution spectroscopy with the GRF filter (1.53-2.52 μm, red grism with R$\sim$980 with a dispersion of 10.22 Å pixel^{-1}) and a $0.6''$ slit due to the wider wavelength range it provides, allowing better constraint on the continuum and possible detection of Hβ and Hγ lines compared with the K_s filter. The K-mag values and exposure time of each target are presented in Table C.1. For the science observations, we used the auto-nod non-destructive readout mode of SOFI provided by the `SOFI_spec_obs_AutoNodNonDestr` template. A telluric star was observed after each AGN observation to enable atmospheric correction and flux calibration. For the spectral calibration and flat fielding, we took xenon and neon arc lamp observations and dome flat exposures before the start of each night. These observations were taken with the `SOFI_spec_cal_Arcs` and `SOFI_spec_cal_DomeFlatsNonDestr` observation templates, respectively, using the same slit and filter as our observations for the night.

3.3 Data reduction

The data were reduced with version 1.5.0 of the SOFI pipeline. The flat fields and arc frames were processed using the `sofi_spc_flat` and `sofi_spc_arc` recipes, respectively. For low-resolution data, we had difficulties obtaining a dispersion solution that matched the H and K bands simultaneously. We, therefore, applied a quadratic correction to each band separately, based on the atmospheric OH lines in the H band and on the arc lines in the K band. The science data were processed using `sofi_spc_jitter` recipe to produce a 2D spectrum. Although this recipe can combine the individual frames and extract a final 1D spectrum, we used our own algorithms for these steps. Each 2D spectrum was trimmed in the spatial direction, and then a line-by-line residual background was fitted away from the object trace and subtracted. The frames were aligned to integer pixel precision based on the spectrally summed trace and then combined while rejecting deviant values. A final iteration of the line-by-line subtraction of the median in each row was then performed on the combined frame. From this 2D product, we extracted a 1D spectrum on which we performed telluric correction and flux calibration.

The spectral extraction was based on the optimal extraction method described by Horne (1986), with some adaptations to match it to the pipeline process and the data properties. A description of the implementation is given in the Enhanced Resolution Imager and Spectrograph (ERIS)-SPIFFIER Pipeline Manual[1]. This method is suitable for sources where the spatial distribution changes only gradually with wavelength, including unresolved sources such as stars and the QSOs in our sample. The routine begins by defining a region around the spectral trace that encompasses all the flux. This defines the source values $D_{x\lambda}$ as a function of spatial location x and wavelength λ, and the variance values $V_{x\lambda}$ as the square of the noise. An initial spectrum is created as $f_\lambda^{initial} = \Sigma_x D_{x\lambda}$ with variance $var[f_\lambda] = \Sigma_x V_{x\lambda}$. A model of the spatial distribution of the source (or point spread function/PSF) $P_{x\lambda}$ is then constructed by normalising each spectral slice so that $P_{x\lambda} = D_{x\lambda}/f_\lambda$. The resulting model $P_{x\lambda}$ is essentially the probability that a detected photon with wavelength λ falls on pixel x. Because $P_{x\lambda}$ is by definition strictly positive, in the first step, any negative values of $P_{x\lambda}$ are set to zero. The second step is to provide some regularisation along the spectral direction, so at each spatial location x, the spectral values of $P_{x\lambda}$ are traced. Rather than fit these with low-order polynomials as was done by Horne (1986), we applied a running median filter. In both cases, the same purpose is achieved: to reject outliers, which is the second core part of the algorithm. Any pixel in $P_{x\lambda}$ for which $(D_{x\lambda} - f_\lambda P_{x\lambda})^2 > \sigma_{clip}^2 V$ is set to zero. The threshold σ_{clip} is derived using a percentile clipping of the values and is calculated for each spectral row to allow for strong variations in the S/N along the spectrum. The spectrum estimator is then defined to be a linear combination of unbiased pixel estimates such that

$$f_\lambda^{unbiased} = \frac{\Sigma_x (W_{x\lambda} D_{x\lambda}/P_{x\lambda})}{\Sigma_x (W_{x\lambda})},$$

where the variance of the weighted mean is minimised by choosing weights that are inversely

[1] Available from https://www.eso.org/sci/software/pipelines

proportional to the variance of the variables, so that

$$1/W_{x\lambda} = var[D_{x\lambda}/P_{x\lambda}] = V_{x\lambda}/P_{x\lambda}^2.$$

Substituting these weights into the equation above, one can find the optimal extraction of the spectrum f such that when it is multiplied by the source model P, the result matches the data D, which has variance V. The initial optimal spectrum can then be expressed as

$$f_\lambda^{optimal} = \frac{\Sigma_x(P_{x\lambda}D_{x\lambda}/V_{x\lambda})}{\Sigma_x(P_{x\lambda}^2 V_{x\lambda})}$$

with variance

$$var[f_\lambda^{optimal}] = \frac{1}{\Sigma_x(P_{x\lambda}^2/V_{x\lambda})}.$$

This process is then iterated a second time replacing the initial estimate of f_λ with the first estimate of the optimised spectrum, to yield the final estimate of the optimised spectrum.

The telluric star was used both to correct the atmospheric absorption and for flux calibration. The former was achieved by modelling the star (spectral type B) as a blackbody with Brγ absorption and normalising the resulting telluric spectrum to a maximum value of 1. The flux calibration was performed by taking the ratio of the counts within 2.0–2.3 μm and the expected K band flux calculated from the magnitude. We compare the measured K_{mag} values of our targets based on their average flux densities with the K_{mag} values from their catalogues, and find that our targets are $\sim$0.44 mag fainter than expected. This translates to a $\sim$33% lower detected flux than expected. We discuss the possible cause of such lower measurement in Sect. 3.4.4.

3.4 Emission line properties

This section focusses on the observed properties of the emission lines. We first applied a line decomposition in order to separate the broad component from other features in the spectrum. We then assessed the properties of the broad line emission, in particular, the full-width-half-maximum (FWHM) to σ ratios and the Hα/Hβ flux ratios of our targets.

3.4.1 Line decomposition

In this Section, we describe the fitting of the Hα, Hβ, Hγ, and [OIII] lines as well as the continuum and iron complex (noting that for the medium resolution data taken with the K_s band filter, only the Hα line is covered). We used the SAGAN code[2] to decompose the spectra.

The Hα lines were fitted with two Gaussian components when there was a clear superposition of a narrower core (that is much broader than the typical width of a narrow-line component expected from the narrow-line region or NLR) and a broader wing component.

[2]https://github.com/jyshangguan/SAGAN

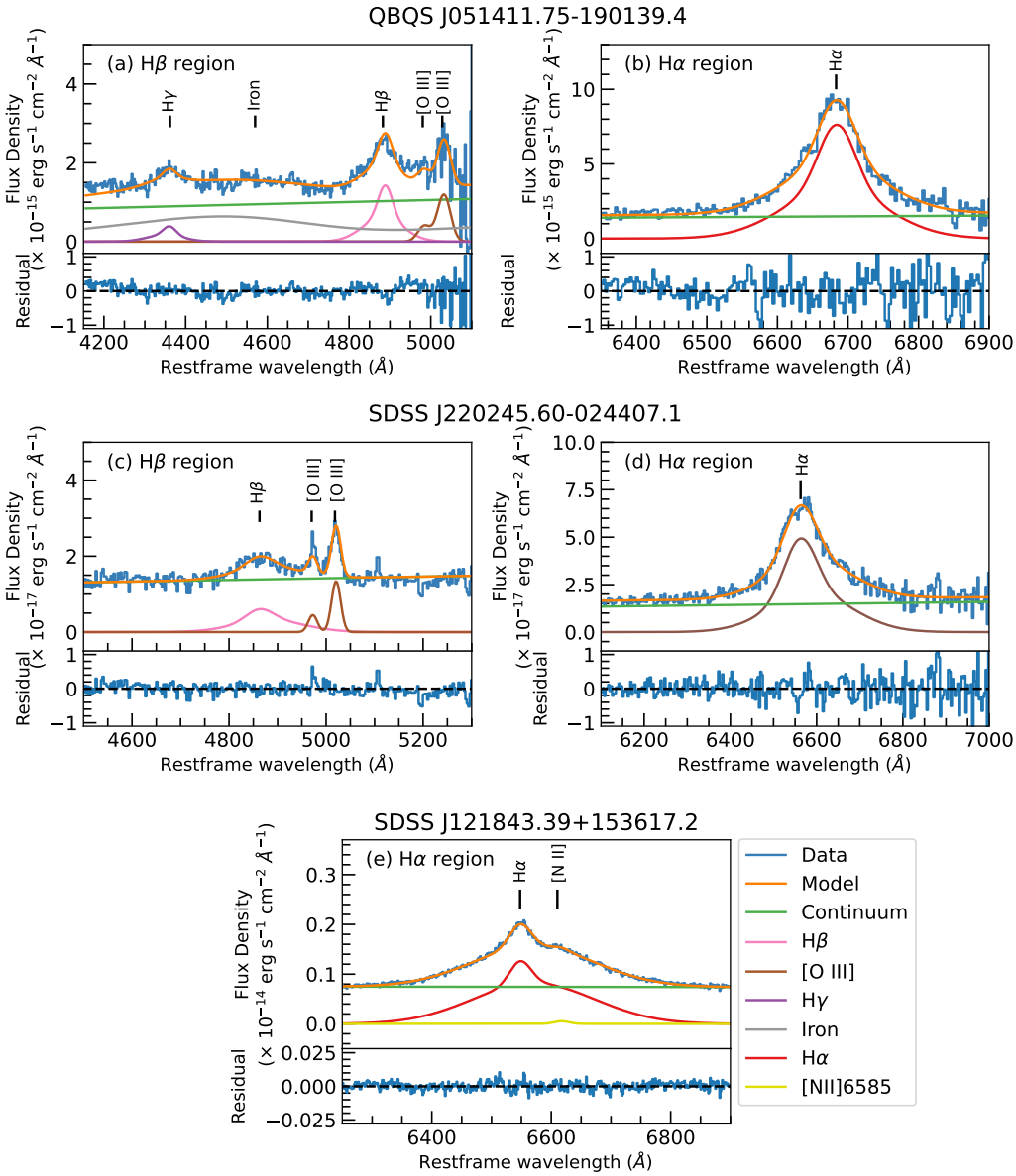

Figure 3.1: Representative line decomposition results for three of our SOFI $z \sim 2$ targets. Each row refers to a different target (QBQS J051411.75-190139.4, SDSS J220245.60-024407.1, and SDSS J121843.39+153617.2), while each column refers to a different spectral region (Hβ and Hα). The observed data are shown in blue, while the cumulative best-fit spectrum is shown as an orange solid line. The different coloured lines pertain to different components in the line decomposition, as shown in the legend. Some of our targets have strong FeII and even clear Hγ emission, as shown in the Hβ region of QBQS J051411.75-190139.4 (panel a). On the other hand, a few targets have prominent (S/N $>$ 3) [OIII] features similar to SDSS J220245.60-024407.1 (panel c). Both of these objects were observed with the GRF filter, hence other Balmer lines aside from Hα are detected. On the other hand, SDSS J121843.39+153617.2 was observed with the K_s filter (panel e). Its Hα spectrum shows a weak [NII]λ6584 feature (see Sect 3.4.2).

We impose criteria to determine whether the double Gaussian model is a better fit than the single Gaussian model. Once all criteria are met, the double Gaussian model is preferred. Otherwise, we follow the single Gaussian model fit. Our criteria are similar to that of Oh2 (2024):

1. The reduced chi-square value of the double Gaussian fitting is less than that of the single Gaussian fitting ($\chi^2_D < \chi^2_S$), where D and S refer to double and single Gaussian model, respectively;

2. The S/N of the wing and core components should be greater than 3;

3. The wing component flux contributes to 10-90 percent of the total flux $f_W/(f_W + f_C)$ where W and C refer to the wing and core components, respectively); and

4. The velocity dispersion of the broad component should be greater than that of the narrow component by at least its uncertainty ($\sigma_W - \sigma_{W,err} > \sigma_C$).

With these criteria, we were able to confidently choose 21/29 Hα lines to be fitted with the double Gaussian model, and the rest were fitted with the single Gaussian model. We also note that most of the emission lines fitted with the single Gaussian model have S/N $\lesssim$ 8. For the Hβ and Hγ lines, we fit them with the same line profile as the Hα line. If the double-Gaussian model is used, the velocity shift difference between the two Gaussian components is also fixed when fitting the other Balmer lines. We do not assume a theoretical flux ratio of $f_{H\alpha}/f_{H\beta}$ = 3-3.5 as shown by previous works (Dong et al., 2008; La Mura et al., 2007) as it fails to produce a meaningful fit, which tells us that our targets do not exhibit such a flux ratio. We found three targets that are exempted from our usual line decomposition method: ID#23, which shows a relatively large deviation between the Hα and Hβ velocity shifts ($\sim$1500 km/s) despite being fitted with a similarly shaped Gaussian component; ID#25, which shows Hβ to be fitted with one Gaussian component while its Hα line is fitted with two Gaussian components; and ID#29, where Hβ is much wider than the Hα line. Tables C.2 and C.3 show the line-fitting results of Hα, Hβ, [OIII], and Hγ lines, while Table C.4 shows the line-fitting results of the three Hβ lines that did not have the same line profile as their Hα lines. We also used the central wavelength of the Hα line to verify or update the redshift of each target taken from the source catalogues.

Balmer lines are usually composed of the broad component originating from the BLR, and the narrow component originating from the NLR. Most works use the [SII] doublet as the narrow line template, but in the case that it is not observable, the [OIII] doublet can be used (Greene and Ho, 2004). However, the [OIII] doublet suffers from possible contamination of outflowing components, which could indicate a dynamic NLR (Whittle, 1985; Boroson, 2005; Marziani et al., 2017), making it a less suitable narrow-line template. To check whether we need to fit the narrow component with a template, we first chose targets with observable [OIII] doublet, that is, the S/N of [OIII] > 3 and the doublet is not obscured by any atmospheric feature. Seven targets were selected using these criteria. Their Balmer lines were then fitted with the single/double Gaussian model (whichever is

suited based on the aforementioned criteria) plus the narrow component with a similar line width as the [OIII] doublet. Afterwards, we measured the narrow components' flux contribution to the fitted Balmer lines. Only three targets (ID #9, 10, and 17) showed a >5% flux contribution of the narrow components on their Balmer lines. We also did not find any drastic change in our results (i.e. best-fit BLR parameters and virial factor; see Sect. 3.5.2 and 3.5.3) and conclusions after removing the fitted narrow components from the Balmer lines of these three targets. Hence, we decided not to include any narrow component fitting in all of our targets.

In most cases, the continuum, which was fit together with the rest of the emission lines, was represented with a power law. However, in a few cases where the power law continuum does not give a good fit (6/29 targets), a 4-degree polynomial was used instead. The polynomial degree was chosen as it is the smallest degree that provides a converging result for these exceptional cases. For these objects fitted with a 4-degree polynomial as their continuum, there is sufficient wavelength range outside the broad line emission. An iron template based on I Zw 1 (Park et al., 2022) was included in the fit when there were clear FeII features around the Hβ and [OIII] lines. Fig. 3.1 shows example results of the line decomposition for three targets with different properties: (a) a target observed with the GRF filter which has strong FeII features but noisy [OIII] lines due to atmospheric absorption (hence it was not chosen for fitting the narrow component with the [OIII] doublet as a template), (b) a target observed with the GRF filter with slightly asymmetric Hα, no FeII features, very strong [OIII] lines and significant narrow components in their Balmer lines, and (c) a target observed with the K_s filter with a strongly asymmetric Hα line that has a bump on the redshifted side of the Hα central wavelength (and which is discussed in Sect. 3.4.2).

The uncertainty in the flux density for all spectral channels was calculated as the standard deviation of the fitting residual. From the decomposition, we measure the line fluxes and luminosities, their FWHM values, and also the dispersions σ defined as the square root of the second moment of the line (Dalla Bontá et al., 2020). Both the FWHM and σ are calculated from the best-fit line and are corrected for instrumental broadening. The 1σ uncertainties of these quantities are derived using Monte Carlo techniques, perturbing the spectrum 1000 times with the uncertainty in the flux density. We normalise the Balmer lines by the continuum for BLR fitting (see Sect. 3.5.2).

3.4.2 Line properties of the $z \sim 2$ targets

Among the 29 targets, 24 have data covering both H and K bands. Of those, 17 have significant Hβ emission, and two also have observable Hγ emission. It is important to bear in mind the number of Gaussian components used to fit the Balmer lines. Most of the Balmer emission lines are fitted with two Gaussian components comprising a narrower core component (with $\sigma \lesssim 1200$ km s^{-1}) and a broad wing component (typically with $1500 \lesssim \sigma \lesssim 3000$ km $^{-1}$).

The corrected redshifts of our targets are almost all consistent within their 1σ uncertainties with the redshifts from their respective catalogues, as expected. For 10 of the 17

targets with Hβ emission lines, the [OIII] doublet has been detected and fitted as well, similarly to SDSS J220245.60-024407.1 (ID#15). Five of these have $\sigma \gtrsim 1000$ km s^{-1} for the [OIII] lines. In addition, six targets have clear FeII signatures in their spectra. We do not investigate these lines or Hγ further, and instead, we focus our analysis on the stronger Balmer lines Hα and Hβ.

As noted previously, one particular target, ID#1 (SDSS J121843.39+153617.2), has a bump on the redshifted side of the Hα peak (see Fig. 3.1). Its wavelength corresponds to a velocity offset of ~ 2300 km s^{-1} with respect to Hα, but only ~ 1450 km s^{-1} with respect to [NII]λ6584 . Although [NII] is a doublet, the other line [NII]λ6548 is a factor 3 fainter (Acker et al., 1989) and so a corresponding feature would not be detectable. In addition, the calculated velocity offsets should not be taken too seriously due to the uncertainty of the redshift taken from the original catalogue, which is $\sigma_z \sim 0.01$, which translates to ~ 3000 km/s (Onken et al., 2023). We therefore consider the bump to be associated with [NII]λ6548 due to the lower velocity offset. We note, however, that the results of our analyses for this target do not change even if the bump is considered as another Hα component. We also do not have any other narrow line present in our spectrum of this target to calculate the redshift.

3.4.3 FWHM versus σ and the BLR model

One of the most important properties of the line emission in terms of BLR modelling is the shape of the line profile. A simple way to quantify this is via the ratio of FWHM to σ, which has been shown to be a good measurement of line shape because FWHM is core sensitive while σ is wing sensitive (Wang et al., 2019). We plot the line shape, quantified in this way, as a function of FWHM in Fig. 3.2 for the Hα lines. We focussed on the Hα lines fitted with the double-Gaussian model, as the targets fitted with the single-Gaussian model will lie at the Gaussian limit (i.e., FWHM/σ = 2.35) shown as a horizontal line, and we found systematic uncertainty in the Hβ lines (see Sect. 3.4.4). Compared with the theoretical line width ratios from Kollatschny and Zetzl (2011) and Kollatschny and Zetzl (2013) (as shown by the black and grey dashed lines), our line width ratios are smaller but show a similar trend as their work and Wang et al. (2019): that the FWHM/σ increases with FWHM. Targets with low FWHM and FWHM/σ have line profiles that more closely resemble a Lorentzian profile: a superposition of a very broad component and a strong, more prominent core. On the other hand, targets with high FWHM and FWHM/σ have line profiles that more closely resemble a Gaussian profile; indeed, at much higher FWHM values, the trend asymptotically reaches the Gaussian limit. Comparing our sample with the low redshift work of Villafaña et al. (2023), Kollatschny and Zetzl (2011), and Kollatschny and Zetzl (2013), we found no significant difference (Pearson correlation p-value $\gg 0.05$) in the distribution of line shape versus FWHM between our sample and their AGN samples.

We discuss below two explanations for such profiles. The first scenario, a two-component BLR, would tend to favour fitting the profile with two distinct components. The second scenario, which explains the profile as a combination of turbulence and rota-

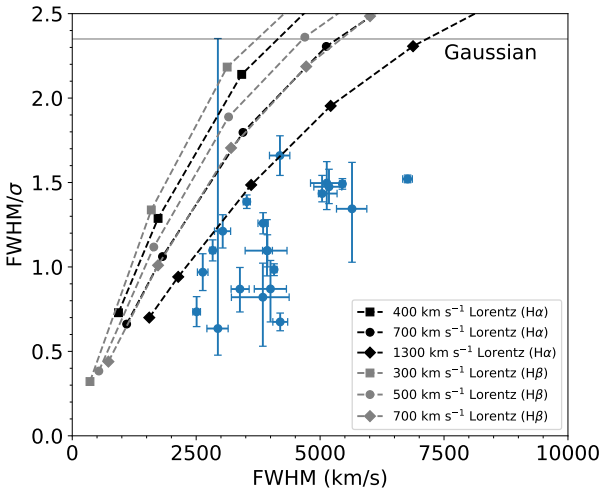

Figure 3.2: Ratio of FWHM to σ (line shape) of Hα lines fitted with the double-Gaussian model as a function of FWHM. The Gaussian limit (FWHM $\sim 2.35\sigma$) is shown as a horizontal grey solid line. The error bars denote 1σ uncertainties. For comparison, we plot the theoretical line width ratios of rotational line broadened Lorentzian profiles for Hα (black dashed lines and markers) and Hβ (grey dashed lines and markers) which were taken from Kollatschny and Zetzl (2011) and Kollatschny and Zetzl (2013). Different markers pertain to different FWHMs of the Lorentzian profiles.

tion, would tend to favour fitting the line with a Voigt profile that is a convolution of a Lorentzian profile with a Gaussian. While we have chosen to fit the profiles with two Gaussians, this is done for the convenience of quantifying σ, and does not imply a preference for one explanation over the other.

Scenario 1: Two-component BLR model

A two-component BLR has been discussed extensively in the literature (e.g. Brotherton et al., 1994; Popović et al., 2004; Zhu et al., 2009; Zhang, 2011; Ludwig et al., 2012; Nagoshi et al., 2024). In this scenario, the BLR is composed of two components. The first one is an inner disc – the very broad line region (VBLR) – that is more closely associated with the accretion disc and is responsible for the broad wings of the observed emission line. Zhu et al. (2009) suggests that the VBLR represents the "traditional" picture of the one-component BLR and is the region responsible for the observed ~ 0.5 slope in the size-luminosity relation. Indeed, there have been recent claims for detecting Keplerian rotation in this inner disc from the variability of its micro-lensing response (Fian et al., 2024). The second component is an outer and more spherical part – the intermediate line region (ILR) – which produces the narrow core of the profile. The ILR, which is situated at a larger distance from the ionising source, is thought to have higher gas density and be flatter than the VBLR; and is suggested to represent the inner boundary layer between the BLR and the dusty torus of the AGN.It has been argued that such BLRs with two

components occur both in the low-redshift (Zhu et al., 2009) and high-redshift (Brotherton et al., 1994) Universe. Zhang (2011) argued that the ILR of the reverberation-mapped AGN PG 0052+251 was strongly obscured because, in contrast to its Hα line, its Hβ line profile does show a clear core component in the line decomposition. While we consider this result uncertain because of the low quality of the spectrum in the Hβ line region of their source, such an explanation could, in principle, apply to the different line widths of Hα and Hβ of ID#15 that was shown in Sect. 3.4.2. Storchi-Bergmann et al. (2017) also finds that aside from the ubiquity of a disc component in most BLRs, an additional line-emitting component arises at higher Eddington ratios and higher luminosities for Seyfert 1 galaxies. This component is reminiscent of the ILR component, and, as suggested by Storchi-Bergmann et al. (2017), may be inflowing (Grier et al., 2013), outflowing (Elitzur et al., 2014), or simply have more elliptical orbits (Pancoast et al., 2014a).

The limitation of this explanation is that there is no clear reason why, when considering these two components together, there should be a relation between FWHM and FWHM/σ as seen in Fig. 3.2. Collin et al. (2006) proposed that this distribution may be associated with the Eddington ratio and, hence, the accretion rate. They suggested that at large radii, where the self-gravity of the disc overcomes the vertical component of the central gravity due to the SMBH, the resulting cloud collisions due to the gravitational instability would heat the disc and increase its turbulence. And, based on a correlation between the ratio of the BLR size to this radius and the Eddington ratio, these authors speculated that gravitational instability may be stronger in AGN with higher Eddington ratios, leading to greater turbulence, which perhaps constitutes the start of a disc wind. This results in a very broad component in the line profile, as exhibited by the low FWHM/σ (i.e. low FWHM) sources. On the other hand, weaker accretion produces a more stable BLR, producing Gaussian-like line profiles.

Scenario 2: Presence of turbulence and rotation

This relation is specifically addressed in the phenomenological approach put forward by Kollatschny and Zetzl (2011). For a disky BLR, the ratio between the turbulent and rotational velocity is proportional to the ratio between the height and radius of the BLR. Since the rotational velocity is found to increase with increasing FWHM (Kollatschny and Zetzl, 2013), objects with high FWHM and, therefore, high FWHM/σ have a fast-rotating geometrically thick and flat BLR. In contrast, objects with low FWHM and, therefore, low FWHM/σ have slow-rotating spherical BLRs. These authors noted that while the Balmer lines tend to originate at moderate distances above the disc plane, the highly ionised lines come from smaller radii and at greater scale height and that the resulting geometries resembled disc winds models. Thus, without explicitly requiring two distinct components, an understanding of the geometry and kinematics of the BLR does lead to insights into the various physical processes occurring in this region. This perspective matches the approach we adopt when modelling the BLR (see Sect. 3.5). We fit the line profile (and differential phase data from GRAVITY/+ when available) with a single model that encompasses both rotation and dispersion without physically separating them. The dispersion comes

directly from the geometry in terms of the thickness, or opening angle, of the BLR and the distribution of clouds within it. It is also affected by whether there is a radial component, whether inflowing or outflow. Thus, here, too, there is a continuous distribution of potential models from a thin rotating disc through a turbulent, thick rotating disc to a combination of rotation and outflow.

The interpretations above seem likely to be different perspectives on the same underlying processes and geometries that invoke a rotating (thick) disc together with a region or component of that disc where the gas has increased turbulence and scale height, and so may be the origin of the expected disc wind. However, there is a major difference between them that needs to be resolved. The wings of the profile trace the rapidly rotating inner disc in the two-component scenario, while they trace the turbulence in the Voigt profile interpretation. Similarly, the core of the profile traces the outer, more spherical distribution in the two-component model while it traces the rotation in the Voigt profile. This aspect needs clarification if we are to fully understand the BLR.

3.4.4 Luminosity ratio (Balmer decrement)

As discussed in the previous section, the Hα lines are mostly fitted with two Gaussians, while the Hβ and Hγ lines are fitted with the same line profiles as their respective Hα lines with the exception of three targets. To further assess the properties of our targets, we investigate the ratio between Hα luminosity and Hβ luminosity (i.e. the Balmer decrement) as a function of Hα luminosity.

Fig. 3.3 shows the Balmer decrement as a function of Hα luminosity. The Balmer decrement does not show a significant correlation with $L_{H\alpha}$ (the probability of it occurring by chance is $p = 0.101$ or 1.3 σ), although it seems to exhibit a positive correlation (correlation coefficient $\rho = 0.41$) similar to previous works (e.g. Domínguez et al., 2013; Reddy et al., 2015). Furthermore, the Balmer decrements of our targets are > 3.5. The large Balmer decrements suggest that we are missing a significant fraction of the Hβ luminosity and therefore, there is a systematic uncertainty associated with the Hβ emission lines that go beyond the nominal statistical uncertainty derived from the fits. This is due to the limitation of the data rather than having a physical cause, and caution is needed when interpreting values related to Hβ, especially the size of the Hβ-emitting region of the BLR.

It is possible that such large Balmer decrements could be due to significant contributions from Wolf-Rayet or late-type OB stars (e.g. Crowther and Bohannan, 1997). However, this reason is unlikely to be the cause of the observed Balmer decrements in our sample since these targets are quasar-dominated as per our check of archival spectral data from SDSS DR16Q and UVQS catalogues. The Balmer decrements of our sample are higher than one would expect from typical star-forming galaxies (SFGs) at $z \sim 2$, which are also found to increase with stellar mass (Shapley et al., 2022; Maheson et al., 2024). Considering also that we found higher Hα/Hβ ratios than the expected value of $\sim$3.1 (Dong et al., 2008; La Mura et al., 2007), these suggest that dust extinction might cause such large Balmer decrements in our sample. To confirm whether dust extinction is the cause of such large Hα/Hβ ratios in our sample, we estimate the typical extinction coefficient (A_V) of our

sample based on our median Hα/Hβ value of ∼7.45. Using Eqns. 4 and 7 of Domínguez et al. (2013), we found $A_V \sim 3$ which translates to a column density of $N_H \sim 6 \times 10^{21}$ cm^{-2}. These values are larger than most SFGs at high-z, but still within the acceptable range of A_V values for Type 1-1.5 AGNs (Burtscher et al., 2016). However, such large A_V should also lead to obscuration of the BLR light, which is not the case for our targets. In addition, an extinction coefficient of $A_V \sim 3$ translates to a detected flux that is ∼10% of the intrinsic flux. However, based on our comparison between our measured and expected K_{mag} values in Sect. 3.3, we found that we are detecting (on average) ∼33% of the intrinsic flux of our sample. Therefore, we cannot conclude with confidence that dust extinction is the root cause of our observed large Balmer decrements.

Nevertheless, other alternative explanations for the large Balmer decrements of AGNs have also been put forward, such as the intrinsic property of the BLR, that is, the BLR consists of clouds with low optical depths and low ionisation parameters (Kwan and Krolik, 1981; Canfield and Puetter, 1981; Goodrich, 1990), or the possible role of accretion rate (Wu et al., 2023). Although we cannot confirm the cause of the large Balmer decrements in our sample, we expect that these should only affect the estimated single-epoch BH masses, BLR radii, and expected differential phase signals of our targets, which are all dependent on the Hα luminosity, but not the geometry and virial factors based on our BLR fitting results (see Sect. 3.5).

3.4.5 BH mass and bolometric luminosity estimation

Two of the important parameters we need for comparison with future GRAVITY+ observations of $z \sim 2$ are SMBH mass ($M_{\rm BH}$) and bolometric luminosity ($L_{\rm bol}$) estimates. We present the first estimates of $M_{\rm BH}$ and $L_{\rm bol}$ in columns 7 and 8 of Table C.2. We present the parameter space that we are probing with our SOFI $z \sim 2$ targets in Fig. 3.4. For comparison, we also show the low-luminosity $z \sim 2$ AGNs from Suh et al. (2020) and the high-luminosity $z \sim 2$ AGNs from the WISSH survey (Bischetti et al., 2021).

In their Eqns. 5 and 6, Woo et al. (2015) calculated the SMBH mass as a function of Hα luminosity and either FWHM or σ. These have different values of the virial factor: for σ, $f = 4.47$, while for FWHM, $f = 1.12$. The resulting SMBH masses of our targets from these equations are consistent with those derived from relations presented elsewhere (e.g., Dalla Bontá et al., 2020). While there are advantages and disadvantages of different line width measurements for calculating SMBH masses (Peterson et al., 2004; Wang et al., 2020), we report the σ-calculated single-epoch BH mass estimates because it has been argued to have a tighter virial relationship than FWHM (Peterson et al., 2004), and FWHM can lead to overestimation at higher SMBH mass and underestimation at lower mass (Dalla Bontá et al., 2020). Because not all targets were observed in the necessary band, the λL_λ(5100 Å) continuum luminosities are instead calculated using Eqn. 4 of Woo et al. (2015) from the Hα luminosity, and the uncertainties are derived by calculating the distribution of SMBH masses via Monte Carlo method, assuming Gaussian distributions of the virial factor f, Hα luminosities and σ values. To convert the λL_λ(5100 Å) to $L_{\rm bol}$, we used the bolometric correction formula from Trakhtenbrot et al. (2017) which is similar to

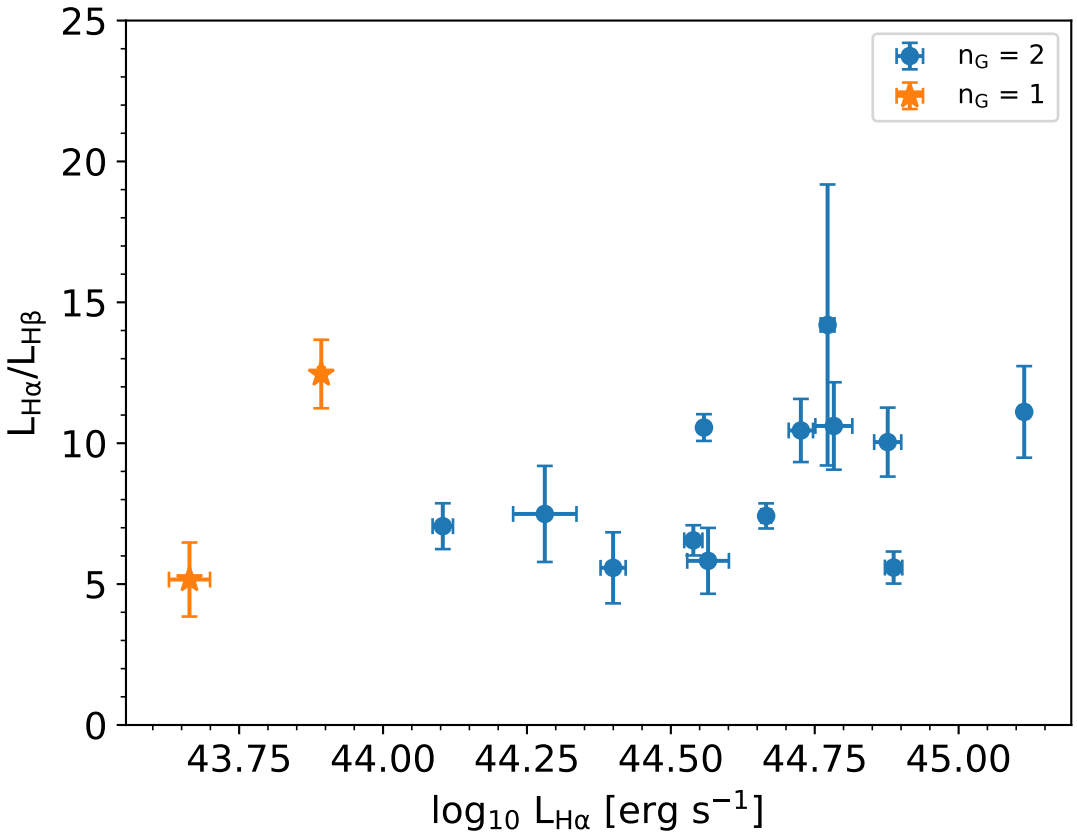

Figure 3.3: Ratio between Hα and Hβ luminosity as a function of Hα luminosity. The blue (orange) points show the targets that are fitted with a double (single) Gaussian model. We remove two targets (from the three exceptions in Table C.4) whose Hβ lines cannot be fitted with the same number of Gaussian components and line shape as that of Hα. The error bars are 1σ uncertainties.

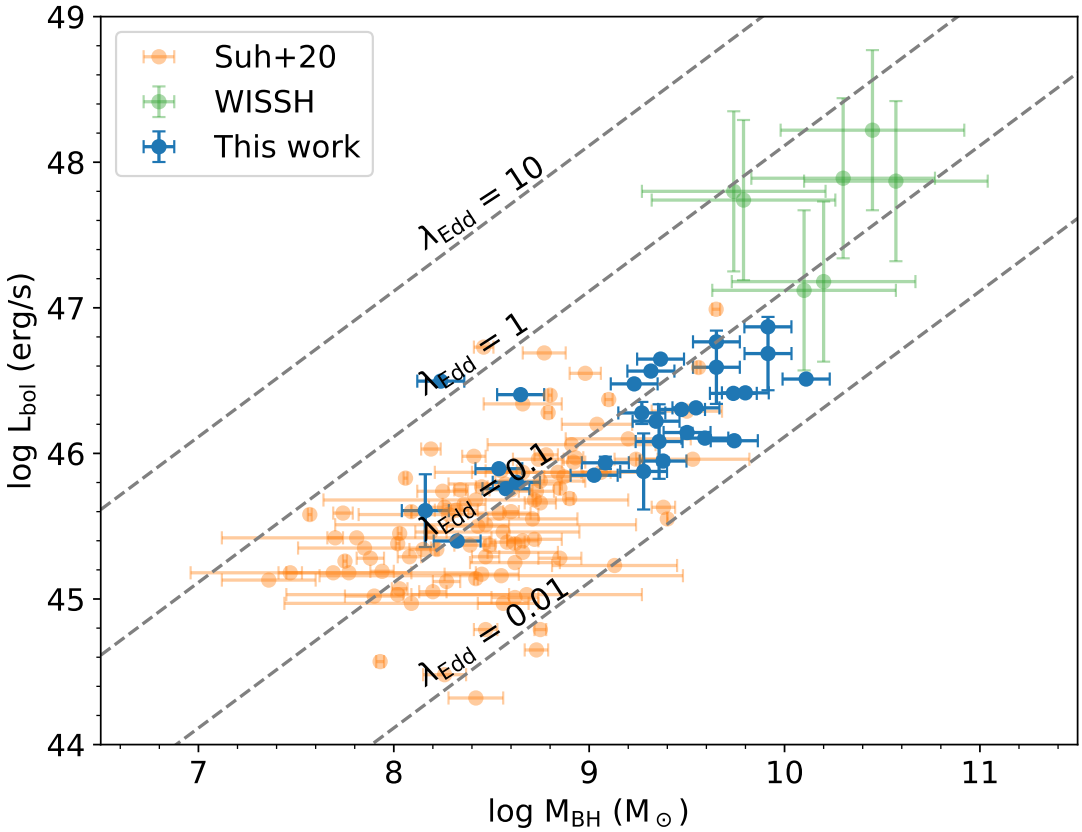

Figure 3.4: Logarithm of bolometric luminosity as a function of the logarithm of BH mass. For the SOFI $z \sim 2$ targets (This work, blue data points), the $L_{\rm bol}$ are estimated from Hα, while the $M_{\rm BH}$ are estimated using Eqn. 6 of Woo et al. (2015) which uses the dispersion (σ) and Hα luminosity as inputs. The typical error of log $L_{\rm bol}$ is shown as the blue vertical error bar on the lower right of the panel. For comparison, we show the sample of z = 1.5 - 2.5 with $L_{\rm bol} < 47$ as orange points (Suh et al., 2020) and high-luminosity quasars from the WISSH survey as green points (Bischetti et al., 2021). The grey dashed lines pertain to the loci of the same Eddington ratio: $\lambda_{\rm Edd}$ = 0.01, 0.1, 1, and 10. For the WISSH quasars, we assume a BH mass uncertainty of $\sim$ 0.47 dex following the prescription for the 1σ relative uncertainty of single-epoch BH mass estimates from Vestergaard and Peterson (2006b). However, we do not include the systematic uncertainties for the absolute calibration of RM masses.

the bolometric correction of Suh et al. (2020) and Bischetti et al. (2021). We see that our SOFI $z \sim 2$ AGNs are located between the two AGN samples, particularly at moderate BH masses ($\log M_{\rm BH} \sim 8 - 10.5$) and bolometric luminosities ($\log L_{\rm bol} \sim 45 - 47$), which translates to moderate accretion rates (Eddington rates of $\lambda_{\rm Edd} \sim 0.1$).

3.5 BLR modelling

Following the assessment of the line profiles, we fitted them with the Pancoast model described in Sect. 2.5. The only difference in how we apply this model in the previous chapter (GRAVITY Collaboration et al., 2024) and this chapter (Santos et al., 2025a) is the input data and the reason for fitting the data with the Pancoast model. For the former, the Pancoast model was used to fit the observed differential phase and flux spectra to yield best-fit parameters. For the latter, only the flux spectrum is present. The Pancoast model is adapted into a Python package called `DyBEL` which can be used to fit either a single line (only Hα) or two or more lines simultaneously (e.g. both Hα and Hβ). By fitting the flux spectra with `DyBEL`, we are able to estimate the interferometric signal of the target (to be discussed in Sect. 3.6). In this section, we discuss the capabilities of `DyBEL` as a fitting code and the results of our BLR fitting, while we refer the readers to Sect. 2.5 for the discussion of the Pancoast model. We finish the section by looking at two targets for which the asymmetry of the line profiles warrants a more detailed approach than the majority of the sample.

3.5.1 Description of `DyBEL`

We followed the BLR model fitting methodology introduced by Kuhn et al. (2024), which was developed based on Pancoast et al. (2014a) and Stock (2018). Rather than model the distribution of BLR clouds and calculate their line emission based on photoionisation physics, we model the distribution of line emission directly. As such, the model focusses on geometry and kinematics without considering the absolute flux scaling. The model is adapted into a Python package called `DyBEL` which can be used to fit either a single line (only Hα) or two or more lines simultaneously (e.g. both Hα and Hβ). The fitted parameters are similar to the previous chapter (GRAVITY Collaboration et al., 2024) with the exception of the inclusion of the angular location of the clouds to the $v_r - v_\phi$ plane, θ_e, as a free parameter. One thing that we want to highlight in the Pancoast model is that the opening angle, θ_0, allows the model to provide a "flared disc" shape. It is the combination of the flared disc shape and the ellipticity of the orbits (see below) that enables our model to fit targets with a variety of FWHM/σ.

Following previous work (Kuhn et al., 2024; GRAVITY Collaboration et al., 2020a, 2024; Abuter et al., 2024), we used the Python package `dynesty` (Speagle, 2020) together with a nested sampling algorithm (Skilling, 2004) to fit the data. We used 1200 live points with the dynamic nested sampler (`DynamicNestedSampler`) and the random walk (`rwalk`) sampling method. The rest of the options in `dynesty` were set to their default

values. Following Kuhn et al. (2024), a temperature parameter T was also defined. This parameter was set to 16 in order to provide likelihood functions with fewer peaks and, hence, a better estimation of the posterior distributions. The spectrum was normalised by the continuum so that we effectively fit the line-to-continuum ratio (as a function of observed wavelength). We note that this is also used to estimate the expected differential phase signal of the target (see Sect. 3.6).

Using a spectrum of NGC 3783, Kuhn et al. (2024) demonstrated that fitting Hα, Hβ, Hγ, HeI, and Paβ lines simultaneously provide tighter constraints on the BLR parameters of NGC 3783 than fitting them separately and that both methods provide consistent geometry with that derived from the RM and GRAVITY data (GRAVITY Collaboration et al., 2021a,b; Bentz et al., 2021). When an object has Hβ and Hγ line profiles available, we include them in the fit after tying many of their parameters. In particular, their central wavelengths are tied so that they all shift by the same small amount $\epsilon = \lambda_{\rm c}/\lambda_{\rm air} - 1$, where λ_c is the theoretical central wavelength of the line, and $\lambda_{\rm air}$ is the wavelength measured in air. There are two exceptions to this where, because of the wavelength calibration method described in Sect. 3.3, leaving ϵ untied yielded better results, and these are indicated in column 3 of Table D. In addition, while allowing the BLR radii derived from each line to be free, we tie the shape of their radial profiles using the β and F parameters. All other parameters are tied except $f_{\rm peak}$, which we set to be free for all lines.

It should be noted that since we fit only the spectrum, $R_{\rm BLR}$ and $M_{\rm BH}$ are fully degenerate because the circular velocities $v_{\rm circ}$ of the clouds depend on the ratio of $M_{\rm BH}$ and $R_{\rm BLR}$. Hence, one of them must be fixed during fitting. We fix $M_{\rm BH}$ to the values estimated in Sect. 3.4.5.

Finally, for all of our targets, we try two variations of the BLR model, similar to our previous chapter (GRAVITY Collaboration et al., 2024): the full model, which fits all the asymmetry parameters (γ, κ, ξ, $f_{\rm flow}$, $f_{\rm ellip}$, and θ_e), and the circular model, for which these are fixed to 'neutral' values ($\gamma = 1$, $\kappa = 0$, $\xi = 1$, $f_{\rm flow}$, and $f_{\rm ellip} = 1$ so that θ_e and $f_{\rm flow}$ have no impact). Our results indicate that in most cases, the resulting BLR geometry and kinematics (in particular, the best-fit values of i, θ_0, and $R_{\rm BLR}$) are fairly similar for both options. However, some targets are definitely fitted better with the full model due to their asymmetric profiles (see Sect. 3.5.2). These can be identified in Table D by the entries for their asymmetry parameters.

3.5.2 BLR fitting results

In this section, we give an overview of the results from our fits, including the characteristic geometry from the ensemble of best-fit BLR models, and the typical range of values for each fitted parameter. Appendix D provides the details, listing all the values of the best-fit parameters for each target.

It is important to note that due to the fact that we are only fitting the spectra of our targets, it is inevitable that our fitting results will yield large uncertainties especially in their best-fit parameters values including those that describe the overall geometry of the BLR such as β, i, and θ_0. Instead of focusing on each individual best-fit parameter values

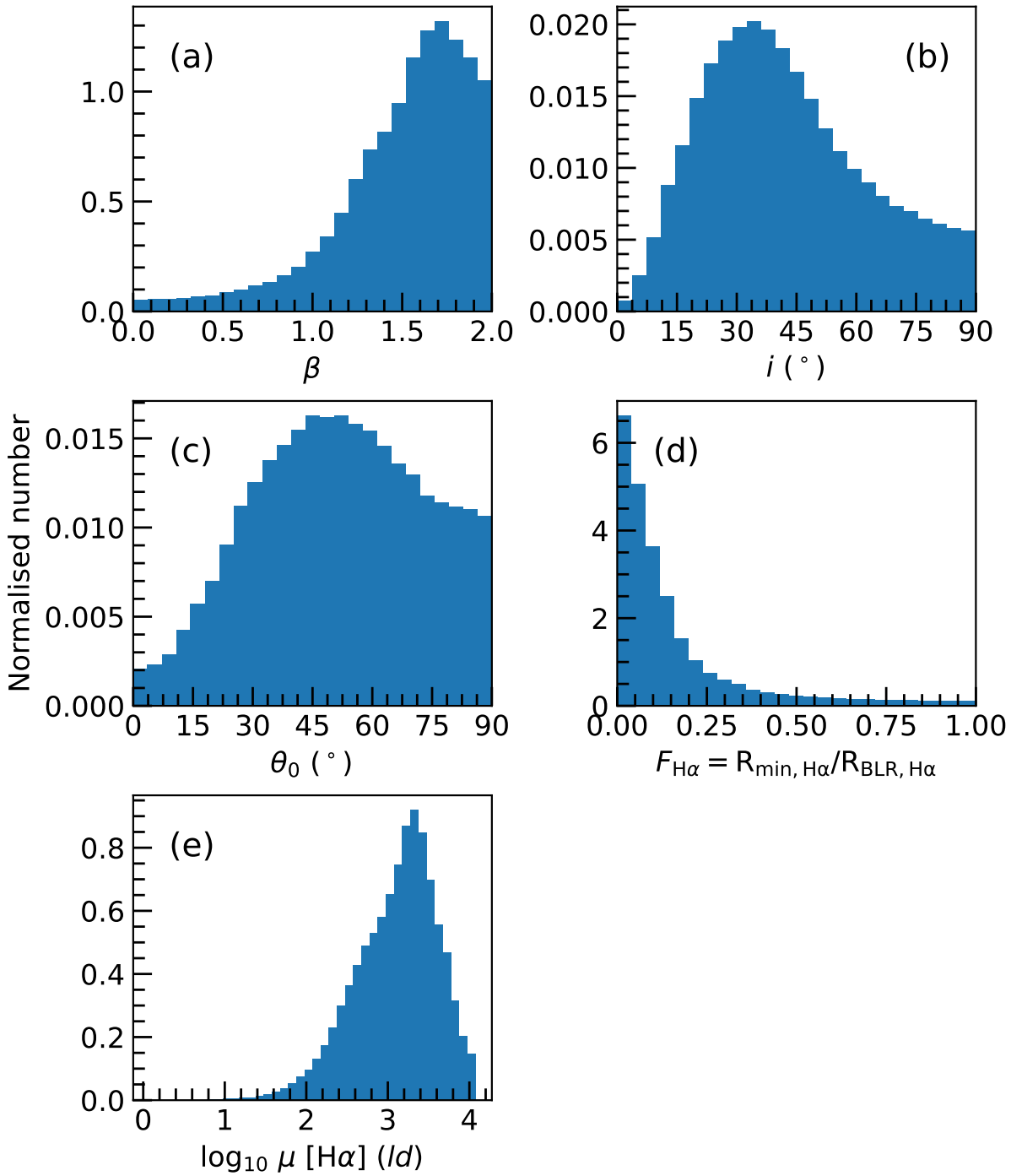

Figure 3.5: Normalised (i.e. independently for each histogram such that the area under the histogram is 1) histograms showing in blue the summed posterior distributions of the BLR parameters from the best fits to all the $z \sim 2$ targets. The panels correspond to (a) the radial distribution of BLR clouds, (b) the inclination angle, (c) the opening angle, with the minimum and maximum values defining the thin disc and spherical shape, respectively, (d) the ratio between the minimum and mean Hα BLR radius, and (e) the mean (emissivity) Hα BLR radius.

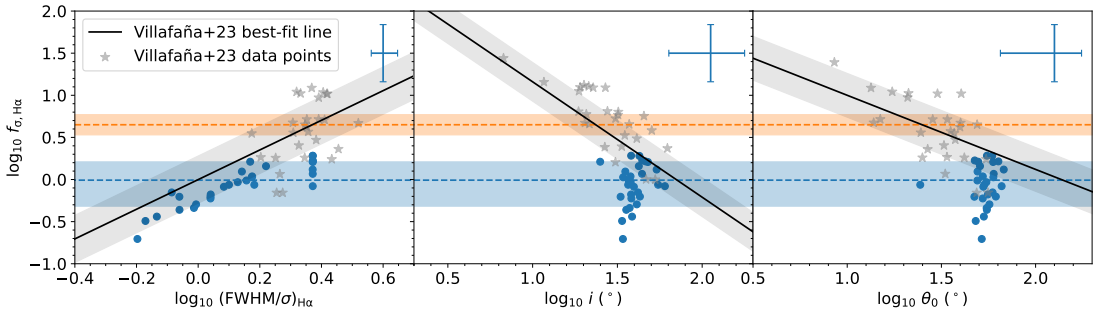

Figure 3.6: Virial factor f_σ derived from the `DyBEL` BLR fitting using σ-derived SMBH masses, as a function of the Hα line shape (left panel), the inclination angle in degrees (middle panel), and the opening angle in degrees (right panel). The average 1σ uncertainties are shown on the upper right of each panel. The orange dashed horizontal line and its 1σ range refer to $f = 4.47$, the virial factor in the scaling relations of Woo et al. (2015) from which we derived the SMBH masses to use as input to the fitting procedure. The blue dashed horizontal line and its 1σ range refer to the average Hα virial factor from our modelling: $\langle f_{\sigma,\ \mathrm{H}\alpha} \rangle = 1.44$. For comparison, we plot the data points from Villafaña et al. (2023) together with a black solid line and a grey region denoting the best-fit relation and its intrinsic scatter.

of our targets, we focus on the summed posterior distribution of the best-fit parameters to shed light on the overall behaviour of our fitting results. Therefore, we caution that the individual best-fit values should not be over-interpreted.

Fig. 3.5 shows the population distributions for several key BLR parameters (β, i, θ_0, $F_{\mathrm{H}\alpha}$, and μ). Their ranges reflect both the distribution and uncertainty of the individual best-fit values. The distribution for β suggests that our targets are typically fitted with a heavy-tailed ($\beta > 1$) radial distribution of BLR clouds with a significant number of line-emitting clouds at larger radii. The inclination peaking at $i < 45°$ indicates that the BLRs are, as expected, generally viewed closer to face-on than edge-on. And the opening angle $\theta_0 \sim 50°$ suggests that they tend to have fairly thick discs. The typical Hα BLR radius spans a range from a few hundred to a few thousand light days, which encompasses the radius reported for the $z = 2.3$ QSO that was derived from modelling GRAVITY data (Abuter et al., 2024). This also reflects the two orders of magnitude range of SMBH mass estimates of our targets as shown in Sect. 3.4.5.

3.5.3 Virial factor and its dependence on the line shape and BLR parameters

The virial factor, which is calculated as $f = GM_{\mathrm{BH}}/(R_{\mathrm{BLR}}v^2)$, does not depend on the assumed M_{BH} value because the M_{BH} the R_{BLR} are degenerate (i.e. scaling together without changing the line profile) and R_{BLR} is set as a free parameter in our BLR fitting (Kuhn et al., 2024). Hence, our fits can produce meaningful virial factors for our targets. We note that the choice of using either the circular or full BLR model does not affect the resulting virial factor. In this Section, we discuss the dependency of the virial factor on various

parameters. One focus is on whether one puts $v = \sigma$ or $v = FWHM$. Another is on i and θ_0, which have been shown to greatly affect the observed line profiles (e.g., Stock, 2018; Raimundo et al., 2019) In addition, Villafaña et al. (2023) investigated correlations of the virial factor with various parameters – including those above – based on 28 low redshift AGNs and dynamical modelling with the same BLR model as Pancoast et al. (2014a). Using the Hβ line, they measured the virial factor for both σ and FWHM, as well as for mean and rms spectra. Most of their observed correlations have marginal significance (2-3σ). For our analysis, we use the $H\alpha$ line and the BLR size derived from it because of the higher S/N of the $H\alpha$ emission line in our data.

To shed light on this matter, we first calculated f_σ using the dispersion of the Hα line profile. Fig. 3.6 shows the distribution of f_σ as a function of Hα line shape (FWHM/σ), inclination angle i, and opening angle θ_0. We overplot the best-fit lines and data points from Villafaña et al. (2023) to compare our results with their work, noting that they used the Hβ line measured in low redshift AGN. There are several takeaway points we can deduce from Fig. 3.6: (1) On the leftmost panel, while our virial factors seem to increase with FWHM/σ, this is not a significant trend ($p \sim 0.18$). This matches what Villafaña et al. (2023) found, and that their steeper trend was not significant when using the mean spectrum, although there was marginal significance for the rms spectrum. For this comparison, it is important to keep in mind that our sample extends to lower values of line shape to $\log_{10}(FWHM/\sigma)_{\mathrm{H}\alpha} \sim -0.3$. (2) Our sample also probes larger values of i and θ_0, as seen in the middle and right panels of the figure. While our data do not show any significant correlation with these parameters ($p > 0.40$), they are consistent with the trends of decreasing f_σ with increasing i and θ_0 reported by Villafaña et al. (2023). (3) The quantities in Fig. 3.6 have relatively large errors because, in most cases, we fit only a single line profile. As such, it is to be expected that the fitted parameters and their derived quantities will be more uncertain compared to cases where multiple lines are fit (Kuhn et al., 2024). (4) The average virial factor $f_\sigma = 1.44$ we derived (shown as the blue horizontal dashed line in Fig. 3.6) is lower than the virial factor $f_\sigma = 4.47$ from Woo et al. (2015) associated with the calculation of the single-epoch SMBH masses that we use as input to our fits. Collin et al. (2006) pointed out that the virial factor differs for different line shapes. For the mean Hβ spectrum, they found $f = 1.5$ for sources with FWHM/$\sigma \lesssim 1.4$. In contrast, Woo et al. (2015) found FWHM/$\sigma \sim 2$ for the $H\alpha$ lines in their sample, close to what is expected for a Gaussian profile, and their resulting f_σ is correspondingly higher and very different to f_{FWHM}. We surmise that the low virial factors we found are due to the highly non-Gaussian shape of the Hα lines with their prominent extended wings. We conclude that the line profile shape is an important parameter in this context. If FWHM/σ of a target AGN is very different from that of the objects used to define a scaling relation, the inferred SMBH mass may be biassed, as lower virial factors due to highly non-Gaussian line shapes will give lower single-epoch BH masses. As such, further investigation of these targets is imperative. Future observations with GRAVITY+ will provide us with an independent and direct measure of the SMBH masses and enable us to assess the error caused by the line shape effects, as well as to create scaling relations specifically for objects where the broad line profile has strong non-Gaussian wings.

3.5.4 Targets fitted with the full model

Most of our targets (27/29) are well-fitted with the simpler, circular model, indicating that the data currently available – the line profiles, in particular, their peaks and wings – are fully consistent with a BLR dominated by Keplerian motion. This includes some sources with slightly asymmetric profiles, in particular where the wings are offset with respect to the core because the spectra have large enough flux uncertainties that the circular model is still a sufficiently good fit. However, the asymmetric shape of the line profiles for two of the targets cannot be fitted well with the circular model, partly due to the higher S/N in their spectra. Instead, for these targets, we use the more complex, full model, which allows anisotropic emission as well as radial motions. Fig. 3.7 shows the spectra and the fitted model profile for these two targets, ID#1 and ID#5 (SDSS J121843.39+153617.2 and Q 0226-1024 respectively). In the former case, we have removed the small bump that we concluded in Sect. 3.4.2 was likely due to [NII]λ6584. This still leaves a broad excess on the long wavelength side of the line profile. If we interpret the small bump as part of the Hα line, this only strengthens the results below because it increases the asymmetry. In ID#5, although the asymmetry is less obvious, the long wavelength wing is significantly stronger and more extended than the short wavelength wing.

In order to assess whether there is a common cause underlying the asymmetric profiles in these objects, we compare their fitted parameters aided by the face-on and edge-on representations of their BLR models in Figs. 3.8 and 3.9. Of the asymmetry parameters, only the midplane transparency is similar for ID#1 and ID#5: $\xi \sim 0.5$. This suggests that there is only moderate opacity in the midplane of both their BLRs. While there is little anisotropy in the emission for ID#5 ($\kappa = -0.01$), for ID#1 there is a preference for emission from the far side of the BLR ($\kappa = -0.39$). This overcomes the effect of the midplane opacity as can be seen in the edge-on projection of the BLR model in Fig. 3.8, where the size of the points, which represent clouds, indicates their relative observed flux: although there are slightly fewer points on the far side of the midplane due to its modest opacity, these blue-shifted points are larger than the red-shifted points, hence the former are brighter than the latter.

In terms of the geometry of the BLR, the angular distribution of the clouds for ID#1 is more concentrated towards the edges ($\gamma = 3.9$) than that of ID#5 ($\gamma = 2.7$). In addition, the model for ID#1 is dominated by radially moving clouds ($f_{\rm ellip} = 0.17$) while that for ID#5 is more evenly shared between circular and elliptical/radial orbits ($f_{\rm ellip} = 0.41$). Nevertheless, in both cases the radial motion is inwards ($f_{\rm flow} < 0.5$). Lastly, $\theta_e \sim 20$ and ~ 36 for ID#1 and ID#5 respectively, suggesting that the elliptical orbits of the former are more elongated and so have higher radial velocities, but in neither case do these reach the maximum velocity allowed by the model.

In conclusion, for ID#1 we purport that the shape of the profile is due to a combination of projection effects resulting from i and θ_0 combined with the effects induced by the asymmetry parameters. First, since i is greater than θ_0 (54.6° versus 25.1°), the observed line profile is double-peaked due to the observed biconical structure of the BLR (Stock, 2018). The inflowing motion means that clouds on the far side are blueshifted, which

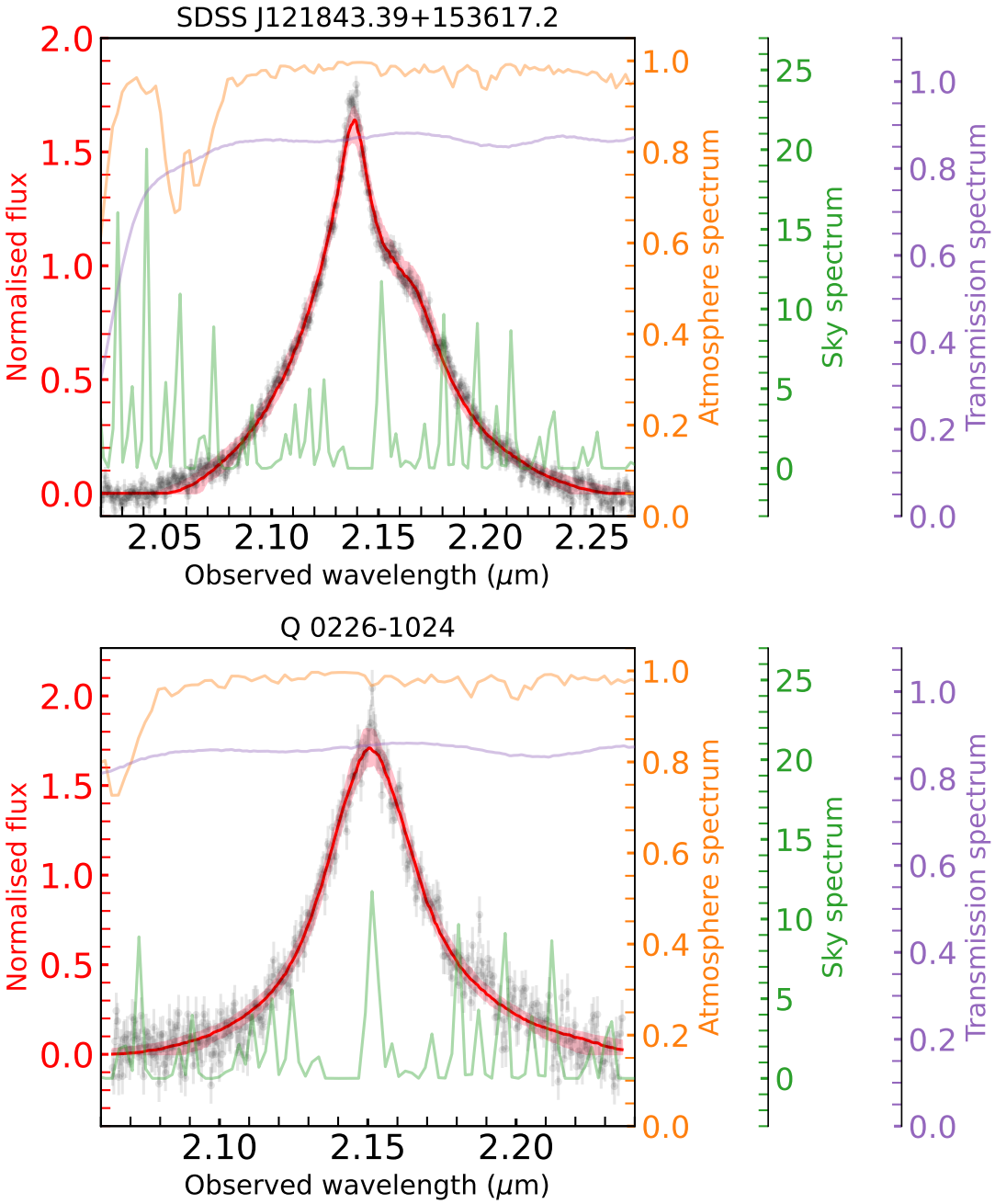

Figure 3.7: Data (black points) and model (solid red line) Hα spectra derived from the best-fit BLR model of two SOFI $z \sim 2$ targets fitted with the full model. The red-shaded regions show the 1σ error of the model spectra. The name of the target is shown on top of each panel. (a) Even after removing the bump on the right side of the Hα emission line, which we believe to be [NII]λ6584, SDSS J121843.39+153617.2 still shows an asymmetric Hα line profile which cannot be fitted with the circular model. (b) The Hα emission line of Q 0226-1024 shows an asymmetry in its wings which is better fitted with the full model. We also present the theoretical OH (sky) spectrum, the theoretical atmospheric profile, and the filter transmission profile of SOFI K_s band in orange, green, and purple lines, respectively. The sky and atmospheric profiles are normalised such that the maximum value is 1, and scaled by a factor of 2. We found that the observed asymmetries of both targets are within the high transmission regions of the SOFI K_s filter where no strong sky lines or atmospheric features are present.

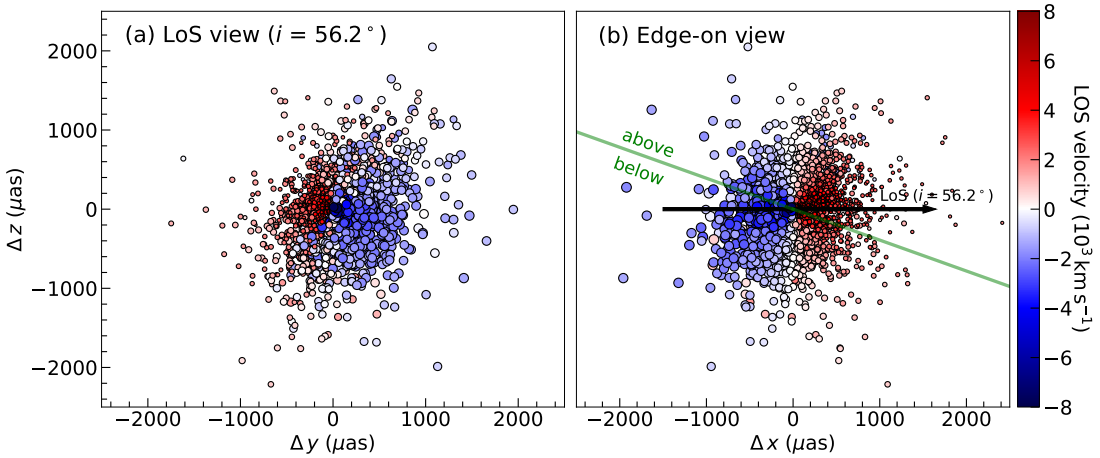

Figure 3.8: The cloud distribution of the best-fit BLR model of ID#1 (SDSS J121843.39+153617.2) shown in two different views: (a) line-of-sight (LoS) or face-on view at the best-fit inclination angle $i = 54.6°$ and (b) edge-on view. The PA of the BLR model to generate the cloud distribution is set so that the BLR is perpendicular to the UT4-UT1 baseline to achieve the maximum possible expected differential phase signal on the baseline. The BLR centre is positioned at the origin. The colour of each cloud refers to the LoS velocity, while the size of each cloud refers to the weight of each cloud on the total emission: the larger the size, the greater its contribution to the broad line emission. The green line on the edge-on view depicts the midplane of the BLR, while the black arrow depicts the LoS of the observer (i.e. the observer is on the $+\Delta$x direction). The LoS is tilted by i which is measured from the line perpendicular to the midplane. Since $i > \theta_0$, the observed flux spectrum is double-peaked. The number of clouds above and below the midplane are the same due to the small midplane opacity. However, the blueshifted clouds have a larger size than the redshifted clouds, indicating the preference of the BLR emission to originate from the far side of the BLR. This explains the relatively strong blueshifted peak of the flux spectrum compared to the redshifted bump.

clouds on the near side are redshifted. In addition, since κ indicates a preference for the emission to originate from the far side of the BLR, the emission tracing the blueshifted part of the line profile is stronger than the redshifted side, leading to the two peaks having different strengths.

Compared to this, ID#5 exhibits less asymmetry in its Hα profile. The edge-on view of its BLR in Fig. 3.9 clearly shows that the blueshifted clouds are fewer in number than the redshifted clouds due to the moderate asymmetry affecting the former more than the latter. This results in an enhancement in the redshifted wing of the Hα emission line of ID#5.

3.6 Differential phase estimation

One of the main goals of this work is to estimate the strength of the differential phase signals of our $z \sim 2$ AGNs to assess their observability with GRAVITY+. The differential phase is

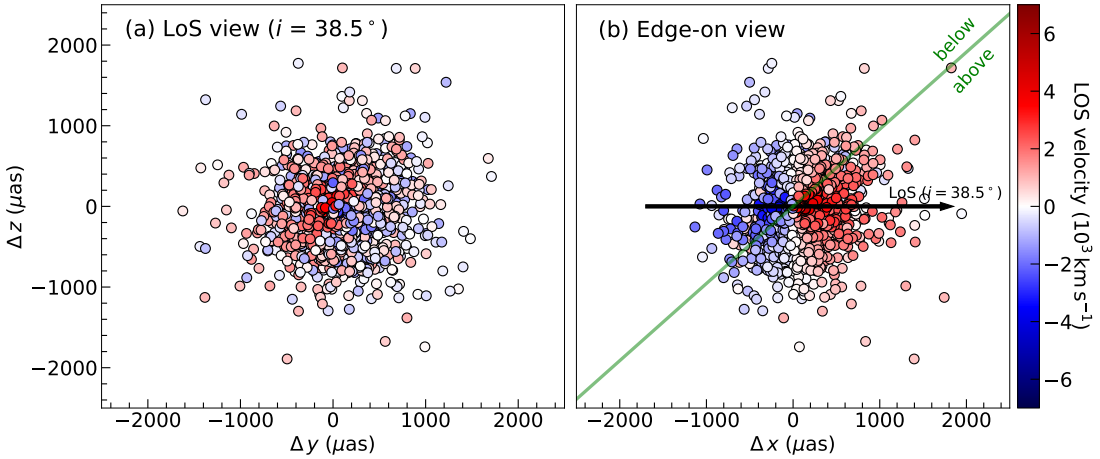

Figure 3.9: Similar to Fig. 3.8 but for the cloud distribution of the best-fit BLR model of ID#5 (Q 0226-1024). The BLR clouds have almost equal sizes, pertaining to the lack of preference of the BLR emission to originate from either side. However, the moderate opacity on the midplane affects the blueshifted clouds more than the redshifted clouds, as indicated by the slightly lower number of blueshifted clouds compared to the redshifted clouds. This causes the redshifted wing of the Hα emission line to be slightly higher than the blueshifted wing.

one of the most important observables in interferometric observations of AGNs (GRAVITY Collaboration et al., 2018, 2020a, 2024). In our context, it is a spatially resolved kinematic signature; specifically, a measure of the astrometric shift of the photocentre of the BLR line emission with respect to that of the continuum as a function of wavelength. More details about the differential phase are presented in GRAVITY Collaboration et al. (2020a). A symmetric rotating BLR is expected to show an S-shape differential phase profile, which has been shown to be the case for several GRAVITY-observed AGNs (GRAVITY Collaboration et al., 2018, 2020a, 2023). However, some AGNs exhibit asymmetric differential phase profiles, which are explained in terms of asymmetry in the BLR, often combined with outflow motions in the BLR (GRAVITY Collaboration et al., 2024).

We derive the expected differential phase of our targets for Hα since this is the only line observable in the K band (at $z \sim 2$) where GRAVITY operates. We use the normalised line profile from the best-fit BLR model while adopting the same flux uncertainties as the data, and calculate the differential phase as a function of wavelength across the whole K band. We use the same equation for the differential phase as Eqn. 2.1. We calculate the 1σ uncertainty of the peak expected differential phase by randomly drawing values of relevant model parameters from the sampled posterior parameter space created during BLR model fitting. This is done 100 times to produce a distribution where the 16th, 50th, and 84th percentile of the peak expected differential phase is calculated.

The position angle PA (measured east of north) rotates the BLR within the sky plane and greatly influences the orientation of the differential phase signal. In order to make a comparative analysis between our targets, we are only interested in the highest possible peak differential phase for each. As such, we focus on the differential phase for the longest

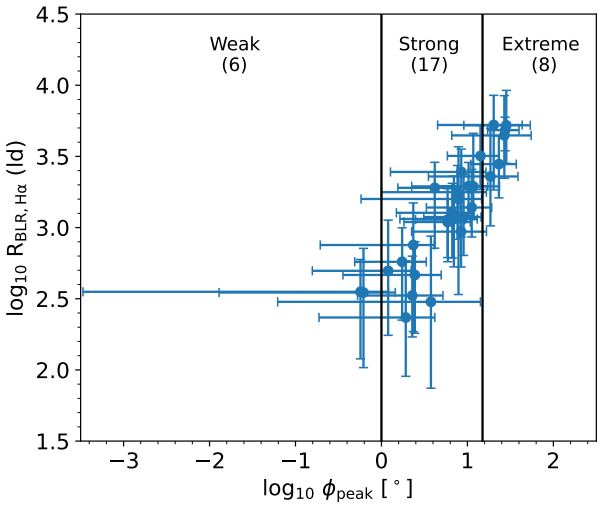

Figure 3.10: Hα BLR size as a function of the peak expected differential phase in logarithm. The error bars correspond to their 1σ errors. The solid vertical lines pertain to the divisions categorising the targets into weak, strong, and extreme targets (see discussion in Sect. 3.6.1). The number of targets for each category is shown in parentheses.

baseline, UT4-UT1, for which it is expected to be strongest. We therefore assume that the *uv* direction of the longest baseline of GRAVITY is parallel to the PA of the BLR model.

3.6.1 Expected differential phase signals and effect of fixed BH mass on the `DyBEL` BLR fitting

Estimating the expected differential phase as described above will provide important guidance in assigning priorities for observations with GRAVITY+, especially for a large sample of AGN. Here, we assessed the effectiveness of such a method for our $z \sim 2$ targets, together with its caveats from the assumptions made during the BLR fitting.

Fig. 3.10 shows the Hα BLR size of our 29 targets as a function of the peak expected differential phase ($\phi_{\rm peak}$) in logarithm. The peak expected differential phase values of all the targets and their 1σ errors are listed in Table D. The targets are divided into three categories: weak ($\phi_{\rm peak} < 1°$), strong ($1° < \phi_{\rm peak} < 15°$), and extreme ($\phi_{\rm peak} > 15°$). The majority of the targets (23/29) have differential phase signals that go as high as $> 1°$. The strong targets (17/29), have signals with strengths between $1° - 15°$, which is of comparable strength to the 1° for the $z = 2.3$ QSO observed with GRAVITY (Abuter et al., 2024). On the other hand, the weak targets (6/29) have signals that are comparable to those of the low redshift type 1 AGNs observed with GRAVITY (GRAVITY Collaboration et al., 2018, 2020a, 2021a). Most of the targets show a symmetric S-shape signal, as expected for a BLR with ordered rotation. This is a direct result of using the circular model for most sources. In contrast, for the two targets that were fitted with the full model, ID#1 and ID#5, we expect an asymmetric differential phase.

The expected differential phase is highly dependent on the assumed (fixed) SMBH mass when fitting the BLR model because the phase signal linearly scales with the BLR size, which is also related to the SMBH mass. However, we expect the SMBH mass not to affect the geometry and the virial factor. Some (6/29) of our targets have very strong differential phase signals ($\geq 15°$). We call these "extreme" targets because the SMBH masses derived from their dispersion σ are much larger than from their FWHM when using the equations from Woo et al. (2015). These targets have FWHM/$\sigma < 1.25$, indicating their line wings to be broad and prominent with respect to their narrow cores. Two of these "extreme" targets, ID#9 and ID#16 (HE 0320-1045 and 2QZ J031527.8-272645 respectively), show very strong narrow cores, with a narrow core to broad wing amplitude ratio > 10, while the other "extreme" targets have ratios in the range 0.1 to 7.0, similar to the non-extreme targets.

Indeed, Kollatschny and Zetzl (2011) argued that FWHM and σ are poor estimators of SMBH mass. They investigated this issue by looking at the turbulent and rotational velocities of several AGNs together with their line shape measurements. Their results suggest that the broadening of the line profiles is due to rotation, and the rotational velocity is a better estimator of SMBH mass than the line dispersion or FWHM. The reason is that AGNs with similar rotation velocities, for which the SMBH mases are the same, may show different values of FWHM/σ. In contrast, the SMBH masses calculated from their FWHM or σ may differ drastically. However, inferring the rotational velocity from the line profile in order to estimate the SMBH mass is outside the scope of this work. An independent and more accurate measurement of the SMBH masses for our targets is crucial to shed light on the size-luminosity relation and the efficacy of the rotation/turbulence interpretation versus the two-component BLR model, underlining the importance of the future GRAVITY+ observations of these targets.

3.7 Conclusions and future prospects

To prepare for the advent of GRAVITY+, we performed NTT/SOFI observations of type-1 AGN candidates in order to predict their expected differential phases and assess their priorities for GRAVITY+ observations. We focus on the 29 $z \sim 2$ targets with prominent Hα emission lines. Among these are 17 for which we have also detected significant Hβ emission, and 2 with Hγ emission. We analyse the line profile shape (FWHM/σ) and fit BLR models using the `DyBEL` code. Our results yield the following conclusions:

1. Most of the Hα line profiles are highly non-Gaussian and so are fitted with two components: one for the narrow core, and another for the broad wings. This is reminiscent of the two-component BLR model, in which the wings represent an inner fast rotating BLR disc, and the lower velocity core represents an outer thicker part of the BLR. An alternative explanation is that the profile results from a convolution of rotation and turbulence, but in which the rotation is most easily seen via its impact in broadening the core of the profile.

2. The average σ-based Hα virial factor of our sample is $f_\sigma \sim 1.44$, which we attribute to the non-Gaussian shape of the emission lines. In contrast, we would expect to recover $f_\sigma = 4.47$ (as used to derive the single-epoch SMBH masses) if our sample were to exhibit more Gaussian-like line profiles.

3. Our sample probes higher inclination i and higher disc thickness θ_0 than those reported by Villafaña et al. (2023), and the values we found are consistent with anti-correlations between these parameters and the virial factor reported by those authors.

4. The line profiles of all except two of the targets, are well fitted with a circular simplification of the BLR model. The two targets that require the full model show asymmetry in their Hα line profiles, and our results suggest tentative evidence for radially dominated motions in these targets, with midplane obscuration and anisotropic emission contributing to the asymmetry in the observed line profiles.

5. The expected differential phase signal is an essential tool for assessing the future observing priorities of our targets with GRAVITY+. Among the 29 targets, 23 have strong signals, with six possessing expected differential phases $> 15°$. These "extreme" targets have very low FWHM/σ, highlighting concerns about applying scaling relations without accounting for differing line profiles because of the impact this has on the inferred SMBH mass. GRAVITY+ observations of these targets will provide an independent dynamical measurement of the SMBH in our targets and will not only further our understanding of varying BLR geometries at different epochs and luminosities but will provide a new baseline for future scaling relations.

Chapter 4

Mock GRAVITY Observations of a Radiative Hydrodynamic BLR Simulation

This chapter is based on an upcoming paper: Santos et al. (2025b), to be submitted to A&A.

4.1 Introduction

We now look into the second extension of our work on studying the physics of the BLR, which is the *improvement of the Pancoast model*. This work aims to investigate potential improvements in the Pancoast model, particularly in its treatment of inflows/outflows and the lack of photoionisation physics in the model. We first briefly discuss the different BLR formation models put forward by previous works. All AGN models agree on the notion that surrounding the central BH is an accretion disk. This accretion disk is then surrounded by the BLR, which is responsible for the broad emission lines detected in its spectra (e.g., Czerny and Hryniewicz, 2011; Peterson, 2006). Its origin is still under debate. Several models have been put forward to explain the origin of the BLR. The main categories of BLR models are as follows:

1. Inflow models (Hu et al., 2008; Wang et al., 2017) - Material from the (inner region of the) torus inflows towards the dust sublimation radius due to loss of momentum via collisions, causing dust to dissipate and some gas to be bound at smaller radii and creating the BLR, while some gas will be ejected as an outflow.

2. Disk instability models (Collin and Zahn, 1999, 2008; Wang et al., 2011, 2012) - The very inner (within a few parsecs) regions of the accretion disc are gravitationally unstable, which tend to collapse to form stars, eventually leading to supernova explosions. Surrounding molecular clouds will be heated by these explosions, forming

hot gas which will escape the disc before being cooled, eventually diffusing to form the BLR.

3. Disc wind/outflow models - Certain mechanisms are used to explain the production of winds in the accretion disc, which eject material (gas and/or dust) from the disc. The ejected material eventually cools down/is dominated by gravitational force, and settles at larger radii from the central region to form the BLR.

    3.1. Magnetically-driven winds (Blandford and Payne, 1982b; Emmering et al., 1992; Bottorff and Ferland, 2000; Chajet and Hall, 2013, 2017) - The magnetic field due to the rotation of the accretion disc causes centrifugally driven outflows to occur.

    3.2. Thermally-driven winds (Begelman et al., 1983; Czerny and King, 1989; Witt et al., 1997; Blandford and Begelman, 1999; Mizumoto et al., 2019) - X-rays produced in the inner part of the accretion disc due to the release of gravitational energy via accretion cause Compton-heated winds to occur. These winds eventually cool via inverse Compton scattering on regions farther from the disc, producing BLR clouds.

    3.3. Radiatively-driven winds - The radiation from the accretion disc serves as the main cause of winds that eventually produce BLR clouds. The winds could be line-driven, i.e. atoms with bound electrons absorbing and scattering photons while creating a net outward motion to the atoms (Murray et al., 1995; Risaliti and Elvis, 2010; Matthews et al., 2020); or dust-driven, i.e. dust clumps being pushed back via radiation pressure of the emitting source (Czerny and Hryniewicz, 2011; Czerny et al., 2015; Galianni and Horne, 2013; Baskin and Laor, 2018).

Radiatively dust-driven models are the newest BLR formation models in explaining the inflow and outflow signatures from broad emission lines (Naddaf et al., 2021). Several other phenomena can be described by these models, such as the stratified BLR structure as purported by different time lags from different emission lines (Matthews et al., 2020), and unification models of AGNs where geometry and orientation play key roles (Higginbottom et al., 2011). These models have shown consistency with (velocity-resolved) RM data (Chiang and Murray, 1996) and even photoionisation models (Ferland et al., 2020). We focus our discussion on the radiatively-driven fountain simulation (henceforth called *RDF* simulation) by Wada (2011). This simulation emphasises the effect of AGN radiation on parsec scales and not just on the sub-pc scales of the accretion disc as done by other dust-driven models (Czerny and Hryniewicz, 2011; Czerny et al., 2015, 2017). The RDF simulation can explain the formation of the dusty torus and integrate it with the BLR into one dynamic structure. This allows the RDF simulation to explain obscuration and emission line regions as a result of the fountain mechanism (Wada, 2011, 2015).

With this in mind, we focus on understanding how well the Pancoast model can recover the BLR properties of a BLR created by the RDF simulation. As discussed in the previous

chapters, the Pancoast model assumes that the BLR is composed of discrete clouds that do not interact with each other and are only influenced by the gravitational potential of the central BH. Its viability in modelling the observed broad emission lines of AGNs has been shown by many RM works (e.g., Pancoast et al., 2014b; Bentz et al., 2023). However, previous works, including Pancoast et al. (2014b), have highlighted potential points for improvement in the model. For instance, the current model cannot include polar flows as potential inflows/outflows, as the model assumes that such radial flows are on the BLR plane. Due to recent GRAVITY(+) observations of low-redshift and high-redshift AGNs, which show evidence of inflow/outflow-dominated BLRs (GRAVITY Collaboration et al., 2024, 2025), the need for a more physically-driven treatment of radial motions is becoming more urgent. Another area of improvement in the model is that it does not consider any photoionisation physics due to its focus on modelling the kinematic and light distribution of the BLR. Instead, the model assumes that the BLR is composed of non-interacting clouds (more accurately described as a "line emitting entity"; Kuhn et al. 2024) and allows fitting of the line emission distribution of the BLR. Due to its simplified representation of the BLR as a collection of point sources, it cannot take into account certain factors, such as radiation pressure exerted by the accretion disk, dependence of the ionising flux from the continuum source with radius, covering factors, and emissivities of gas in the BLR, all of which could be circumvented with the introduction of photoionisation physics in the model (Raimundo et al., 2020).

Sect. 4.2 presents the background of the RDF simulation investigated in this work, while Sect. 4.3 describes the mock GRAVITY observations of the RDF simulation based on NGC 3783, a low-redshift ($z = 0.0097$) AGN whose BLR has already been spatially resolved with GRAVITY (GRAVITY Collaboration et al., 2021a). Sect. 4.4 presents the results of the Pancoast model fitting after generating the expected flux and phase spectra of the RDF simulation. Sect. 4.5 briefly presents the comparison of this work with previous studies. Finally, Sect. 4.6 shows the conclusions and prospects of this work.

4.2 Simulation

We explore the Pancoast model's capability to recover the RDF simulation's intrinsic properties. We refer the readers to Sect. 2.5 for the description of the Pancoast model. We use the snapshot data from an axisymmetric radiation-hydrodynamic simulation (the RDF simulation), generated by our collaborator, Keiichi Wada (henceforth called *KW*), in a quasi-steady state. While the hydrodynamical simulations are done and published separately (Wada et al., 2023; Kudoh et al., 2023), they are also updated and revised to match NGC 3783 as part of a collaboration. KW used these data to calculate the expected flux spectrum via radiative transfer, which we use afterwards to calculate the expected differential phase via photocentre calculations. In this section, we focus our discussion on the RDF simulation, including the basic equations needed to generate the model and the numerical methods required to solve them.

Description

The RDF simulation was initially conceptualised to explain the formation of the obscuring tori around AGNs (Wada, 2011). It combines the high-resolution numerical simulation of the interstellar medium (ISM) within the central region of the galaxy (Wada et al., 2009) with radiative heating and pressure due to direct radiation from the central ionising source. In this model, the accretion disc is considered a point source and is the main source of the radiation field. The quasi-steady initial condition without radiative feedback is first generated by creating an axisymmetric, dynamically settled, and rotationally supported thin disc model with a uniform density profile. After creating the disc, the radiative feedback is turned on. The radiation pressure on the dusty gas and the X-ray heating of cold, warm, and hot ionising gas are considered. Three-dimensional hydrodynamic equations are solved by an Eulerian hydrodynamic code to solve the dynamics of a disc composed of gas and dust accreting to a central BH under the effect of an anisotropic central radiation field. Following Wada (2015), outflows in the form of flowing material dominated by infrared radiation in a parsec-scale torus are expected as a result of AGN feedback (Dorodnitsyn et al., 2012). Aside from radiation pressure, the RDF simulation also accounts for the self-gravity of the gas, radiative cooling, uniform ultraviolet (UV) radiation for photoelectric heating, H_2 formation and destruction, but not supernova feedback. In the RDF simulation used in this work, the assumed black hole mass and Eddington ratio are based on NGC 3783, one of the low-redshift AGNs observed by GRAVITY Collaboration et al. (2021a). The assumed BH mass of the system is $10^{7.4}$ $M_\odot$ (GRAVITY Collaboration et al., 2021b) and the 5100 Å continuum luminosity of NGC 3783 is log $\lambda L_{5100\text{Å}} = 42.93$ erg s^{-1}(Bentz et al., 2013).

4.2.1 Basic equations

The three equations to be solved are the continuity equation, Navier-Stokes equation, and energy equation, which correspond to mass conservation, momentum conservation, and energy conservation, respectively:

$$\frac{\partial \rho}{\partial t} + \nabla \cdot (\rho \vec{v}) = 0 \tag{4.1}$$

$$\frac{\partial \rho \vec{v}}{\partial t} + \nabla \cdot \left[\rho \vec{v}\vec{v} + P_g \vec{I}\right] = \vec{f}_{\text{rad}} + \vec{f}_{\text{grav}} + \vec{f}_{\text{vis}} \tag{4.2}$$

$$\frac{\partial e}{\partial t} + \nabla \cdot [(e + P_g)\vec{v}] = -\rho \mathcal{L} + \vec{v} \cdot \vec{f}_{\text{rad}} + \vec{v} \cdot \vec{f}_{\text{grav}} + W_{\text{vis}} \tag{4.3}$$

In the equations above, ρ is the total density of gas and dust assuming a dust-to-gas mass ratio of 0.01, $\vec{v}$ is the velocity, P_g is the gas pressure, $\vec{I}$ is the identity tensor, $\vec{f}_{\text{rad}} \equiv \int \nabla \cdot F_v \hat{e_r} dv$ is the radiation force where F_v is the radiation flux, $\vec{f}_{\text{grav}} \equiv -\rho G M_{\text{BH}} \hat{e_r}/r^2$ is the gravitational force where G is the gravitational constant, $r = \sqrt{R^2 + z^2}$ is the distance of a point from the centre of the BH where R is the horizontal distance of the point from the central BH and z is the height of the point from the disc plane, $\mathcal{L}$ is the net heating/cooling

rate per unit mass, and $e = P_g/(\gamma - 1) + \rho v^2/2$ is the total energy density where $\gamma = 5/3$ is the specific heat ratio for adiabatic processes. To account for viscosity, the viscosity parameter α is assumed to be dependent on the presence of gas supply around the disc midplane following a thin disc geometry:

$$\alpha = \begin{cases} 0.1 & n > 10^3 \text{ cm}^{-3} \text{and } T_\text{g} < 10^3 \text{ K} \\ 0 & \text{otherwise} \end{cases} \tag{4.4}$$

where n and T_g are the gas density and temperature, respectively. The viscosity velocity is therefore calculated as $v_\text{vis} = \alpha c_s^2/\Omega_K$ where c_s is the speed of sound and Ω_K is the Keplerian angular speed (Shakura and Sunyaev, 1973). The viscous force $\vec{f}_\text{vis}$ and viscous heating W_vis are then calculated using the prescription from Ohsuga et al. (2005):

$$\vec{f}_\text{vis} \equiv \frac{\hat{e}}{R^2}\frac{\partial}{\partial R}\left[R^2 \alpha P_g \frac{R^2}{v_\phi}\frac{\partial}{\partial R}\left(\frac{v_\phi}{R}\right)\right] \tag{4.5}$$

$$W_\text{vis} \equiv \alpha P_g \frac{R}{v_\phi}\left[R\frac{\partial}{\partial R}\left(\frac{v_\phi}{R}\right)\right]^2 \tag{4.6}$$

where $\hat{e}$ is the azimuthal direction unit vector. Heating by UV and X-ray (Maloney et al., 1996; Meijerink and Spaans, 2005; Wada, 2011) and optically thin radiative cooling (Meijerink and Spaans, 2005; Wada et al., 2009) are considered in viscous heating. Following the work of Wada et al. (2023), dust destruction can occur via dust sublimation due to AGN radiation and thermal sputtering due to thermal gas. When the sputtering timescale is shorter than the dynamical timescale, the dusty gas in a particular grid cell is considered dust-free. These timescales are calculated as:

$$t_\text{sp} = 5.5 \text{ yr}\left(\frac{n_\text{g}}{10^3 \text{ cm}^{-3}}\right)\left(\frac{a}{0.01\ \mu\text{m}}\right)\left[\left(\frac{2\times 10^6 \text{ K}}{T_\text{gas}}\right)^{2.5} + 1\right] \tag{4.7}$$

$$t_\text{dyn} \sim 4.7 \text{ yr}\left(\frac{r}{0.01 \text{ pc}}\right)^{1.5}\left(\frac{M_\text{BH}}{10^7\ M_\odot}\right)^{-0.5} \tag{4.8}$$

where Eqn. 4.7 is based on Tsai and Mathews (1995) (see also Draine and Salpeter 1979 and Namekata and Umemura 2016). In Eqn. 4.7, n_g is the density of the grains, a is the radius of the grain, and T_gas is the gas temperature. On the other hand, the dust temperature per cell is calculated assuming a local thermal equilibrium with the incoming radiation flux. Dust sublimation occurs at the dust sublimation temperature $T_\text{sub} = 1500$ K. Fig. 4.1 shows a sample of the RDF simulation used by Kudoh et al. (2023) for visual purposes.

4.2.2 Numerical methods and radiative transfer with `CLOUDY`

To solve the equations above, KW used the public magnetohydrodynamic simulation (MHD) code `CANS+` (Matsumoto et al., 2019) with an additional module to evaluate radiation force and radiative heating/cooling from frequency-dependent radiation sources via

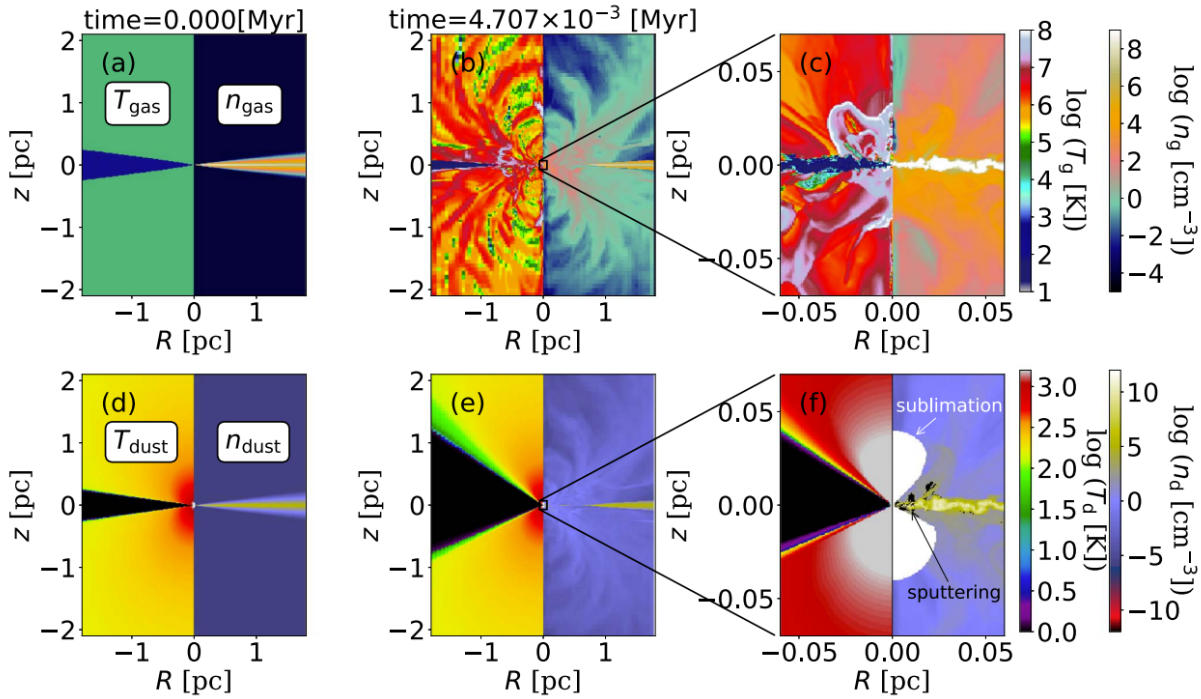

Figure 4.1: Snapshot of the RDF simulation taken from Kudoh et al. (2023). Each panel is divided into two sections, showing the gas's temperature (left side) and density (right side) in the snapshots. The top row shows panels related to gas, and the bottom row shows panels related to dust. The leftmost panels (a and d) show the initial condition of the RDF simulation at $t = 0$ yr. The middle panels (b and e) show the evolution of the RDF simulation at $t = 4.71 \times 10^3$ yr. The rightmost panels (c and f) are the same as the middle panels but zoomed in within ∼0.12 pc of the central region. In the dust number density distribution portion of the panel (f), the regions where dust sublimation and thermal sputtering occurred are denoted by white and black regions, respectively. This RDF simulation from Kudoh et al. (2023) uses a BH mass of $10^{7.5}$ $M_\odot$ and a bolometric luminosity of 10^{44} erg s^{-1}, which is slightly different but close to our assumed values (offset of about 0.1 dex for both the BH mass and bolometric luminosity). Hence, we do not expect drastic changes in the RDF simulation of Kudoh et al. (2023) and this work.

ray tracing. Magnetic fields are ignored in the simulation. In particular, KW focussed on solving the evolution of a dusty gas disc with mass inflow irradiated by a central accretion disc in a computational box of 0.03 × 0.03 × 0.015 pc, about 1/8 of the original computational box from Wada et al. (2023), which yields much higher spatial resolutions than previous RDF simulations (Wada, 2011, 2015; Wada et al., 2023). From the 6000 cells (synonymous with "clouds" in the context of our work, but will be henceforth called "cells" to emphasise their simulated origin) selected within the computational box, only 3815 cells had non-zero flux values and were then used to generate the spectrum of the RDF simulation.

KW used the `CLOUDY` code ver. 23.09 (Ferland et al., 2009; Chatzikos et al., 2023) to generate the flux spectrum of the RDF simulation. `CLOUDY` is a spectral synthesis code that simulates the ISM's radiative processes to predict the gas's physical conditions and its emitted spectrum. The AGN module of `CLOUDY` calls the input SED of the central source, which is based on (Korista et al., 1997) and is given by:

$$F_\nu = \nu^{\alpha_{\rm UV}} \exp(-h\nu/kT_{\rm BB}) \exp(-kT_{\rm IR}/h\nu) \cos i + a\nu^{\alpha_{\rm X}} \exp(-h\nu/E_1) \exp(-E_2/h\nu) \quad (4.9)$$

where $\alpha_{\rm UV}$ = -0.5 is the assumed power-law index of the UV part of the SED, $T_{\rm BB} = 10^5$ K is the assumed temperature of the big blue bump, $\alpha_{\rm X}$ = -0.7 is the assumed soft X-ray spectral slope, a is a constant that gives $\alpha_{\rm OX}$ = -1.4 which is the assumed X-ray to UV flux ratio, $T_{\rm IR}$ is the temperature at the infrared wavelengths so that $kT_{\rm IR} = 0.01$ Ryd (1 Ryd = 13.6 eV), $E_1 = 300$ keV and $E_2 = 0.1$ Ryd which correspond to the energy ranges where the X-ray part of the SED has considerable amount of flux, and i is the angle measured from the rotational axis (z-axis). The AGN SED (Eqn. 4.9) is composed of the UV radiation term (first term) and the X-ray component term (second term), with the former derived from the geometrically thin and optically thick disc and expected to be anisotropic (i.e. proportional to cos i), and the latter expected to be isotropic.

Aside from the form of the AGN SED, KW also assumed that all dust had sublimated in the data used in `CLOUDY`, and the system possesses Solar metallicity. Upon calculating the SED in the innermost cell, the resulting SED was used as an incident SED for the next outward radial cell. This process is iterated up to the outermost cell (i.e. $r \sim 1$ pc). for a given radial ray (Wada et al., 2018). After `CLOUDY` finishes all calculations, the resulting system is observed along the line of sight with viewing angle $i = 30°$ (i.e. a face-on view of the system refers to $i = 0°$). The wavelength resolution corresponds to ~ 200 km s^{-1} at 6000 Å and the generated spectrum has a wavelength range of 1000 to 22000 Å.

A more thorough discussion of the model is presented in Wada et al. (2009), Wada (2011), and Kudoh et al. (2023).

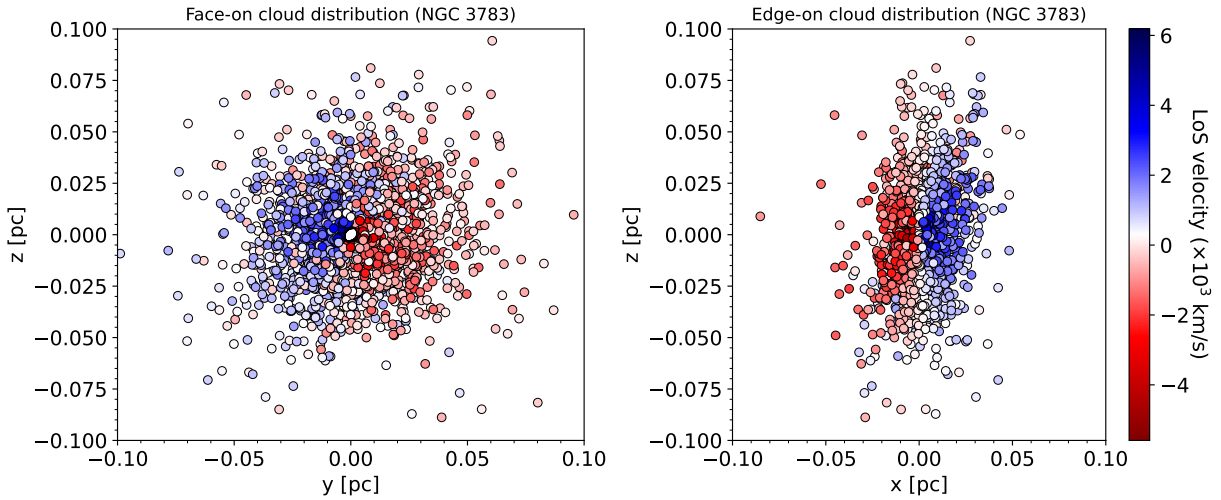

Figure 4.2: The expected cloud distribution of NGC 3783 based on modelling observations with the best-fit Pancoast model (GRAVITY Collaboration et al., 2021a). Different panels pertain to different orientations: (a) face-on and (b) edge-on orientation. The clouds are colour-coded based on their LoS velocities. The LoS is pointing towards the $+\Delta$x direction. The size of the clouds do not pertain to the weight of each cloud on the total emission in contrast to Figs. 2.7 and 3.9.

4.3 Mock GRAVITY observations of the RDF simulation

After generating an RDF simulation based on the BH mass and AGN luminosity of NGC 3783 and its expected flux spectrum with `CLOUDY`, the next step is to generate mock observations of the simulation with GRAVITY. We "observe" the RDF simulation by reorienting it based on the expected on-sky orientation of NGC 3783 as observed by GRAVITY before calculating the simulated differential phase spectra of the simulation.

The snapshot of the RDF simulation provides the position and velocity components in Cartesian coordinates and the absolute flux emission of each grid cell. These data are crucial for calculating the photocentres and the expected differential phase spectrum of the simulation. For our mock observations, we assume similar VLTI baselines to those of GRAVITY Collaboration et al. (2021a). However, we do not bin the baselines in terms of their *uv*-coordinates for simplicity. We note that *uv*-binning does not greatly affect our results.

As discussed in the previous chapters (Sect. 2.3.2 and 3.6), the differential phase is an essential observable in differential interferometry as it measures the astrometric shift of the BLR photocentres with respect to the continuum photocentre as a function of wavelength. To estimate the differential phase spectrum of the RDF simulation, we first reorient the RDF simulation to match the orientation of NGC 3783 as observed by GRAVITY (GRAVITY Collaboration et al., 2021a). We recreated the face-on and edge-on view of the BLR of NGC 3783 based on its best-fit model taken from GRAVITY Collaboration et al. (2021a)

(Fig. 4.2). After getting the BLR cloud distribution fitted to the NGC 3783 observations, we rotate the RDF simulation to match this distribution. This procedure aims to match the simulation with the observed on-sky orientation (of the velocity gradient) of NGC 3783 so that the orientation of the simulated differential phase spectrum also matches that of the observed interferometric signal. To achieve this, we first rotated the RDF simulation along the y-axis by an inclination angle of 30° and then along the x-axis by a position angle (measured East of North; Stock 2018) of 210°, which we find to produce the cell distribution that is closest to the cloud distribution in Fig. 4.2. Fig. 4.3 shows the cell distribution of the RDF simulation before and after re-orientation. There is a slight offset in the angle of the edge-on view of the cell distribution and the cloud distribution, but the direction of velocity gradient of the former after re-orientation matches that of the latter.

After re-orientation, the BLR photocentres are calculated by summing the product of the position coordinate and the absolute flux per velocity bin in each axis, normalised by the flux of each spectral channel. The expected differential phase is then calculated as:

$$\Delta\phi_\lambda = -2\pi \frac{f_\lambda}{1+f_\lambda}(u y_{\mathrm{cent}} + v z_{\mathrm{cent}}) \tag{4.10}$$

The equation above is similar to Eqn. 2.1, but with the dot product of the baseline $\vec{u}$ and the BLR photocentre $x_{\vec{\mathrm{BLR}},\lambda}$ expanded such that $\vec{u} = (u, v)$ and the BLR photocentres are regarded as the photocentres in the y- and z-axes, which correspond to the relative RA and Dec axes (ΔRA and ΔDec) in the astronomical system. Note, however, that the y-axis in the Cartesian system has to be flipped to match the RA axis of the astronomical system to preserve the correct definition of PA. The flux spectrum is taken as the `CLOUDY` Brγ flux spectrum of the RDF simulation convolved and resampled to match the spectral resolution of GRAVITY ($R = 500$).

Fig. 4.4 shows the differential phase and flux spectra of the RDF simulation compared with the differential phase signal derived from the best-fit BLR model of NGC 3783 and the SINFONI flux spectrum of NGC 3783, all taken from GRAVITY Collaboration et al. (2021a). The error bars of the simulated data are taken as the median error of the observed data of NGC 3783. We find that the differential phase signals of the RDF simulation for each baseline have the same scale as the best-fit differential phase signals of NGC 3783, although not exactly matching, especially for UT3-UT1 and UT2-UT1 where the simulation's differential phase is smaller than their observed counterparts. In the GRAVITY observations of NGC 3783 (GRAVITY Collaboration et al., 2021a), the three longest baselines UT4-UT2, UT4-UT1, and UT3-UT1 show the strongest interferometric signals. This is the same for the RDF simulation, except with UT3-UT1 replaced with UT4-UT3, although the signal in the former baseline is only slightly lower than the latter. Nevertheless, the orientation of the "S-shapes" of each signal matches that of the best-fit differential phase signals of NGC 3783. The simulated Brγ spectrum of NGC 3783 based on `CLOUDY` simulations shows a double-peaked line shape. We argue in Sect. 4.3.1 that this is due to the very thin, rotation-dominated disc produced by the simulation, whose opening angle is smaller than the inclination angle of the simulation. This causes the observer to see the biconical structure of the BLR (Stock, 2018). Another possible reason for the double-horned

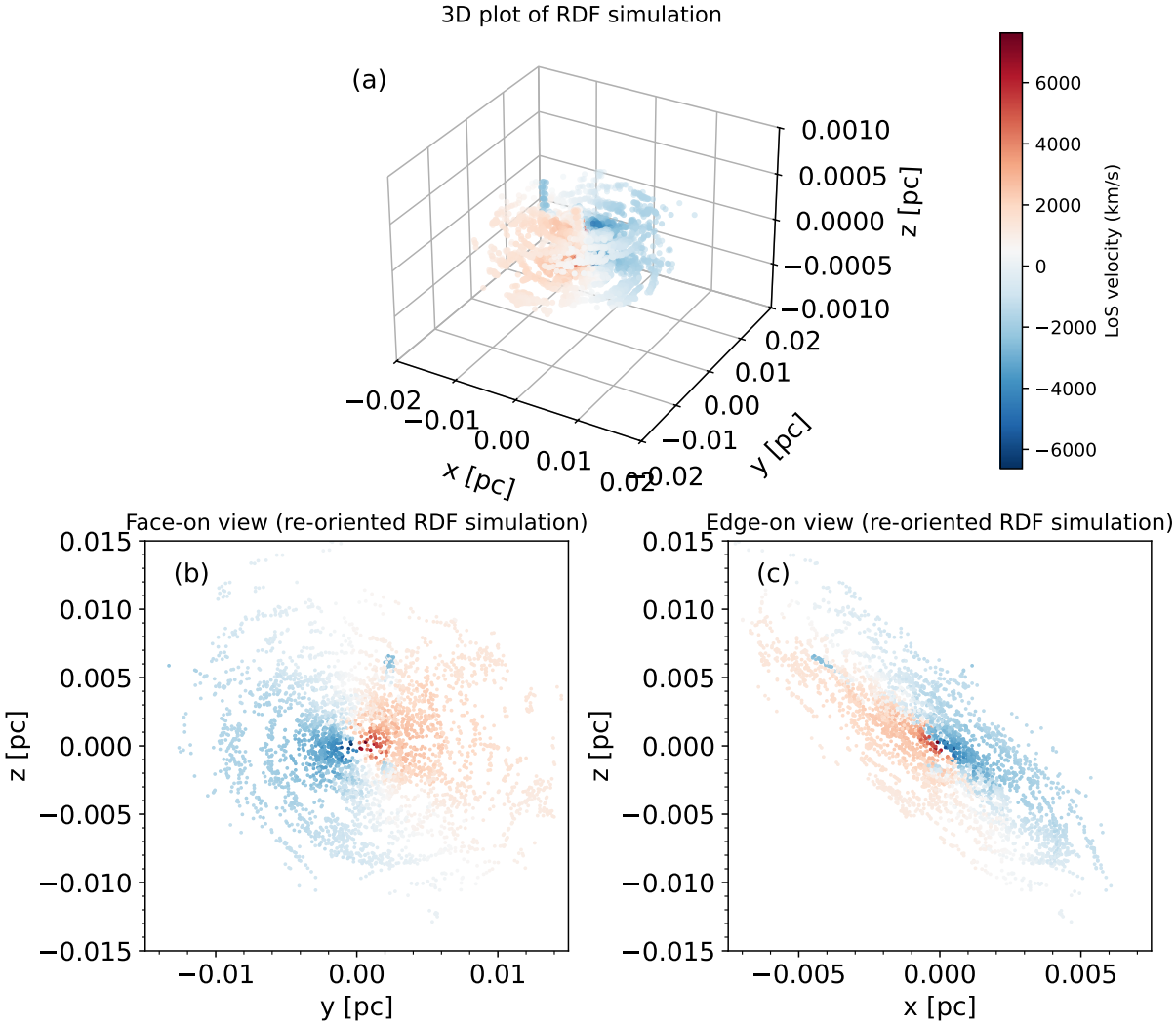

Figure 4.3: The cell distribution of the RDF simulation before (panel a) and after (panels b and c) re-orientation. The RDF simulation before re-orientation is plotted in a 3D Cartesian coordinate system. On the contrary, the RDF simulation after re-orientation ($i = 30°$ and PA $= 210°$) is plotted in 2D to easily facilitate comparison with the BLR cloud distribution fitted to the NGC 3783 observations in Fig. 4.2.

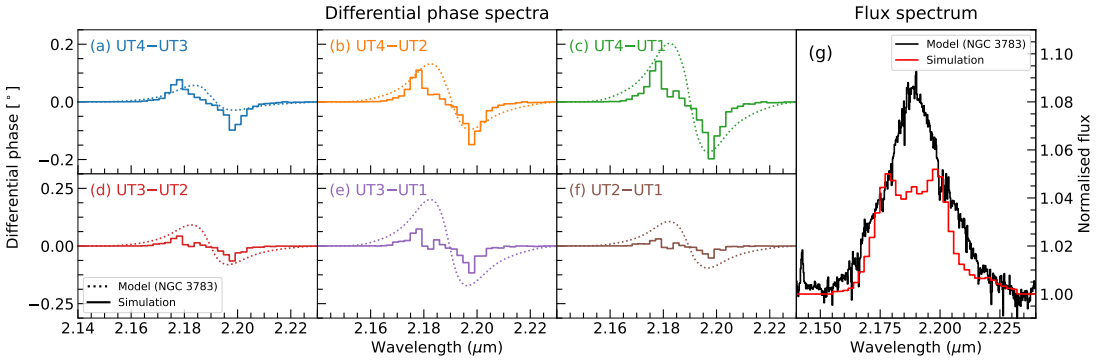

Figure 4.4: The differential phase spectra (panels a-f) of the RDF simulation (dashed lines) for each baseline compared with the best-fit BLR differential phase signals of the best-fit BLR model of NGC 3783 (dotted lines) taken from GRAVITY Collaboration et al. (2021a). The median differential phase errors of the observed data from panels a-f are ±0.21°, ±0.21°, ±0.19°, ±0.24°, ±0.20°, and ±0.19°, respectively, and these are assumed as the errors of the differential phase spectra of the RDF simulation. The Brγ flux spectrum (panel g) of the RDF simulation (red solid line) is also compared with the SINFONI spectrum of NGC 3783 (black solid line). Note the double-peaked shape and lower normalised peak flux of the simulated spectrum compared to the actual flux spectrum of NGC 3783. The median normalised flux error of the SINFONI flux spectrum is 0.0052, which is used to set the flux error of the simulated flux spectrum.

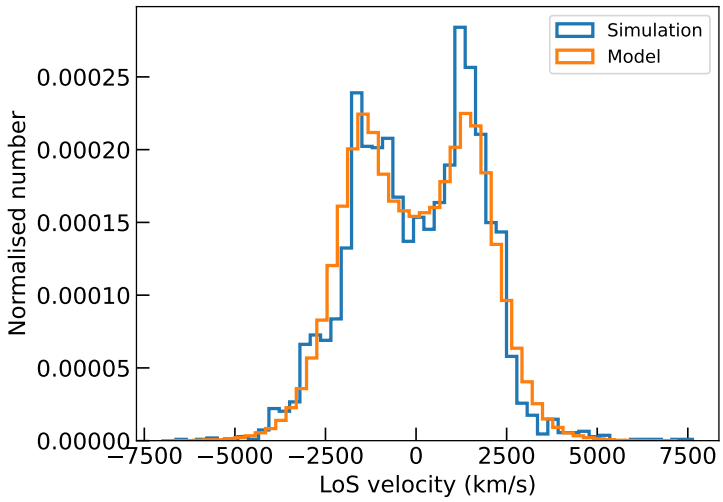

Figure 4.5: Distribution of LoS velocities in the RDF simulation (blue histogram) and best-fit Pancoast model (orange histogram). The LoS velocity of each cell/cloud in the simulation is calculated as the projection of the total velocity in the $+x$-direction, which is the LoS direction. We purport that such an asymmetric distribution of the LoS velocities is an intrinsic property of the RDF simulation, which explains the asymmetric phase and flux spectra of the simulation.

profile of the simulation could be due to inner gaps in its radial distribution (Eracleous and Halpern, 1994; Strateva et al., 2003; Storchi-Bergmann et al., 2017). We defer the discussion of the radial distribution of the simulation to the next subsection. Aside from the difference in the line shapes of the simulated and observed flux spectra, their peak normalised fluxes are also different. As presented in Fig. 4.4, the peak normalised flux of the simulated flux data goes up to $\sim$0.05 only, whereas the observed Brγ flux of NGC 3783 goes as high as $\sim$0.09.

Nevertheless, the double-peaked line shape does not match our observed flux spectrum for NGC 3783. One possible solution is to make the simulated flux spectrum smoother so that the peak becomes more of a single than a double peak. For example, adding electron and/or Rayleigh scattering physics would introduce smoothness to the simulated spectrum by causing additional broadening of the line profile aside from the Doppler broadening due to thermal motions of gas (Laor, 2006b; Gaskell, 2009; Gaskell and Goosmann, 2013). Currently, the RDF simulation does not have any scattering physics. Hence, adding it would be a good point for improvement. As for the lack of emission in the core region of the line, this could indicate that the intricate physical processes of the BLR may not be fully captured by CLOUDY, as suggested by previous works (Dong et al., 2007; Devereux, 2016).

Furthermore, the simulated differential phase spectra of NGC 3783 show slight asymmetry, as the negative peak on the redshifted side of the central wavelength is slightly higher than the positive peak on the blueshifted side for all baselines. We look into the LoS velocities of the cells in the simulation, which is calculated as the projection of the total velocity in the $+x$-direction (LoS direction). We find that the LoS velocity distribution of the simulation is asymmetric (Fig. 4.5), and we purport that this drives the slight asymmetry in the interferometric signal of the simulation. The wings of the LoS velocity distribution are also asymmetric, which could also explain the asymmetric wings of the simulated flux data. We therefore conclude that the asymmetry in the simulated data is due to its asymmetry in its LoS velocity distribution. It is unclear what physical reason drives the asymmetry in the LoS velocity distribution of the RDF simulation; pinpointing such physics will be the goal of our future work.

4.3.1 Intrinsic properties of the RDF simulation

We aim to fit the differential phase and flux spectra generated from the RDF simulation with the Pancoast model, and compare the best-fit parameters of the Pancoast model to those of the intrinsic properties of the RDF simulation. To create such a comparison, we measure the geometric (related to the radial and angular distribution of the cells in the simulation), kinematic (tangential and radial velocities of the cells), and asymmetric properties (anisotropic emission and midplane obscuration) of the RDF simulation following prescriptions of the Pancoast model in defining these properties. In this subsection, we briefly discuss how we calculated these properties of the RDF simulation, which will serve as our ground truths. Overall, we find the RDF simulation, due to its intrinsically asymmetric nature, to possess more complicated properties that cannot be well-described

with the simplistic prescriptions of the Pancoast model, which are intrinsically symmetric.

Geometric properties of the RDF simulation

The distance of each cell to the origin in the RDF simulation can be easily calculated as $r = \sqrt{x^2 + y^2 + z^2}$ based on the Cartesian coordinates of the simulation cells. The radial distribution of the RDF simulation can then be fitted with a shifted Gamma function (Eqn. 2.2). We then fit for r_0, α, and θ which we use to calculate μ, β, and F (Eqns. 2.4-2.5). Fig. 4.6a shows the radial distribution of the RDF simulation fitted with the shifted Gamma function. Our best-fit shifted Gamma function shows that the RDF simulation has an (emissivity-weighted) average BLR size of $R_{\rm BLR}$ ∼0.0065 pc (7.8 ld), and a minimum BLR size of $R_{\rm BLR,min} \sim 0.0003$ pc (0.37 ld). This translates to a ratio between the minimum and average BLR size of $F = 0.048$. These values are consistent with what we derive by calculating the flux-weighted average radius without fitting a shifted Gamma function. The fitted β is 0.26, indicating a radial distribution that is nearly Gaussian. We note that the geometric parameter values of the RDF simulation are smaller than those of the best-fit BLR model of NGC 3783 (GRAVITY Collaboration et al., 2021a), but again, we remind the readers that comparing the two is not the goal of this work and a close match cannot be expected.

As shown in Fig. 4.6a, there is a slight discontinuity in the radial distribution of cells in the simulation, i.e. the number of cells suddenly decreases beyond $r \sim 0.004$ pc. This results in an abrupt lack of cells in the inner region of the simulation, which can also be seen in Fig. 4.3b, wherein there are patches with no cells in the inner region of the face-on view of the simulation. This could also explain the double-horned line profile of the simulation, but previous works have shown that such an effect is secondary, and the orientation effects remain more influential in dictating the emission line shape (Eracleous and Halpern, 1994; Strateva et al., 2003; Storchi-Bergmann et al., 2017).

We also look into the angular distribution of the cells in the RDF simulation by measuring the angle of each cell from the midplane of the disc. In the RDF simulation, this translates into $\theta' = \left|\sin^{-1}\left(\frac{z}{r}\right)\right|$. Fig. 4.6b shows the angular distribution of the RDF simulation. Most of the cells are found at $\theta' < 5°$, suggesting that the simulation is dominated by a very thin disc structure. We therefore measure the opening angle θ_0 of the RDF simulation in three ways to determine how sensitive the Pancoast model is in recovering the correct angular distribution of the RDF simulation: (1) the average value, (2) the 95% percentile value, and (3) the maximum value of θ'. These values are also shown in Fig. 4.6b.

We do not fit the angular distribution function of the Pancoast model (Eqn. 2.7) to the angular distribution of the RDF simulation because the latter resembles the angular distribution from a Pancoast model with the angular distribution turned off (see Sect. 2.5). Hence, we do not consider the angular distribution parameter γ as a free parameter when fitting the Pancoast model with our data. Nevertheless, both the radial and angular distributions of the RDF simulation will be compared later on with the best-fit Pancoast model derived from fitting the generated differential phase and flux spectra of the simulation.

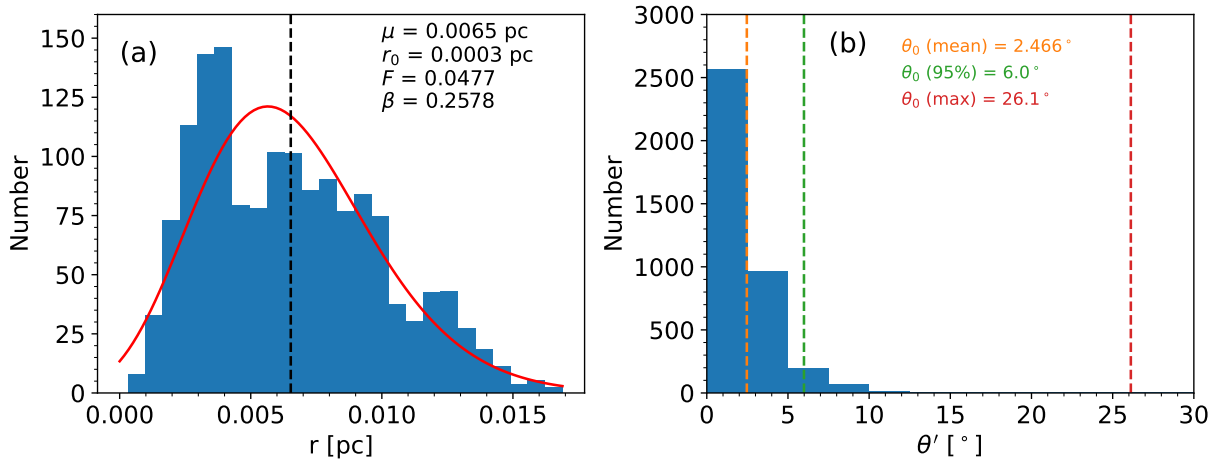

Figure 4.6: The BLR geometric properties of the RDF simulation following Pancoast model prescriptions. (a) The radial distribution of the RDF simulation (blue histogram) is fitted with a shifted Gamma function (red solid line) to derive the following parameters shown on the upper right corner of the panel: the (emissivity-weighted) average BLR size $R_{\rm BLR}$ (defined as μ), the minimum BLR radius $R_{\rm BLR,min}$ (defined as r_0), and the unit standard deviation of the BLR radial profile (defined as β). The ratio of the $R_{\rm BLR,min}$ to $R_{\rm BLR}$ is defined as F. A black vertical dashed line shows the value of $R_{\rm BLR}$. (b) The angular distribution of the RDF simulation resembles that of a thin disc with a large number of cells at very small angles ($\theta' < 5°$). This suggests that the angular distribution parameter γ should not be fitted and the angular distribution must be turned off (see Sect. 2.5). As shown on the upper right part of the panel, we define the opening angle θ_0 in three ways: the average, the 95% percentile, and the maximum value of the angular distribution, all represented by the black vertical dashed lines in the panel.

Kinematic properties of the RDF simulation

We calculate the tangential and radial velocities of the RDF simulation by converting the Cartesian velocities to their spherical coordinate system counterparts. The tangential velocity v_ϕ is represented by the azimuthal velocity component, and the radial velocity v_r is represented by itself. Fig. 4.7a shows the cells of the RDF simulation in the v_ϕ-v_r phase space. The velocities are normalised by the circular velocity $v_{\rm circ} = \sqrt{\frac{GM_{\rm BH}}{r}}$ where $M_{\rm BH} = 10^{7.4} M_\odot$. Following the prescription of Pancoast's model in defining circular bound and elliptical/radial orbits, we highlight the points where the Gaussian distributions of velocities are centred (red-filled dots for circular orbits, red-filled stars for elliptical/radial orbits). The majority ($\sim$ 96%) of the cells in the RDF simulation are centred around the upper red-filled dot and therefore possess Keplerian/circular orbits. Therefore, the $f_{\rm ellip}$ of the RDF simulation is 0.96. Only $\sim$1% of the cells are slightly offset above the right red-filled star in Fig. 4.7a. These cells are outflowing as they have positive v_r values. Since there are no cells in the RDF simulation that are located on the inflowing side of the v_ϕ-v_r phase space (left red-filled star), we can safely say that the $f_{\rm flow}$ of the RDF simulation is >0.5 (outflowing). Upon calculating the $\theta_e = \tan^{-1}(|v_\phi/v_r|)$ of each cell in the outflowing group, we get their median value, which determines the θ_e of the simulation: $\theta_e \sim 8.3°$.

Aside from the circular and radial orbits in the RDF simulation, about 4% of the cells are neither within nor near the red-filled dots and stars, indicating that these cells possess neither strongly circular nor elliptical orbits. These cells are inside the dotted ellipse, indicating their total velocities to be $\lesssim v_{\rm circ}$. We divided these cells into two further distinctions: Group 2 cells (orange stars), which are closer to the upper red-filled dot, and Group 3 cells (green triangles), which are closer to (v_r, v_ϕ) = (0,0). In the Pancoast model, such cells cannot be realised as the clouds in the Pancoast model can only have velocities that are on the dotted ellipse, which has a semiminor axis of $v_{\rm circ}$ and a semimajor axis of $\sqrt{2}v_{\rm circ}$. Physically speaking, most of the cells in Groups 2 and 3 are also moving outwards from the central region (similar to the outflowing cells), but they are still within the gravitational influence of the central BH as their total velocities do not reach the escape velocity.

Lastly, we calculate the radial and angular standard deviations of the circular and outflowing cell of the RDF simulation. Fig. 4.8 shows the distribution of $v_r/v_{\rm circ}$ and $v_\phi/v_{\rm circ}$ of the circular bound and outflowing cells in Fig. 4.7. We fit a Gaussian distribution for each histogram to calculate its mean and standard deviation. The $v_r/v_{\rm circ}$ and $v_\phi/v_{\rm circ}$ distributions of the circular bound cells show that these cells are slightly offset above the (v_r=0, v_ϕ=$v_{\rm circ}$) point where it is supposed to be centred at, as shown by the average of the $v_\phi/v_{\rm circ}$ distribution of the circular bound cells much larger than zero. On the contrary, the $v_r/v_{\rm circ}$ and $v_\phi/v_{\rm circ}$ distributions of the outflowing cells show average values greater than zero, indicative of a non-zero θ_e. The $\sigma_{\rho,{\rm circ}}$, $\sigma_{\rho,{\rm radial}}$, $\sigma_{\Theta,{\rm circ}}$, and $\sigma_{\Theta,{\rm radial}}$ are shown in Fig. 4.8.

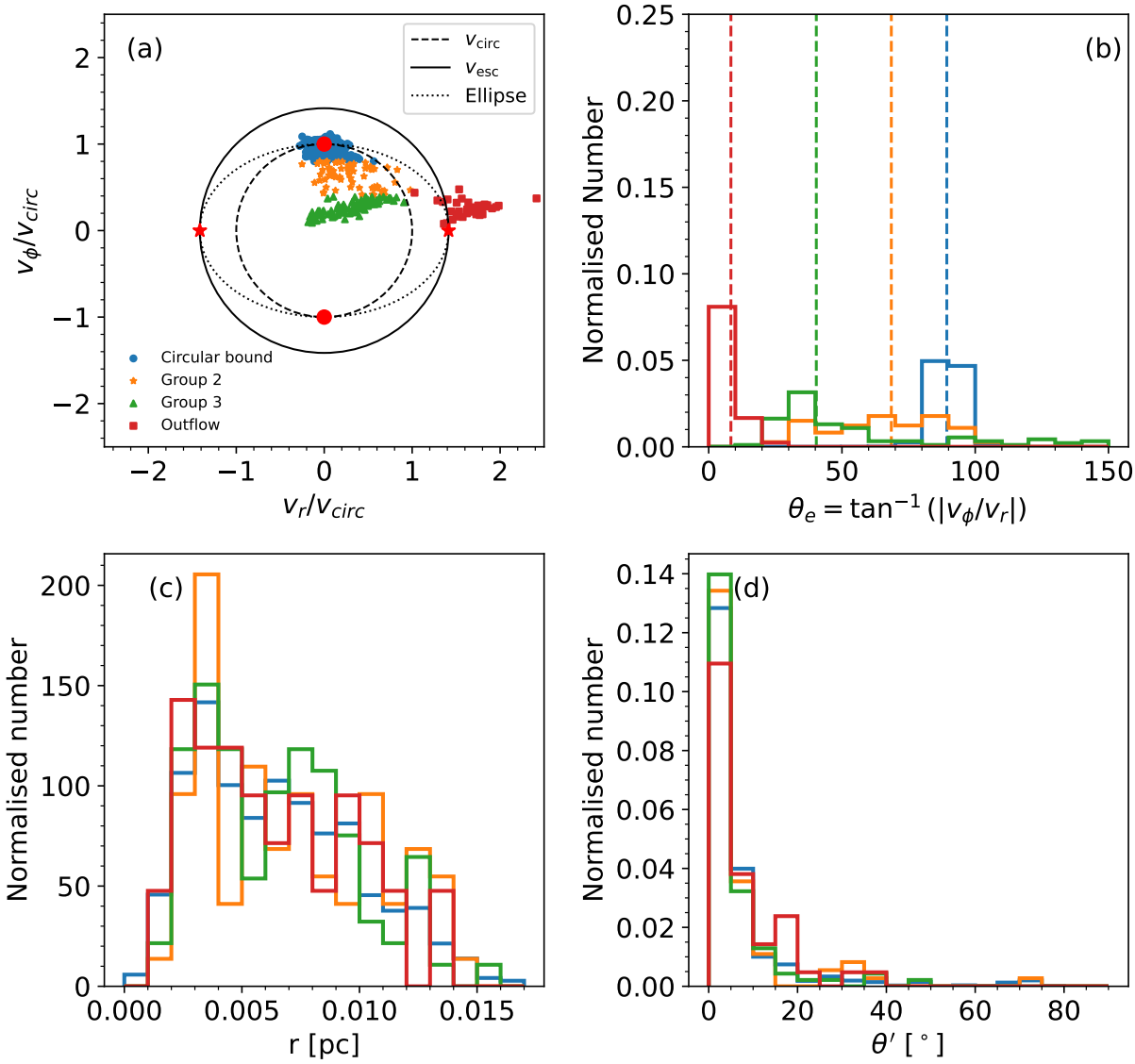

Figure 4.7: The BLR kinematic properties of the RDF simulation. (a) The cells in the RDF simulation are plotted in the v_ϕ-v_r phase space normalised by the circular velocity $v_{\rm circ}$. The black dotted line shows the ellipse with semiminor and semimajor axes equal to $v_{\rm circ}$ and $v_{\rm esc}$ = $\sqrt{2}v_{\rm circ}$, respectively. The outer solid black circle has a radius of $v_{\rm esc}$ while the inner dashed black circle has a radius of $v_{\rm circ}$. In the Pancoast model, the red-filled dots at (v_r, v_ϕ) = (0, $\pm v_{\rm circ}$) show the centres of Gaussian distributions where the clouds with circular orbits are taken from. On the other hand, the red-filled stars at (v_r, v_ϕ) = ($\pm v_{\rm esc}$, 0) are the centres of Gaussian distributions where the clouds with outflowing/inflowing escape velocities are taken from. The cells in the RDF simulation are grouped into four distinctions depicted by their varying symbols and colours depending on their position in the v_ϕ-v_r phase space (see text at Sect. 4.3.1). (b) Each of these groups of cells has a different distribution of θ_e, with the median value of θ_e in each distribution shown as a vertical dashed line. The median θ_e of the circular bound, Group 2, Group 3, and outflowing clouds are 89.3°, 68.5°, 40.4°, and 8.3°, respectively. (c) The radial distributions and (d) angular distributions of the four cell groups do not show any significant difference (K-S p-value $\gg$ 0.05).

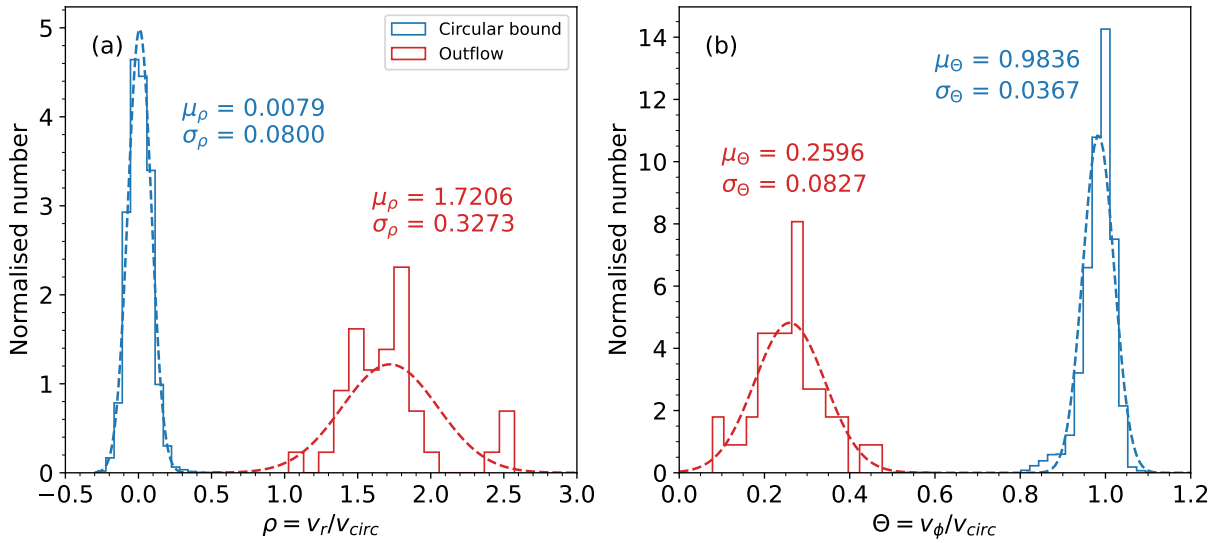

Figure 4.8: Histograms (solid lines) of $v_r/v_{\rm circ}$ (panel a) and $v_\phi/v_{\rm circ}$ (panel b) of the circular bound (blue) and outflowing (red) cells of the RDF simulation defined in Fig. 4.7. The best-fit Gaussian distribution for each histogram is shown as a dashed line. The average and standard deviation of each Gaussian distribution are shown as well. The standard deviations in panel (a) refer to all σ_ρ values, while the ones in panel (b) refer to all σ_Θ values.

Cell groups in the simulation

Although θ_e is defined only by the inflowing/outflowing clouds in the model, it is still interesting to see the distribution of θ_e of the other cell groups, which is shown in Fig. 4.7b. We define θ_e of the RDF simulation by the median value of the angular location of the outflowing (red histogram) cells in the $v_r - v_\phi$ phase space, which is $\sim$8.3°. The distribution of the circular bound cells (blue histogram) shows a median θ_e of $\sim$90°, which is not surprising considering the definition of θ_e for Keplerian-dominated clouds. Groups 2 and 3 reveal much wider distributions of θ_e compared to the first two groups, and their median θ_e values, which are $\sim$68° and $\sim$40°, respectively, lie between the median θ_e values of the first two groups.

We also investigate these cloud groups to find whether they show any preferential radial and angular distribution. Fig. 4.7c and d show the radial and angular distribution of the four cloud groups using the same colour scheme as the other panels. A Kolmogorov-Smirnov (K-S) test shows that there is no significant difference among the radial and angular distributions ($p \gg 0.05$), indicating the absence of any preferential position of the cell groups. This also means that the non-circular bound cells are all scattered around the cell distribution of the simulation. This is not surprising considering the fact that the simulation's density distribution is more akin to a continuous fluid, and it is mostly composed of circular bound cells.

In addition, we test the effect of these cloud groups in the flux and phase spectra of the simulation by recalculating the simulated flux and phase spectra after removing the

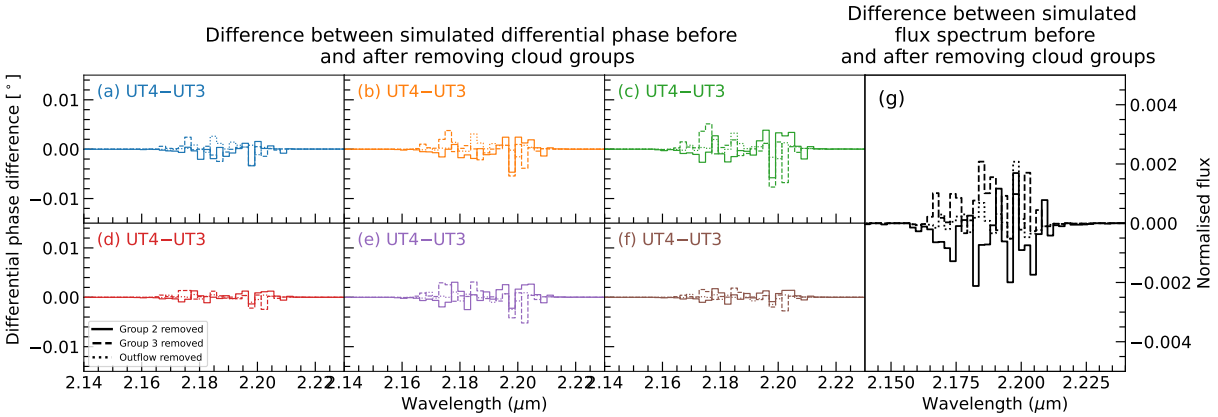

Figure 4.9: Difference in the phase and flux spectra of the RDF simulation before and after removing the three non-circular bound cloud groups as defined in Sect. 4.3.1. Different line styles refer to different cloud groups removed, as shown in the label.

non-circular bound cells. We find that their removal in our calculation of the simulated data produces negligible results (Fig. 4.9). We also fitted the RDF simulation's resulting phase and flux spectra after removing the three non-circular bound cell groups. Our test reveals no stark difference in the best-fit parameters, radial and angular distribution, and the distribution of the cells in the $v_r - v_\phi$ phase space of the resulting Pancoast model. We therefore conclude that the non-circular bound cells of the simulation do not greatly affect the flux and phase spectra of the simulation.

Asymmetry properties of the RDF simulation and nuisance parameters

As we rotate the RDF simulation to match the on-sky orientation of NGC 3783 during GRAVITY observations, we implicitly assume that each simulation cell produces isotropic emission and such emission is optically thin, which leads to emission independent of our rotation. Consequently, we assume that the simulation does not consider any flux weighting in each of its cells and therefore, anisotropic emission can be ignored ($\kappa = 0$). This also follows that there is no midplane obscuration involved in the simulation ($\xi = 1$)

The expected Brγ central wavelength of NGC 3783 and the peak (normalised) flux value of the RDF simulation flux spectrum are considered nuisance parameters in the Pancoast model and are named as λ_c and $f_{\rm peak}$, respectively. We calculate $\lambda_c \sim 2.19$ and $f_{\rm peak} \sim 0.05$ in the RDF simulation. However, we do not compare these values with the best-fit values of the Pancoast model, as these do not greatly affect the geometry, kinematics, and asymmetry of the Pancoast model. Following this same reasoning, we do not fit the BLR offset from the origin, (x_0, y_0), and assume its value to be at the origin (0,0).

Summary of ground truth and priors

Table 4.1 summarises the intrinsic properties of the RDF simulation, which will serve as our "ground truth" values. We aim to compare these values with the best-fit parameters of the Pancoast model fitted to the differential phase and flux spectra of the RDF simulation. Aside from comparing these numbers, we also compare the radial and angular distributions and the $v_\phi - v_r$ phase space distributions of the RDF simulation and the Pancoast model.

We show in Table 4.1 the priors of each fitted parameter in the Pancoast model during fitting. The priors are similar to those of GRAVITY Collaboration et al. (2020a), except for the nuisance parameters λ_c and $f_{\rm peak}$, and $\sigma_{\Theta,\rm circ}$, $\sigma_{\rho,\rm radial}$, and $\sigma_{\Theta,\rm rad}$. We note that the priors for the nuisance parameters have a negligible effect on our main conclusions. As for the velocity dispersions, Williams and Treu (2022) noted that the priors of $\sigma_{\Theta,\rm circ}$ and $\sigma_{\Theta,\rm rad}$ must be set to LogUniform(0.001 to 0.1) to avoid complications in the distinction between inflow/outflow and circular orbits when these parameters reach values greater than 0.1. We set the prior of $\sigma_{\rho,\rm radial}$ to 0.001 to 1 instead of the default prior 0.001 to 0.1 to achieve the ground truth value of $\sigma_{\rho,\rm radial}$, which is greater than 0.1.

4.4 Pancoast model fitting results

In this section, we present the results of fitting the inferred spectra of the RDF simulation with the Pancoast model. Table 4.1 shows the parameter values, and Fig. 4.10a shows the flux and phase spectra of the best-fit Pancoast model in comparison with the simulated data. Fig. E.1 shows the corresponding corner plot of the best-fit Pancoast model. Our main finding is that the best-fit Pancoast model is able to derive a thin-disc BLR structure that is Keplerian dominated, similar to the RDF simulation. Nonetheless, the Pancoast model fails to properly recover the correct radial and angular distributions and the outflowing component of the RDF simulation.

Judging only on the best-fit parameters in Table 4.1, we find that BH mass of the best-fit model is smaller than its ground truth value even when considering its 1σ uncertainty. However, the $R_{\rm BLR}$ of the best-fit model is slightly larger but consistent within its 1σ uncertainty compared to the simulation's ground truth $R_{\rm BLR}$. The radial distribution parameter β of the best-fit model is also larger than our ground truth value, but its value is < 1, which is still indicative of a Gaussian-like radial distribution. The inclination angle i of the best-fit Pancoast model is larger than the ground truth value, but the opening angle θ_0 of the model is much more consistent with the maximum θ_0 of the simulation.

The corner plot in Fig. E.1 shows the posterior distributions of the fitted parameters in the Pancoast model. Interestingly, the geometry parameters show different results in their posterior distributions. The $R_{\rm BLR}$, $\rm M_{BH}$, β, and θ_0 posterior distributions have a clear single peak, although the distribution for $R_{\rm BLR}$ and $\rm M_{BH}$ show strong tails on their left sides, indicating some preference for smaller average BLR sizes and BH masses. The posterior distribution peaks of i and θ_0 are not as clear as the other peaks of the geometry parameters.

As for the asymmetry parameters, κ shows a slightly lower value but still consistent within 1σ uncertainty compared with our ground truth value, whereas ξ is lower than its ground truth value, indicating that the Pancoast model prefers slight opacity in the BLR midplane. Their posterior distributions in Fig. E.1 also differ in their overall behaviour, as the distribution of κ is strongly peaked, whereas ξ is not. The kinematic parameters show a variety in their consistency with their ground truth values as well. Although $\sigma_{\Theta,\mathrm{circ}}$, $\sigma_{\rho,\mathrm{radial}}$ and $\sigma_{\Theta,\mathrm{radial}}$ are consistent with their ground truth values within their 1σ uncertainties, the rest of the kinematic parameters (f_{ellip}, θ_e, and $\sigma_{\rho,\mathrm{circ}}$) are not. However, the Pancoast model still predicts a BLR model that is predominantly Keplerian ($f_{\mathrm{ellip}} \sim 0.7$). Interestingly, the best-fit value of θ_e is much closer to the θ_e value of the Group 2 cells in the RDF simulation. Overall, we find that the Pancoast model finds it challenging to reconcile the kinematics of the outflowing cells, as if the outflowing clouds of the Pancoast model are more akin to the *average distribution* of all non-circular bound cells in the RDF simulation. We conclude that the Pancoast model struggles to recover the more complex distribution of the RDF simulation's non-circular bound cells due to its simplistic prescription of radial-dominated clouds. This is not surprising considering that only $\sim$5% of the cells in the RDF simulation are outflowing, hence making it difficult for the Pancoast model to constrain these kinematic parameters related to the outflowing cells.

Fig. 4.10a shows that the (averaged) differential phase spectrum of the best-fit Pancoast model is slightly lower but still matches that of the RDF simulation, considering its 1σ uncertainty. We also find a similar conclusion with the flux spectrum of the best-fit Pancoast model, although the slight bump on the redshifted side of the simulated flux spectrum cannot be fitted well by the Pancoast model. The average simulated phase spectrum also has a slightly pronounced peak on its redshifted side, whereas the best-fit differential phase is more symmetric.

Fig. 4.10b shows the radial distribution of the best-fit Pancoast model compared to the RDF simulation. We find that the radial distributions of the two models are significantly different ($p \ll 0.05$). Due to the slightly larger F and R_{BLR} recovered by the Pancoast model, the resulting radial distribution of the model has a slight offset with respect to the ground truth distribution. The radial distribution of the Pancoast model spans an extensive range of BLR radii, even beyond the maximum radius of the RDF simulation at $r \sim 0.018$ pc. One area of improvement that future works could implement is the addition of a maximum BLR radius in the list of fitted parameters in the model. Such a change could lead to achieving a radial distribution from the model that is more consistent with that of the current simulation.

Fig. 4.10c presents the angular distributions of the best-fit Pancoast model and RDF simulation. The angular distribution of the simulation abruptly decreases beyond $\theta' > 5°$, which the angular distribution of the model cannot replicate. Instead, the latter mildly decreases with increasing θ', until it reaches the best-fit θ_0. It is no surprise that the K-S p-value for the two distributions is $\ll 0.05$, suggesting they are significantly different distributions. Interestingly, even though the radial and angular distributions of the two models do not match, the best-fit Pancoast model still well-reproduces the double-peaked line shape of the flux spectrum by producing a BLR model that has a similar physical

interpretation as the RDF simulation: a thin disc-like BLR with a small opening angle and small inclination angle. We conclude, therefore, that while the Pancoast model does not exactly reproduce all of the detailed geometrical properties of the RDF simulation, it does successfully recover the overall average properties of the simulation.

Aside from the radial and angular distributions, we also look into the $v_r - v_\phi$ phase space as shown in Fig. 4.10d. As mentioned earlier, the θ_e of the outflowing clouds in the model matches that of the Group 2 cells in the simulation. However, their distribution in the $v_r - v_\phi$ phase space does not match either of the non-circular cloud groups in the model (K-S $p \ll 0.05$), even the outflowing cells (red circles). Interestingly, the outflowing clouds of the Pancoast model seem to recover the *average* properties of the non-circular bound cells of the simulation. However, the distribution of the circular bound clouds of the Pancoast model is quite close to that of the simulation, although the K-S test yields $p \ll 0.05$.

We briefly emphasise that we tried different iterations of fitting the simulated data to the Pancoast model by testing different priors for BLR size, F, and i to achieve best-fit values that are consistent with the ground truths: LogUniform(1.19×10^1, 1.19×10^2 ld), Uniform(0.01, 0.1), and Uniform($\cos i(0, \pi/4)$). We also tried changing the weights of the simulated data to see the effect of such weighting in the model fitting. Overall, we find that pushing the priors of the geometry parameters to lower ranges yields values that are consistent with the ground truths, but this also results in pushing the BH mass to much lower values and the model differential phase to much smaller values. On the contrary, changing the weight of the flux and phase data does not drastically affect the Pancoast model fitting results.

We also point out that the RDF simulation is *intrinsically asymmetric*, as reflected by its radial distribution (Fig. 4.6) whose shape cannot be well-represented by a skewed Gaussian distribution derived from the shifted Gamma function, and distribution of its cells in the $v_r - v_\phi$ phase space (Fig. 4.8) which shows a minority of its cells deviating from the usual circular bound and inflowing/outflowing definition of the Pancoast model. This is in contrast with the best-fit Pancoast model, which is *intrinsically symmetric*. This can be seen in Fig. 4.10a, where the best-fit differential phase is symmetric, which is in contrast with the simulated differential phase and in Fig. 4.10d, where the outflowing clouds of the best-fit model have a distribution that spans both $v > v_{\rm esc}$ and $v < v_{\rm esc}$. We clarify that the Pancoast model, in general, can introduce asymmetries in its model as discussed in Sect. 2.5. However, the best-fit Pancoast model fails to recover the outflowing/asymmetrical nature of the RDF simulation, which further proves its symmetrical nature.

4.5 Comparison with previous works

There is a dearth of previous literature that focuses on the improvements of the Pancoast model. Although Pancoast et al. (2014a) described the limitations and possible areas of improvement of the model, only Mangham et al. (2019) has tackled the problem by pursuing a similar methodology as our work, but using a rotating, biconical accretion disc wind

Table 4.1: Ground truth values of the Pancoast model parameters based on the RDF simulation, together with the priors used in fitting the simulated flux and differential phase spectra of the RDF simulation, and the best-fit values from the Pancoast model fitting taken as the median value of the posterior distribution of each fitted parameter.

Parameter	Ground Truth	Prior	Best-fit Pancoast model
$\log\,(M_{\rm BH}/M_\odot)$	7.4	LogUniform(10^5, 10^{10} $M_\odot$)	$7.08^{+0.26}_{-1.34}$
$\log\,(R_{\rm BLR,ave})$ [ld]	0.89	LogUniform(1.19×10^{-1}, 1.19×10^{4} ld)	$1.05^{+0.27}_{-1.32}$
$\mathrm{F} = R_{\rm BLR,min}/R_{\rm BLR,ave}$	0.048	Uniform(0, 1)	$0.29^{+0.29}_{-0.23}$
β	0.25	Uniform(0, 1)	$0.71^{+0.15}_{-0.30}$
i [°]	30	Uniform($\cos i$(0, 90°))	54^{+30}_{-16}
θ_0 [°]	2.5 (ave.) 6.0 (95% per.) 26.1 (max.)	Uniform(0, 90°)	16^{+44}_{-6}
κ	0	Uniform(-0.5, 0.5)	$-0.23^{+0.29}_{-0.09}$
ξ	1	Uniform(1, 5)	$0.44^{+0.44}_{-0.22}$
$f_{\rm ellip}$	0.96	Uniform(0, 1)	$0.66^{+0.20}_{-0.34}$
$f_{\rm flow}$	>0.5	Uniform(0, 1)	0.7^{b}
θ_e [°]	8.8	Uniform(0, 90°)	51^{+28}_{-38}
$\sigma_{\rho,\rm circ}$	0.080	LogUniform(0.001, 0.1)	$0.0491^{+0.0003}_{-0.0469}$
$\sigma_{\Theta,\rm circ}$	0.037	LogUniform(0.001, 0.1)^c	$0.0105^{+0.0417}_{-0.0075}$
$\sigma_{\rho,\rm radial}$	0.33	LogUniform(0.001, 1)^d	$0.4363^{+0.0727}_{-0.4324}$
$\sigma_{\Theta,\rm radial}$	0.08	LogUniform(0.001, 0.1)^c	$0.0059^{+0.0492}_{-0.0035}$

Note: [a]Our Pancoast model follows the new angular distribution from Williams and Treu (2022). The prior is fixed to a lower range of values to better produce the angular distribution of the RDF simulation. Caution is also needed in interpreting the ground truth γ (see Sect. 4.3.1).

[b]The parameter $f_{\rm flow}$ is fixed to 0.7 to create an outflow version of the Pancoast model.

[c] Following Williams and Treu (2022), we set the priors to avoid complications in the distinction between inflow/outflow and circular orbits when these parameters reach values greater than 0.1.

[d] We adjust the upper limit of the prior to achieve the ground truth value of the RDF simulation, which is > 0.1.

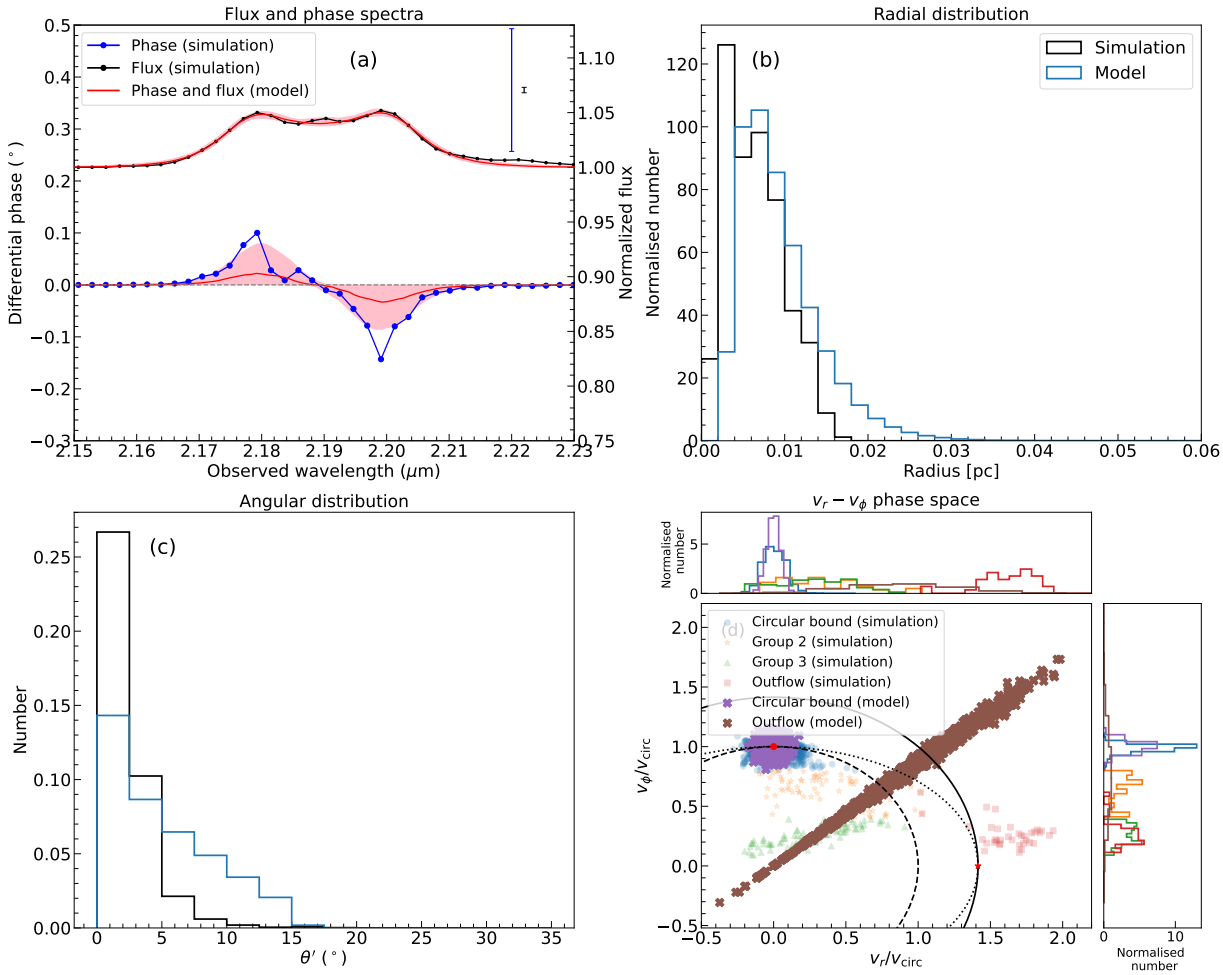

Figure 4.10: The best-fit Pancoast model in comparison with the RDF simulation. Different panels pertain to different quantities: (a) The phase and flux spectra of the best-fit Pancoast model and its 1σ confidence interval are shown as the red line and red shaded region, respectively. The blue and black lines correspond to the simulated phase and flux spectra of the RDF simulation, respectively. The phase spectra shown are an average of the differential phase spectra of the three longest baselines: UT4-UT1, UT3-UT1, and UT4-UT2. The error bars on the upper right corner of panel a are the typical errors of the phase and flux spectra taken from NGC 3783 observations (GRAVITY Collaboration et al., 2021a). (b) The radial distribution and (c) the angular distribution of the RDF simulation (black line) and the best-fit Pancoast model (blue line) are overplotted together. (d) The $v_r - v_\phi$ phase space is shown, highlighting the four cloud groups of the RDF simulation (similar line scheme as Fig. 4.7 but are made transparent for visual purposes). The circular bound and outflowing clouds of the Pancoast model are also plotted as purple and brown points, respectively. On the upper and right side of the panel, the histograms of the $v_r/v_{\rm circ}$ and $v_\phi/v_{\rm circ}$ of the different cloud groups are also shown for comparison.

model of the BLR (Long and Knigge, 2002). From this model, two distinct mock datasets of Hα emission line responses were generated to pertain to two different types of sources:

a Seyfert galaxy ($M_{\rm BH} = 10^7\ M_\odot$) and a quasar (QSO; $M_{\rm BH} = 10^9\ M_\odot$). They tested two widely used RM methods: MEMECHO (Horne, 1994) and CARAMEL (Pancoast et al., 2011, 2014a,b). The goal of MEMECHO is to recover the 2D response function/velocity-delay map with its physical interpretation left to an expert, while CARAMEL, which is the basis for our model in this work, employs forward modelling of the spectroscopic time-series. Their results show that the Seyfert model produces negative responsivities (i.e. a measure of increase/decrease in the line emission as the continuum of the emitting source changes), which both methods fail to recover, and is highlighted as a limitation of both methods. Nevertheless, neither model produced any misleading or spurious results. Both models were also able to recover the geometric picture of the underlying BLR model of the QSO model. Although MEMECHO was able to recover the input velocity-delay map of the QSO model, it yielded an overestimated BLR size by about 50%. On the other hand, while CARAMEL calculated a consistent time delay with the input QSO data, it struggled to distinguish between inflow and outflow components within the BLR. CARAMEL also produced its best-fit flux spectrum consistent with the QSO model. Still, the velocity-delay maps and root-mean-square (RMS) line profiles derived by CARAMEL do not strongly match the input data. Mangham et al. (2019) did not present a physical explanation for such a discrepancy between CARAMEL and the input data from the disc wind model; they speculated that this is due to the two models' difference in their assumption of how the emission lines respond to variations in the continuum emission. CARAMEL assumes that the response is *linear* - i.e. the resulting emission line flux at a certain time is directly proportional to the continuum flux at earlier times. MEMECHO assumes that the response is *linearised* - i.e. the resulting emission line flux has a nonlinear proportionality with the continuum emission, hence a linear approximation (usually around some average continuum level), which could be more effective in considering other factors that may cause non-linear responsivities such as optical depth and changes in the ionisation structure. Overall, both methods were not able to capture the disc wind property of the underlying BLR model: in MEMECHO, the Hα line-forming region is located at the rotation-dominated dense base of the wind, while in CARAMEL, its RMS line profile has a single-peaked line shape reminiscent of a rotation-dominated BLR, which does not match the double-peaked line shape of the disc wind model.

Similar to Mangham et al. (2019), we highlight that one is limited by what one observes in the responsive parts of the line-forming region. The flux spectrum, the (velocity-resolved) delay maps, and even the differential phase observed from the BLR only reflect the parts of the BLR that dominate the responsivity-weighted line emission, and therefore are not a perfect representation of the whole BLR structure. It is possible that the responsive part of the BLR is rotation-dominated, but is just an inner part of a larger-scale outflow. In addition, as Mangham et al. (2019) emphasised, physically-based models of the BLR can exhibit intricate geometries and kinematic behaviours that may remain difficult to interpret, even when analysing 2D response functions. This is also true in our work, wherein we were also unable to recover the more complicated radial distribution and the cloud distributions in the $v_r - v_\phi$ phase space of the RDF simulation.

4.6 Conclusion and future works

To understand the points of improvement of the Pancoast model as a phenomenological model of the BLR, we study the radiation-driven fountain (RDF) simulation by Wada (2011) which is a more physically-driven model of the BLR that can reproduce the properties of the BLR and the dusty torus via radiative pressure from the accretion disc. We estimate the flux spectrum of the RDF simulation assuming a BH mass and luminosity similar to that of NGC 3783 by running CLOUDY simulations on cells selected in a computational box defined by certain conditions (i.e. density, temperature, volume, distance from the central region). We also estimate the differential phase spectra of the same snapshot by calculating the BLR photocentres assuming the same baselines as those of GRAVITY observations of NGC 3783. We reorient the RDF simulation snapshot to match the on-sky observations of NGC 3783 as closely as possible, and we fit the simulated phase and flux spectra with the Pancoast model. We defined our ground truths by measuring the intrinsic properties of the RDF simulation following the definitions of the Pancoast model and investigating the radial, angular, and velocity distributions of the RDF simulation. After fitting the simulated data with the Pancoast model, we compare the properties of our best-fit Pancoast model with our ground truths. Our main results are as follows:

1. The RDF simulation possesses specific properties in its radial, angular, and velocity distributions that cannot be well-reconciled by the Pancoast model due to its simplistic descriptions of the distributions mentioned. For instance, its radial and angular distribution cannot be well-matched by the shifted Gamma distribution (Eqn. 2.2) and angular distribution prescription (Eqn. 2.7) of the Pancoast model, respectively.

2. The $v_r - v_\phi$ phase space reveals outflowing cell groups in the RDF simulation that are still within the gravitational influence of the central region, in addition to the strongly outflowing cells that have velocities larger than $v_{\rm esc}$. The best-fit Pancoast model to the simulated data produces outflowing clouds that possess an average characteristic of all non-circular bound cells in the RDF simulation.

3. Both points above highlight the intrinsically asymmetric nature of the simulation and the intrinsically symmetric nature of the (best-fit) Pancoast model. However, the physical reason for the asymmetry of the RDF simulation is yet to be discussed in the near future.

4. The Pancoast model is able to recover the BLR size and the simulated flux and differential phase spectra of the RDF simulation. However, it cannot fully recover the actual BLR geometric, asymmetry, and kinematic properties of the RDF simulation. Nevertheless, the best-fit Pancoast model produces a BLR model that is Keplerian-dominated, has outflowing clouds, and has a similar (on-average) geometrical description as that of the RDF simulation, which is a thin disc BLR with very few cells at larger angles from the BLR midplane, which are more concentrated at the emissivity-weighted average radius of the BLR.

5. The simulated differential phase and flux spectra of the RDF simulation are slightly asymmetric. We argue that this is due to the increased number of cells in the RDF simulation with positive LoS velocities, which cause more pronounced peaks on the positive side of the simulated phase and flux spectra.

This work highlights several areas of improvement, including the following aspects:

1. Including scattering physics (Laor, 2006b; Gaskell, 2009; Gaskell and Goosmann, 2013) in the RDF simulation could produce a more realistic Brγ emission line profile. In addition, investigating an RDF simulation with a much larger number of outflowing cells could also serve as another area to look into.

2. One could also look into several snapshots of the RDF simulation to investigate the evolution of the BLR in terms of its properties as described by the Pancoast model.

3. Another way to expand this work is by looking into the super-Eddington case, wherein we change the initial conditions of the RDF simulation into a BH mass and luminosity of a super-Eddington AGN (i.e. Mrk 509 for low-redshift (GRAVITY Collaboration et al., 2024) or J0920 for high-redshift (Abuter et al., 2024), both already observed by GRAVITY).

4. After looking into different cases of the BLR as described above, it is recommended to investigate other prescriptions of the radial and angular distributions and the kinematics of the Pancoast model to potentially bridge the gap between physically motivated models and phenomenological models of the BLR.

5. Lastly, we look forward to investigating other BLR models, such as FRADO (Czerny and Hryniewicz, 2011), to better investigate the physics of the BLR and how a phenomenological model such as the Pancoast model can reproduce such physics.

Chapter 5

Summary, Conclusions, & Outlooks

In this thesis, I present our efforts in understanding the physics of the BLR with GRAVITY(+) observations through three separate but interconnected studies that investigate the greater goal in different ways: first with an independent R-L relation derived from interferometric observations with GRAVITY, second with a spectroscopic survey with the NTT/SOFI instrument, and third by confronting a radiation-driven fountain simulation with a model fit similar to that applied to GRAVITY data.

The first part of this thesis focuses on the analysis of four new low-redshift AGNs observed with GRAVITY, which show that their BLRs are spatially resolved (GRAVITY Collaboration et al., 2024). Through this, we could measure their BH masses and BLR sizes via dynamical modelling of their interferometric and flux spectra. Several key results of this work are as follows:

- Combining our results with the results from the three previously analysed low-redshift GRAVITY-AGNs, we find that the majority of our targets possess symmetric S-shaped differential phase signals and photocentre velocity gradients that are perpendicular to their radio jets, all of which are better described with a Keplerian-dominated BLR. On the other hand, two of our targets, Mrk 509 and PDS 456, exhibit asymmetric differential phase signals and photocentre velocity gradients that are not perpendicular to their radio jets, which are better described with a BLR dominated by outflowing motions.

- We fit an R-L relation with all seven low-redshift GRAVITY-AGNs, which shows a shallower slope, i.e. $R \propto L^{0.37}$, compared to the canonical R-L relation based on RM measurements, i.e. $R \propto L^{0.50}$. Several possible reasons to explain such a slope include the possibility that accretion rate plays an active role in lowering measured BLR sizes at higher luminosities through self-shadowing (Wang et al., 2014), and the possibility that the assumption that all AGNs have the same ionising spectra is wrong.

- With GRAVITY's unprecedented precision in resolving the BLR region, we were also able to measure the spatial offset of the BLR photocentres and the continuum

photocentre, which we find to have a positive correlation with AGN luminosity. We devise a possible explanation for such an offset, which explains that the hot dust has a fainter and brighter side. Further investigation with larger AGN samples is crucial to shed light on this phenomenon.

- Lastly, we calculated the individual virial factors of all seven low-redshift GRAVITY-AGNs without any assumption on their $M_{BH} - \sigma_*$ relations, and found that their average virial factors are consistent with previous works that also calculated the individual virial factors of their targets, albeit assuming a similar $M_{BH} - \sigma_*$ relation between AGNs and quenched galaxies (Onken et al., 2004; Woo et al., 2010; Park et al., 2012; Batiste et al., 2017).

While the first part of this thesis focuses on the great capability of GRAVITY in studying the R-L relation, the second and third parts of this thesis focus on two separate endeavours in expanding our horizons to a wider perspective. Specifically, the second part of this thesis focuses on the prospect of high-redshift AGN observations with GRAVITY+, which complements the low-redshift focus in the initial section (Santos et al., 2025a). We conducted a preparatory spectroscopic survey with NTT/SOFI to observe 29 $z \sim 2$ AGNs that can be observed with GRAVITY+ to confirm their quasar nature, observability, and BLR properties through their near-infrared spectra. Our main results are as follows:

- All targets show broad Balmer lines indicative of their quasar nature. The majority of the Hα emission lines have FWHM/$\sigma < 2.35$, which reflects their almost-Lorentzian line shape consisting of a narrower core component and a broader wing component. Such line shapes can be explained by either the presence of turbulence and rotation in their BLRs or the possibility of having a two-component BLR, with an inner part much closer to the accretion disc and responsible for the observed broad wing, and the outer part acting as an inner boundary between the BLR and the dusty torus and responsible for the observed core component.

- We find that the virial factors of our targets are lower than the average virial factor used to estimate their BH masses as an initial guess during BLR fitting. We purport that such a result is due to the smaller FWHM/σ values of our targets' Hα lines, which could then lead to biased BH masses that use single-epoch BH mass estimations that assume Gaussian line shapes.

- Most targets are well-fitted with the simpler Keplerian Pancoast model, while two are fitted with the more complicated elliptical and radial (full) Pancoast model. These two targets exhibit asymmetric flux spectra that can only be fitted with outflow-dominated BLRs.

- Lastly, we calculate the expected differential phase signals detected by the longest baseline of VLTI, assuming that the BLRs of our targets are perpendicular to this baseline to achieve the maximum possible interferometric signal. Our expected values

serve as an upper limit, as the resulting numbers are sensitive to the assumed BH masses, which were derived using the wing-sensitive line dispersion (σ) instead of the core-sensitive FWHM, and the former being usually larger than the latter for most of our targets. We find six extreme targets with expected differential phase signals $> 15°$, whose expected signals could be due to their very low FWHM/σ values.

The third and final section of this thesis highlights our endeavour to test our BLR model by conducting a comparative study between the Pancoast model and the radiative-driven fountain (RDF) simulation from Wada (2011) (Santos et al., 2025b). The main objective of this work and its future improvements is to realise a more physical description of inflows and outflows in the Pancoast model, which will help derive more reliable parameters in fitting asymmetric interferometric signals.An RDF simulation assuming the BH mass and luminosity of NGC 3783 was created and analysed to measure its intrinsic properties following definitions from the Pancoast model. The generated flux and phase spectra of the simulation are then fitted with the Pancoast model to confirm whether the model can recover the properties of the simulation. Our main results are as follows:

- We find that the radial, angular, and velocity distributions of the clouds/cells in the simulation cannot be well-described by the prescriptions of the Pancoast model due to the latter's simplistic descriptions of the aforementioned distributions. Due to this, the Pancoast model finds it difficult to capture the correct radial and angular distributions and kinematics of the circular-bound and outflowing clouds.

- However, the Pancoast model is successful in recovering the BLR size and the simulated flux and differential phase spectra despite most of the best-fit parameters being inconsistent with the ground truths derived from the simulation. Nevertheless, the Pancoast model is able to derive a thin disc BLR that is Keplerian-dominated, which is consistent with the description of the RDF simulation.

- We find that the RDF simulation is intrinsically asymmetric, i.e. its LoS velocity distribution and radial distribution are asymmetric, leading to a slight asymmetry in its interferometric signal, and plotting its cells on the velocity phase space reveals asymmetric distributions of non-circular bound cells. On the other hand, the Pancost model is intrinsically symmetric, i.e. its LoS velocity distribution and radial distribution are symmetric, and its outflowing clouds have a symmetric distribution along the velocity phase space.

- Further work is highly recommended to formulate potential improvements in the Pancoast model. Future work should involve additional scattering physics, investigating several snapshots and additional cases (i.e. QSO case) of the RDF model, and even analysing other BLR models such as FRADO (Czerny and Hryniewicz, 2011).

To conclude this work, we find through spectro-interferometry, a method that is independent of RM and other BH mass measurement methods, that the R-L relation of

GRAVITY-observed AGNs becomes shallower at higher luminosities. This presents several challenges to our current understanding of BLR physics. Whether the accretion state or the ionising spectrum of an AGN determines its position on the R–L relation remains an open question for future investigation. Additionally, our sample of $z \sim 2$ AGNs observed with NTT/SOFI exhibits Lorentzian-like Hα lines and smaller virial factors compared to the virial factor assumed to estimate their BH masses. These findings further challenge the prevailing understanding of BLR geometry, suggesting that the BLR may consist of two distinct components or result from a combination of rotational and turbulent motions. To address all these questions more definitively, improvements to the Pancoast model, which is widely used in GRAVITY-related studies, are necessary. Upon testing the Pancoast model against the RDF simulation, we identify several areas for improvement, not only within the model itself but also in the RDF simulation employed in this work. Nevertheless, our preliminary results indicate that the Pancoast model, due to its simplistic parameter definitions, fail to reliably recover the geometry and kinematics of the RDF simulation.

Looking ahead, GRAVITY+ is expected to observe more high-redshift quasars. Currently, only one $z \sim 2$ quasar, J0920 (Abuter et al., 2024), has had its SMBH mass dynamically measured with GRAVITY+. Four additional $z \sim 2$ AGNs have been recently observed with GRAVITY+ and their dynamically measured BH masses and BLR sizes will be published soon (GRAVITY Collaboration et al., 2025). There are also ongoing efforts on observing quasars at $z > 2$. These observations, once successful, will allow us to explore the redshift evolution of the R-L relation, investigate the origins of SMBHs, examine the relationship between SMBH and host galaxy growth, and ultimately provide a clearer picture of the SMBH-galaxy coevolution scenario. In parallel with these developments, we anticipate a refined version of the Pancoast model that could accurately model inflowing/outflowing motion, which will help in dynamically modelling BLRs with such components.

Appendix A

Corner plots of BLR model fits

The posterior probability density distributions of the fitted parameters for the four low-redshift targets analysed in Chapter 2 (GRAVITY Collaboration et al., 2024) are shown in Figs. A.1 to A.4 as corner plots.

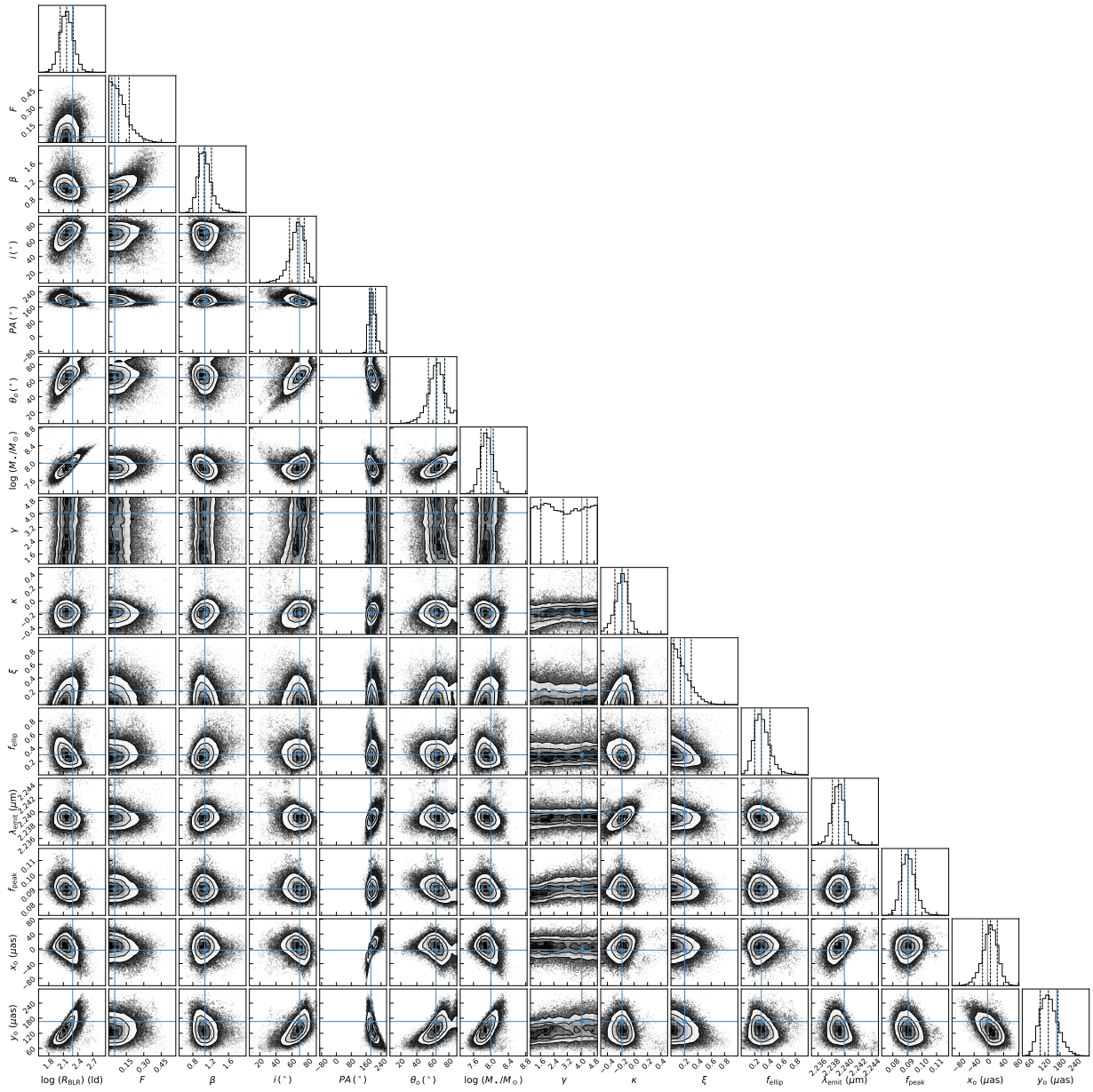

Figure A.1: Posterior probability distribution of the fitted parameters from the elliptical and radial model fitting Mrk 509 data. The blue lines and cross points refer to the maximum a posteriori value. The vertical dashed lines represent the 68% (1σ) credible intervals.

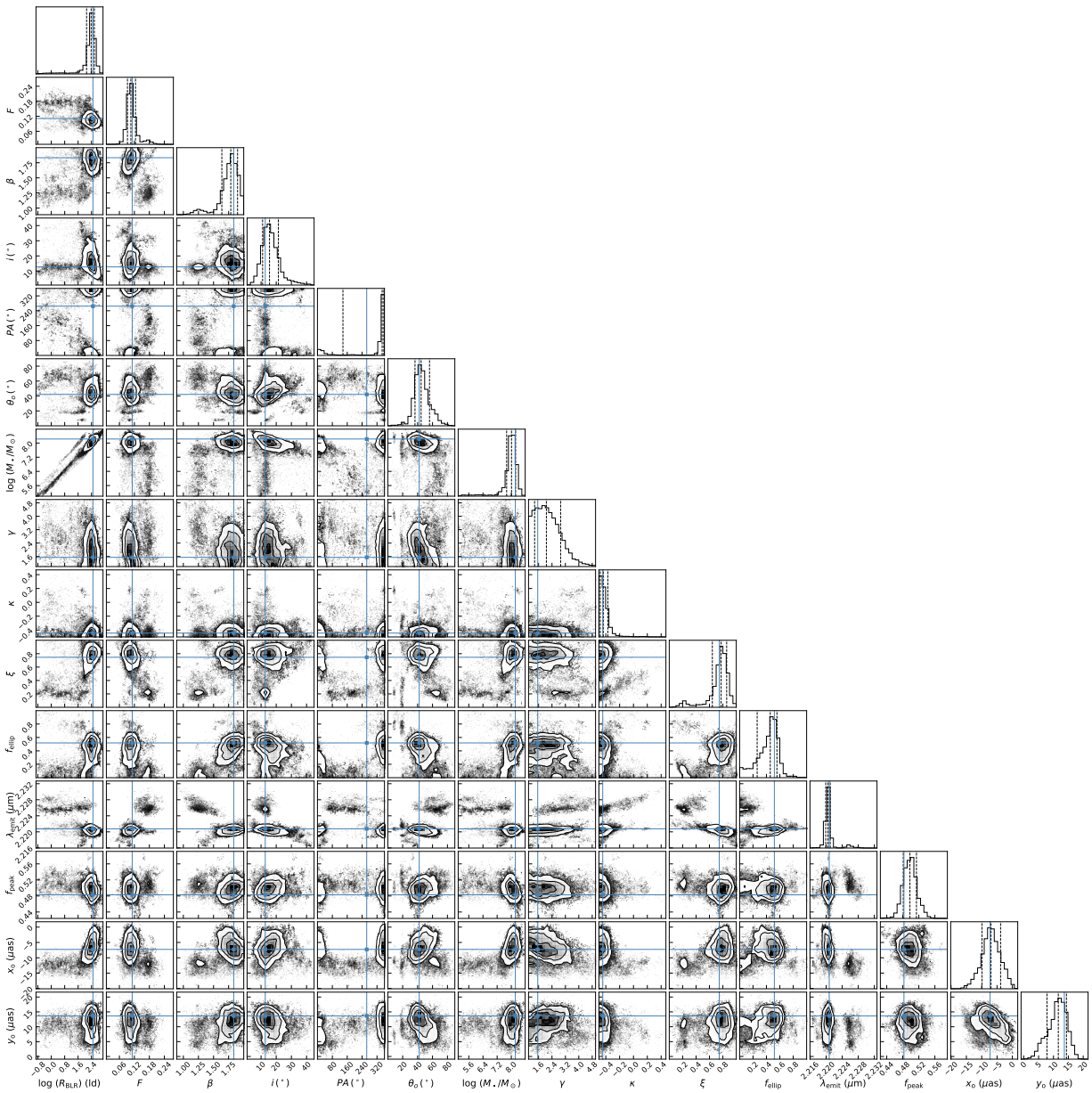

Figure A.2: Similar to Fig. A.1 but for PDS 456.

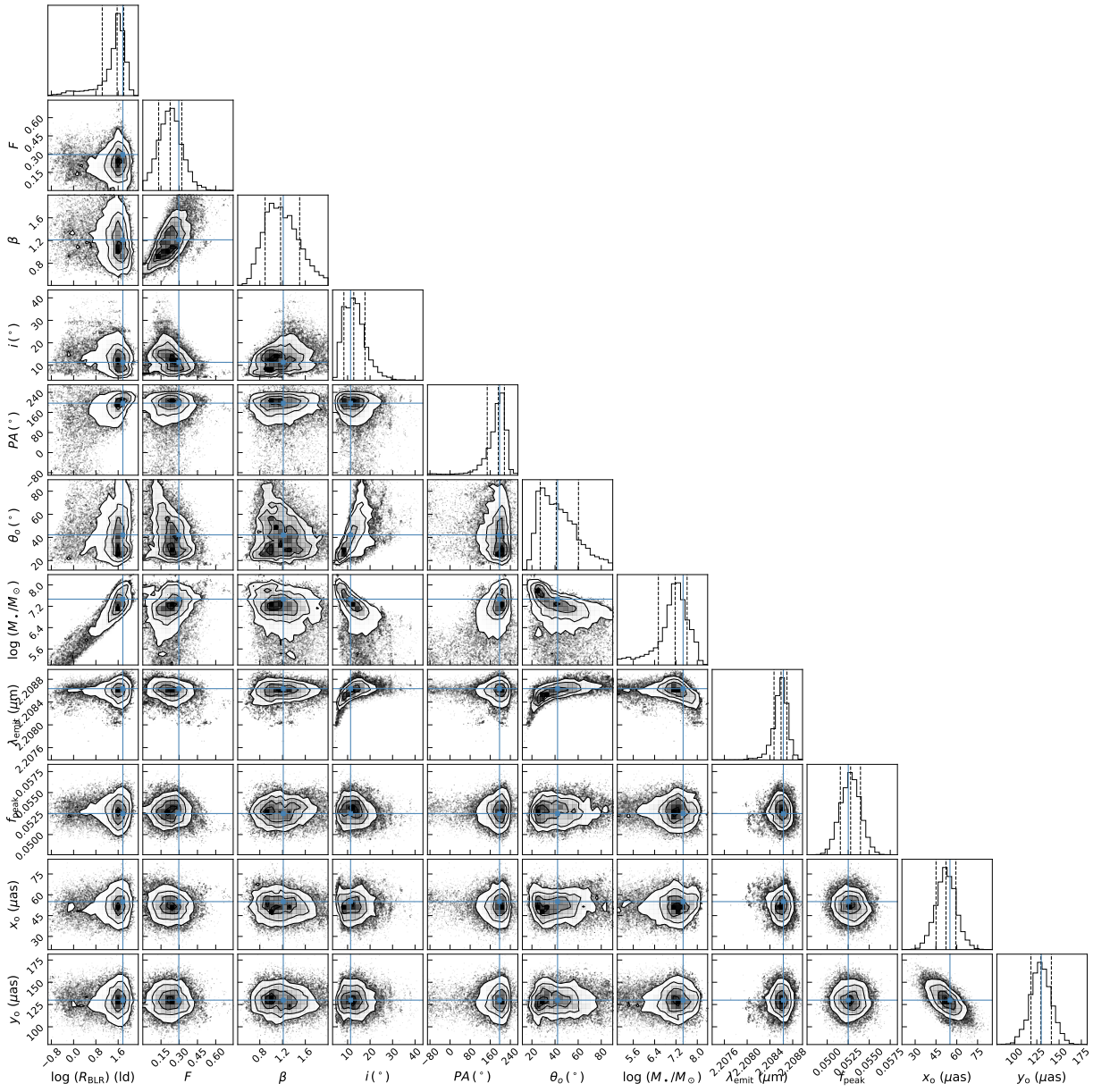

Figure A.3: Posterior probability distribution of the fitted parameters from the circular model fitting Mrk1239 data. The legends from Fig. A.1 still apply.

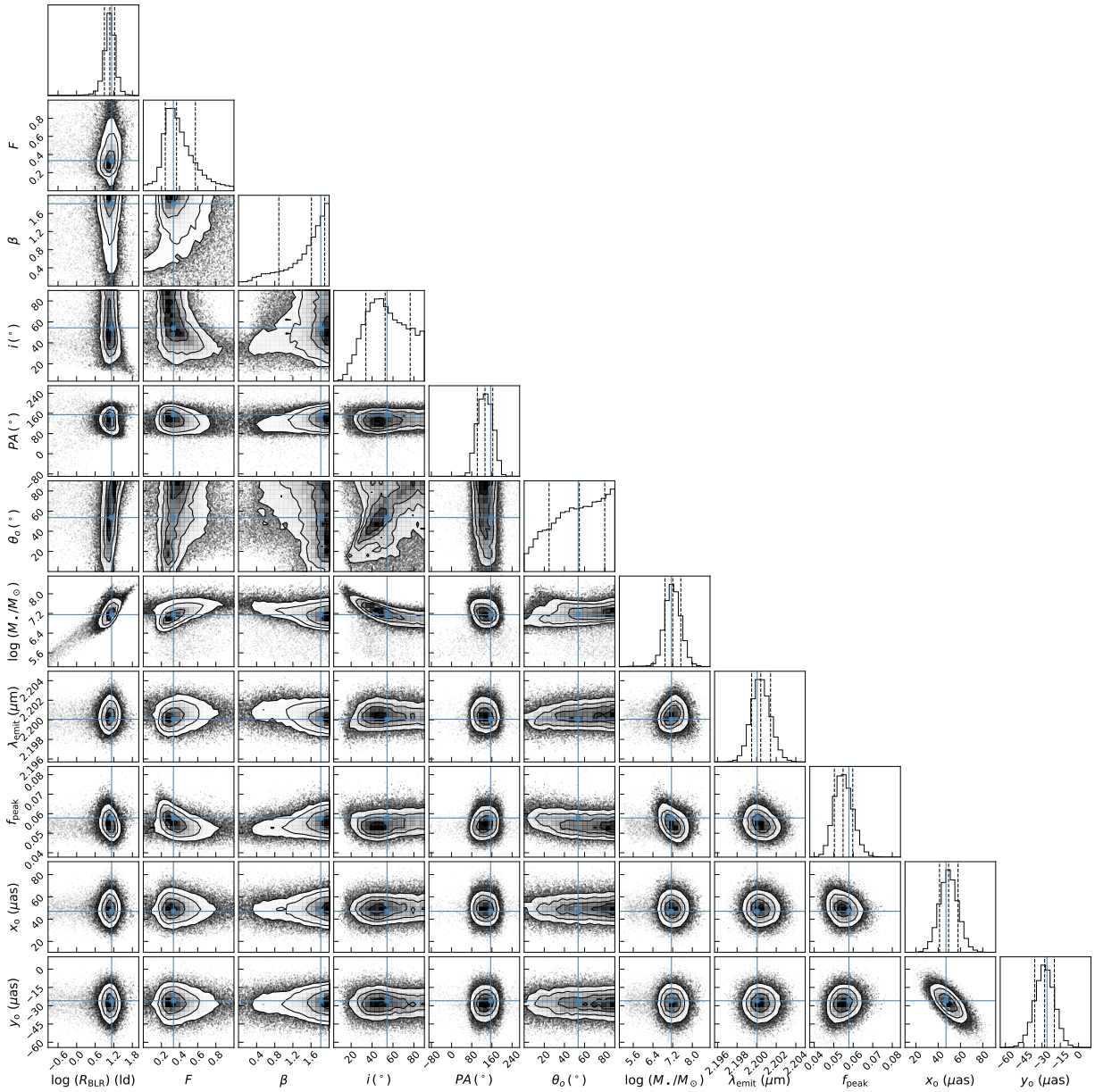

Figure A.4: Similar to Fig. A.3 but for IC 4329A.

Appendix B

Derivation of the flux ratio of two sides of the hot dust

We present here the full derivation of the flux ratio of the two sides of the hot dust as presented in Sect. 2.10 taken from GRAVITY Collaboration et al. (2024).

First, let $P_{\rm cont}$ be the distance of the hot dust photocentre to the origin:

$$P_{\rm cont} = \frac{\Sigma w_i r_i}{\Sigma w_i} \tag{B.1}$$

where $w_{\rm i}$ is the weight/flux of a dust clump at $r_{\rm i}$. We define $P_{\rm BLR}$ as the photocentre position of the BLR. In our simple model, the central BH is located at the origin of our coordinate system, and $P_{\rm BLR}$ is also situated at the origin. Considering the left and right side of the BLR, we have

$$P'_{\rm cont} = \frac{\Sigma w_l r_l + \Sigma w_r r_r}{\Sigma w_l + \Sigma w_r} \tag{B.2}$$

where the subscripts l and r refer to the left and right sides of the hot dust, respectively. The summations must be converted into definite integrals with the range of angles encompassing the left and right sides as their respective limits:

$$\begin{aligned} P_{\rm cont} = & \frac{1}{\int_{\pi/2}^{3\pi/2} w_l {\rm d}\theta + \int_{-\pi/2}^{\pi/2} w_r {\rm d}\theta} (W_{\rm l} R_{\rm dust} \int_{\pi/2}^{3\pi/2} \cos\theta \ {\rm d}\theta \\ & + W_{\rm r} R_{\rm dust} \int_{-\pi/2}^{\pi/2} \cos\theta \ {\rm d}\theta) \end{aligned} \tag{B.3}$$

where $W_{\rm l}$ and $W_{\rm r}$ are the total flux of the left and right sides of the hot dust, respectively. $R_{\rm dust}$ is the average size of the hot dust (we disregard the effect of a possible large discrepancy between the inner and outer radius of the hot dust ring for simplicity). The equation simplifies to:

$$P_{\rm cont} = \frac{2R_{\rm dust}(W_r - W_l)}{\pi(W_l + W_r)}. \tag{B.4}$$

If we re-define $R_{\rm off} = P_{\rm cont}$ (since $P_{\rm BLR}$ coincides with the origin and the continuum photocentre simply represents the actual offset), we get $\frac{R_{\rm off}}{R_{\rm dust}} = \frac{2}{\pi}\frac{W_{\rm r}-W_{\rm l}}{W_{\rm r}+W_{\rm l}}$. To calculate $W_{\rm r}/W_{\rm l}$, we have:

$$\frac{W_r}{W_l} = \frac{2 + \pi R_{\rm ratio}}{2 - \pi R_{\rm ratio}} \tag{B.5}$$

where $R_{\rm ratio} = \frac{R_{\rm off}}{R_{\rm dust}}$.

Appendix C

Target list and emission line properties

The following tables show the properties of the 29 $z \sim 2$ AGNs observed by SOFI presented in Chapter 3. The tables are taken from Santos et al. (2025a), which include their observation logs and emission line properties from their line decomposition.

Table C.1: All high-redshift targets with clear Hα detection from their SOFI spectra.

ID	Name	z	Date	Ave. Seeing ($''$)	Air-mass	Filter	K band mag.	Exp. time (s)	S/N
(1)	(2)	(3)	(4)	(5)	(6)	(7)	(8)	(9)	(10)
1	SDSS J121843.39+153617.2	2.266	17/04/22	0.71	1.42	Ks	13.7	120	45.3
2	SDSS J140632.73+091130.4	2.165			1.27	Ks	16.0	240	10.6
3	SDSS J112521.73+193843.9	2.328	20/04/22	1.79	1.53	Ks	16.0	240	6.1
4	SDSS J162449.39+092347.6	2.274			1.41	Ks	15.2	240	8.8
5	Q 0226-1024	2.276	09/09/22	2.23	1.21	Ks	13.9	90	18.3
6	SDSS J223116.24+224510.8	2.367	11/09/22	1.43	1.69	GRF	15.4	240	39.6
7	LAMOSTJ225948.68+052616.1	2.178	13/09/22	1.98	1.84	GRF	15.8	240	8.7
8	HE 0037-5155	2.127	11/11/22	1.96	1.11	GRF	15.1	240	21.5
9	HE 0320-1045	2.282	12/11/22	1.83	1.06	GRF	14.5	240	24.2
10	CTS A33.02	2.360			1.00	GRF	12.9	90	23.2
11	SDSS J074556.97+182509.7	2.339			1.59	GRF	15.8	240	6.4
12	SDSS J220607.48+203407.4	2.455	13/11/22	1.91	1.59	GRF	15.8	240	9.6
13	QBQS J051411.75-190139.4	2.609			1.03	GRF	15.7	240	59.7
14	SDSS J083713.14+191851.1	2.277	14/11/22	0.93	2.01	GRF	15.9	240	4.4
15	SDSS J2245.60-024407.1	2.403			1.15	GRF	15.6	240	29.1
16	2QZ J031527.8-272645	2.611			1.59	GRF	15.9	240	25.6
17	SDSS J025221.12-085515.6	2.296			1.07	GRF	15.5	240	11.5
18	CT 635	2.370	12/12/22	1.05	1.09	GRF	15.3	240	51.2
19	SDSS J022819.99-062010.5	2.522			1.09	GRF	15.9	240	9.6
20	SDSS J090938.71+041525.9	2.449	10/02/23	1.22	1.24	GRF	15.5	240	13.2
21	LAMOSTJ111209.45+072448.6	2.462	11/02/23	1.72	1.34	GRF	15.3	240	21.1
22	2QZ J113630.3+011949	2.138	12/02/23	0.85	1.38	GRF	15.7	240	10.7
23	FOCAP QNY4:53	2.180			1.67	GRF	15.8	240	7.6
24	J0504+0055	2.340	13/02/23	1.17	1.24	GRF	13.0	90	54.3
25	SDSS J093134.31+192622.1	2.392			1.94	GRF	16.0	240	15.2
26	SDSS J122654.39-005430.6	2.611			1.45	GRF	16.1	240	7.3
27	SDSS J153712.90+102557.1	2.362			2.10	GRF	15.9	240	13.2
28	J1006-6246	2.320	14/02/23	1.02	1.30	GRF	15.5	240	8.2
29	J1315+5206	2.145			1.40	GRF	15.1	240	12.3

Notes: The columns show the (1) ID numbers, (2) names, (3) redshifts taken from the catalogues where they are picked from, (4) dates of observation, (5) average seeing, and (6) airmass during observation, (7) used filters for their observations, (8) K band magnitudes taken from Flesch (2021) and Storey-Fisher et al. (2024), (9) total integration time, and (10) S/N based on the peak line flux of Hα line. K_s refers to the K short filter (2.00-2.30 μm) while GRF refers to the red grism (1.53-2.52 μm).

Table C.2: Emission line measurements of our high-redshift SOFI targets in the Hα spectral region.

	Hα						
ID	FWHM (km/s)	σ (km s^{-1})	$z_{\rm corr}$	$f_{\rm H\alpha}$ ($\times$ 10^{-15})	No. of Gaussian Comp. (Hα)	$M_{\rm BH}$ $\times$ 10^9 ($M_\odot$)	$\log_{10}$ $L_{\rm bol}$ (erg s^{-1})
(1)	(2)	(3)	(4)	(5)	(6)	(7)	(8)
1	6765	4448	2.269	22.90	2	$8.23^{+2.61}_{-1.99}$	46.69
2	3928	3691	2.167	2.434	2	$1.90^{+0.60}_{-0.46}$	45.88
3	2973	1264	2.328	0.932	1	$0.15^{+0.05}_{-0.04}$	45.61
4	5179	2284	2.276	3.924	2	$2.28^{+0.72}_{-0.55}$	46.08
5	5040	3500	2.276	17.27	2	$4.48^{+1.42}_{-1.08}$	46.59
6	2833	2589	2.369	7.538	2	$1.70^{+0.54}_{-0.41}$	46.48
7	5135	3464	2.178	5.251	2	$2.39^{+0.76}_{-0.58}$	45.95
8	3850	3067	2.132	8.015	2	$2.20^{+0.70}_{-0.53}$	46.22
9	3999	4815	2.282	8.860	2	$6.30^{+2.00}_{-1.52}$	46.42
10	4195	6260	2.366	12.03	2	$12.94^{+4.11}_{-3.13}$	46.51
11	4373	1858	2.341	1.682	1	$0.42^{+0.14}_{-0.10}$	45.80
12	3666	1558	2.456	0.720	1	$0.21^{+0.07}_{-0.05}$	45.40
13	3521	2541	2.615	7.932	2	$1.86^{+0.59}_{-0.45}$	46.28
14	4871	2069	2.276	1.235	1	$0.45^{+0.14}_{-0.45}$	46.40
15	5450	3654	2.403	7.592	2	$3.52^{+1.12}_{-0.85}$	46.31
16	3937	3620	2.613	4.473	2	$2.97^{+0.94}_{-0.72}$	46.30
17	5644	4436	2.299	4.462	2	$3.91^{+1.24}_{-0.94}$	46.11
18	3382	4008	2.378	13.48	2	$5.47^{+1.74}_{-1.32}$	46.41
19	3845	5036	2.522	4.280	2	$5.53^{+1.76}_{-1.34}$	46.09
20	4190	2529	2.455	11.93	2	$2.07^{+0.66}_{-0.50}$	46.57
21	2509	3467	2.463	15.30	2	$4.48^{+1.43}_{-1.08}$	46.77
22	2633	2757	2.143	3.496	2	$1.21^{+0.39}_{-0.29}$	45.94
23	4079	1733	2.182	2.082	1	$0.38^{+0.12}_{-0.09}$	45.76
24	4071	4142	2.342	29.14	2	$8.22^{+2.61}_{-1.99}$	46.87
25	2938	4309	2.393	2.918	2	$3.17^{+1.01}_{-0.77}$	46.14
26	5996	2547	2.612	2.310	1	$1.06^{+0.34}_{-0.26}$	45.85
27	3035	2517	2.363	16.90	2	$2.34^{+0.74}_{-0.56}$	46.65
28	3160	1343	2.325	1.060	1	$0.17^{+0.06}_{-0.04}$	46.50
29	4248	1805	2.422	1.504	1	$0.35^{+0.11}_{-0.08}$	45.90

Notes: The columns show the (1) ID number, (2) FWHM in km/s, (3) line dispersion (square root of the second moment of the line profile or σ) in km/s, (4) the corrected redshift based on the velocity offset of Hα with respect to its theoretical central wavelength, $z_{\rm corr}$, (5) integrated Hα flux in ergs cm^{-2} s^{-1}, (6) the number of Gaussian components used to fit the Hα line profile, (7) single-epoch BH mass estimate using Eqn. 6 of Woo et al. (2015), and (8) bolometric luminosity using the bolometric correction from Trakhtenbrot et al. (2017) to convert the λL_λ(5100 Å) to $L_{\rm bol}$. For ID#1-5 that were observed with the K_s filter, the λL_λ(5100 Å) were estimated from their Hα luminosity using Eqn. 4 of Woo et al. (2015), and the typical error of their $\log_{10}$ $L_{\rm bol}$ is $\sim$ 0.25. For the rest of the targets that were observed with the GRF filter, the λL_λ(5100 Å) were measured via Monte Carlo analysis of best-fit continuum after 1000 instances of fitting, and the typical error of their $\log_{10}$ $L_{\rm bol}$ is $\sim$ 0.014.

Table C.3: Emission line measurements of our high-redshift SOFI targets for Hβ, [OIII] doublet, and Hγ emission lines.

Hβ		[OIII]				Hγ
ID	$f_{H\beta}$ ($\times 10^{-15}$)	FWHM (km s^{-1})	σ (km s^{-1})	$f_{5007\ Å}$ ($\times 10^{-16}$)	$f_{4959\ Å}$ ($\times 10^{-16}$)	$f_{H\gamma}$ ($\times 10^{-16}$)
(1)	(2)	(3)	(4)	(5)	(6)	(7)
6	1.154	5330	2269	2.996	0.9960	
9	1.503	1015	435	2.968	0.9866	
10	1.121	2998	1274	5.949	1.977	
13	1.068	2273	967	4.987	1.657	0.1696
15	0.7207	1350	576	3.318	1.103	
16*	0.7679	4880	2113	-	8.093	1.805
17	0.6001	1848	787	1.812	0.6024	
18	1.245	8679	3385	3.919	1.302	
20	0.8404	4190	703	4.034	1.236	
21	3.543	1356	578	3.339	1.110	
22	0.503					
24	2.630	6248	3254	5.963	1.978	
27	3.024	1183	506	10.70	3.557	
28	0.2048					

Note: The columns show the (1) ID number (2) integrated Hβ flux, (3) FWHM of [OIII] doublet, (4) line dispersion (σ) of [OIII] doublet, (5) integrated flux of [O III]λ5007 emission line, (6) integrated flux of [OIII]λ4959 emission line, and (7) integrated Hγ flux. Each [OIII] line is fitted with one Gaussian component. All fluxes have units of ergs cm^{-2} s^{-1}.
*Only [O III] 4959 is fitted.

Table C.4: Emission line measurements of three high-redshift SOFI targets in the Hβ region where the Hα and Hβ line shapes are not fixed to be similar as discussed in Sec. 3.4.1.

Hβ (exceptions)				
ID	FWHM (km s^{-1})	σ (km s^{-1})	$f_{H\beta}$ ($\times 10^{-15}$ ergs cm^{-2} s^{-1})	No. of Gaussian Comp.
(1)	(2)	(3)	(4)	(5)
23	4079	1733	0.167	1
25	2741	1171	2.170	1
29	5449	7987	10.15	2

Appendix D

Summary of DyBEL BLR fitting results

Table D.1: Results of fitting the BLR model to the line profiles.

ID	Model	Tied?	Hα $R_{\rm BLR}$ [ld]	β	ϵ $\times 10^{-3}$	i [°]	θ_0 [°]	κ	γ	ξ	$f_{\rm flow}$	$f_{\rm ellip}$	θ_e [°]	$\Delta\phi_{\rm peak}$
(1)	(2)	(3)	(4)	(5)	(6)	(7)	(8)	(9)	(10)	(11)	(12)	(13)	(14)	(15)
1	F	-	2442^{+1123}_{-1582}	$1.36^{+0.18}_{-0.21}$	$+4.20^{+0.69}_{-8.27}$	55^{+23}_{-27}	25^{+23}_{-6}	$-0.39^{+0.74}_{-0.02}$	$3.92^{+0.48}_{-1.81}$	$0.45^{+0.33}_{-0.31}$	$0.43^{+0.26}_{-0.27}$	$0.17^{+0.27}_{-0.08}$	19^{+35}_{-7}	$9.3^{+7.3}_{-7.9}$
2	C	-	1128^{+457}_{-554}	$1.86^{+0.07}_{-0.31}$	$-0.34^{+0.45}_{-0.56}$	43^{+16}_{-19}	61^{+17}_{-24}							$4.6^{+4.2}_{-2.5}$
3	C	-	348^{+248}_{-229}	$1.56^{+0.20}_{-0.92}$	$0.22^{+0.74}_{-1.34}$	53^{+24}_{-27}	67^{+12}_{-43}							$0.3^{+1.2}_{-0.3}$
4	C	-	597^{+400}_{-373}	$1.83^{+0.03}_{-0.48}$	$-0.12^{+0.46}_{-0.55}$	25^{+20}_{-10}	50^{+18}_{-23}							$0.9^{+1.9}_{-0.6}$
5	F	-	1899^{+974}_{-1175}	$1.76^{+0.13}_{-0.21}$	$+0.91^{+1.09}_{-1.84}$	37^{+27}_{-20}	49^{+28}_{-23}	$-0.01^{+0.36}_{-0.34}$	$2.69^{+1.48}_{-1.12}$	$0.48^{+0.37}_{-0.31}$	$0.35^{+0.38}_{-0.24}$	$0.41^{+0.34}_{-0.27}$	36^{+35}_{-25}	$3.6^{+3.4}_{-2.7}$
6	C	Y	1552^{+1316}_{-335}	$1.76^{+0.13}_{-0.21}$	$-0.11^{+0.21}_{-0.23}$	33^{+20}_{-9}	50^{+24}_{-11}							$9.6^{+9.4}_{-4.2}$
7	C	-	905^{+1058}_{-378}	$1.48^{+0.35}_{-0.32}$	$-0.05^{+1.07}_{-0.88}$	37^{+33}_{-14}	53^{+25}_{-25}							$6.2^{+9.5}_{-4.3}$
8	C	-	1492^{+1074}_{-632}	$1.56^{+0.28}_{-0.28}$	$-0.32^{+0.54}_{-0.55}$	38^{+23}_{-16}	56^{+23}_{-21}							$7.7^{+8.6}_{-4.9}$
9	C	Y	2931^{+2272}_{-1089}	$1.80^{+0.11}_{-0.28}$	$-0.23^{+0.55}_{-0.36}$	34^{+22}_{-12}	52^{+24}_{-17}							$25.3^{+19.0}_{-16.4}$
10	C	Y	5199^{+3995}_{-2373}	$1.87^{+0.07}_{-0.29}$	$-0.44^{+0.68}_{-0.68}$	33^{+18}_{-14}	48^{+25}_{-17}							$21.5^{+30.0}_{-14.0}$
11	C	-	525^{+955}_{-339}	$1.23^{+0.50}_{-0.76}$	$-0.50^{+2.93}_{-2.50}$	53^{+29}_{-6}	44^{+33}_{-26}							$1.1^{+4.2}_{-0.9}$
12	C	-	252^{+338}_{-161}	$0.94^{+0.80}_{-0.45}$	$-0.06^{+1.67}_{-2.18}$	37^{+39}_{-10}	70^{+7}_{-50}							$0.9^{+2.6}_{-0.7}$
13	C	N	1354^{+1017}_{-717}	$1.64^{+0.22}_{-0.31}$	$-0.28^{+0.37}_{-0.54}$	34^{+21}_{-16}	53^{+23}_{-22}							$6.3^{+10.2}_{-3.7}$

Table D.1: continued.

ID	Model	Tied?	Hα $R_{\rm BLR}$ [ld]	β	ϵ $\times 10^{-3}$	i [°]	θ_0 [°]	κ	γ	ξ	$f_{\rm flow}$	$f_{\rm ellip}$	θ_e [°]	$\Delta\phi_{\rm peak}$
(1)	(2)	(3)	(4)	(5)	(6)	(7)	(8)	(9)	(10)	(11)	(12)	(13)	(14)	(15)
14	C	-	330^{+423}_{-220}	$1.39^{+0.38}_{-0.77}$	$-0.14^{+2.14}_{-1.98}$	48^{+27}_{-23}	59^{+18}_{-40}							$1.0^{+1.2}_{-1.0}$
15	C	Y	1273^{+776}_{-664}	$1.68^{+0.13}_{-0.35}$	$0.65^{+0.39}_{-0.80}$	35^{+28}_{-16}	60^{+19}_{-29}							$6.1^{+6.8}_{-4.1}$
16	C	Y	2339^{+2263}_{-12}	$1.46^{+0.39}_{-0.27}$	$-0.51^{+0.78}_{-0.80}$	41^{+27}_{-19}	59^{+19}_{-29}							$8.9^{+17.4}_{-6.1}$
17	C	Y	1151^{+718}_{-533}	$1.44^{+0.33}_{-0.28}$	$-0.53^{+0.59}_{-0.77}$	39^{+18}_{-18}	53^{+25}_{-18}							$5.8^{+5.8}_{-2.9}$
18	C	Y	2746^{+1645}_{-1140}	$1.79^{+0.11}_{-0.20}$	$-0.07^{+0.26}_{-0.30}$	32^{+12}_{-12}	47^{+18}_{-14}							$15.6^{+16.4}_{-6.8}$
19	C	-	1072^{+1645}_{-1140}	$1.56^{+0.22}_{-0.98}$	$+0.95^{+4.44}_{-2.93}$	36^{+40}_{-10}	53^{+24}_{-32}							$3.8^{+18.6}_{-3.1}$
20	C	Y	1150^{+1150}_{-620}	$1.40^{+0.40}_{-0.55}$	$-1.60^{+1.20}_{-1.22}$	42^{+26}_{-20}	51^{+25}_{-25}							$3.6^{+10.6}_{-2.5}$
21	C	Y	5510^{+2999}_{-3670}	$1.69^{+0.18}_{-0.44}$	$-0.05^{+0.51}_{-0.64}$	40^{+13}_{-23}	55^{+17}_{-31}							$19.8^{+35.1}_{-12.8}$
22	C	Y	1776^{+956}_{-946}	$1.79^{+0.14}_{-0.19}$	$-0.004^{+0.296}_{-0.292}$	37^{+22}_{-18}	55^{+22}_{-23}							$12.8^{+12.8}_{-7.8}$
23	C	Y	333^{+297}_{-162}	$1.61^{+0.22}_{-0.45}$	$-0.33^{+0.75}_{-0.55}$	38^{+31}_{-16}	55^{+22}_{-25}							$1.5^{+3.7}_{-1.1}$
24	C	Y	4651^{+1307}_{-1185}	$1.65^{+0.11}_{-0.11}$	$-0.26^{+0.17}_{-0.19}$	40^{+9}_{-9}	54^{+14}_{-10}							$25.4^{+14.2}_{-7.8}$
25	C	Y	4252^{+4221}_{-29}	$1.79^{+0.11}_{-0.49}$	$-0.15^{+0.67}_{-0.66}$	33^{+26}_{-13}	54^{+22}_{-26}							$21.1^{+28.6}_{-13.3}$
26	C	-	606^{+518}_{-430}	$1.48^{+0.26}_{-0.96}$	$-0.55^{+3.29}_{-2.63}$	48^{+28}_{-22}	61^{+16}_{-41}							$0.6^{+1.7}_{-0.5}$
27	C	Y	2112^{+2855}_{-1083}	$1.61^{+0.21}_{-0.68}$	$0.08^{+0.89}_{-0.98}$	38^{+33}_{-16}	69^{+9}_{-41}							$11.1^{+35.5}_{-7.1}$
28	C	Y	351^{+515}_{-277}	$1.56^{+0.21}_{-1.07}$	$-0.02^{+1.56}_{-2.09}$	35^{+30}_{-14}	43^{+33}_{-18}							$0.3^{+1.9}_{-0.3}$
29	C	N	436^{+359}_{-256}	$1.73^{+0.12}_{-0.52}$	$+23.32^{+0.41}_{-0.73}$	44^{+33}_{-18}	51^{+25}_{-42}							$1.1^{+3.7}_{-0.8}$

Note: The columns show (1) the ID number, (2) the model used (C for circular, F for full), (3) whether the central wavelength of Hβ and Hγ was tied to that of Hα whenever the other Balmer lines are available, (4) the Hα BLR size in ld, (5) the shape parameter of the radial cloud distribution, (6) the amount of shift on the central wavelength of the Balmer line(s), (7) inclination angle, (8) position angle, (9) anisotropy parameter, (10) vertical distribution of clouds, (11) midplane obscuration, (12) binary switch for inflowing ($f_{\rm flow} < 0.5$) and outflowing ($f_{\rm flow} > 0.5$) radial motion, (13) fraction of clouds in circular/bound orbits, (14) angular location for radial orbit distribution, and (15) the peak expected differential phase. All errors are 1σ uncertainties. More details about the BLR model parameters are discussed in Sect. 3.5, while the calculation of the peak expected differential phase is shown in Sect. 3.6.

Appendix E

Corner plot of the best-fit Pancoast model to the RDF simulation data

Fig. E.1 shows the corner plot of the best-fit Pancoast model discussed in Sect. 4.4..

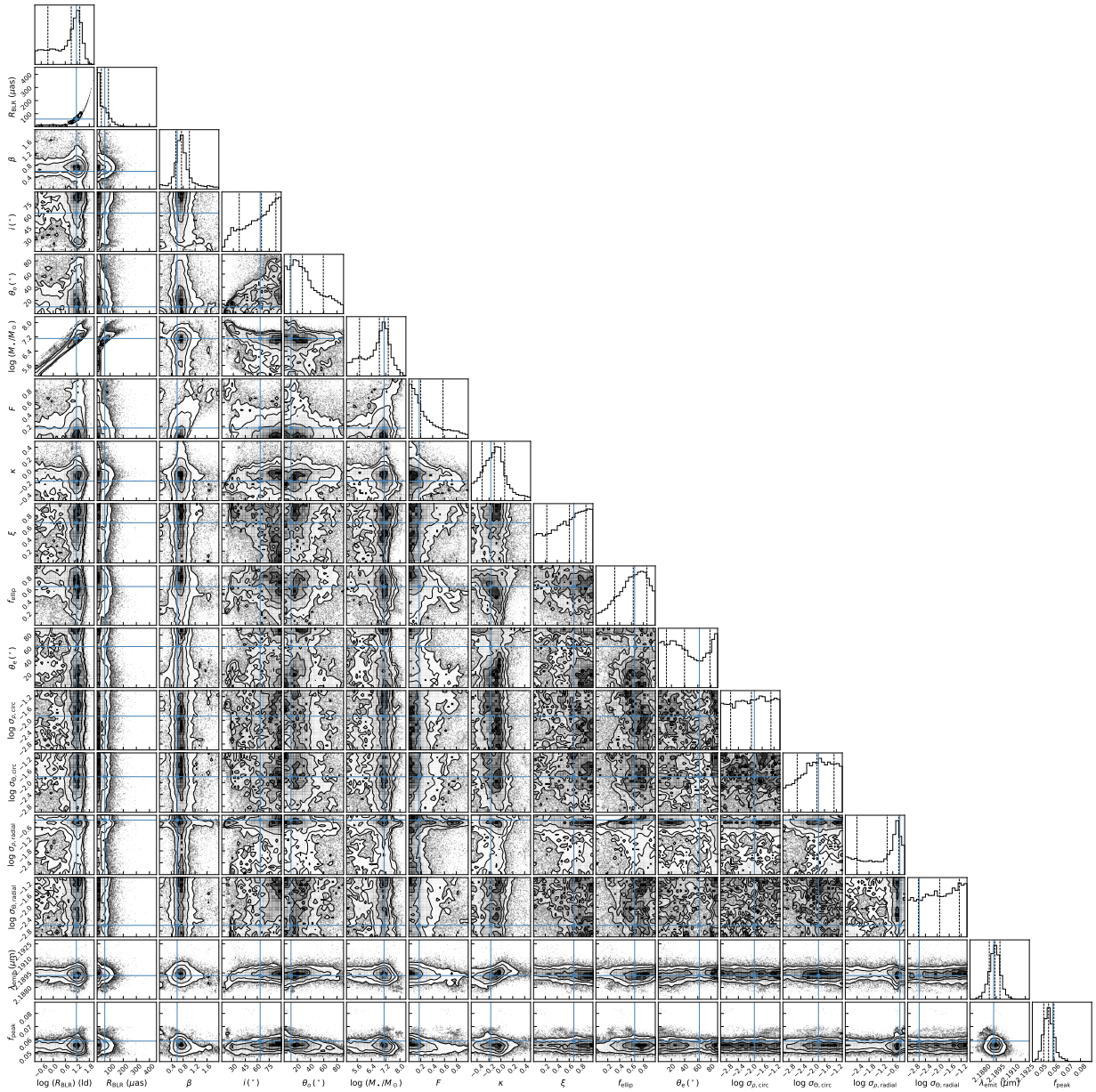

Figure E.1: Corner plot of the Pancoast model that best fits the simulated flux and phase data of the RDF simulation, as discussed in Sect. 4.4. The legends are similar to those of the previous corner plots (Figs. A.1, A.2, A.3, and A.4).

Bibliography

The SAMI Galaxy Survey: impact of star formation and AGN feedback processes on the ionized gas velocity dispersion. *MNRAS*, 531:4017–4032, 2024.

R. Abuter, F. Allouche, A. Amorim, C. Bailet, A. Berdeu, J. P. Berger, P. Berio, A. Bigioli, O. Boebion, M. L. Bolzer, H. Bonnet, et al. A dynamical measure of the black hole mass in a quasar 11 billion years ago. *Nature*, 627:281–285, 2024.

A. Acker, J. Köppen, M. Samland, and B. Stenholm. On the theoretical ratio of some nebular lines. *The Messenger*, 58:44–46, 1989.

A. Adamo, H. Atek, E. Bagley, M. B.and Bañados, K. S. Barrow, D. A. Berg, R. Bezanson, M. Bradač, G. Brammer, A. C. Carnall, and J. Chisholm. The First Billion Years, According to JWST. *arXiv:2405.21054*, 2024.

I. Almeida, R. Nemmen, and R.A. Riffel. Quenching star formation with low-luminosity AGN winds. *MNRAS*, 526(1):217, 2023.

G. F. Alvarez, J. R. Trump, Y. Homayouni, C. J. Grier, Y. Shen, K. Horne, I. Jennifer, H. Li, W. N. Brandt, L. C. Ho, and B. M. Peterson. The Sloan Digital Sky Survey Reverberation Mapping Project: The Hβ Radius–Luminosity Relation. *ApJ*, 899(1):73, 2020.

R. Antonucci. Unified models for active galactic nuclei and quasars. *ARA&A*, 31:473–521, 1993.

N. Arav, T. A. Barlow, A. Laor, and R. D. Blandford. Keck high-resolution spectroscopy of Mrk 335: Constraints on the number of emitting clouds in the broad-line region. *MNRAS*, 288(4):1015–1021, 1997.

N. Arav, T. A. Barlow, A. Laor, W. L. Sargent, and R. D. Blandford. Are AGN broad emission lines formed by discrete clouds? Analysis of Keck high-resolution spectroscopy of NGC 4151. *MNRAS*, 297(4):990–998, 1998.

H. Arp. Peculiar galaxies and radio sources. *Science*, 151(3715):1214–1216, 1966.

R. Arsenault, J. Alonso, H. Bonnet, J. Brynnel, B. Delabre, R. Donaldson, C. Dupuy, E. Fedrigo, J. Farinato, N.N. Hubin, L. Ivanescu, M. E. Kasper, J. Paufique, S. Rossi, S. Tordo, S. Stroebele, J.-L. Lizon, P. Gigan, F. Delplancke, A. Silber, M. Quattri, and R. Reiss. Macao-vlti: an adaptive optics system for the eso interferometer. *Adaptive Optical System Technologies II*, 4839:174, 2003. ISSN 0277786X. doi: 10.1117/12.458836.

J. N. Bahcall, B. Z. Kozlovsky, and E. E. Salpeter. On the time dependence of emission-line strengths from a photoionized nebula. *ApJ*, 171:467, 1972.

J. A. Baldwin, M. M. Phillips, and R. Terlevich. Classification parameters for the emission-line spectra of extragalactic objects. *PASP*, 93(551):5, 1981.

J. A. Baldwin, G. J. Ferland, K. T. Korista, F. Hamann, and A. LaCluyzé. The origin of Fe II emission in active galactic nuclei. *ApJ*, 615(2):610, 2004.

A. Baskin and A. Laor. Dust inflated accretion disc as the origin of the broad line region in active galactic nuclei. *MNRAS*, 474(2):1970–1994, 2018.

M. Batiste, M. C. Bentz, S. I. Raimundo, M. Vestergaard, and C.A. Onken. Recalibration of the M_{BH}–σ_* Relation for AGN. *ApJ*, 838:L10, 2017.

W. H. Baumgartner, J. Tueller, C. B. Markwardt, G. K. Skinner, S. Barthelmy, R. F. Mushotzky, P. A. Evans, and N. Gehrels. The 70 month Swift-BAT all-sky hard X-ray survey. *ApJS*, 207(2):19, 2013.

V. Beckmann and C. Shrader. *Active galactic nuclei.* John Wiley & Sons, 2012.

M. C. Begelman, C. F. McKee, and G. A. Shields. Compton heated winds and coronae above accretion disks. I. Dynamics. *ApJ*, 271:70, 1983.

M. C. Bentz, B. M. Peterson, R. W. Pogge, M. Vestergaard, and C.A. Onken. The radius-luminosity relationship for active galactic nuclei: the effect of host-galaxy starlight on luminosity measurements. *ApJ*, 644(1):133, 2006.

M. C. Bentz, B. M. Peterson, H. Netzer, R. W. Pogge, and M. Vestergaard. The radius–luminosity relationship for active galactic nuclei: the effect of host-galaxy starlight on luminosity measurements. II. The full sample of reverberation-mapped AGNs. *ApJ*, 697(1):160, 2009.

M. C. Bentz, K. Horne, A. J. Barth, V. N. Bennert, G. Canalizo, A. V. Filippenko, E. L. Gates, M. A. Malkan, T. Minezaki, T. Treu, and J.H. Woo. The Lick AGN monitoring project: Velocity-delay maps from the maximum-entropy method for Arp 151. *ApJ*, 720 (1):L46, 2010.

M. C. Bentz, K. D. Denney, C. J. Grier, A. J. Barth, B. M. Peterson, M. Vestergaard, V. N. Bennert, G. Canalizo, G. De Rosa, A. V. Filippenko, E. L. Gates, J. E. Greene, W. Li, M. A. Malkan, R. W. Pogge, D. Stern, T. Treu, and J. H. Woo. The low-luminosity end of the radius-luminosity relationship for active galactic nuclei. *ApJ*, 767(2):149, 2013.

M. C. Bentz, P. R. Williams, R. Street, C. A. Onken, M. Valluri, and T. Treu. A detailed view of the broad-line region in ngc 3783 from velocity-resolved reverberation mapping. *ApJ*, 920(2):112, 2021.

M. C. Bentz, R. Street, C. A. Onken, and M. Valluri. Robotic reverberation mapping of the southern Seyfert NGC 3783. *ApJ*, 906(1):50, 2021a.

M. C. Bentz, P. R. Williams, R. Street, C. A. Onken, M. Valluri, and T. Treu. A Detailed View of the Broad-line Region in NGC 3783 from Velocity-resolved Reverberation Mapping. *ApJ*, 920(2):112, 2021b.

M. C. Bentz, P. R. Williams, and T. Treu. The Broad Line Region and Black Hole Mass of NGC 4151. *ApJ*, 934(2):168, 2022.

M. C. Bentz, C. A. Onken, R. Street, and M. Valluri. Reverberation Mapping of IC4329A. *ApJ*, 944(1):29, 2023.

J.P. Berger and D. Segransan. An introduction to visibility modeling. *New Astron. Rev.*, 51(8-9):576, 2007.

L. Binette, C. G. Magris, G. Stasinska, and A.G. Bruzual. Photoionization in elliptical galaxies by old stars. *A&A*, 292(1):13, 1994.

J. Binney and S. Tremaine. *Galactic dynamics, 2nd edition.* Princeton University Press, 2008.

M. Bischetti, E. Piconcelli, C. Feruglio, F. Fiore, S. Carniani, M. Brusa, C. Cicone, C. Vignali, A. Bongiorno, G. Cresci, , V. Mainieri, R. Maiolino, A. Marconi, E. Nardini, and L. Zappacosta. The gentle monster PDS 456: Kiloparsec-scale molecular outflow and its implications for QSO feedback. *A&A*, 628:A118, 2019.

M. Bischetti, C. Feruglio, E. Piconcelli, F. Duras, Pérez-Torres M., R. Herrero, G. Venturi, S. Carniani, G. Bruni, I. Gavignaud, and V. Testa. The WISSH quasars project-IX. Cold gas content and environment of luminous QSOs at z $\sim$ 2.4–4.7. *A&A*, 645:A33, 2021.

C. Blain, J. C. Christou, C. Clergeon, R. Diaz, A. Garcia-Rissmann, V. Garrel, S. Goodsell, M. Lamb, G. Singh, and G. Sivo. Adaptive optics at Gemini observatories: Past, present, and future. *In Adaptive Optics Systems IX, SPIE*, 13097:123, 2024.

R. D. Blandford and M.C. Begelman. On the fate of gas accreting at a low rate on to a black hole. *MNRAS*, 303(1):L1, 1999.

R. D. Blandford and C. F. McKee. Reverberation mapping of the emission line regions of Seyfert galaxies and quasars. *ApJ*, 255:419, 1982a.

R. D. Blandford and D. G. Payne. Hydromagnetic flows from accretion discs and the production of radio jets. *MNRAS*, 199(4):883, 1982b.

B. D. Boizelle, A.J. Barth, J. L. Walsh, D. A. Buote, A. J. Baker, J. Darling, and L.C. Ho. A precision measurement of the mass of the black hole in ngc 3258 from high-resolution alma observations of its circumnuclear disk. *ApJ*, 881:10, 2019.

F. Bollati, A. Lupi, M. Dotti, and F. Haardt. Exploring the connection between AGN radiative feedback and massive black hole spin. *A&A*, 690:A194, 2024.

T. Boller, W. N. Brandt, and H. Fink. Soft X-ray properties of narrow-line Seyfert 1 galaxies. *A&A*, 305:53, 1996.

J. G. Bolton and G. J. Stanley. Variable source of radio frequency radiation in the constellation of Cygnus. *Nature*, 161(4087):312–313, 1948.

J. G. Bolton, G. J. Stanley, and O. B. Slee. *Positions of three discrete sources of galactic radio-frequency radiation. In A Source Book in Astronomy and Astrophysics.* Harvard University Press, 1979.

C. M. Booth and J. Schaye. Dark matter haloes determine the masses of supermassive black holes. *MNRAS*, 405(1):L1–L5, 2010.

T. Boroson. Blueshifted [O III] emission: Indications of a dynamic narrow-line region. *ApJ*, 130(2):381, 2005.

T. A. Boroson. Black hole mass and Eddington ratio as drivers for the observable properties of radio-loud and radio-quiet QSOs. *ApJ*, 565(1):78, 2002.

M. C. Bottorff and G. J. Ferland. Magnetic confinement, magnetohydrodynamic waves and smooth line profiles in active galactic nuclei. *MNRAS*, 316(1):103, 2000.

L. W. Brenneman, C. S. Reynolds, M. A. Nowak, R. C. Reis, M. Trippe, A. C. Fabian, K. Iwasawa, J. C. Lee, J. M. Miller, and R. F. Mushotzky. The Spin of the Supermassive Black Hole In NGC 3783. *ApJ*, 736:103, 2011.

M. S. Brotherton, B. J. Wills, P. J. Francis, and C.C. Steidel. The intermediate line region of QSOs. *ApJ*, 430:495–504, 1994.

M.Z. Buhariwalla, S.G. Waddell, L.C. Gallo, D. Grupe, and S Komossa. Uncovering the Primary X-Ray Emission and Possible Starburst Component in the Polarized NLS1 Mrk 1239. *ApJ*, 901:118, 2020.

L. Burtscher, R. I. Davies, J. Graciá'-Carpio, M. J. Koss, M. Y. Lin, D. Lutz, P. Nandra, H. Netzer, G. O. de Xivry, C. Ricci, and D.J. Rosario. On the relation of optical obscuration and x-ray absorption in seyfert galaxies. *A&A*, 586:A28, 2016.

D. F. Buscher and M. Longair. *Practical Optical Interferometry: Imaging at Visible and Infrared Wavelengths*. Cambridge University Press, 2015.

L. Byrne, C. A. Faucher-Giguére, J. Stern, D. Anglés-Alcázar, S. Wellons, A. B. Gurvich, and P. F. Hopkins. Stellar feedback-regulated black hole growth: Driving factors from nuclear to halo scales. *MNRAS*, 520(1):722, 2023.

E. M. Cackett, M. C. Bentz, and E. Kara. Reverberation mapping of active galactic nuclei: From X-ray corona to dusty torus. *Science*, 24, 2021. doi: 10.1016/j.isci. URL `https://doi.org/10.1016/j.isci.`

T. Caglar, L. Burtscher, B. Brandl, J. Brinchmann, R. I. Davies, E. K. S. Hicks, M. Koss, M.-Y. Lin, W. Maciejewski, F. Müller-Sánchez, R. A. Riffel, R. Riffel, D. J. Rosario, M. Schartmann, M. Schnorr-Müller, T. T. Shimizu, T. Storchi-Bergmann, S. Veilleux, G. O. de Xivry, and V. N. Bennert. LLAMA: The M_{BH}- σ_* relation of the most luminous local AGNs. *A&A*, 634:A114, 2020.

R. C. Canfield and R.C. Puetter. Theoretical Quasar Emission Line Ratios-Part Two-Hydrogen Lyman-Alpha Balmer and Paschen Lines and the Balmer Continuum. *ApJ*, 390:390, 1981.

P. R. Capelo, M. Volonteri, M. Dotti, J. M. Bellovary, L. Mayer, and F. Governato. Growth and activity of black holes in galaxy mergers with varying mass ratios. *MNRAS*, 447(3): 2123, 2015.

P. R. Capelo, C. Feruglio, R. C. Hickox, and F. Tombesi. *Black hole-galaxy co-evolution and the role of feedback*. In Handbook of X-ray and Gamma-ray Astrophysics, Singapore: Springer Nature Singapore, 2024.

M. Cappi, F. Tombesi, S. Bianchi, M. Dadina, M. Giustini, G. Malaguti, L. Maraschi, G. G. C. Palumbo, P. O. Petrucci, G. Ponti, C. Vignali, and T. Yaqoob. X-ray evidence for a mildly relativistic and variable outflow in the luminous Seyfert 1 galaxy Mrk 509. *A&A*, 504:401–407, 2009.

T. E. Carone, B. M. Peterson, J. Bechtold, R. Bertram, K. Bischoff, M. Dietrich, A. V. Filippenko, L. C. Ho, J. P. Huchra, W. Kollatschny, and K.T. Korista. Optical continuum and emission-line variability of the Seyfert 1 galaxy Markarian 509. *ApJ*, 471:737, 1996.

R. Carraro, G. Rodighiero, P. Cassata, M. Brusa, F. Shankar, I. Baronchelli, E. Daddi, I. Delvecchio, A. Franceschini, R. Griffiths, and C. Gruppioni. Coevolution of black hole accretion and star formation in galaxies up to z= 3.5. *A&A*, 642:A65, 2020.

L. S. Chajet and P.B. Hall. Magnetohydrodynamic disc winds and linewidth distributions. *MNRAS*, 465:2314, 2013.

L. S. Chajet and P.B. Hall. Magnetohydrodynamic disc winds and line width distributions–II. *MNRAS*, 465(2):1741, 2017.

M. Chatzikos, S. Bianchi, F. Camilloni, P. Chakraborty, C.M. Gunasekera, F. Guzmán, J.S. Milby, A. Sarkar, G. Shaw, P.A. van Hoof, and G.J. Ferland. The 2023 release of Cloudy. *RMxAA*, 59(2):327, 2023.

J. Chiang and N. Murray. Reverberation Mapping and the Disk-Wind Model of the Broad-Line Region. *ApJ*, 466:704, 1996.

M. Cisternas, K. Jahnke, A. Bongiorno, K. J. Inskip, C. D. Impey, A. M. Koekemoer, A. Merloni, M. Salvato, and J.R. Trump. Secular Evolution and a Non-evolving Black-hole-to-galaxy Mass Ratio in the Last 7 Gyr. *ApJ*, 741(1):L11, 2011.

E. J. Colbert, S. A. Baum, J. F. Gallimore, C. P. O'Dea, and J.A. Christensen. Large-Scale Outflows in Edge-on Seyfert Galaxies. II. Kiloparsec-Scale Radio Continuum Emission. *ApJ*, 467:551, 1996.

S. Collin and J. P. Zahn. Star formation in accretion disks around massive black holes and pregalactic enrichment. *Ap&SS*, 265:501, 1999.

S. Collin and J.P. Zahn. Star formation in accretion discs: From the Galactic center to active galactic nuclei. *MNRAS*, 477(2):419, 2008.

S. Collin, T. Kawaguchi, B. M. Peterson, and M. Vestergaard. Systematic effects in measurement of black hole masses by emission-line reverberation of active galactic nuclei: Eddington ratio and inclination. *A&A*, 456(1):75–90, 2006. doi: 10.1051/0004-6361:20064878.

A. Comastri. *Compton-thick AGN: the dark side of the X-ray background.* In Supermassive Black Holes in the Distant Universe, Dordrecht: Springer Netherlands, 2004.

P. A. Crowther and B. Bohannan. The distinction between OIafpe and WNLha stars. A spectral analysis of HD 151804, HD 152408 and HDE 313846. *A&A*, 317:532–547, 1997.

S. J. Curran. *Seyfert Galaxies: A Review.* PhD thesis, Chalmers University of Technology, Göteborg, Sweden, 2000. URL `https://ned.ipac.caltech.edu/level5/Curran/Curran_contents.html`.

M. C. Cushing, W. D. Vacca, and J. T. Rayner. Spextool: A spectral extraction package for SpeX, a 0.8–5.5 micron cross-dispersed spectrograph. *PASP*, 116(818):362, 2004.

B. Czerny and K. Hryniewicz. The origin of the broad line region in active galactic nuclei. *A&A*, 525:L8, 2011.

B. Czerny, J. Modzelewska, F. Petrogalli, W. Pych, T. P. Adhikari, P. T. Życki, K. Hryniewicz, M. Krupa, A. Świe, and M. Nikołajuk. The dust origin of the Broad Line Region and the model: Consequences for AGN unification scheme. *Adv. in Space Res.*, 55(7):1806–1815, 2015.

B. Czerny, Y. R. Li, K. Hryniewicz, S. Panda, C. Wildy, M. Sniegowska, J. M. Wang, J. Sredzinska, and V. Karas. Failed radiatively accelerated dusty outflow model of the broad line region in active galactic nuclei. I. Analytical solution. *ApJ*, 846(2):154, 2017.

M. Czerny and A. R. King. Accretion disc winds and coronae. *MNRAS*, 236(4):843, 1989.

E. Daddi, D. M. Alexander, M. Dickinson, R. Gilli, A. Renzini, D. Elbaz, A. Cimatti, R. Chary, D. Frayer, F. E. Bauer, and W. N. Brandt. Multiwavelength study of massive galaxies at z $\sim$ 2. II. Widespread compton-thick active galactic nuclei and the concurrent growth of black holes and bulges. *ApJ*, 670(1):173, 2007.

E. Dalla Bontá, B. M. Peterson, M. C. Bentz, W. N. Brandt, S. Ciroi, G. De Rosa, G. F. Alvarez, C. J. Grier, P. B. Hall, J. V. H. Santisteban, and L. C. Ho. The Sloan Digital Sky Survey Reverberation Mapping Project: Estimating masses of black holes in quasars with single-epoch spectroscopy. *ApJ*, 903(2):112, 2020.

R. Davies and M. Kasper. Adaptive optics for astronomy. *ARA&A*, 50(1):305, 2012.

R. I. Davies, L. J. Tacconi, and R. Genzel. The Nuclear Gas Dynamics and Star Formation Of NGC 7469. *ApJ*, 602:148, 2004a.

R. I. Davies, L. J. Tacconi, and R. Genzel. The Nuclear Gas Dynamics and Star Formation of Markarian 231. *ApJ*, 613:781, 2004b.

T. A. Davis. A figure of merit for black hole mass measurements with molecular gas. *MNRAS*, 443:911, 2014.

T. A. Davis, M. Bureau, M. Cappellari, M. Sarzi, and L. Blitz. A black-hole mass measurement from molecular gas kinematics in NGC4526. *Nature*, 494:328–330, 2013. doi: 10.1038/nature11819.

I. de La Calle Pérez, A. L. Longinotti, M. Guainazzi, S. Bianchi, M. Dovčiak, M. Cappi, G. Matt, G. Miniutti, P. O. Petrucci, E. Piconcelli, and G. Ponti. FERO: Finding extreme relativistic objects — I. Statistics of relativistic Fe Kα lines in radio-quiet Type 1 AGN. *A&A*, 524:A50, 2010.

M. Dehghanian, G. J. Ferland, B. M. Peterson, G. A. Kriss, K. T. Korista, M. Chatzikos, F. Guzmán, N. Arav, G. De Rosa, M. R. Goad, and M. Mehdipour. A Wind-based Unification Model for NGC 5548: Spectral Holidays, Nondisk Emission, and Implications for Changing-look Quasars. *ApJ*, 882(2):L30, 2019.

J. P. Delvaille, M. J. Geller, and H. W. Schnopper. X-Ray Observation Of IC 4329A. *ApJ*, 226:L69, 1978.

I. Delvecchio, E. Daddi, F. Shankar, J. R. Mullaney, G. Zamorani, J. Aird, E. Bernhard, A. Cimatti, D. Elbaz, M. Giavalisco, and L.P. Grimmett. The Galaxy's Gas Content Regulated by the Dark Matter Halo Mass Results in a Superlinear M_{BH}–M_* Relation. *ApJ*, 885(2):L36, 2019.

R. Dempsey and N. L. Zakamska. The size–luminosity relationship of quasar narrow-line regions. *MNRAS*, 477(4):4615–4626, 2018.

M. den Brok, A. C. Seth, A. J. Barth, D. J. Carson, N. Neumayer, M. Cappellari, V. P. Debattista, L. C. Ho, C. E. Hood, and R.M. McDermid. Measuring the mass of the central black hole in the bulgeless galaxy NGC 4395 from gas dynamical modeling. *ApJ*, 809(1):101, 2015.

K. D. Denney, B. M. Peterson, R. W. Pogge, A. Adair, D. W. Atlee, K. Au-Yong, M. C. Bentz, J. C. Bird, D. J. Brokofsky, E. Chisholm, and M.L. Comins. Diverse kinematic signatures from reverberation mapping of the broad-line region in AGNs. *ApJ*, 704(2): L80, 2009.

C. D. Dermer, S.J. Sturner, and R. Schlickeiser. Nonthermal Compton and synchrotron processes in the jets of active galactic nuclei. *ApJS*, 109(1):103, 1997.

N. Devereux. Photoionization Modeling of the Low-luminosity Seyfert 1 Nucleus in NGC 3516. *ApJ*, 822(2):69, 2016.

A. M. Diamond-Stanic and G.H. Rieke. The Relationship between Black Hole Growth and Star Formation in Seyfert Galaxies. *ApJ*, 726(2):168, 2012.

E. A. Dibai. On the Difference Between Seyfert 1 and Seyfert-2 Galaxies. *Pis'ma v Astron. Zh.*, 7:248–252, 1971.

M. Dietrich, S. J. Wagner, T. L. Courvoisier, H. Bock, and P. North. Structure of the broad-line region of 3C 273. *A&A*, 351:31–42, 1999.

X. Ding, M. Onoue, J. D. Silverman, Y. Matsuoka, T. Izumi, M. A. Strauss, K. Jahnke, C. L. Phillips, J. Li, M. Volonteri, and Z. Haiman. Detection of stellar light from quasar host galaxies at redshifts above 6. *Nature*, 621(7977):51–55, 2023.

Y. Ding, R. Li, L. C. Ho, and C. Ricci. Accretion Disk Outflow during the X-Ray Flare of the Super-Eddington Active Nucleus of I Zwicky 1. *ApJ*, 931:77, 2022.

A. Doi, K. Wajima, Y. Hagiwara, and M. Inoue. A Fanaroff-Riley Type I candidate in Narrow-Line Seyfert 1 galaxy Mrk 1239. *ApJ*, 798:L30, 2015.

A. Domiciano de Souza, J. Zorec, S. Jankov, F. Vakili, L. Abe, and E. Janot-Pacheco. Stellar differential rotation and inclination angle from spectro-interferometry. *A&A*, 418 (2):781–794, 2004.

A Domínguez, B. Siana, A. L. Henry, C. Scarlata, A. G. Bedregal, M. Malkan, H. Atek, N. R. Ross, J. W. Colbert, H. I. Teplitz, M. Rafelski, P. McCarthy, A. Bunker, N. P. Hathi, A. Dressler, C. L. Martin, and Masters D. Dust extinction from Balmer decrements of star-forming galaxies at $0.75 < z < 1.5$ with HST/WFC3 spectroscopy from the WISP survey. *ApJ*, 763(2):145, 2013.

C. Done and J. H. Krolik. Kinemtaics of the Broad Emission Line Region in NGC 5548. *ApJ*, 463:144–147, 1996.

X. Dong, T. Wang, J. Wang, W. Yuan, H. Zhou, H. Dai, and K. Zhang. Broad-line Balmer decrements in blue active galactic nuclei. *MNRAS*, 383(2):581, 2007.

Xiaobo Dong, Tinggui Wang, Jianguo Wang, Weimin Yuan, Hongyan Zhou, Haifeng Dai, and Kai Zhang. Broad-line Balmer decrements in blue active galactic nuclei. *MNRAS*, 383(2):581–592, 2008. doi: 10.1111/j.1365-2966.2007.12560.x.

A. Dorodnitsyn, T. Kallman, and G. S. Bisnovatyi-Kogan. AGN obscuration through dusty, infrared-dominated flows. II. Multidimensional, radiation-hydrodynamics modeling. *ApJ*, 747(1):8, 2012.

B. T. Draine and E. E. Salpeter. On the physics of dust grains in hot gas. *ApJ*, 231:77, 1979.

P. Du and J. M. Wang. The radius–luminosity relationship depends on optical spectra in active galactic nuclei. *ApJ*, 886(1):42, 2019.

P. Du, J. M. Wang, C. Hu, D. Valls-Gabaud, J. A. Baldwin, J. Q. Ge, and S.J. Xue. Outflows from active galactic nuclei: the BLR–NLR metallicity correlation. *MNRAS*, 438(4):2828, 2014a.

P. Du, C. Hu, K. X. Lu, F. Wang, J. Qiu, Y. R. Li, J. M. Bai, S. Kaspi, H. Netzer, J. M. Wang, and SEAMBH collaboration. Supermassive black holes with high accretion rates in active galactic nuclei. I. First results from a new reverberation mapping campaign. *ApJ*, 782(1):45, 2014b.

P. Du, C. Hu, K. X. Lu, Y. K. Huang, C. Cheng, J. Qiu, Y. R. Li, Y. W. Zhang, X. L. Fan, J. M. Bai, and W. H. Bian. Supermassive black holes with high accretion rates in active galactic nuclei. IV. Hβ time lags and implications for super-Eddington accretion. *ApJ*, 806(1):22, 2015.

P. Du, K. X. Lu, C. Hu, J. Qiu, Y. R. Li, Y. K. Huang, F. Wang, J. M. Bai, W. H. Bian, Y. F. Yuan, and L. C. Ho. Supermassive black holes with high accretion rates in active galactic nuclei. VI. Velocity-resolved reverberation mapping of the Hβ line. *ApJ*, 820(1): 27, 2016a.

P. Du, J. M. Wang, C. Hu, L. C. Ho, Y. R. Li, and J. M. Bai. The fundamental plane of the broad-line region in active galactic nuclei. *ApJ*, 818(1):L14, 2016b.

P. Du, M. S. Brotherton, K. Wang, Z. P. Huang, C. Hu, D. H. Kasper, W. T. Chick, M. L. Nguyen, J. Maithil, D. Hand, and Y.R. Li. Monitoring AGNs with Hβ asymmetry. I. First results: velocity-resolved reverberation mapping. *ApJ*, 869(2):142, 2018a.

P. Du, Z. X. Zhang, K. Wang, Y. K. Huang, Y. Zhang, K. X. Lu, C. Hu, Y. R. Li, J. M. Bai, W. H. Bian, and Y. F. Yuan. Supermassive black holes with high accretion rates in active galactic nuclei. IX. 10 New Observations of reverberation mapping and shortened Hβ lags. *ApJ*, 856(1):6, 2018b.

A. S. Eddington. *The Internal Constitution of the Stars*. Cambridge: Cambridge University Press, 1926.

F. Eisenhauer, J. D. Monnier, and O. Pfuhl. Advances in optical/infrared interferometry. *ARA&A*, 61(1):237, 2023.

M. Elitzur, L.C. Ho, and J.R. Trump. Evolution of broad-line emission from active galactic nuclei. *MNRAS*, 438(4):3340, 2014.

M. Elvis. A structure for quasars. *ApJ*, 545(1):63, 2000.

R. T. Emmering, R.D. Blandford, and I. Shlosman. Magnetic acceleration of broad emission-line clouds in active galactic nuclei. *ApJ*, 385:460, 1992.

M. Eracleous and J.P. Halpern. Doubled-peaked emission lines in active galactic nuclei. *ApJS*, 90(1):1–30, 1994.

Planck Collaboration et al. Planck 2015 results-XIII. Cosmological parameters. *A&A*, 594: A13, 2016.

R. N. Eze. Fe Kα line in hard X-ray emitting symbiotic stars. *MNRAS*, 437(1):857, 2004.

A. C. Fabian, A. Lohfink, R. Belmont, J. Malzac, and P. Coppi. Properties of AGN coronae in the NuSTAR era–II. Hybrid plasma. *MNRAS*, 467(3):2566–2570, 2017.

R. Falomo, J. K. Kotilainen, C. Pagani, R. Scarpa, and A. Treves. The cosmic evolution of quasar host galaxies. *ApJ*, 604(2):495, 2004.

E. A. Fath. The spectra of some spiral nebulae and globular star clusters. *Lick Obs. Bull.*, 5:71, 1909.

G. J. Ferland, C. Hu, J. M. Wang, J. A. Baldwin, R. L. Porter, P. A. Van Hoof, and R. J. R. Williams. Implications of infalling Fe II-emitting clouds in active galactic nuclei: anisotropic properties. *ApJ*, 707(1):L82, 2009.

G. J. Ferland, C. Done, C. Jin, H. Landt, and M. J. Ward. State-of-the-art AGN SEDs for photoionization models: BLR predictions confront the observations. *MNRAS*, 494 (4):5917, 2020.

L. Ferrarese and H. Ford. Supermassive black holes in galactic nuclei: Past, present and future research. *Space Sci. Rev.*, 116(3):523–624, 2005.

C. Fian, J. Jiménez-Vicente, E. Mediavilla, J. A. Muñoz, D. Chelouche, S. Kaspi, and R. Forés-Toribio. First Direct Evidence for Keplerian Rotation in Quasar Inner Broad-line Regions. *ApJ*, 972(1):L7, 2024. doi: 10.3847/2041-8213/ad654d.

T. C. Fischer, D. M. Crenshaw, S. B. Kraemer, H. R. Schmitt, T. Storchi-Bergmann, and R. A. Riffel. A minor merger caught in the act of fueling the active galactic nucleus in Mrk 509. *ApJ*, 799(2):234, 2015.

E. W. Flesch. The Million Quasars (Milliquas) v7.2 Catalogue, now with VLASS associations. The inclusion of SDSS-DR16Q quasars is detailed. *arXiv:2105.12985*, 2021.

N. Förster-Schreiber, R. Genzel, N. Bouche, G. Cresci, R. Davies, P. Buschkamp, K. Shapiro, L. J. Tacconi, E. K. S. Hicks, S. Genel, and A.E. Shapley. The SINS survey: SINFONI integral field spectroscopy of $z \sim 2$ star-forming galaxies. *ApJ*, 706: 1364, 2009.

A. Franceschini, J. Manners, M. Polletta, C. J. Lonsdale, E. Gonzalez-Solares, J. Surace, D. Shupe, F. Fan, C. K. Xu, D. Farrah, and S. Berta. Complete Multiwavelength Characterization of Faint Chandra X-ray Sources Seen in the Spitzer Wide-Area IR Extragalactic (SWIRE) Survey. *AJ*, 129:2074, 2005.

D. L. Fried. *Atmospheric turbulence optical effects: understanding the adaptive-optics implications*, volume 423. NATO ASI Series C Mathematical and Physical Sciences-Advanced Study Institute, 1994.

P. Galianni and K. Horne. A test of the failed disc wind scenario for the origin of the broad-line region in active galactic nuclei. *MNRAS*, 435:3122, 2013.

C. M. Gaskell. A redshift difference between high and low ionization emission-line regions in QSOs—Evidence for radial motions. *ApJ*, 263:79–86, 1982.

C. M. Gaskell. A look at what is (and isn't) known about quasar broad line regions and how narrow-line Seyfert 1 galaxies fit in. *New Astronomy Reviews*, 44:563, 2000.

C. M. Gaskell. What broad emission lines tell us about how active galactic nuclei work. *New Astron. Rev.*, 53(7-10):140, 2009.

C. M. Gaskell. *Inflow of the Broad-Line Region and the Fundamental Limitations of Reverberation Mapping*, volume 427. In Accretion and Ejection in AGN: a Global View, 2010.

C .M. Gaskell and R. W. Goosmann. Line shifts, broad-line region inflow, and the feeding of active galactic nuclei. *ApJ*, 769(1):30, 2013.

K. Gebhardt, D. Richstone, J. Kormendy, T. R. Lauer, E. A. Ajhar, R. Bender, A. Dressler, S. M. Faber, C. Grillmair, J. Magorrian, and S. Tremaine. Axisymmetric, Three-Integral Models of Galaxies : A massive black hole in NGC 3379. *ApJ*, 119:1157, 2000.

M. R. Goad, K. T. Korista, and A.J. Ruff. The broad emission-line region: the confluence of the outer accretion disc with the inner edge of the dusty torus. *MNRAS*, 426(4): 3086–3111, 2012.

P. Goldschmidt, M. J. Kukula, L. Miller, and J.S. Dunlop. A comparison of the optical properties of radio-loud and radio-quiet quasars. *ApJ*, 511(2):612, 1999.

R. W. Goodrich. Spectropolarimetry of 'narrow-line' Seyfert 1 galaxies. *ApJ*, 342:224, 1989.

R.W. Goodrich. Pa-beta measurements and reddening in seyfert 1.8 and 1.9 galaxies. *ApJ*, 355, 1990.

A. W. Graham, C. A. Onken, E. Athanassoula, and F. Combes. An expanded M_{BH}–σ diagram, and a new calibration of active galactic nuclei masses. *MNRAS*, 412(4):2211, 2011.

GRAVITY Collaboration et al. First light for gravity: Phase referencing optical interferometry for the very large telescope interferometer. *A&A*, 602:A94, 2017.

GRAVITY Collaboration et al. Spatially resolved rotation of the broad-line region of a quasar at sub-parsec scale. *Nature*, 563:657, 2018.

GRAVITY Collaboration et al. The spatially resolved broad line region of IRAS 09149-6206. *A&A*, 643:A154, 2020a.

GRAVITY Collaboration et al. An image of the dust sublimation region in the nucleus of NGC 1068. *A&A*, 634:A1, 2020b.

GRAVITY Collaboration et al. The resolved size and structure of hot dust in the immediate vicinity of AGN. *A&A*, 635:A92, 2020c.

GRAVITY Collaboration et al. The central parsec of NGC 3783: A rotating broad emission line region, asymmetric hot dust structure, and compact coronal line region. *A&A*, 648: A117, 2021a.

GRAVITY Collaboration et al. A geometric distance to the supermassive black hole of NGC 3783. *A&A*, 654:A85, 2021b.

GRAVITY+ Collaboration et al. First light for GRAVITY Wide-Large separation fringe tracking for the Very Large Telescope Interferometer. *A&A*, 665, 2022a.

GRAVITY+ Collaboration et al. The GRAVITY+ Project: Towards All-sky, Faint-Science, High-Contrast Near-Infrared Interferometry at the VLTI. *The Messenger*, 189, 2022b.

GRAVITY Collaboration et al. Towards measuring supermassive black hole masses with interferometric observations of the dust continuum. *A&A*, 669:A14, 2023.

GRAVITY Collaboration et al. The size-luminosity relation of local active galactic nuclei from interferometric observations of the broad-line region. *A&A*, 684:A167, 2024.

GRAVITY Collaboration et al. GRAVITY observations of four new $z \sim 2$ AGNs. *To be submitted at A&A*, 2025.

J. E. Greene and L. C. Ho. Active galactic nuclei with candidate intermediate-mass black holes. *ApJ*, 610(2):722, 2004.

J. E. Greene and L. C. Ho. Estimating Black Hole Masses in Active Galaxies using the H Emission Line. *ApJ*, 630:122, 2005.

J. E. Greene, C. Y. Peng, M. Kim, C. Y. Kuo, J. A. Braatz, C. V. Impellizzeri, J. J. Condon, K. Y. Lo, C. Henkel, and M.J. Reid. Precise black hole masses from megamaser disks: black hole–bulge relations at low mass. *ApJ*, 721:26, 2010.

J. E. Greene, A. Seth, M. Kim, R. Läsker, A. Goulding, F. Gao, J. A. Braatz, C. Henkel, J. Condon, K. Y. Lo, and W. Zhao. Megamaser disks reveal a broad distribution of black hole mass in spiral galaxies. *ApJ*, 826(2):L32, 2016.

J. E. Greene, J. Strader, and L.C. Ho. Intermediate-mass black holes. *ARA&A*, 58:257, 2020.

J. L. Greenstein and M. Schmidt. The Quasi-Stellar Radio Sources 3C 48 and 3C 273. *ApJ*, 140:1, 1964.

C. J. Grier, B. M. Peterson, K. Horne, M. C. Bentz, R. W. Pogge, K. E. Denney, G. De Rosa, P. Martini, C. S. Kochanek, Y. Zu, and B. Shappee. The structure of the broad-line region in active galactic nuclei. I. Reconstructed velocity-delay maps. *ApJ*, 764:47, 2013.

C. J. Grier, B. M. Peterson, K. Horne, M. C. Bentz, R. W. Pogge, K. E. Denney, G. De Rosa, P. Martini, C. S. Kochanek, Y. Zu, and B. Shappee. The structure of the broad-line region in active galactic nuclei. I. Reconstructed velocity-delay maps. *ApJ*, 764(1):47, 2013a.

C. J. Grier, P. Martini, L. C. Watson, B. M. Peterson, M. C. Bentz, K. M. Dasyra, M. Dietrich, L. Ferrarese, R. W. Pogge, and Y. Zu. Stellar velocity dispersion measurements in high-luminosity quasar hosts and implications for the AGN black hole mass scale. *ApJ*, 773:90, 2013b.

C. J. Grier, A. Pancoast, A. J. Barth, M. M. Fausnaugh, B. J. Brewer, T. Treu, and B.M. Peterson. The structure of the broad-line region in active galactic nuclei. II. Dynamical modeling of data from the AGN10 reverberation mapping campaign. *ApJ*, 849(2):146, 2017a.

C. J. Grier, J. R. Trump, Y. Shen, K. Horne, K. Kinemuchi, I. D. McGreer, D. A. Starkey, W. N. Brandt, P. B. Hall, C. S. Kochanek, and Y. Chen. The Sloan Digital Sky Survey reverberation mapping project: Hα and Hβ reverberation measurements from first-year spectroscopy and photometry. *ApJ*, 851(1):21, 2017b.

J. E. Gunn. On the Distances of the Quasi-Stellar Objects. *ApJ*, 151(164):L113, 1971.

X. Guo, Q. Gu, N. Ding, X. Yu, and Y. Chen. Multiwavelength Selected Compton-thick AGNs in Chandra Deep Field-South Survey. *ApJ*, 908(2):169, 2021.

M.J. Hardcastle and J.H. Croston. Radio galaxies and feedback from AGN jets. *New Astronomy Reviews*, 88:101539, 2020.

P. Hariharan. *Basics of interferometry*. Elsevier, 2010.

N. Häring and H. W. Rix. On the black hole mass-bulge mass relation. *ApJ*, 604(2):L89, 2004.

C.M. Harrison and C. Ramos Almeida. Observational Tests of Active Galactic Nuclei Feedback: An Overview of Approaches and Interpretation. *Galaxies*, 12(2):17, 2024.

T. M. Heckman. An optical and radio survey of the nuclei of bright galaxies - Activity in normal galactic nuclei. *A&A*, 87(1-2):152, 1980.

T.M. Heckman and P.N. Best. The coevolution of galaxies and supermassive black holes: Insights from surveys of the contemporary universe. *ARAA*, 52:589–660, 2014.

L. Hermosa-Muñoz, S. Cazzoli, I. Márquez, and J. Masegosa. Optical spectroscopy of type 2 LINERs. *A&A*, 635:A50, 2020.

L. Hernández-García, J. Masegosa, O. González-Martín, and I. Márquez. X-ray spectral variability of Seyfert 2 galaxies. *A&A*, 579:A90, 2015.

F. Herpich, A. Mateus, G. Stasińska, R. Cid Fernandes, and N. Vale Asari. The many faces of LINER-like galaxies: A WISE view. *MNRAS*, 462(2):1826–1833, 2016.

J. S Hey, J. W. Phillips, and S. J. Parsons. Cosmic radiations at 5 metres wavelength. *Nature*, 157(3984):296, 1946.

R. C. Hickox and D.M. Alexander. Obscured active galactic nuclei. *ARA&A*, 56(1):625, 2018.

E. K. Hicks and M. A. Malkan. Circumnuclear Gas in Seyfert 1 Galaxies: Morphology, kinematics, And direct measurement Of black hole masses. *ApJ Supplement Series*, 174: 31, 2008.

N. Higginbottom, C. Knigge, K. S. Long, S. A. Sim, and J.H. Matthews. A simple disc wind model for broad absorption line quasars. *MNRAS*, 436(2):1390, 2011.

L. C. Ho, A. V. Filippenko, and W. L. W. Sargent. *Multi-Wavelength Continuum Emission of AGN*. In IAU Symp. 159, ed. Courvosier, T. J.-L. and Blecha, A., Kluwer Academic Publishers: Dordrecht, 1994.

C. Hoffmeister. 354 neue Veränderliche. *Astronomische Nachrichten*, 236:2333, 1929.

S.F. Hönig. Redefining the torus: a unifying view of AGNs in the infrared and submillimeter. *ApJ*, 884(2):171, 2019.

K. Horne. An optimal extraction algorithm for CCD spectroscopy. *PASP*, 98:609, 1986.

K. Horne. Reverberation Mapping of the Broad-Line Region in Active Galactic Nuclei in Gondhalekar P. M., Horne K., Peterson B. M., eds. In *ASP Conf. Ser.*, volume 69. Astron. Soc. Pac., San Francisco, 1994.

F. Hoyle, W. A. Fowler, and E. M. Burbidge. On Relativistic Astrophysics. *ApJ*, 139:909, 1964.

C. Hu, J. M. Wang, L. C. Ho, Y. M. Chen, H. T. Zhang, W. H. Bian, and S. J. Xue. A systematic analysis of Fe II emission in quasars: Evidence for inflow to the central black hole. *ApJ*, 687(1):78, 2008.

E. P. Hubble. A general study of diffuse galactic nebulae. *ApJ*, 56:162–199, 1922.

B. Husemann, L. Wisotzki, S. F. Sánchez, and K. Jahnke. Jet-driven galaxy-scale gas outflows in the hyperluminous quasar 3C 273. *ApJ*, 549:A43, 2013.

B. Husemann, V. N. Bennert, K. Jahnke, T. A. Davis, J. H. Woo, J. Scharwächter, A. Schulze, M. Gaspari, and M.A. Zwaan. Jet-driven galaxy-scale gas outflows in the hyperluminous quasar 3C 273. *ApJ*, 879(2):75, 2019.

D. Ilić, J. Kovačević, and L. Č. Popović. The line parameters and ratios as the physical probe of the line emitting regions in AGN. *New Astron. Reviews*, 53(7-10):149–155, 2009.

A. Irbah, J. Borgnino, D. Djafer, L. Damé, and P. Keckhut. Solar seeing monitor MISOLFA: A new method for estimating atmospheric turbulence parameters. *A&A*, 591:A150, 2016.

K. G. Jansky. Directional studies of atmospherics at high frequencies. *Proceedings of the Institute of Radio Engineers*, 20(12):1920–1932, 1932.

J. Jiang, M. Baloković, M. Brightman, H. Liu, F.A. Harrison, and G.B. Lansbury. A highly accreting low-mass black hole hidden in the dust: Suzaku and NuSTAR observations of the NLS1 Mrk 1239. *MNRAS*, 505:702–712, 2021.

P. H. Johansson, T. Naab, and A. Burkert. The Relationship between Black Hole Growth and Star Formation in Seyfert Galaxies. *Astronomische Nachrichten: Astronomical Notes*, 329(9-10):956, 2008.

M. H. Jones, R. J. A. Lambourne, and S. Serjeant. *An introduction to Galaxies and Cosmology (2nd ed.)*. Cambridge University Press/Open University, Cambridge, 2015.

P. Jovanović. The broad Fe Kα line and supermassive black hole. *MNRAS*, 56(2-3):37, 2012.

S. Kaspi, P. S. Smith, H. Netzer, D. Maoz, B.T. Jannuzi, and U. Giveon. Reverberation measurements for 17 quasars and the size-mass-luminosity relations in active galactic nuclei. *ApJ*, 533(2):631, 2000.

S. Kaspi, D. Maoz, H. Netzer, B. M. Peterson, M. Vestergaard, and B. T. Jannuzi. The relationship between Luminosity and Broad-Line Region Size in Active Galactic Nuclei. *ApJ*, 629:61, 2005.

S. Kaspi, W. N Brandt, D. Maoz, H. Netzer, D. P. Schneider, O. Shemmer, and C. J. Grier. Taking a Long Look: A Two-decade Reverberation Mapping Study of High-luminosity Quasars. *ApJ*, 915(2):129, 2021. doi: 10.3847/1538-4357/ac00aa.

T. Kawaguchi and M. Mori. Orientation effects on the inner region of dusty torus of active Galactic nuclei. *ApJ*, 724(2):L183, 2010.

T. Kawaguchi and M. Mori. Near-infrared reverberation by dusty clumpy tori in active galactic nuclei. *ApJ*, 737(2):105, 2011.

B. C. Kelly. Some aspects of measurement error in linear regression of astronomical data. *ApJ*, 665(2):1489, 2007.

L. Kewley, B. Groves, G. Kauffmann, , and T. Heckman. The host galaxies and classification of active galactic nuclei. *MNRAS*, 372:961, 2006.

B. E. Kinch, J. D. Schnittman, T. R. Kallman, and J.H. Krolik. Fe Kα profiles from simulations of accreting black holes. *ApJ*, 826(1):52, 2016.

E. S. Klimek, C. M. Gaskell, and C. H. Hedrick. Optical variability of narrow-line Seyfert 1 galaxies. *ApJ*, 609(1):69, 2004.

W. Kollatschny and M. Dietrich. Balmer emission-line profile variations in NGC 4593. *A&A*, 323:5, 1997.

W. Kollatschny and M. Zetzl. Broad-line active galactic nuclei rotate faster than narrow-line ones. *Nature*, 470(7334):366–368, 2011.

W. Kollatschny and M. Zetzl. The shape of broad-line profiles in active galactic nuclei. *A&A*, 549:A100, 2013.

K. Korista, J. Baldwin, G. Ferland, and D. Verner. An atlas of computed equivalent widths of quasar broad emission lines. *ApJS*, 108(2):401, 1997.

K. T. Korista and M. R. Goad. What the optical recombination lines can tell us about the broad-line regions of active galactic nuclei. *ApJ*, 606:749, 2004.

J. Kormendy and L. C. Ho. Coevolution (or not) of supermassive black holes and host galaxies. *ARA&A*, 51:511–653, 2013.

J. Kormendy and R. C. Kennicutt Jr. Secular evolution and the formation of pseudobulges in disk galaxies. *ARA&A*, 42(1):603, 2004.

S. Koshida, T. Minezaki, Y. Yoshii, Y. Kobayashi, Y. Sakata, S. Sugawara, K. Enya, M. Suganuma, H. Tomita, T. Aoki, and B.A. Peterson. Reverberation measurements of the inner radius of the dust torus in 17 Seyfert galaxies. *ApJ*, 788(2):159, 2014.

M. Koss, B. Trakhtenbrot, C. Ricci, I. Lamperti, K. Oh, S. Berney, K. Schawinski, M. Baloković, L. Baronchelli, D. M. Crenshaw, T. Fischer, N. Gehrels, F. Harrison, Y. Hashimoto, D. Hogg, K. Ichikawa, N. Masetti, R. Mushotzky, L. Sartori, D. Stern, E. Treister, Y. Ueda, S. Veilleux, and L. Winter. BAT AGN Spectroscopic Survey. I. Spectral Measurements, Derived Quantities, and AGN Demographics. *ApJ*, 850:74, 2017.

D. Krajnović, M. Cappellari, R. M. McDermid, S. Thater, K. Nyland, P. T. de Zeeuw, J. Falcón-Barroso, S. Khochfar, H. Kuntschner, M. Sarzi, and L. M. Young. A quartet of black holes and a missing duo: probing the low end of the M_{BH}-σ relation with the adaptive optics assisted integral-field spectroscopy. *MNRAS*, 477(3):3030, 2018.

Coleman M. Krawczyk, Gordon T. Richards, Sajjan S. Mehta, Michael S. Vogeley, S. C. Gallagher, Karen M. Leighly, Nicholas P. Ross, and Donald P. Schneider. Mean Spectral Energy Distributions and Bolometric Corrections for Luminous Quasars. *ApJS*, 206(1): 4, 2013. doi: 10.1088/0067-0049/206/1/4.

J. H. Krolik. *Active galactic nuclei: from the central black hole to the galactic environment.* Princeton University Press, 1999.

J. H. Krolik and M.C. Begelman. Molecular tori in Seyfert galaxies-Feeding the monster and hiding it. *ApJ*, 329:702–711, 1988.

Y. Kudoh, K. Wada, N. Kawakatu, and M. Nomura. Multiphase Gas Nature in the Sub-parsec Region of the Active Galactic Nuclei. I. Dynamical Structures of Dusty and Dust-free Outflow. *ApJ*, 950:72, 2023.

L. Kuhn, J. Shangguan, R. Davies, A. W. S. Man, Y. Cao, J. Dexter, F. Eisenhauer, N. M. Förster Schreiber, H. Feuchtgruber, R. Genzel, S. Gillesen, S. Hönig, D. Lutz, H. Netzer, T. Ott, S. Rabien, D. J. D. Santos, T. Shimizu, E. Sturm, and L. J. Tacconi. Broad-line region geometry from multiple emission lines in a single-epoch spectrum. *A&A*, 685: A52, 2024.

C. Y. Kuo, J. A. Braatz, C. M. V. Impellizzeri, F. Gao, D. Pesce, M.J. Reid, J. Condon, F. Kamali, C. Henkel, and J. E. Greene. The Megamaser Cosmology Project-XII. VLBI imaging of H_2O maser emission in three active galaxies and the effect of AGN winds on disc dynamics. *MNRAS*, 498:1609–1627, 2020. doi: 10.1093/mnras/staa2260.

J. Kwan and J.H. Krolik. The formation of emission lines in quasars and seyfert nuclei. *ApJ*, 250:478–507, 1981.

G. La Mura, L. Č. Popović, S. Ciroi, P. Rafanelli, and D. Ilić. Detailed Analysis of Balmer Lines in a Sloan Digital Sky Survey Sample of 90 Broad-Line Active Galactic Nuclei. *ApJ*, 671(1):104–117, 2007. doi: 10.1086/522821.

A. Lamastra, N. Menci, R. Maiolino, F. Fiore, and A. Merloni. The building up of the black hole–stellar mass relation. *MNRAS*, 405(1):29–40, 2010.

H. Landt, M. C. Bentz, B. M. Peterson, M. Elvis, M. J. Ward, K. T. Korista, and M. Karovska. The near-infrared radius—luminosity relationship for active galactic nuclei. *MNRAS*, 413(1):L106–L109, 2011.

A. Laor. On quasar masses and quasar host galaxies. *ApJ*, 505(2):L83, 1998.

A. Laor. Evidence for line broadening by electron scattering in the broad-line region of NGC 4395. *ApJ*, 643(1):112, 2006b.

A. Laor, A. J. Barth, L. C. Ho, and A.V. Filippenko. Is the broad-line region clumped or smooth? Constraints from the Hα profile in NGC 4395, the least luminous Seyfert 1 galaxy. *ApJ*, 636(1):83, 2006a.

A. Lapi, S. Raimundo, R. Aversa, Z. Y. Cai, M. Negrello, A. Celotti, G. De Zotti, and L. Danese. The coevolution of supermassive black holes and massive galaxies at high redshift. *ApJ*, 782:69, 2014.

A. Lawrence and M. Elvis. Misaligned disks as obscurers in active galaxies. *ApJ*, 714(1): 561, 2010.

P. Lawson. *Principles of long baseline stellar interferometry*. JPL, 2000.

K. M. Leighly. A comprehensive spectral and variability study of narrow-line Seyfert 1 galaxies observed by ASCA. I. Observations and time series analysis. *ApJS*, 125(2):297, 1999.

J. I. H. Li, H. Li, Y. Shen, L. C. Ho, W. N. Brandt, C. J. Grier, P. B. Hall, Y. Homayouni, A. M. Koekemoer, D. P. Schneider, and J. R. Trump. The Sloan Digital Sky Survey Reverberation Mapping Project: The Black Hole Mass–Stellar Mass Relations at $0.2 \lesssim z \lesssim 0.8$. *ApJ*, 954:173, 2023.

C. H. Lin, K. J. Chen, and C.Y. Hwang. Rapid Growth of Galactic Supermassive Black Holes through Accreting Giant Molecular Clouds during Major Mergers of Their Host Galaxies. *ApJ*, 952(2):121, 2023.

P. Lira, S. Kaspi, H. Netzer, I. Botti, N. Morrell, J. Mejía-Restrepo, P. Sánchez-Sáez, J. Martínez-Palomera, and P. López. Reverberation Mapping of Luminous Quasars at High-z. *ApJ*, 865:56, 2018. doi: 10.3847/1538-4357/aada45.

H. T. Liu, H. C. Feng, S. S. Li, J. M. Bai, and H.Z. Li. Measuring the Virial Factor in SDSS DR7 Active Galactic Nuclei with Redshifted Hβ and Hα Broad Emission Lines. *ApJ*, 963(1):30, 2024.

K. S. Long and C. Knigge. Modeling the spectral signatures of accretion disk winds: a new Monte Carlo approach. *ApJ*, 579(2):725, 2002.

R. R. Ludwig, J. E. Greene, A. J. Barth, and L.C. Ho. Physical properties of the narrow-line region of low-mass active galaxies. *ApJ*, 756:51, 2012.

A. Luminari, E. Piconcelli, F. Tombesi, L. Zappacosta, F. Fiore, L. Piro, and F. Vagnetti. Constraining the geometry of the nuclear wind in PDS 456 using a novel emission model. *A&A*, 619:A149, 2018.

B. W. Lyke, A. N. Higley, J. N. McLane, D. P. Schurhammer, A. D. Myers, A.J. Ross, K. Dawson, S. Chabanier, P. Martini, H. D. M. Des Bourboux, and M. Salvato. The sloan digital sky survey quasar catalog: Sixteenth data release. *ApJS*, 250(1):8, 2020.

D. Lynden-Bell and M.J. Rees. On quasars, dust and the galactic centre. *MNRAS*, 152 (4):461–475, 1971.

J. M. MacLeod and B. H. Andrew. The radio source VRO 42.22.01. *Ap. Lett.*, 1:243, 1968.

P. Madau and M. Dickinson. Cosmic star-formation history. *ARA&A*, 52:415–486, 2014.

G. M. Madejski, A. A. Zdziarski, T. J. Turner, C. Done, R. F. Mushotzky, R.C. Hartman, N. Gehrels, A. Connors, A. C. Fabian, K. Nandra, A. Celotti, M. J. Rees, W. N. Johnson, J. E. Grove, and C. H. Starr. Joint ROSAT-Compton GRO observations of the X-ray bright Seyfert galaxy IC 4329A. *ApJ*, 438:672, 1995.

J. Magorrian, S. Tremaine, D. Richstone, R. Bender, G. Bower, A. Dressler, S. M. Faber, K. Gebhardt, R. Green, C. Grillmair, and J. Kormendy. The demography of massive dark objects in galaxy centers. *ApJ*, 115(6):2285, 1998.

G. Maheson, R. Maiolino, M. Curti, R. Sanders, S. Tacchella, and L. Sandles. Unravelling the dust attenuation scaling relations and their evolution. *MNRAS*, 527:8213–8233, 2024.

R. Maiolino, J. Scholtz, J. Witstok, S. Carniani, F. D'Eugenio, A. de Graaff, H. Übler, S. Tacchella, E. Curtis-Lake, S. Arribas, and A.. Bunker. A small and vigorous black hole in the early Universe. *Nature*, 627(8002):59, 2024.

P. R. Maloney, D. J. Hollenbach, and A. G. G. M. Tielens. X-Ray - irradiated molecular gas. I. physical processes and general results. *ApJ*, 466:561, 1996.

A. K. Mandal, J. H. Woo, S. Wang, S. Rakshit, H. Cho, D. Son, and C.S. Stalin. Revisiting the Dust Torus Size–Luminosity Relation Based on a Uniform Reverberation-mapping Analysis. *ApJ*, 968(2):59, 2024.

S. W. Mangham, C. Knigge, P. Williams, K. Horne, A. Pancoast, J. H. Matthews, K. S. Long, S. A. Sim, and N. Higginbottom. Do reverberation mapping analyses provide an accurate picture of the broad-line region? *MNRAS*, 488(2):2780, 2019.

A. Markowitz, R. Edelson, and S. Vaughan. Long-term X-ray spectral variability in Seyfert 1 galaxies. *ApJ*, 598(2):935, 2003.

P. Marziani, C. A. Negrete, D. Dultzin, M. L. Martínez-Aldama, A. Del Olmo, M. D'Onofrio, and G. M. Stirpe. Quasar massive ionized outflows traced by CIV λ1549 and [OIII] $\lambda\lambda$4959, 5007. *Frontiers in Astro. and Space Sci.*, 4:16, 2017.

P. Marziani, K. G. Luna, A. Floris, A. del Olmo, A. Deconto-Machado, T. M. Buendia-Rios, C. A. Negrete, and D. Dultzin. Super-Eddington Accretion in Quasars. *Universe*, 11(2):59, 2024.

Y. Matsumoto, Y. Asahina, Y. Kudoh, T. Kawashima, J. Matsumoto, H. R. Takahashi, T. Minoshima, S. Zenitani, T. Miyoshi, and R. Matsumoto. Magnetohydrodynamic simulation code CANS+: Assessments and applications. *PASJ*, 71(4):83, 2019.

J. H. Matthews, C. Knigge, K. S. Long, S. A. Sim, N. Higginbottom, and S.W. Mangham. Testing quasar unification: Radiative transfer in clumpy winds. *MNRAS*, 458(1):293, 2016.

J. H. Matthews, C. Knigge, N. Higginbottom, K. S. Long, S. A. Sim, S. W. Mangham, E. J. Parkinson, and H. A. Hewitt. Stratified disc wind models for the AGN broad-line region: ultraviolet, optical, and X-ray properties. *MNRAS*, 492(4):5540, 2020.

T. A. Matthews, W. W. Morgan, and M. Schmidt. A Discussion of Galaxies Indentified with Radio Sources. *ApJ*, 140(35):35, 1964.

G. A. Matzeu, J. N. Reeves, V. Braito, E. Nardini, D. E. McLaughlin, A. P. Lobban, F. Tombesi, and M. T. Costa. Evidence for a radiatively driven disc-wind in PDS 456? *MNRAS*, 472:L15–L19, 2017.

S. McAlpine, C. M. Harrison, D. J. Rosario, D. M. Alexander, S. L. Ellison, P. H. Johansson, and D. R. Patton. Galaxy mergers in EAGLE do not induce a significant amount of black hole growth yet do increase the rate of luminous AGN. *MNRAS*, 494(4):5713, 2020.

R. J. McLure and J.S. Dunlop. On the black hole-bulge mass relation in active and inactive galaxies. *MNRAS*, 331(3):795–804, 2002.

R. Meijerink and M. Spaans. Diagnostics of irradiated gas in galaxy nuclei—I. A far-ultraviolet and x-ray dominated region code. *ApJ*, 436(2):397, 2005.

C. Messier. Catalogue des Nebuleuses et des amas d'étoiles. *Connoissance des Temps ou des Mouvements Célestes*, pages 227–267, 1781.

K. G. Metzroth, C. A. Onken, and B. M. Peterson. The mass of the central black hole in the Seyfert galaxy NGC 4151. *ApJ*, 647(2):901, 2006.

A. Michelson. On the Application of Interference Methods to Astronomical Measurements. *Astrophys. J.*, 516:267–62, 1920.

Y. Minowa, Y. Hayano, S. Oya, M. Watanabe, M. Hattori, O. Guyon, S. Egner, Y. Saito, M. Ito, H. Takami, and V. Garrel. Performance of Subaru adaptive optics system AO188. *In Adaptive Optics Systems II, SPIE*, 7736:1302, 2010.

M. Mizumoto, C. Done, R. Tomaru, and I. Edwards. Thermally driven wind as the origin of warm absorbers in AGN. *MNRAS*, 489(1):1152, 2019.

A. Monreal-Ibero, S. Arribas, and L. Colina. LINER-like extended nebulae in ULIRGs: shocks generated by merger-induced flows. *ApJ*, 637(1):138, 2006.

T. R. Monroe, J. X. Prochaska, N. Tejos, G. Worseck, J. F. Hennawi, T. Schmidt, J. Tumlinson, and Y. Shen. The UV-bright quasar survey (UVQS): DR1. *Frontiers in Astronomy and Space Sciences*, 152(1):25, 2016.

E. C. Moran, A. J. Barth, L. E. Kay, and A. V. Filippenko. The Frequency of Polarized Broad Emission Lines in Type 2 Seyfert Galaxies. *ApJ*, 540(2):L73, 2000.

R. Morganti. The many routes to AGN feedback. *Frontiers in Astronomy and Space Sciences*, 4:42, 2017.

D. Mortlock. *Quasars as Probes of Cosmological Reionization in Understanding the Epoch of Cosmic Reionization: Challenges and Progress*. Springer, 2016.

A. L. Müller and G.E. Romero. Radiation from the impact of broad-line region clouds onto AGN accretion disks. *A&A*, 636:A92, 2020.

N. Murray and J. Chiang. Disk winds and disk emission lines. *ApJ*, 474(1):91, 1997.

N. Murray, J. Chiang, S. A. Grossman, and G.M. Voit. Accretion disk winds from active galactic nuclei. *ApJ*, 451:498, 1995.

R. Mushotzky. *How are AGN found?* In Supermassive Black Holes in the Distant Universe, Dordrecht: Springer Netherlands, 2004.

M. Naddaf. The Effect of Outflow Launching Radial Efficiency of Accretion Disk on the Shape of Emission-Line Profiles. *Universe*, 11(1), 2024.

M. H. Naddaf, B. Czerny, and R. Szczerba. The Picture of BLR in 2.5D FRADO: Dynamics and Geometry. *ApJ*, 920:30, 2021.

T. Nagao, T. Murayama, and Y. Taniguchi. The narrow-line region of seyfert galaxies: narrow-line Seyfert 1 galaxies versus broad-line Seyfert 1 galaxies. *ApJ*, 546:744, 2001.

T. Nagao, K. S. Kawabata, T. Murayama, Y. Ohyama, Y. Taniguchi, R. Sumiya, and S.S. Sasaki. Detection of the Polarized Broad Emission Line in the Seyfert 2 Galaxy Markarian 573. *AJ*, 128(1):109, 2006.

S. Nagoshi, F. Iwamuro, S. Yamada, Y. Ueda, Y. Oikawa, M. Otsuka, K. Isogai, and S. Mineshige. Probing the origin of the two-component structure of broad-line region by reverberation mapping of an extremely variable quasar. *MNRAS*, 529:393–408, 2024.

D. Namekata and M. Umemura. Sub-parsec-scale dynamics of a dusty gas disc exposed to anisotropic AGN radiation with frequency-dependent radiative transfer. *ApJ*, 460(1): 980, 2016.

K. Nandra and K. A. Pounds. Ginga observations of the X-ray spectra of Seyfert galaxies. *MNRAS*, 268:405, 1994.

E. Nardini, J. N. Reeves, J. Gofford, F. A. Harrison, G. Risaliti, V. Braito, M. T. Costa, G. A. Matzeu, D. J. Walton, E. Behar, and S. E. Boggs. Black hole feedback in the luminous quasar PDS 456. *Science*, 347:860–863, 2015.

M. Nenkova, M. M. Sirocky, Ž. Ivezić, and M. Elitzur. Dust in the narrow-line region of active galactic nuclei. *ApJ*, 685(1):147, 2008.

H. Netzer. *in Active Galactic Nuclei, ed. R. D. Blandford et al.*, volume 57. Berlin:Springer, 1990.

H. Netzer. Revisiting the unified model of active galactic nuclei. *ARA&A*, 53(1):365–408, 2015.

H. Netzer. Bolometric correction factors for active galactic nuclei. *MNRAS*, 488(4):5185, 2019.

H. Netzer. Testing broad-line region models with reverberation mapping. *MNRAS*, 494: 1611–1621, 2020.

H. Netzer and A. Laor. Dust in the narrow-line region of active galactic nuclei. *ApJ*, 404 (2):L51–L54, 1993.

D. D. Nguyen, A. C. Seth, N. Neumayer, S. Kamann, K. T. Voggel, M. Cappellari, A. Picotti, P. M. Nguyen, T. Böker, V. Debattista, and N. Caldwell. Nearby early-type galactic nuclei at high resolution: Dynamical black hole and nuclear star cluster mass measurements. *ApJ*, 858(2):118, 2018.

D. D. Nguyen, A. C. Seth, N. Neumayer, S. Iguchi, M. Cappellari, J. Strader, L. Chomiuk, E. Tremou, F. Pacucci, K. Nakanishi, and A. Bahramian. Improved dynamical constraints on the masses of the central black holes in nearby low-mass early-type galactic nuclei and the first black hole determination for NGC 205. *ApJ*, 872(1):104, 2019.

P. T. O'Brien, M. R. Goad, and P. M. Gondhalekar. The luminosity-dependent broad-line region in active galactic nuclei. *MNRAS*, 275(4):1125–1145, 1995.

S. Ogawa, Y. Ueda, S. Yamada, A. Tanimoto, and T. Kawaguchi. Application of Clumpy Torus Model to Broadband X-Ray Spectra of Two Seyfert 1 Galaxies: IC 4329A and NGC 7469. *ApJ*, 875(2):115, 2019.

K. Ohsuga, M. Mori, T. Nakamoto, and S. Mineshige. Supercritical accretion flows around black holes: Two-dimensional, radiation pressure-dominated disks with photon trapping. *ApJ*, 628(1):368, 2005.

E. Oliva, L. Origlia, R. Maiolino, and A. F. M. Moorwood. Starbursts in active galaxy nuclei: Observational constraints from IR stellar absorption lines. *A&A*, 350:9, 1999.

C. A. Onken, L. Ferrarese, D. Merritt, B. M. Peterson, R. W. Pogge, M. Vestergaard, and A Wandel. Supermassive black holes in active galactic nuclei. II. Calibration of the black hole mass-velocity dispersion relationship for active galactic nuclei. *ApJ*, 615(2): 645, 2004.

C. A. Onken, C. Wolf, W. J. Hon, S. Lai, P. Tisserand, and R Webster. AllBRICQS: The All-sky BRIght, Complete Quasar Survey. *PASA*, 40:e010, 2023.

G. Orban De Xivry, R. Davies, M. Schartmann, S. Komossa, A. Marconi, E. Hicks, H. Engel, and L. Tacconi. The role of secular evolution in the black hole growth of narrow-line Seyfert 1 galaxies. *MNRAS*, 417(4):2721, 2011.

M. Orienti and M. A. Prieto. Radio structures of the nuclei of nearby Seyfert galaxies and the nature of the missing diffuse emission. *MNRAS*, 401(4):2599, 2010.

J. Osorno, N. Nagar, T. Richtler, P. Humire, K. Gebhardt, and K. Gultekin. Revisiting the black hole mass of M87 using VLT/MUSE adaptive optics integral field unit data-I. Ionized gas kinematics. *A&A*, 679:A37, 2023.

D. E. Osterbrock. Observational model of the ionized gas in seyfert and radio-galaxy nuclei. *Proceedings of the National Academy of Sciences*, 75(2):540, 1978.

D.E. Osterbrock and R.W. Pogge. The spectra of narrow-line Seyfert 1 galaxies. *ApJ*, 297: 166–176, 1985.

P. Padovani, D. M. Alexander, R. J. Assef, B. De Marco, P. Giommi, R. C. Hickox, G. T. Richards, V. Smolčić, E. Hatziminaoglou, V. Mainieri, and M. Salvato. Active galactic nuclei: what's in a name? *A&AR*, 25:1, 2017.

M. J. Page, M. Symeonidis, J. D. Vieira, B. Altieri, A. Amblard, V. Arumugam, H. Aussel, T. Babbedge, A. Blain, J. Bock, and A. Boselli. The suppression of star formation by powerful active galactic nuclei. *Nature*, 487(7397):213, 2012.

X. Pan, H. Zhou, C. Yang, L. Sun, P.S. Smith, T. Ji, N. Jiang, P. Jiang, W. Liu, H. Lu, and X. Shi. Mrk 1239: a Type-2 Counterpart of Narrow-line Seyfert-1? *ApJ*, 912:118, 2021.

A. Pancoast, B.J. Brewer, and T. Treu. Geometric and dynamical models of reverberation mapping data. *ApJ*, 730(2):139, 2011.

A. Pancoast, B. J. Brewer, and T. Treu. Modelling reverberation mapping data–I. Improved geometric and dynamical models and comparison with cross-correlation results. *MNRAS*, 445:3055, 2014a.

A. Pancoast, B. J. Brewer, T. Treu, D. Park, A. J. Barth, M. C. Bentz, and J.H. Woo. Modelling reverberation mapping data II. Dynamical modelling of the Lick AGN Monitoring Project 2008 data set. *MNRAS*, 445(3):3073–3091, 2014b.

D. Park, B. C. Kelly, J. H. Woo, and T. Treu. Recalibration of the virial factor and M_{BH}–σ relation for local active galaxies. *ApJS*, 2013(1):6, 2012.

D. Park, A. J. Barth, L. C. Ho, and A. Laor. A new iron emission template for active galactic nuclei. I. Optical template for the Hβ region. *ApJS*, 258(2):38, 2022.

C. Y. Peng, C. D. Impey, L. C. Ho, E. J. Barton, and H.W. Rix. Probing the coevolution of supermassive black holes and quasar host galaxies. *ApJ*, 640(1):114, 2006.

W. J. Percival, L. Miller, R. J. McLure, and J. S. Dunlop. The host galaxies of luminous radio-quiet quasars. *MNRAS*, 322(4):843–858, 2001.

B. M. Peterson. Reverberation mapping of active galactic nuclei. *PASP*, 105:247–268, 1993.

B. M. Peterson. *An introduction to active galactic nuclei.* Cambridge University Press, 1997.

B. M. Peterson. Emission-line variability in seyfert galaxies. *PASP*, 100(623):18, 1998.

B. M. Peterson. *The broad-line region in active galactic nuclei. In Physics of Active Galactic Nuclei at all Scales.* Berlin, Heidelberg: Springer Berlin Heidelberg, 2006.

B. M. Peterson and A. Wandel. Keplerian motion of broad-line region gas as evidence for supermassive black holes in active galactic nuclei. *ApJ*, 521(2):L95, 1999.

B. M. Peterson, L. Ferrarese, K. M. Gilbert, S. Kaspi, M. A. Malkan, D. Maoz, D. Merritt, H. Netzer, C. A. Onken, R. W. Pogge, and M. Vestergaard. Central masses and broad-line region sizes of active galactic nuclei. II. A homogeneous analysis of a large reverberation-mapping database. *ApJ*, 613:682, 2004.

R. G. Petrov. Differential interferometry. In D. M. Alloin and J.-M. Mariotti, editors, *Diffraction-Limited Imaging with Very Large Telescopes*, volume 274. Springer Science & Business Media, 1989.

R. G. Petrov and S. Lagarde. *Differential speckle interferometry applied to double stars*, volume 135, pages 477–485. Cambridge University Press, 1992.

R.G. Petrov, S. Lagarde, and M. N'guyen van Ky. *Symposium-International Astronomical Union*, volume 176, chapter Differential interferometry imaging, pages 181–190. Cambridge University Press, 1996.

L. Piro, M. Yamauchi, and M. Matsuoka. X-Ray Spectral Signatures of Very Thick Cold Matter in the spectra of the Seyfert 1 Galaxies NGC 7469 And IC 4329A. *ApJ*, 360: 35–38, 1990.

L. Č Popović, E. Mediavilla, E. Bon, and D Ilić. Contribution of the disk emission to the broad emission lines in agns: Two-component model. *A&A*, 423(3):909–918, 2004.

A. Prieto, A. Rodríguez-Ardila, S. Panda, and M. Marinello. A novel black hole mass scaling relation based on coronal gas, and its dependence with the accretion disc. *MNRAS*, 510:1010–1030, 2022.

J. Prieto, A. Escala, G. C. Privon, and J. d'Etigny. Black hole fuelling in galaxy mergers: a high-resolution analysis. *MNRAS*, 508(3):3672, 2021.

S. I. Raimundo, A. Pancoast, M. Vestergaard, M. R. Goad, and A.J. Barth. Modelling the AGN broad line region using single-epoch spectra–I. The test case of Arp 151. *MNRAS*, 489(2):1899, 2019.

S. I. Raimundo, M. Vestergaard, M. R. Goad, C. J. Grier, P. R. Williams, B. M. Peterson, and T. Treu. Modelling the AGN broad-line region using single-epoch spectra II. Nearby AGNs. *MNRAS*, 493(1):1227, 2020.

S. Rakshit, R. G. Petrov, A. Meilland, and S. F. Hönig. Differential interferometry of QSO broad-line regions–I. Improving the reverberation mapping model fits and black hole mass estimates. *MNRAS*, 447(3):2420, 2015.

M. Ramolla, M. Haas, C. Westhues, F. P. Nuñez, C. S. Figaredo, J. Blex, M. Zetzl, W. Kollatschny, K. W. Hodapp, R. Chini, and M. Murphy. Simultaneous Hα and dust reverberation mapping of 3C 120: Testing the bowl-shaped torus geometry. *A&A*, 620: A137, 2018.

G. Reber. Cosmic static. *ApJ*, 100:279, 1944.

N. A. Reddy, M. Kriek, A. E. Shapley, W. R. Freeman, B. Siana, A. L. Coil, B. Mobasher, S. H. Price, R. L. Sanders, and I. Shivaei. The MOSDEF survey: measurements of balmer decrements and the dust attenuation curve at redshifts z $\sim$ 1.4–2.6. *ApJ*, 806: 256, 2015.

M. J. Rees. Black hole models for active galactic nuclei. *ARA&A*, 22(1):471, 1984.

J. N. Reeves, P. T. O'Brien, S. Vaughan, D. Law-Green, M. Ward, C. Simpson, K. A. Pounds, and R. Edelson. PDS 456: an extreme accretion rate quasar? *MNRAS*, 312(2): L17, 2000.

J. N. Reeves, P. T. O'Brien, and M. J. Ward. A Massive X-Ray Outflow from the Quasar PDS 456. *ApJ*, 593:L65, 2003.

J. N. Reeves, P. T. O'Brien, V. Braito, E. Behar, L. Miller, T. J. Turner, A. C. Fabian, S. Kaspi, R. Mushotzky, and M. Ward. A compton-thick wind in the high-luminosity quasar, PDS 456. *ApJ*, 701:493–507, 2009.

A. E. Reines and M. Volonteri. Relations between central black hole mass and total galaxy stellar mass in the local universe. *ApJ*, 813(2):82, 2015.

G. Risaliti and M. Elvis. A non-hydrodynamical model for acceleration of line-driven winds in active galactic nuclei. *A&A*, 516:A89, 2010.

F. Roddier. Optical propagation and image formation through the turbulent atmosphere. In D. M. Alloin and J.-M. Mariotti, editors, *Diffraction-Limited Imaging with Very Large Telescopes*, volume 274. Springer Science & Business Media, 1989.

F. Roddier. *Adaptive Optics in Astronomy.* Cambridge University Press, 1999.

E. I. Rosenblatt, M. A. Malkan, W. L. Sargent, and A. Readhead. The broad emission line and continuum variations of Seyfert galaxies. *ApJS*, 81(1):59–81, 1999.

R. R. Ross, A. C. Fabian, and S. Mineshige. The spectra of accretion discs in active galactic nuclei. *MNRAS*, 258(1):189–197, 1992.

G. Rousset, F. Lacombe, P. Puget, N. N. Hubin, E. Gendron, J. M. Conan, P. Y. Kern, P. Y. Madec, D. Rabaud, D. Mouillet, and A. M. Lagrange. Design of the Nasmyth adaptive optics system (NAOS) of the VLT. *In Adaptive optical system technologies, SPIE*, 3353:508, 1998.

G. Rousset, F. Lacombe, P. Puget, E. Gendron, R. Arsenault, P. Y. Kern, D. Rabaud, P. Y. Madec, N. N. Hubin, G. Zins, and E. Stadler. Status of the VLT Nasmyth adaptive optics system (NAOS). *In Adaptive optical system technologies, SPIE*, 4007:72, 2000.

H. R. Russell, P. E.J. Nulsen, A. C. Fabian, T. E. Braben, W. N. Brandt, L. Clews, M. McDonald, C. S. Reynolds, J. S. Sanders, and S. Veilleux. A cooling flow around the low-redshift quasar H1821+643. *MNRAS*, 528(2):1863, 2024.

C. J. Ryan, M. M. De Robertis, S. Virani, A. Laor, and P. C. Dawson. The central engines of Narrow-Line Seyfert 1 Galaxies. *ApJ*, 654:799, 2007.

R. P. Saglia, M. Opitsch, P. Erwin, J. Thomas, A. Beifiori, M. Fabricius, X. Mazzalay, N. Nowak, S. P. Rusli, and R. Bender. The SINFONI black hole survey: the black hole fundamental plane revisited and the paths of (co) evolution of supermassive black holes and bulges. *ApJ*, 818(1):47, 2016.

D. J. Saikia. Jets in radio galaxies and quasars: An observational perspective. *Journal of Astrophysics and Astronomy*, 43(2):97, 2022.

E. E. Salpeter. Accretion of interstellar matter by massive objects. *Publications of Goddard Space Flight Center*, 1:165, 1964.

D. J. D. Santos, T. Shimizu, R. Davies, Y. Cao, J. Dexter, P. T. de Zeeuw, F. Eisenhauer, N. M. Förster-Schreiber, H. Feuchtgruber, R. Genzel, S. Gillessen, L. Kuhn, D. Lutz, T. Ott, S. Rabien, J. Shangguan, E. Sturm, and L. J. Tacconi. Spectroscopic active galactic nucleus survey at $z\sim2$ with NTT/SOFI for GRAVITY+ observations. *A&A*, 696:A30, 2025a.

D. J. D. Santos, T. Shimizu, R. Davies, Y. Cao, J. Dexter, P. T. de Zeeuw, F. Eisenhauer, N. M. Förster-Schreiber, H. Feuchtgruber, R. Genzel, S. Gillessen, L. Kuhn, D. Lutz, T. Ott, S. Rabien, J. Shangguan, E. Sturm, and L. J. Tacconi. Mock GRAVITY Observations of a Radiative Hydrodynamic BLR Simulation. *to be submitted at A&A*, 2025b.

M. Schmidt. The Discovery of Quasars Investigation of the Radio Source 3C 273 by the Method of Lunar Occultations. *Nature*, 197:1037, 1963.

P. Schneider. *Extragalactic Astronomy and Cosmology*. Springer Berlin Heidelberg, Berlin, Heidelberg, 2015.

P. Severgnini, A. Caccianiga, and R. Della Ceca. A new technique to efficiently select Compton-thick AGN. *A&A*, 542:A46, 2012.

C. K. Seyfert. Nuclear Emission in Spiral Nebulae. *ApJ*, 97:28, 1943.

E. Shablovinskaya, L. Č. Popović, R. Uklein, E. Malygin, D. Ilić, S. Ciroi, D. Oparin, L. Crepaldi, L. Slavcheva-Mihova, B. Mihov, and Y. Nikolov. Polarimetric Reverberation Mapping in Medium-Band Filters. *Universe*, 9(1):52, 2023.

N. I. Shakura and R. A. Sunyaev. Black Holes in Binary Systems. Observational Appearance. *A&A*, 24:337, 1973.

Z. Shang, M. S. Brotherton, R. F. Green, G. A. Kriss, J. Scott, J. K. Quijano, O. Blaes, I. Hubeny, J. Hutchings, M. E. Kaiser, and A. Koratkar. Quasars and the big blue bump. *ApJ*, 619(1):41, 2005.

J. Shangguan, L. C. Ho, F. E. Bauer, R. Wang, and E. Treister. AGN feedback and star formation of quasar host galaxies: Insights from the molecular gas. *ApJ*, 899(2):112, 2020.

A. E. Shapley, R. L. Sanders, S. Salim, N. A. Reddy, M. Kriek, B. Mobasher, A. L. Coil, B. Siana, S. H. Price, I. Shivaei, and J.S Dunlop. The MOSFIRE Deep Evolution Field Survey: Implications of the Lack of Evolution in the Dust Attenuation–Mass Relation to z $\sim$ 2. *ApJ*, 926:145, 2022.

A. I. Shapovalova, L.Č. Popović, N. G. Bochkarev, A. N. Burenkov, V. H. Chavushyan, S. Collin, V. T. Doroshenko, D. Ilić', and A. Kovačević. Long-term variability of the Broad Emission Line profiles in AGN. *New Astronomy Reviews*, 53(7-10):191–197, 2009.

S. Sharma, J. Bland-Hawthorn, J. Binney, K. C. Freeman, M. Steinmetz, C. Boeche, O. Bienayme, B. K. Gibson, G. F. Gilmore, E.K. Grebel, A. Helmi, G. Kordopatis, U. Munari, J. F. Navarro, Q. A. Parker, W. A. Reid, G. M. Seabroke, A. Siebert, F. Watson, M. E. K. Williams, R. F. G. Wyse, and T. Zwitter. Kinematic modeling of the milky way using the RAVE and GCS stellar surveys. *ApJ*, 793:51, 2014. doi: 10.1088/0004-637X/793/1/51.

Y. Shen. Astrometric reverberation mapping. *ApJ*, 757(2):152, 2012b.

Y. Shen and X. Liu. Comparing single-epoch virial black hole mass estimators for luminous quasars. *ApJ*, 753:125, 2012.

Y. Shen and X. Liu. Comparing single-epoch virial black hole mass estimators for luminous quasars. *ApJ*, 753:125, 2012a.

Y. Shen, C. J. Grier, K. Horne, Z. Stone, J. I. Li, Q. Yang, Y. Homayouni, J. R. Trump, S. F. Anderson, W. N. Brandt, and P. B. Hall. The Sloan Digital Sky Survey Reverberation Mapping Project: Key Results. *ApJ*, 272(2):26, 2023.

G. A. Shields. A brief history of active galactic nuclei. *PASP*, 111(760):661, 1999.

J. Silk. Ultraluminous starbursts from supermassive black hole-induced outflows. *MNRAS*, 364(4):1337, 2005.

J. Silk. Unleashing positive feedback: Linking the rates of star formation, supermassive black hole accretion, and outflows in distant galaxies. *ApJ*, 772:112, 2013.

C. Simpson, M. Ward, P. O'Brien, and J. Reeves. Optical and infrared observations of the luminous quasar PDS 456: a radio-quiet analogue of 3C 273? *MNRAS*, 303:L23–L28, 1999.

J Skilling. Nested Sampling. In Rainer Fischer, Roland Preuss, and Udo Von Toussaint, editors, *Bayesian Inference and Maximum Entropy Methods in Science and Engineering: 24th International Workshop on Bayesian Inference and Maximum Entropy Methods in Science and Engineering*, volume 735 of *American Institute of Physics Conference Series*, pages 395–405, 2004. doi: 10.1063/1.1835238.

V. M. Slipher. The spectrum and velocity of the nebula NGC 1068 (M77). *Lowell Obs. Bull.*, 3:59, 1917.

R. J. Smethurst, B. D. Simmons, C. J. Lintott, and J. Shanahan. Secularly powered outflows from AGNs: The dominance of non-merger driven supermassive black hole growth. *MNRAS*, 489(3):4016, 2019.

J. E. Smith, A. Robinson, D. M. Alexander, S. Young, D. J. Axon, and E. A. Corbett. Seyferts on the edge: polar scattering and orientation-dependent polarization in Seyfert 1 nuclei. *MNRAS*, 350:140–160, 2004.

A. Soltan. Masses of quasars. *MNRAS*, 200:115, 1982.

R. S. Somerville, P. Behroozi, V. Pandya, A. Dekel, S. M. Faber, A. Fontana, A. M. Koekemoer, D. C. Koo, P. G. Pérez-González, J. R. Primack, and P. Santini. The relationship between galaxy and dark matter halo size from $z \sim 3$ to the present. *MNRAS*, 473(2): 2714–2736, 2018.

J. S. Speagle. dynesty: A dynamic nested sampling package for estimating Bayesian posteriors and evidences. *MNRAS*, 493:3132, 2020.

A. Stemo, J. M. Comerford, R. S. Barrows, D. Stern, R. J. Assef, and R.L. Griffith. A Catalog of AGN Host Galaxies Observed with HST/ACS: Correlations between Star Formation and AGN Activity. *ApJ*, 888(2):78, 2020.

D. Stern, R. J. Assef, D. J. Benford, A. Blain, R. Cutri, A. Dey, P. Eisenhardt, R. L. Griffith, T. H. Jarrett, S. Lake, and F. Masci. Mid-infrared selection of active galactic nuclei with the wide-field infrared survey explorer. I. Characterizing WISE-selected active galactic nuclei in COSMOS. *ApJ*, 753(1):30, 2012.

M. Stickel, P. Padovani, C. M. Urry, J. W. Fried, and H. Kuehr. The complete sample of 1 Jansky BL Lacertae objects. *ApJ*, 374:431–439, 1991.

M. R. Stock. Spectro-Interferometric Signatures of the Broad Line Regions in Active Galactic Nuclei. Master's thesis, Technische Universität München, 2018.

T. Storchi-Bergmann, J. D. S. Schimoia, B. M. Peterson, M. Elvis, K. D. Denney, M. Eracleous, and R.S. Nemmen. Double-peaked profiles: ubiquitous signatures of disks in the broad emission lines of active galactic nuclei. *ApJ*, 835:236, 2017.

Kate Storey-Fisher, David W. Hogg, Hans-Walter Rix, Anna-Christina Eilers, Giulio Fabbian, Michael R. Blanton, and David Alonso. Quaia, the Gaia-unWISE Quasar Catalog: An All-sky Spectroscopic Quasar Sample. *ApJ*, 964(1):69, 2024. doi: 10.3847/1538-4357/ad1328.

I. V. Strateva, M. A. Strauss, L. Hao, D. J. Schlegel, P. B. Hall, J. E. Gunn, L. X. Li, Z. Ivezic, G. T. Richards, N. L. Zakamska, and W. Voges. Double-peaked low-ionization emission lines in active galactic nuclei. *ApJ*, 126(41):1720, 2003.

E. Sturm, M. Schweitzer, D. Lutz, A. Contursi, R. Genzel, M. D. Lehnert, L. J. Tacconi, S. Veilleux, D. S. Rupke, D. C. Kim, and A. Sternberg. Silicate emissions in active galaxies: from LINERs to QSOs. *ApJ*, 629(1):L21, 2005.

E. Sturm, D. Rupke, A. Contursi, D. C. Kim, D. Lutz, H. Netzer, S. Veilleux, R. Genzel, M. Lehnert, L. J. Tacconi, and D. Maoz. Mid-infrared diagnostics of LINERS. *ApJ*, 653 (1):L13, 2006.

H. Suh, F. Civano, B. Trakhtenbrot, F. Shankar, G. Hasinger, D .B. Sanders, and V. Allevato. No significant evolution of relations between black hole mass and galaxy total stellar mass up to z $\sim$ 2.5. *ApJ*, 889(1):32, 2020.

L. J. Tacconi, R. Genzel, and A. Sternberg. The evolution of the star-forming interstellar medium across cosmic time. *ARA&A*, 58:157, 2020.

M. Tajer, M. Polletta, L. Chiappetti, L. Maraschi, G. Trinchieri, D. Maccagni, S. Andreon, O. Garcet, J. Surdej, M. Pierre, and O. Le Fèvre. Obscured and unobscured AGN populations in a hard-X-ray selected sample of the XMDS survey. *A&A*, 467(1):73, 2006.

J. Terrell. Quasi-stellar diameters and intensity fluctuations. *Science*, 145(3635):918–919, 1964.

S. Thater, D. Krajnović, M. Cappellari, T. A. Davis, P.T. de Zeeuw, R. M. McDermid, and M. Sarzi. Six new supermassive black hole mass determinations from adaptive-optics assisted SINFONI observations. *A&A*, 625:A62, 2019.

A.T. Tokunaga. *New generation ground-based optical/infrared telescopes.* In Encyclopedia of the Solar System; Elsevier, 2014.

C. A. Torres, G. R. Quast, R. Coziol, F. Jablonski, R. de la Reza, J. R. Lepine, and J. Gregorio-Hetem. Discovery of a Luminous Quasar In The Nearby Universe. *ApJ*, 488: 19–22, 1997.

P. Tozzi, R. Gilli, V. Mainieri, C. Norman, G. Risaliti, P. Rosati, J. Bergeron, S. Borgani, R. Giacconi, G. Hasinger, and M. Nonino. X-ray spectral properties of active galactic nuclei in the Chandra Deep Field South. *A&A*, 451(2):457, 2006.

B. Trakhtenbrot, C. Ricci, M. J. Koss, K. Schawinski, R. Mushotzky, Y. Ueda, S. Veilleux, I. Lamperti, K. Oh, E. Treister, and D. Stern. BAT AGN Spectroscopic Survey (BASS)–VI. The ΓX–L/L Edd relation. *MNRAS*, 470(1):800–814, 2017.

T. Treu, M. A. Malkan, and R. D. Blandford. The Relation between Black Hole Mass and Velocity Dispersion At $z \sim 0.37$. *ApJ*, 615:L97, 2004.

K. R. Tristram and M. Schartmann. On the size-luminosity relation of AGN dust tori in the mid-infrared. *A&A*, 531:A99, 2011.

J. C. Tsai and W.G. Mathews. Interstellar Grains in Elliptical Galaxies: Grain Evolution. *ApJ*, 448:84, 1995.

D. Tytler and X. M. Fan. Systematic QSO emission-line velocity shifts and new unbiased redshifts. *ApJS*, 79:1–36, 1992.

V. U, A. J. Barth, H. A. Vogler, H. Guo, T. Treu, V. N. Bennert, G. Canalizo, A. V. Filippenko, E. Gates, F. Hamann, and M.D. Joner. The Lick AGN Monitoring Project 2016: velocity-resolved Hβ lags in luminous Seyfert galaxies. *ApJ*, 925(1):52, 2022.

M. H. Ulrich and K. Horne. A month in the life of NGC 4151: Velocity-delay maps of the broad-line region. *MNRAS*, 283(3):748, 1996.

J. S. Ulvestad and A. S. Wilson. Radio structures of Seyfert galaxies. V-A flux-limited sample of Markarian galaxies. *ApJ*, 278:544, 1984.

C. M. Urry. An overview of blazar variability, in Richard Miller, H., Webb, J. R. and Noble, J .C., eds. In *ASP Conf. Ser.*, volume 110. Astron. Soc. Pac., San Francisco, 1996.

C. M. Urry and P. Padovani. Unified schemes for radio-loud active galactic nuclei. *PASP*, 107(715):803, 1995.

W. D. Vacca, M. C. Cushing, and J.T. Rayner. A Method of Correcting Near-Infrared Spectra for Telluric Absorption. *PASP*, 115(805):389, 2003.

P. H. van Cittert. Die wahrscheinliche Schwingungsverteilung in einer von einer Lichtquelle direkt oder mittels einer Linse beleuchteten Ebene. *Physica*, 1(1-6):201–210, 1934.

R. C. van den Bosch, J. E. Greene, J.A. Braatz, A. Constantin, and C. Y Kuo. Toward Precision Supermassive Black Hole Masses using Megamaser Disks. *ApJ*, 819:11, 2016. doi: 10.3847/0004-637x/819/1/11.

R. V. Vasudevan and A. C. Fabian. Piecing together the X-ray background: Bolometric corrections for active galactic nuclei. *MNRAS*, 381(3):1235, 2007.

S. Veilleux and D. Osterbrock. Spectral classification of emission-line galaxies. *ApJS*, 63: 295, 1987.

M. P. Véron-Cetty, P. Véron, and A.C. Gonçalves. A spectrophotometric atlas of Narrow-Line Seyfert 1 galaxies. *A&A*, 372(3):730–754, 2001.

M. Vestergaard. Determining central black hole masses in distant active galaxies. *ApJ*, 571(2):733, 2002.

M. Vestergaard and B. M. Peterson. Determining central black hole masses in distant active galaxies and quasars. II. Improved optical and UV scaling relationships. *ApJ*, 641 (2):689, 2006a.

M. Vestergaard and B.M. Peterson. Determining central black hole masses in distant active galaxies and quasars. ii. improved optical and uv scaling relationships. *ApJ*, 641(2):689, 2006b.

M. Vestergaard, K. D. Denney, P. Osmer, and B. M. Peterson. Black hole mass estimations: Limitations and uncertainties Active galaxy nuclei. *In Proceedings of the Workshop "Narrow-Line Seyfert"*, 1, 2011.

L. Villafaña, P. R. Williams, T. Treu, B. J. Brewer, A. J. Barth, V. N. Bennert, H. Guo, M. C. Bentz, G. Canalizo, A. V. Filippenko, and E. Gates. What Does the Geometry of the Hβ BLR Depend On? *ApJ*, 948(2):95, 2023.

K. Wada. Radiation-driven fountain and origin of torus around active galactic nuclei. *ApJ*, 758(1):66, 2011.

K. Wada. Obscuring fraction of active galactic nuclei: implications from radiation-driven fountain models. *ApJ*, 812(1):82, 2015.

K. Wada, P.P. Papadopoulos, and M. Spaans. Molecular gas disk structures around active galactic nuclei. *ApJ*, 702(1):63, 2009.

K. Wada, K. Yonekura, and T. Nagao. Circumnuclear Multiphase Gas in Circinus Galaxy. III. Structure of the Nuclear Ionized Gas. *ApJ*, 867(1):49, 2018.

K. Wada, Y. Kudoh, and T. Nagao. Multiphase gas nature in the sub-pc region of the active galactic nuclei–II. Possible origins of the changing-state AGNs. *MNRAS*, 526(2): 2717–2723, 2023.

A. Y. Wagner, G. V. Bicknell, M. Umemura, R. S. Sutherland, and J. Silk. Galaxy-scale AGN feedback–theory. *Astronomische Nachrichten*, 337(1-2):167, 2016.

J. Wagner. 22 GHz water maser search in 37 nearby galaxies: Four new water megamasers in Seyfert 2 and OH maser/absorber galaxies. *A&A*, 560:A12, 2013.

D. J. Walton, W. N. Alston, P. Kosec, A. C. Fabian, L. C. Gallo, J. A. Garcia, J. M. Miller, E. Nardini, M. T. Reynolds, C. Ricci, and D. Stern. A full characterization of the supermassive black hole in IRAS 09149–6206. *MNRAS*, 499:1480–1498, 2020.

A. Wandel, B.M. Peterson, and M.A. Malkan. Central masses and broad-line region sizes of active galactic nuclei. I. Comparing the photoionization and reverberation techniques. *ApJ*, 526(2):579, 1999.

J. M. Wang, J. Q. Ge, C. Hu, J. A. Baldwin, Y. R. Li, G. J. Ferland, F. Xiang, C. S. Yan, and S. Zhang. Star formation in self-gravitating disks in active galactic nuclei. I. Metallicity gradients in broad-line regions. *ApJ*, 739(1):3, 2011.

J. M. Wang, P. Du, J. A. Baldwin, J. Q. Ge, C. Hu, and G.J. Ferland. Star formation in self-gravitating disks in active galactic nuclei. II. Episodic formation of broad-line regions. *ApJ*, 746(2):137, 2012.

J. M. Wang, J. Qiu, P. Du, and L.C. Ho. Self-shadowing effects of slim accretion disks in active galactic nuclei: the diverse appearance of the broad-line region. *ApJ*, 797(1):65, 2014.

J. M. Wang, P. Du, M. S. Brotherton, C. Hu, Y. Y. Songsheng, Y. R. Li, Y. Shi, and Z.X. Zhang. Tidally disrupted dusty clumps as the origin of broad emission lines in active galactic nuclei. *Nature Astron.*, 1(11):775, 2017.

J. X. Wang, S. Malhotra, J. E. Rhoads, and C.A. Norman. Identifying high-redshift active galactic nuclei using X-ray hardness. *ApJ*, 612(2):L109, 2004.

S. Wang, Y. Shen, L. Jiang, K. Horne, W. N. Brandt, C. J. Grier, L. C. Ho, Y. Homayouni, I. Jennifer, H. Li, and D. P. Schneider. The Sloan Digital Sky Survey Reverberation Mapping Project: Low-ionization Broad-line Widths and Implications for Virial Black Hole Mass Estimation. *MNRAS*, 882:4, 2019.

S. Wang, Y. Shen, L. Jiang, C. J. Grier, K. Horne, Y. Homayouni, B. M. Peterson, J. R. Trump, W. N. Brandt, P. B. Hall, and L.C. Ho. he sloan digital sky survey reverberation mapping project: how broad emission line widths change when luminosity changes. *ApJ*, 903:51, 2020.

T. Waters, A. Kashi, D. Proga, M. Eracleous, A. J. Barth, and J. Greene. Reverberation mapping of the broad line region: application to a hydrodynamical line-driven disk wind solution. *ApJ*, 827(1):53, 2016.

M. Whittle. The narrow line region of active galaxies – i. nuclear [o iii] profiles. *ApJ*, 213 (1):1–31, 1985.

P. R. Williams, A. Pancoast, T. Treu, B. J. Brewer, A. J. Barth, V. N. Bennert, T. Buehler, G. Canalizo, S. B. Cenko, K. I. Clubb, and M. C. Cooper. The Lick AGN monitoring project 2011: dynamical modeling of the broad-line region. *ApJ*, 866(2):75, 2018.

P.R. Williams and T. Treu. CARAMEL-gas: A Step toward Fast Empirical Models of the Broad-line-emitting Gas. *ApJ*, 935(2):128, 2022.

B.J. Wills and I. W. A. Browne. Relativistic beaming and quasar emission lines. *ApJ*, 302: 56–63, 1986.

A. S. Wilson and E.J. Colbert. The difference between radio-loud and radio-quiet active galaxies. *ApJ*, 438:62, 1994.

C. Winge, B. M. Peterson, M. G. Pastoriza, and T. Storchi-Bergmann. Spectroscopic Monitoring of Active Galactic Nuclei from CTIO. II. IC 4329A, ESO 141-G55, Arakelian 120, and Fairall 9. *ApJ*, 469:648, 1996.

Lisa M. Winter, Sylvain Veilleux, Barry McKernan, and T. R. Kallman. The Swift Burst Alert Telescope Detected Seyfert 1 Galaxies: X-Ray Broadband Properties and Warm Absorbers. *ApJ*, 745(2):107, 2012.

H. J. Witt, B. Czerny, and P.T. Zycki. Accretion discs with accreting coronae in active galactic nuclei–II. The nuclear wind. *MNRAS*, 286(4):848, 1997.

P. L. Wizinowich, D. Le Mignant, A. H. Bouchez, R. D. Campbell, J. C. Chin, A. R. Contos, M. A. van Dam, S. K. Hartman, E. M. Johansson, R. E. Lafon, and H. Lewis. The WM Keck Observatory laser guide star adaptive optics system: Overview. *PASP*, 118(840):297, 2006.

J. Woo, S. Wang, S. Rakshit, H. Cho, D. Son, V. N. Bennert, E. Gallo, E. Hodges-Kluck, T. Treu, A. J. Barth, W. Cho, A. Foord, J. Geum, H. Guo, Y. Jadhav, Y. Jeon, K. M. Kabasares, W. S. Kang, C. Kim, M. Kim, T. W. Kim, H. A. N. Le, M. A. Malkan, A. K. Mandal, D. Park, C. Spencer, J. Shin, H. Sung, V. U, P. R. Williams, and N. Yee. The Seoul National University AGN Monitoring Project III: Hβ lag measurements of 32 luminous AGNs and the high-luminosity end of the size-luminosity relation. *arXiv*, 2311.15518, 2023.

J. H. Woo, T. Treu, A. J. Barth, S. A. Wright, J. L. Walsh, M. C. Bentz, P. Martini, V. N. Bennert, G. Canalizo, A. V. Filippenko, and E. Gates. The Lick AGN monitoring project: the M_{BH}–σ_* relation for reverberation-mapped active galaxies. *ApJ*, 716(1):269, 2010.

J. H. Woo, Y. Yoon, S. Park, D. Park, and S. C. Kim. The black hole mass–stellar velocity dispersion relation of narrow-line seyfert 1 galaxies. *ApJ*, 801:38, 2015.

S. C. Wright, I. M. McHardy, and R.G. Abraham. Host galaxies of the optically violently variable quasars PKS 0736+017, OJ 287 and LB 2136. *MNRAS*, 295(4):799–812, 1998.

J. Wu, Q. Wu, H. Xue, W. Lei, and B. Lyu. Steep Balmer Decrement in Weak AGNs May Not Be Caused by Dust Extinction: Clues from Low-luminosity AGNs and Changing-look AGNs. *ApJ*, 950(2):106, 2023.

G. Yang, W. N. Brandt, F. Vito, C. J. Chen, J. R. Trump, B. Luo, M. Y. Sun, Y. Q. Xue, A. M. Koekemoer, D. P. Schneider, and C. Vignali. Linking black hole growth with host galaxies: the accretion–stellar mass relation and its cosmic evolution. *MNRAS*, 475(2): 1887, 2017.

J. Yang, Z. Paragi, E. Nardini, W. A. Baan, L. Fan, P. Mohan, E. Varenius, and T. An. The nearby extreme accretion and feedback system PDS 456: Finding a complex radio-emitting nucleus. *MNRAS*, 500:2620–2626, 2021.

S. Yazici, T. Sukegawa, M. Mayer, F. Eisenhauer, Y. Okura, K. Perraut, L. Jocou, S. Gillessen, F. Haussmann, A. Buron, and D. Huber. GRAVITY upgrade with high-performance grisms with factor > 2 enhanced throughput. *Optical and Infrared Interferometry and Imaging VII*, 11446:493–520, 2021.

L. M. Yu, W. H. Bian, C. Wang, B. X. Zhao, and X. Ge. Calibration of the virial factor f in supermassive black hole masses of reverberation-mapped AGNs. *MNRAS*, 488(2): 1519, 2019.

L. M. Yu, B. X. Zhao, W. H. Bian, C. Wang, and X. Ge. An extended size–luminosity relation for the reverberation-mapped AGNs: The role of the accretion rate. *MNRAS*, 491(4):5881–5896, 2020.

Q. Yu and Y. Lu. Fe Kα line: A tool to probe massive binary black holes in Active Galactic Nuclei? *A&A*, 377(1):17, 2001.

Z. Yu, P. Martini, A. Penton, T. M. Davis, U. Malik, C. Lidman, B. E. Tucker, R. Sharp, C. S. Kochanek, B. M. Peterson, and M. Aguena. OzDES Reverberation Mapping Programme: the first Mg II lags from 5 yr of monitoring. *MNRAS*, 507(3):3771–3788, 2021.

M. S. Yun, N. A. Reddy, N. Z. Scoville, D. T. Frayer, E. I. Robson, and R. P. J. Tilanus. Multiwavelength Observations of the Gas-Rich Host Galaxy of PDS 456: A New Challenge for The ULIRG-to-QSO Transition Scenario. *ApJ*, 601:723, 2004.

F. Zernicke. The concept of degree of coherence and its application to optical problems. *Physica*, 5:785–795, 1938.

X. G. Zhang. Evidence for the Intermediate Broad-line Region of Reverberation-mapped Active Galactic Nucleus PG 0052+251. *ApJ*, 741(2):104, 2011. doi: 10.1088/0004-637X/741/2/104.

L. Zhu, S. N. Zhang, and S. Tang. Evidence for an intermediate line region in active galactic nuclei's inner torus region and its evolution from narrow to broad line seyfert i galaxies. *ApJ*, 700:1173, 2009.

M. Y. Zhuang and L. C. Ho. Evolutionary paths of active galactic nuclei and their host galaxies. *Nature*, 7:1376, 2023.

K. Zubovas and M.A. Bourne. Do AGN outflows quench or enhance star formation? *MNRAS*, 468(4):4956, 2017.

Acknowledgments

First of all, I would like to thank the Lord God for giving me the opportunity to pursue my dream of becoming an astrophysicist. Because of this opportunity, I was able to meet so many people who have influenced me to become my best current self.

I extend my heartfelt gratitude to my official supervisor, Reinhard Genzel, for allowing me to be part of the MPE Infrared group, and most especially to my project supervisor, Taro Shimizu, for being the most patient, empathetic, and excellent mentor I could ever wish for. I would also like to thank Richard Davies for his support and guidance. Both Taro and Ric have become my "compass", always pointing me in the direction where I could thrive and prosper. I wish to emulate their excellence in the field as I reach wider horizons in my new journey.

I am indebted to all the people under the GRAVITY-AGN group in the MPE Infrared group: Jinyi Shangguan, who has patiently taught me many things during my first few years in the group; Yixian Cao, who served as my PhD mentor and reminded me once of how everyone in the group wanted me to succeed; and Eckhard Sturm and Dieter Lutz, whose insights have proven to be crucial not just for my works but also for my own improvement. I will always consider myself lucky that I was able to work with these amazing people in the field. I am also thankful to the GALEV group led by Natascha Förster Schreiber for the interesting discussions on galaxy evolution and AGNs, and to Keiichi Wada for being a helpful and wonderful collaborator.

Furthermore, I am grateful to my colleagues at MPE with whom I have shared my joy and grief over my four years of stay in the institute. I would like to mention Antonia Drescher, whose kindness and brilliance are unparalleled; Lilian Lai Yee Lee, with whom I shared packed lunches and meals from our respective kitchens; Capucine Barféty, whose compassion and energy lifted up the group's mood; Claudia Pulsoni, who I consider a great mother to her family and a big sister to the group; Federico Biondi and Vishaal Gopinath, whom I always joke around with in the group; Guillaume Bourdarot, Juan Manuel Espejo, Şenol Yazıcı, and Jean-Baptiste Jolly, whose wisdom are exceptional yet witty; Felix Mang, who have helped me many times with German translations; Felix Widmann, whose convictions I will always admire; and Jianhang Chen, who has always cheered me up with his assurances. I would also like to share a toast to the rest of the younger members in the group who have made the group a much livelier one: Stavros Pastras, Diogo Ribeiro, Matteo Sadun-Bordoni, Kateryna Kravchenko, Giulia Tozzi, Nicolas Kurtovic, Sierra Grant, and even the ones who stayed at MPE for only a short time and yet left an indelible mark on

the group: Martina Scialpi, Thomas Pichon, Pauline Simonet, Lucas Kuhn, Jonas Sauter, Eleonora Parlanti, Julie Beck, Leticia Scaloni, and the rest of the IMPRS PhD cohort. My PhD experience will never be the same if not for these amazing people.

I will never forget the Filipinos and other friends I have met outside the institute, who served as my second family in Munich. I am forever indebted to my parents-in-Christ, Mylene and Alexander Wollboldt, for always supporting me; Estephanie Kleßinger, for being my first Filipino friend and caring older sister, and her husband, Ulrich, for his silent yet unwavering support; Mae Hoffmann and Toni Österreicher, for being my first friends in Munich; Kat Valeros, Donna Handschuch, Marlyn Rena, Rosario Pergament, and Virginia Enriquez, for their funny stories, laughter, and great food; Albert Cruz, April Dianne Llagas, and Ronald Rosenberg, for being my older brothers and sister in Munich; Stephanie Tumampos, for our long dinners and catch-ups; and the rest of my Filipino circles of friends who I cannot name individually anymore due to their large numbers. I am thankful to Feast Light München for being a family in Munich where I can always come back to; the English-Speaking Catholic Mission (ESCM) Munich led by Fr. Stephan Kappler and supported by Fr. Markus Dreher, and the Filipino Catholic Community led by Fr. Jonas Piodo for allowing me to serve in the commmunity and in their respective churches; to the Sunday School volunteers and Young Adult Ministry of ESCM for their dedication and support; and to all the Filipinos that I have met along my journey in Munich. Every time I am with them, I always feel like I am just within my own country. Special thanks as well to Christian Vogt for being one of my great German friends in Munich.

I will also remember the support I received from my friends in Taiwan and the Philippines: my previous colleagues from National Tsing Hua University; my high-school friends from Cayetano Science High School, my college friends from De La Salle University; my friends from the Episcopal Church of the Holy Spirit where I was once active in volunteering at; and the Filipino astronomers and space scientists that have paved the way for a more prosperous Filipino astronomy community in which I look forward to contributing to: Reinabelle Reyes, Kristine Jane Atienza, Mark Angelo Purio, Harlee Quizzagan, and Lovely Andeo.

Last but not least, I owe my degree to my family who tirelessly pray for my safety and love me for who I am. I hope that someday, I will be able to repay their sacrifice for me in the near future.

I dedicate this work to all these people who have now become a part of me. As I pursue the next stage of my life, I carry with me their heartfelt hopes and wishes. *Maraming salamat sa inyong lahat!*